



## City Research Online

### City, University of London Institutional Repository

---

**Citation:** Skrekas, P. (2018). Seismic structural assessment scenarios of RC structures subjected to pounding. (Unpublished Doctoral thesis, City, University of London)

This is the accepted version of the paper.

This version of the publication may differ from the final published version.

---

**Permanent repository link:** <https://openaccess.city.ac.uk/id/eprint/22337/>

**Link to published version:**

**Copyright:** City Research Online aims to make research outputs of City, University of London available to a wider audience. Copyright and Moral Rights remain with the author(s) and/or copyright holders. URLs from City Research Online may be freely distributed and linked to.

**Reuse:** Copies of full items can be used for personal research or study, educational, or not-for-profit purposes without prior permission or charge. Provided that the authors, title and full bibliographic details are credited, a hyperlink and/or URL is given for the original metadata page and the content is not changed in any way.

# **Seismic structural assessment scenarios of RC structures subjected to pounding**

**Thesis by  
PASCHALIS SKREKAS**

In partial fulfilment for the degree of  
Doctor of Philosophy



**CITY, UNIVERSITY OF LONDON**

**School of Mathematics, Computer Science & Engineering  
Department of Civil Engineering  
Research Center for Civil Engineering Structures**





CITY UNIVERSITY OF LONDON

School of Mathematics

Computer Science & Engineering

Department of Civil Engineering

*Research Center for Civil Engineering*

*Structures*

# **Seismic structural assessment scenarios of RC structures subjected to pounding**

Doctoral Candidate: Paschalis Skrekas

Supervisor: Dr Agathoklis Giaralis

Co-Supervisor: Prof. Anastasios Sextos

London, September 2018



# Contents

<b>ACKNOWLEDGEMENTS .....</b>	<b>IV</b>
<b>DECLARATION.....</b>	<b>VI</b>
<b>ABSTRACT.....</b>	<b>VIII</b>
<b>CHAPTER 1 INTRODUCTION .....</b>	<b>1</b>
1.1 BACKGROUND AND MOTIVATION .....	1
1.2 AIMS AND OBJECTIVES .....	3
1.3 THESIS ORGANISATION.....	6
<b>CHAPTER 2 INTERACTION OF ADJACENT BUILDING STRUCTURES DURING EARTHQUAKES .....</b>	<b>8</b>
2.1 OVERVIEW.....	8
2.2 MITIGATING POUNDING .....	13
2.3 CONTACT MODELLING FOR EISP APPLICATIONS.....	16
2.3.1 <i>Theory of Stereomechanics for Contact Modelling</i> .....	17
2.3.2 <i>Contact Elements</i> .....	18
2.4 STUDIES ON THE MINIMUM SAFETY DISTANCE.....	20
2.5 INFLUENCE OF EISP ON THE SEISMIC RESPONSE OF ADJACENT STRUCTURES .....	22
2.6 RESEARCH GAPS .....	23
<b>CHAPTER 3 THE PERFORMANCE BASED EARTHQUAKE ENGINEERING FRAMEWORK.....</b>	<b>26</b>
3.1 OVERVIEW.....	26
3.2 INCREMENTAL DYNAMIC ANALYSIS .....	28
3.3 STATISTICAL ANALYSIS OF IDA CURVES.....	30
3.4 SELECTING IDA PARAMETERS .....	32
<b>CHAPTER 4 INFLUENCE OF BI-DIRECTIONAL POUNDING ON THE INELASTIC DEMAND DISTRIBUTION OF THREE ADJACENT MULTI-STOREY RC BUILDINGS.....</b>	<b>37</b>
4.1 OVERVIEW.....	37
4.2 BUILDING BLOCK CASE STUDIED.....	39
4.2.1 <i>Design considerations</i> .....	39

4.2.2	<i>Finite Element (FE) modelling assumptions</i> .....	40
4.2.3	<i>Material Nonlinearity</i> .....	44
4.2.4	<i>Geometric Nonlinearity</i> .....	45
4.3	REPRESENTATION OF SEISMIC INPUT ACTION.....	46
4.4	EFFECT OF BI-DIRECTIONAL POUNDING ON THE INELASTIC DEMAND DISTRIBUTION OF THREE COUPLED BUILDINGS.....	48
4.5	INFLUENCE OF STRONG GROUND MOTION SEVERITY.....	57
4.6	CLOSURE.....	58
<b>CHAPTER 5 FRAGILITY SENSITIVITY OF RC COLLIDING BUILDINGS ON THE MODELLING PARAMETERS OF THE LINEAR AND LINEAR VISCOELASTIC CONTACT MODEL.....</b>		<b>60</b>
5.1	OVERVIEW.....	60
5.2	RELATED WORK AND MOTIVATION.....	61
5.3	ADOPTED BENCHMARK STRUCTURAL MODELS.....	62
5.4	CASES OF POUNDING MODEL PARAMETERS CONSIDERED.....	66
5.5	SELECTED IM AND GROUND MOTION SUITE.....	69
5.5.1	<i>Record selection and scaling</i> .....	69
5.5.2	<i>A proposed IM for EISP case studies</i> .....	70
5.6	NUMERICAL RESULTS AND DISCUSSION.....	71
5.6.1	<i>Uncoupled Response</i> .....	71
5.6.2	<i>Coupled Response Time Histories</i> .....	73
5.6.3	<i>IDA Curves of Interacting Oscillators with Zero Gap</i> .....	73
5.6.4	<i>Impact of Gap on Fragility Curves of Interacting Oscillators</i> .....	75
5.6.5	<i>Impact of <math>K_p</math> on Fragility Curves</i> .....	80
5.6.6	<i>Influence of Energy Dissipation During Collisions</i> .....	85
5.6.7	<i>Impact of Energy Dissipation on The Number of Pounding Events and Magnitude of Pounding Forces</i> .....	89
5.7	CLOSURE.....	90
<b>CHAPTER 6 PROBABILISTIC SEISMIC PERFORMANCE ASSESSMENT OF ADJACENT RC BUILDING FRAMES INTERACTING AT FLOOR LEVELS.</b>		
<b>93</b>		
6.1	OVERVIEW.....	93
6.2	STRUCTURAL MODELING ASSUMPTIONS.....	94
6.3	SELECTED IM AND GROUND MOTION SUITE.....	98
6.3.1	<i>Record selection and scaling</i> .....	98
6.4	NUMERICAL RESULTS AND DISCUSSION.....	101

6.4.1	<i>IDA curves</i> .....	103
6.4.2	FRAGILITY CURVES .....	105
6.4	COMPARING PROBABILISTIC PREDICTIONS BASED ON SDOF AND MDOF BUILDING FRAMES .....	109
6.5	CLOSURE .....	111
<b>CHAPTER 7 CONCLUSIONS</b> .....		<b>113</b>
7.1	SUMMARY AND MAIN CONTRIBUTIONS .....	113
7.2	RECOMMENDATIONS FOR FUTURE WORK .....	117
	Appendix A - Parameters of Inelastic Elements .....	130
	Appendix B - Ground Motions Catalogue .....	132
	Appendix C - IDA Curves .....	135
	Appendix D - Fragility Curves .....	152
	Appendix E - Fragility Curves Statistics .....	164
	Appendix F - Pounding Event Heat-maps .....	176
	Appendix G - Co-authored Publications .....	182

# Acknowledgements

First and foremost, I would like to thank my supervisor, *Dr Agathoklis Giaralis* for his mentorship, guidance and continuous support throughout my Ph.D studies. Over the last years, Dr Giaralis has offered me unique opportunities that substantially contributed towards my academic and professional development, which I gratefully acknowledge.

I am also particularly grateful to Prof. A. G. Sextos for his valuable contribution throughout my Ph.D studies. He provided guidance and insightful comments that made this work possible.

Last but not least, I would like to thank my family for supporting me spiritually through writing this thesis and my life in general.



# Declaration

I grant powers of discretion to the University Librarian to allow the thesis to be copied in whole or in part without further reference to the author. This permission covers only single copies made for study purposes, subject to normal conditions of acknowledgement.



# Abstract

During earthquake induced strong ground motion (GM) adjacent buildings with inadequate clearance will interact/collide resulting in the development of pounding forces at locations of contact. Typically, forces due to earthquake induced seismic pounding (EISP), and their consequences, are not accounted for in the seismic design of buildings as contemporary codes of practice for earthquake resistance specify minimum clearance among neighbouring structures regarded as adequate to minimise EISP occurrence/consequences likelihood at least for the nominal design earthquake level. However, field observations in congested cities in the aftermath of several recent major seismic events suggest that considerable seismic loss is due to EISP as code-prescribed clearances are not implemented in practice.

These observations triggered significant research efforts since the late 1980s to develop efficient finite element (FE) modelling schemes capturing EISP, to study the influence of EISP in seismic demands of colliding structures, and to propose methods of mitigating EISP consequences. Nevertheless, to date, most relevant computational-based research works adopted simplified structural models used as proxies of the colliding buildings, such as planar multi degree-of-freedom (MDOF) frames arranged in series or single degree-of-freedom (SDOF) pounding oscillators, to study EISP via nonlinear response history analyses (NRHA). Further, uncertainty quantification due to record-to-record GM variability to inelastic seismic demands under EISP has not been addressed within modern probabilistic performance-based earthquake engineering (PBEE) context.

To this end, this thesis aims, first, to assess the influence of EISP to inelastic demands at structural member level in a case-study real-life building block and, second, to quantify EISP influence to fragility curves of commonly adopted simplified structural models (i.e., inelastic SDOF oscillators and inelastic planar MDOF frame structures) as a measure of seismic vulnerability of colliding structures in a statistical framework accounting for record-to-record variability. The thesis focuses on reinforced concrete (rc) code-compliant building structures and treats exclusively slab-to-slab

interaction/pounding assuming that no significant local failure occurs at locations of collision.

The first aim is addressed by developing detailed three-dimensional lumped-plasticity FE models of three adjacent irregular in-plan rc structures with coupled frame-wall lateral load resisting systems in an L-shaped arrangement and with unequal number of floors. Series of NRHA is conducted for a pair of spectrum-compatible GMS with increasing intensity (i.e., incremental dynamic analysis-IDA) acting along two horizontal perpendicular axes for FE models with and without EISP. Variations of inelastic demands across all building floors for different types of structural members (i.e., beams, columns, and walls) are reported due to EISP for different GM intensities. Considerable floor-wise spread of differences of inelastic demands due to EISP is found in all 3 structures and types of members. This novel finding suggests that EISP influence to local member inelastic demands may not be accurately quantified through simplified planar FE MDOF models which cannot capture the response of complex building blocks colliding bi-directionally and accounting for torsional response. Therefore, it is recommended that detailed spatial FE models are adopted for seismic vulnerability assessment of existing case-specific structures subject to EISP in several directions.

The second aim is pursued by putting forth a performance based seismic assessment (PBSA) approach which can readily account for record-to-record variability, following standard PBEE steps, through application of IDA for a suite of judiciously selected GMs to simplified inelastic FE models capturing EISP. In doing so, a novel intensity measure (IM), namely the geometric mean of the spectral acceleration at the fundamental natural period of the pounding/interacting structures,  $avgS_a$ , is proposed. It is proved numerically that  $avgS_a$  is much more efficient than peak ground acceleration (PGA) which is exclusively used as the IM in all EISP studies found in the literature. This is established by noting that  $avgS_a$  reduces significantly the spread of IDA curves compared to PGA, gauged via the standard deviation of log-normal distributions fitted to the IDA curves data at different limit states, for several different pairs of colliding inelastic SDOF oscillators used as proxies to 5 different 8-storey and 12-storey benchmark rc multi-storey frame structures design to the current Eurocode 2 and 8 subject to a suite of 72 GMs. Moreover, novel probabilistic models in terms of fragility curves of adjacent rc structures are presented and discussed derived for both the above inelastic SDOF oscillators and for the detailed MDOF lumped-plasticity models of the planar

multi-storey frame structures. Sensitivity analyses is undertaken to quantify the influence of various pounding model parameters to inelastic demand statistics (i.e., shape of fragility curves) indicating that stiffness and damping properties of the pounding model is not as influential as clearance between structures. Lastly, mean and standard deviation of IDA curves data obtained by interacting MDOF models and their equivalent (i.e., derived through pushover analysis) inelastic SDOF oscillators are compared. It is found that interacting SDOF proxies capture accurately record-to-record variability expressed through the standard deviation of fitted log-normal distributions to IDA curves but tend to underestimate peak inelastic demands in the mean sense compared to the MDOF models. Thus, it is again concluded that caution need to be exercised in adopting simplified models for capturing EISP.

Overall, the PBSA tools developed in this thesis and the numerical data furnished shed new light on the influence of EISP to different levels of sophistication in structural modelling of building structure and to the uncertainty in inelastic seismic demands due to record-to-record variability. These tools together with foreseeable extensions pave the way for seismic risk analyses in congested urban environments accounting for EISP phenomena to improve the accuracy of seismic loss predictions.

# List of Figures

FIGURE 1.1: WORKFLOW FOR COMPARATIVE SEISMIC STRUCTURAL PERFORMANCE QUANTIFICATION OF ADJACENT STRUCTURES WITH AND WITHOUT INTERACTION (I.E., SLAB-TO-SLAB POUNDING/COLLISIONS) DENOTED AS COUPLED AND UNCOUPLED MODEL CASES. ....	4
FIGURE 1.2: MATRIX THAT ILLUSTRATES THE SEISMIC ACTION AND BUILDING MODELLING COMPLEXITY COMBINATIONS ADOPTED IN THIS THESIS WITH THE CORRESPONDING CHAPTERS.. ....	5
FIGURE 2.1: SEVERE DAMAGES INCLUDING CONCRETE SPALLING AND COLUMN SHEARING, OBSERVED ON TWO ADJACENT RC BUILDINGS IN THE AFTERMATH OF THE 2014 KEFALONIA EARTHQUAKE. ....	9
FIGURE 2.2: EARTHQUAKE INDUCED STRUCTURAL POUNDING BETWEEN BUILDINGS WITH A) UNEQUAL FLOOR HEIGHTS AND/OR B) DIFFERENT FOUNDATION LEVELS, LEADS TO FLOOR-SLAB TO COLUMN COLLISIONS WITH A POTENTIAL ABRUPT FAILURE OF COLUMNS, DUE TO COLUMN SHEARING (JENG AND TZENG, 2000). ....	9
FIGURE 2.3: POUNDING BETWEEN A STIFF AND A FLEXIBLE STRUCTURE WITH EQUAL FLOOR HEIGHTS (JENG AND TZENG, 2000). ....	10
FIGURE 2.4: POUNDING BETWEEN BUILDINGS WITH DIFFERENT FLOOR ELEVATIONS (JENG AND TZENG, 2000).....	11
FIGURE 2.5: SCHEMATIC THAT ILLUSTRATES THE CASE OF POUNDING BETWEEN BUILDINGS THAT EXHIBIT IN PLAN ECCENTRICITY (JENG AND TZENG, 2000). POUNDING OCCURS AT ONE CORNER, TYPICALLY CAUSING EXTENSIVE DAMAGES TO THE COLUMN THAT IS LOCATED AT THAT CORNER. ....	12
FIGURE 2.6: SCHEMATIC FOR THE CASE OF POUNDING BETWEEN BUILDINGS IN SERIES WITH EQUAL FLOOR HEIGHTS (JENG AND TZENG, 2000). TYPICALLY, POUNDING HAS A DETRIMENTAL IMPACT ON THE STRUCTURAL INTEGRITY OF THE BUILDINGS THAT ARE LOCATED AT THE ENDS. ....	12
FIGURE 2.7: COLLISION SHEAR WALLS LOCATED AT THE PROPERTY LINE IN ORDER TO PREVENT COLUMN SHEARING FROM FLOOR TO COLUMN COLLISIONS (ANAGNOSTOPOULOS AND KARAMANEAS, 2008). ....	15
FIGURE 2.8: THE LINEAR AND NON-LINEAR (HERTZ) IMPACT MODELS THAT CONSISTS OF A LINEAR SPRING AND A NON-LINEAR SPRING CORRESPONDINGLY WITH A STIFFNESS $K$ IN SERIES WITH A GAP ELEMENT. THE STIFFNESS $K$ HAS TYPICALLY A VALUE THAT IS PROPORTIONAL TO THE STIFFNESS OF THE COLLIDING STRUCTURES. ....	18
FIGURE 2.9: CONFIGURATION OF THE LINEAR VISCOELASTIC (KELVIN - VOIGT) AND NON-LINEAR VISCOELASTIC (HERTZDAMP) IMPACT MODELS THAT CONSISTS OF A LINEAR SPRING AND A NON-LINEAR SPRING CORRESPONDINGLY IN PARALLEL WITH A VISCOUS DAMPER THAT ALLOWS FOR THE MODELLING OF ENERGY LOSSES DURING IMPACT. ....	19
FIGURE 3.1: THE FOUR DISTINCT STAGES OF THE PERFORMANCE BASED EARTHQUAKE ENGINEERING (PBEE) FRAMEWORK (YANG ET AL, 2009). ....	27
FIGURE 3.2: TYPICAL OBSERVABLE PATTERNS IN AN IDA CURVE (SKREKAS AND GIARALIS, 2013). ....	29

FIGURE 3.3: IDA CURVES OBTAIN FOR A SPECIFIC STRUCTURE EXCITED UNDER A COLLECTION OF GROUND MOTIONS SCALES TO VARIOUS INTENSITY LEVELS TO REPRESENT VARIOUS SEISMIC HAZARD SCENARIOS (VAMVATSIKOS AND CORNELL, 2002).	30
FIGURE 3.4: EXAMPLE OF SUMMARIZED IDA CURVES AND CORRESPONDING LIMIT STATES (VAMVATSIKOS AND CORNELL, 2002).	31
FIGURE 3.5: DISPERSION OF IDA CURVES FOR TWO INTENSITY MEASURES IN (A) AND IN (B) DEMONSTRATING THE EFFICIENCY PROPERTY OF THE SECOND INTENSITY MEASURE IN (B) (TOTHONG AND CORNELL, 2007).	33
FIGURE 4.1: THE CONSIDERED THREE-BUILDING COMPLEX A) TYPICAL FLOOR PLAN; B) LOCATIONS OF THE POTENTIAL POUNDING; C) ILLUSTRATION OF THE REAL CASE THAT IS USED AS A BASIS OF THE EXAMINED CASE; AND D) 3-DIMENSIONAL FINITE ELEMENT MODEL OF THE CORNER BUILDING “K”	40
FIGURE 4.2: PLAN VIEW OF BUILDING K, DEPICTING VARIOUS DIMENSIONS (IN METERS) AND STRUCTURAL ELEMENT SIZES (IN CENTIMETRES).	41
FIGURE 4.3: PLAN VIEW OF BUILDING K1 AND K2 DEPICTING VARIOUS DIMENSIONS (IN METERS) AND STRUCTURAL ELEMENT SIZES (IN CENTIMETRES).	42
FIGURE 4.4: FINITE ELEMENT MODELLING ASSUMPTIONS FOR SHEAR WALLS AND CORES AND CONSIDERED LUMPED PLASTICITY MOMENT-ROTATION LAW.	43
FIGURE 4.5: A) EC8 SPECTRUM AND RESPONSE SPECTRA OF SPECTRUM COMPATIBLE ACCELEROGRAMS CONSIDERED. B) TIME TRACES OF SPECTRUM COMPATIBLE ACCELEROGRAMS.	47
FIGURE 4.6: AVERAGE DUCTILITY DEMAND AT THE BASE OF THE SHEAR WALLS (TOP), THE EDGE OF THE BEAMS (MIDDLE) AND COLUMNS (BOTTOM) OF THE GROUND FLOOR FOR THE CORNER BUILDING “K” WITH AND WITHOUT POUNDING AND DIFFERENT LEVELS OF SEISMIC INTENSITY (PGA).	50
FIGURE 4.7: AVERAGE DUCTILITY DEMAND INDUCED AT THE BEAMS OF THE FIFTH (BOTTOM), SIXTH (MIDDLE) AND SEVENTH FLOOR(TOP) FOR THE CORNER BUILDING “K”, WITH AND WITHOUT POUNDING AND DIFFERENT LEVELS OF SEISMIC INTENSITY (PGA).	52
FIGURE 4.8: VARIATION OF INELASTIC DEMAND ( $M \pm \Sigma$ ) DUE TO STRUCTURAL POUNDING (COLUMNS, $AG = 0.5 G$ ).	53
FIGURE 4.9: VARIATION OF INELASTIC DEMAND ( $M \pm \Sigma$ ) DUE TO STRUCTURAL POUNDING (BEAMS, $AG = 0.5 G$ ).	54
FIGURE 4.10: VARIATION OF INELASTIC DEMAND ( $M \pm \Sigma$ ) DUE TO STRUCTURAL POUNDING (COLUMNS, $AG = 0.9 G$ ).	55
FIGURE 4.11: VARIATION OF INELASTIC DEMAND ( $M \pm \Sigma$ ) DUE TO STRUCTURAL POUNDING (BEAMS, $AG = 0.9 G$ ).	56

FIGURE 4.12: AVERAGE DUCTILITY DEMAND OF SHEAR WALLS AT THE GROUND FLOOR OF BUILDING “K1”, WITH POUNDING (LINKED) AND WITHOUT POUNDING (UN-LINKED) FOR DIFFERENT LEVELS OF SEISMIC INTENSITY (PGA).....	58
FIGURE 5.1: PROPERTIES AND GEOMETRIC CHARACTERISTICS OF THE FIVE ADOPTED RC BUILDINGS FRAMES.....	63
FIGURE 5.2: A) MOMENT - ROTATION BILINEAR BACKBONE CURVE AND B) NON-LINEAR SDOF SYSTEMS MODELLED IN OPENSEES WITH AN ELASTIC ELEMENT AND A ZERO-LENGTH NON-LINEAR SPRING WITH A BI-LINEAR MOMENT - ROTATION LAW.....	65
FIGURE 5.3: PUSHOVER CURVES OF THE FIVE ADOPTED NON-LINEAR SDOF SYSTEMS.....	65
FIGURE 5.4: MODELLING POUNDING FORCES BY MEANS OF THE A) LINEAR CONTACT MODEL AND B) LINEAR VISCOELASTIC POUNDING MODEL, FOR POUNDING BETWEEN TWO BODIES WITH MASSES $M_1$ AND $M_2$ AND CORRESPONDING STIFFNESSES $K_1$ AND $K_2$ .....	67
FIGURE 5.5: PLOTS OF THE A) MAGNITUDE $M_w$ VS THE DISTANCE $R$ FOR THE ALL THE ACCELEROGRAMS IN THE ADOPTED GROUND MOTION SUITE.....	70
FIGURE 5.6: IDA CURVES AND DISTRIBUTIONS OF THE SEISMIC INTENSITY LEVELS AT WHICH THE EXCEEDANCE OF THE 0.427 (M) DISPLACEMENT LIMIT STATE (LIGHT DAMAGE) OCCURS - UNCOUPLED RESPONSE OF THE 12RFDCH SDOF SYSTEM - $\mu$ AND $\sigma$ ARE THE MEAN AND THE STANDARD DEVIATION OF THE LOGNORMAL DISTRIBUTION THAT CORRESPONDS TO THE BEST FIT A) $IM = PGA$ AND B) $IM = GM$ .....	72
FIGURE 5.7: IDA CURVES AND DISTRIBUTIONS OF THE SEISMIC INTENSITY LEVELS AT WHICH THE EXCEEDANCE OF THE 1.441 (M) DISPLACEMENT LIMIT STATE (SEVERE DAMAGE) OCCURS - UNCOUPLED RESPONSE OF THE 12RFDCH SDOF SYSTEM - $\mu$ AND $\sigma$ ARE THE MEAN AND THE STANDARD DEVIATION OF THE LOGNORMAL DISTRIBUTION THAT CORRESPOND THE BEST FIT A) $IM = PGA$ AND B) $IM = GM$ .....	72
FIGURE 5.8: FRAGILITY CURVES FOR THE UNCOUPLED RESPONSE OF THE FIVE NON-LINEAR SDOF SYSTEMS FOR THE TWO LIMIT STATES THAT CORRESPOND TO LIGHT AND SEVERE DAMAGE.....	73
FIGURE 5.9: POUNDING BETWEEN 12RFDCH AND 8SWDCH SDOF SYSTEMS - DISTRIBUTION OF THE SEISMIC INTENSITY LEVELS AT WHICH THE EXCEEDANCE OF THE 0.338 (M) DISPLACEMENT LIMIT STATE OCCURS - COUPLED RESPONSE OF THE 8SWDCH BUILDING WITH GAP = 0.00 (M) - CONTACT FORCES ARE MODELLED VIA THE LINEAR CONTACT MODEL WITH $K_p = HIGH$ - $\mu$ AND $\sigma$ ARE THE MEAN AND THE STANDARD DEVIATION OF THE LOGNORMAL DISTRIBUTION THAT CORRESPONDS TO THE BEST FIT A) $IM = PGA$ AND B) $IM = GM$ .....	74
FIGURE 5.10: POUNDING BETWEEN 12RFDCH AND 8SWDCH SDOF SYSTEMS - DISTRIBUTION OF THE SEISMIC INTENSITY LEVELS AT WHICH THE EXCEEDANCE OF THE 0.962 (M) DISPLACEMENT LIMIT STATE OCCURS - COUPLED RESPONSE OF THE 8SWDCH BUILDING WITH GAP = 0.00 (M) - CONTACT FORCES ARE MODELLED VIA THE LINEAR CONTACT MODEL WITH $K_p = HIGH$ - $\mu$ AND $\sigma$ ARE THE MEAN AND THE STANDARD DEVIATION OF THE LOGNORMAL DISTRIBUTION THAT CORRESPONDS TO THE BEST FIT A) $IM = PGA$ AND B) $IM = GM$ .....	74
FIGURE 5.11: FRAGILITY CURVES OF THE 12RFDCH INELASTIC OSCILLATOR FOR VARIOUS GAP SIZES AND LIGHT DAMAGE LS - POUNDING BETWEEN 12RFDCH AND 8SWDCH - POUNDING FORCES MODELLED IN TERMS OF THE LINEAR POUNDING MODEL.....	75

FIGURE 5.12: FRAGILITY CURVES OF THE 8SWDCH INELASTIC OSCILLATOR FOR VARIOUS GAP SIZES AND LIGHT DAMAGE LS - POUNDING BETWEEN 12RFDCH AND 8SWDCH - POUNDING FORCES MODELLED IN TERMS OF THE LINEAR POUNDING MODEL..... 76

FIGURE 5.13: CONTOUR PLOT OF THE MAGNITUDE OF POUNDING FORCES (UNITS MN) PER GROUND MOTION AND SEISMIC INTENSITY. POUNDING BETWEEN 12RFDCH AND 8SWDCH SDOF OSCILLATORS WITH GAP = 0% OF SD. .... 77

FIGURE 5.14: CONTOUR PLOT OF THE MAGNITUDE OF POUNDING FORCES (UNITS MN) PER GROUND MOTION AND SEISMIC INTENSITY. POUNDING BETWEEN 12RFDCH AND 8SWDCH SDOF SYSTEMS WITH GAP = 10% OF SD. .... 77

FIGURE 5.15: CONTOUR PLOT OF THE NUMBER OF POUNDING EVENTS PER GROUND MOTION AND SEISMIC INTENSITY. POUNDING BETWEEN 12RFDCH AND 8SWDCH SDOF SYSTEMS WITH GAP = 0% OF SD. .... 78

FIGURE 5.16: CONTOUR PLOT OF THE NUMBER OF POUNDING EVENTS PER GROUND MOTION AND SEISMIC INTENSITY. POUNDING BETWEEN 12RFDCH AND 8SWDCH SDOF SYSTEMS WITH GAP = 10% OF SD. .... 78

FIGURE 5.17: FRAGILITY CURVES OF THE 12RFDCH INELASTIC OSCILLATOR FOR VARIOUS GAP SIZES AND SEVERE DAMAGE LS - POUNDING BETWEEN 12RFDCH AND 8SWDCH - POUNDING FORCES MODELLED IN TERMS OF THE LINEAR POUNDING MODEL..... 79

FIGURE 5.18: FRAGILITY CURVES OF THE 8SWDCH INELASTIC OSCILLATOR FOR VARIOUS GAP SIZES AND SEVERE DAMAGE LS - POUNDING BETWEEN 12RFDCH AND 8SWDCH - POUNDING FORCES MODELLED IN TERMS OF THE LINEAR POUNDING MODEL..... 79

FIGURE 5.19: FRAGILITY CURVES OF THE 12RFDCL INELASTIC OSCILLATOR FOR VARIOUS GAP SIZES AND LIGHT DAMAGE LS - POUNDING BETWEEN 12RFDCL AND 8IFDCH - POUNDING FORCES MODELLED IN TERMS OF THE LINEAR POUNDING MODEL..... 80

FIGURE 5.20: FRAGILITY CURVES OF THE 8IFDCH INELASTIC OSCILLATOR FOR VARIOUS GAP SIZES AND LIGHT DAMAGE LS - POUNDING BETWEEN 12RFDCL AND 8IFDCH - POUNDING FORCES MODELLED IN TERMS OF THE LINEAR POUNDING MODEL..... 81

FIGURE 5.21: FRAGILITY CURVES OF THE 12RFDCL INELASTIC OSCILLATOR FOR VARIOUS GAP SIZES AND SEVERE DAMAGE LS - POUNDING BETWEEN 12RFDCL AND 8IFDCH - POUNDING FORCES MODELLED IN TERMS OF THE LINEAR POUNDING MODEL..... 81

FIGURE 5.22: FRAGILITY CURVES OF THE 8IFDCH INELASTIC OSCILLATOR FOR VARIOUS GAP SIZES AND LIGHT DAMAGE LS - POUNDING BETWEEN 12RFDCL AND 8IFDCH - POUNDING FORCES MODELLED IN TERMS OF THE LINEAR POUNDING MODEL..... 82

FIGURE 5.23: CONTOUR PLOT OF THE NUMBER OF POUNDING EVENTS PER GROUND MOTION AND SEISMIC INTENSITY. POUNDING BETWEEN 12RFDCL AND 8IFDCH SDOF SYSTEMS WITH GAP = 0% OF SD. .... 83

FIGURE 5.24: CONTOUR PLOT OF THE NUMBER OF POUNDING EVENTS PER GROUND MOTION AND SEISMIC INTENSITY. POUNDING BETWEEN 12RFDCL AND 8IFDCH SDOF SYSTEMS WITH GAP = 5% OF SD. .... 83

FIGURE 5.25: POUNDING BETWEEN 12RFDCL AND 8IFDCH. DISPLACEMENT RESPONSE HISTORIES FOR BOTH OSCILLATORS WITH ZERO INITIAL SEPARATION DISTANCE AND  $K_p$ =HIGH. A) SEISMIC INTENSITY AT 0.12 G (GM) AND B) SEISMIC INTENSITY AT 0.87 G (GM). .... 84

FIGURE 5.26: POUNDING BETWEEN 12RFDCH AND 8WDCL SDOF SYSTEMS - LIGHT DAMAGE LIMIT STATE AND $K_p = High$ A) MEAN VALUES OF THE FRAGILITY MODELS OF THE TWO ADOPTED CONTACT MODELS AS A FUNCTION OF THE INITIAL SEPARATION DISTANCE B) STANDARD DEVIATION VALUES OF THE FRAGILITY MODELS FOR THE TWO ADOPTED CONTACT MODELS AS A FUNCTION OF INITIAL SEPARATION DISTANCE C) PERCENTAGE DIFFERENCE BETWEEN THE MEAN VALUES OF THE TWO ADOPTED CONTACT MODELS AS A FUNCTION OF THE INITIAL SEPARATION DISTANCE AND B) PERCENTAGE DIFFERENCE BETWEEN THE STANDARD.....	87
FIGURE 5.27: POUNDING BETWEEN 12RFDCH AND 8SWDCH - LINEAR POUNDING MODEL - GAP = 0.00 (M) AND $K_p = High$ A) CONTOUR PLOT OF THE NUMBER OF POUNDING EVENTS PER GROUND MOTION AND INTENSITY LEVEL B) CONTOUR PLOT OF THE MAGNITUDE OF THE POUNDING FORCES PER GROUND MOTION AND INTENSITY LEVEL.....	89
FIGURE 5.28: DURATION OF THE 72 GROUND MOTIONS CONSIDERED IN THIS STUDY.....	90
FIGURE 6.1: DESIGNATIONS AND DIMENSIONS OF THE TWO HEREIN ADOPTED RC BUILDINGS, ASSUMED TO BE IN INITIAL CONTACT. SLAB TO SLAB POUNDING IS MODELLED BY MEANS OF THE LINEAR VISCO-ELASTIC POUNDING MODEL.....	95
FIGURE 6.2: A) FORCE DEFORMATION MODEL FOR RC BEAMS, COLUMNS AND SHEAR WALLS (OPENSEES CONCRETE02 UNIAXIAL MATERIAL) B) FORCE - DEFORMATION RELATIONSHIP FOR THE CONTACT ELEMENT (OPENSEES ELASTICPPGAP UNIAXIAL MATERIAL) C) FORCE DEFORMATION MODEL FOR THE REINFORCEMENT STEEL (OPENSEES STEEL01 UNIAXIAL MATERIAL).....	96
FIGURE 6.3: STATIC PUSHOVER CURVES OF THE 2D RC BUILDINGS FRAMES JUXTAPOSED THE TARGET PROTOTYPE IDEALIZED BILINEAR PUSHOVER CURVE A) 12RFDCH AND B) 8SWDCH BUILDING.....	97
FIGURE 6.4: DISTRIBUTION OF GROUND MOTIONS IN A) PGA - MW SPACE (B) PGA - R SPACE (C) $M_w$ - R SPACE AND (D) THE PSEUDO SPECTRAL ACCELERATIONS OF THE ADOPTED GROUND MOTION SUITE (TABLE 6.1).....	99
FIGURE 6.5: DISPLACEMENT AND ACCELERATION RESPONSE HISTORIES FOR BOTH BUILDINGS EXCITED WITH GROUND MOTION #3 SCALED AT 0.5G (PGA) A) 8TH FLOOR DISPLACEMENTS AND POUNDING FORCES B) 8TH FLOOR ACCELERATION RESPONSE HISTORY WITH THE DISTINCT ACCELERATION PULSES.....	101
FIGURE 6.6: AVERAGE IDR VALUES AND THEIR SPREAD CONSIDERING ALL GROUND MOTIONS IN THE SUITE SCALED TO 0.5G (PGA) A) WITH POUNDING AND B) WITHOUT POUNDING.....	102
FIGURE 6.7: AVERAGE IDR VALUES AND THEIR SPREAD CONSIDERING ALL GROUND MOTIONS IN THE SUITE SCALED TO 1.0G (PGA) A) WITH POUNDING AND B) WITHOUT POUNDING.....	103
FIGURE 6.8: IDA CURVES FOR THE 8SWDCH BUILDING A) COUPLED WITH 0.0 M INITIAL SEPARATION DISTANCE AND $IM=PGA$ B) COUPLED WITH 0.0 M INITIAL SEPARATION DISTANCE AND $IM= AvgSa$ c) UNCOUPLED AND $IM=PGA$ d) UNCOUPLED AND $IM= AvgSa$ .....	104
FIGURE 6.9: IDA CURVES FOR THE LOWER EIGHT FLOORS OF 12RFDCH BUILDING A) COUPLED WITH 0.0 M INITIAL SEPARATION DISTANCE AND $IM=PGA$ B) COUPLED WITH 0.0 M INITIAL SEPARATION DISTANCE AND $IM= AvgSa$ c) UNCOUPLED AND $IM=PGA$ d) UNCOUPLED AND $IM= AvgSa$ .....	105
FIGURE 6.10: IDA CURVES FOR THE UPPER FOUR FLOORS OF THE 12RFDCH BUILDING A) COUPLED WITH INITIAL SEPARATION DISTANCE AND $IM=PGA$ B) COUPLED WITH INITIAL SEPARATION DISTANCE AND $IM= AvgSa$ c) UNCOUPLED AND $IM=PGA$ d) UNCOUPLED AND $IM= AvgSa$ .....	105

FIGURE 6.11: PARAMETERS OF THE LOGNORMAL FIT FOR THE 1% IDR LIMIT STATE - 8SWDCH BUILDING A) COUPLED B) UNCOUPLED.....	106
FIGURE 6.12: FRAGILITY CURVES FOR THE 8SWDCH BUILDING FOR THE COUPLED AND UNCOUPLED CASE. ....	106
FIGURE 6.13: PARAMETERS OF THE LOGNORMAL FIT FOR THE 1% IDR LIMIT STATE - 12RFDCH BUILDING A) COUPLED B) UNCOUPLED.....	107
FIGURE 6.14: FRAGILITY CURVES FOR THE LOWER 8 FLOORS OF THE 12RFDCH BUILDING FOR THE COUPLED AND UNCOUPLED CASE.....	107
FIGURE 6.15: PARAMETERS OF THE LOGNORMAL FIT FOR THE 1% IDR LIMIT STATE - 12RFDCH BUILDING A) COUPLED B) UNCOUPLED.....	108
FIGURE 6.16: FRAGILITY CURVES FOR THE UPPER 4 FLOORS OF THE 12RFDCH BUILDING FOR THE COUPLED AND UNCOUPLED CASE.....	108
FIGURE 6.17: IDA CURVES FOR A) 12RFDCH - SDOF MODEL B) 8SWDCH - SDOF MODEL C) 12RFDCH - FRAME D) 8SWDCH - FRAME.....	110
FIGURE 6.18: PERCENTAGE DIFFERENCE OF PARAMETERS OF THE LOGNORMAL DISTRIBUTIONS FOR THE TWO BUILDING FRAMES VS THE SDOF MODELS.....	111

# List of Tables

TABLE 4.1: NATURAL PERIODS OF THE CONSIDERED BUILDINGS.....	43
TABLE 5.1: PROPERTIES OF THE EQUIVALENT FIVE NON-LINEAR SDOF SYSTEMS (SOURCE: <i>KATSANOS, SEXTOS AND ELNASHAI, 2014</i> ).....	64
TABLE 5.2: PERIOD, MASS AND ELASTIC STIFFNESS RATIOS FOR THE THREE ADOPTED PAIRS OF NON-LINEAR SDOF SYSTEMS THAT ARE CONSIDERED IN THIS STUDY. ....	66
TABLE 5.3: LIST OF THE CONSIDERED CASES WITH THE ADOPTED VALUES OF THE PARAMETERS OF THE LINEAR CONTACT MODEL FOR EACH BUILDING PAIR.....	68
TABLE 5.4: LIST OF THE CONSIDERED CASES WITH THE ADOPTED VALUES OF THE PARAMETERS OF THE LINEAR CONTACT MODEL FOR EACH BUILDING PAIR.....	68
TABLE 5.5: ADOPTED DISPLACEMENT LIMIT STATES FOR EACH CONSIDERED PAIR OF SDOF SYSTEMS CORRESPONDING TO LIGHT AND SEVERE DAMAGE. ....	69
TABLE 5.6: SUMMARY OF THE UPPER AND LOWER BOUNDS (MAX AND MIN) OF THE PERCENTAGE DIFFERENCES OF THE MEAN AND THE STANDARD DEVIATION VALUES FOR THE TWO ADOPTED LIMIT STATES (LIGHT DAMAGE/SEVERE DAMAGE).....	88
TABLE 6.1 VALUES OF THE VARIOUS MATERIAL PROPERTIES USED IN THE MODELLING OF THE TWO INELASTIC MDOF SYSTEMS. ....	97
TABLE 6.2: GROUND MOTIONS USED IN THE STUDY AND RELATED INFORMATION (PEER-NCA, CHIOU ET AL). ....	99

# Glossary of ACRONYMS

DR	Ductility Ratio
DV	Decision Variables
EDP	Engineering Demand Parameter
EISP	Earthquake Induced Structural Pounding
FE	Finite Element
GM	Ground Motion
IDA	Incremental Dynamic Analysis
IDR	Inter-storey Drift Ratio
IM	Intensity Measure
LS	Limit States
MDOF	Multi-Degree Of Freedom
MRD	Magneto-Rheological Dampers
MSD	Minimum Safety Distance
NRHA	Nonlinear Response History Analysis
PBEE	Performance Based Earthquake Engineering
PBSA	Performance Based Seismic Assessment
PGA	Peak Ground Acceleration
PSDA	Probabilistic Seismic Demand Analysis
PSHA	Probabilistic Seismic Hazard Analysis
RC	Reinforced Concrete
RHA	Response History Analysis
SDOF	Single-Degree Of freedom
SRSS	Square Root of the Sum of Squares

SSSI

Structure-Soil-Structure Interaction

VED

Visco-Elastic Damper



# Chapter 1

## Introduction

### 1.1 Background and Motivation

Damage due to Earthquake Induced Structural Pounding (EISP) between closely spaced civil engineering structures with dissimilar dynamic characteristics, has been repeatedly observed in past major seismic events (e.g. *San Fernando* 1971, *Mexico City* 1985, *Loma Prieta* 1989, *Chile* 2010, *Christchurch* 2011). Given an inefficient separation, buildings and components of bridges (e.g. deck and abutments) will interact under strong ground motion excitation. During this interaction, forces that are termed in the pertinent literature as pounding forces, develop at the areas of contact. Typically, these pounding forces are not accounted for during the design process and may exceed design limits, causing local damages or lead to a sudden full or partial structural collapse (*Efraimiadou, et al., 2013*). Therefore, EISP may threaten the structural integrity and, thus, property and life.

This threat is acknowledged by modern aseismic codes of practice that impose a Minimum Safety Distance (MSD) in order to prevent pounding. In practice however, especially in densely built urban areas, the MSD is rarely implemented due to the lack of building space and the high cost of land (*Favvata, 2017*). Further, several existing buildings were constructed in accordance with older versions of the building codes and therefore, the MSD requirement may not be satisfied. In addition, the MSD is determined based on methodologies that account only implicitly for the nonlinear structural response and therefore, it may not guarantee that pounding is prevented.

In reality, EISP represents a very complex and highly nonlinear phenomenon (*Dimitrakopoulos, et al., 2009*). The impact of the phenomenon on the seismic structural response, depends on a large number of factors such as the initial separation distance, the relative dynamic characteristics (e.g. relative mass and stiffness) of the interacting structures, build materials, support

conditions and the characteristics of the input ground motion excitation (e.g. frequency content, duration etc).

Along these lines, during the last decades, several experimental and analytical research efforts have focused on EISP in an attempt to better understand the phenomenon. However, the validity/accuracy of analytical studies on the influence of EISP on the structural response entails the accurate representation/modelling of contact between bodies. [To this extend, the vast majority of past analytical studies on EISP, modelled contact either based on the theory of stereo-mechanics \(Papadrakakis et al.,1991; Athanassiadou et al 1994; Malhotra, 1998; DesRoches and Muthukumar, 2002\) or by means of force-based impact/contact elements \(e.g. Anagnostopoulos, 1988; Vega et al, 2009\).](#)

The analytical representation of contact via the stereo-mechanical model, is based on the principal of the conservation of momentum and the coefficient of restitution that characterises the level of plasticity during impact. However, the analytical representation of contact via impact elements is the approach most commonly adopted as it can be incorporated into structural analysis software without any significant programming efforts. Impact elements, introduce a (constant) gap ( $\text{gap} \geq 0$ ) between the bodies in order to simulate the initial stand-off distances. Then, during Response History Analysis (RHA) the elements are activated when the relevant distance between the two bodies is less than the defined gap.

Along these lines, several types of impact elements with a varying degree of complexity and ability to accurately model pounding forces, have been proposed in the literature. The most commonly adopted impact element models are a) the linear pounding model b) the nonlinear pounding model (Davis, 1992) c) the linear viscoelastic (Kelvin) pounding model (Anagnostopoulos, 2004) and d) the non-linear viscoelastic (Jankowski, 2005). However, the calibration of the contact model parameters is a non-trivial task. Typically, the values of the parameters are judiciously selected based on sensitivity studies and/or experimental tests.

Such experimental investigations typically involve shake table tests of prototype (scaled down) structures. In (Papadrakakis and Mouzakis, 1995; Filiatrault and Wagner, 1995; Chau et al, 2003; Khatiwada et al., 2013), the authors conducted shake table tests in order to study pounding between structures (RC or steel frames) with different dynamic characteristics (e.g. between a flexible and a stiff structure). The studies reported a good

agreement between the seismic responses obtained via analytical methods and those recorded during the experiments. In these studies, the input ground motion was described in terms of a sinusoidal excitation or an excitation based on a limited number of historical accelerograms.

In fact, all the experimental investigations and the vast majority of analytical studies on EISP considered either a small number of arbitrarily chosen ground motions and/or relatively simple/academic structural models that may not be able to capture the full effects of seismic pounding. Indeed, in most studies, SDOF oscillators are used as proxies of MDOF structures while the uncertainty to inelastic seismic demand under seismic pounding is not accounted for, due to record-to-record variability. In addition, very limited work is done in order to quantify the influence of pounding in seismic risk assessment studies. The latter utilises fragility models of structures to account for the inherent uncertainty in the seismic input. Therefore, in this thesis, performance based seismic assessment (PBSA) is pursued relying on the Performance Based Earthquake Engineering (PBEE) framework of the Pacific Earthquake Engineering Research (PEER) Centre (Porter 2003, Moehle and Deierlein 2004) to assess the influence of pounding in probabilistic terms.

### **1.2 Aims and Objectives**

The overarching aim of this research work is to quantify the influence of slab-to-slab seismic pounding to the inelastic demands of adjacent reinforced concrete building structures for different (increasing) intensity of the seismic action. In this manner, the seismic performance of adjacent structures interacting (colliding) during seismic events can be comparatively assessed with respect to the seismic performance of the same structures where no pounding/interaction occurs using Performance-Based Seismic Assessment (PBSA) as diagrammatically shown in Figure 1.1. This assessment is herein pursued through series of Nonlinear Response History Analyses (NRHA) with gradually increasing seismic input intensity, commonly termed in the literature as Incremental Dynamic Analysis (IDA) (Vamvatsikos and Cornell 2002). The consideration of IDA is deemed necessary for the purposes of this work in order to capture the impact/collision phenomenon, which is inherently dynamic and nonlinear, as well as the potentially inelastic behaviour of RC structures due to yielding at relatively high intensity levels of seismic excitation. In this context, attention is focused on quantifying seismic

demands away from global structural instability/collapse which is of most practical interest in discussing new/code compliant structures.

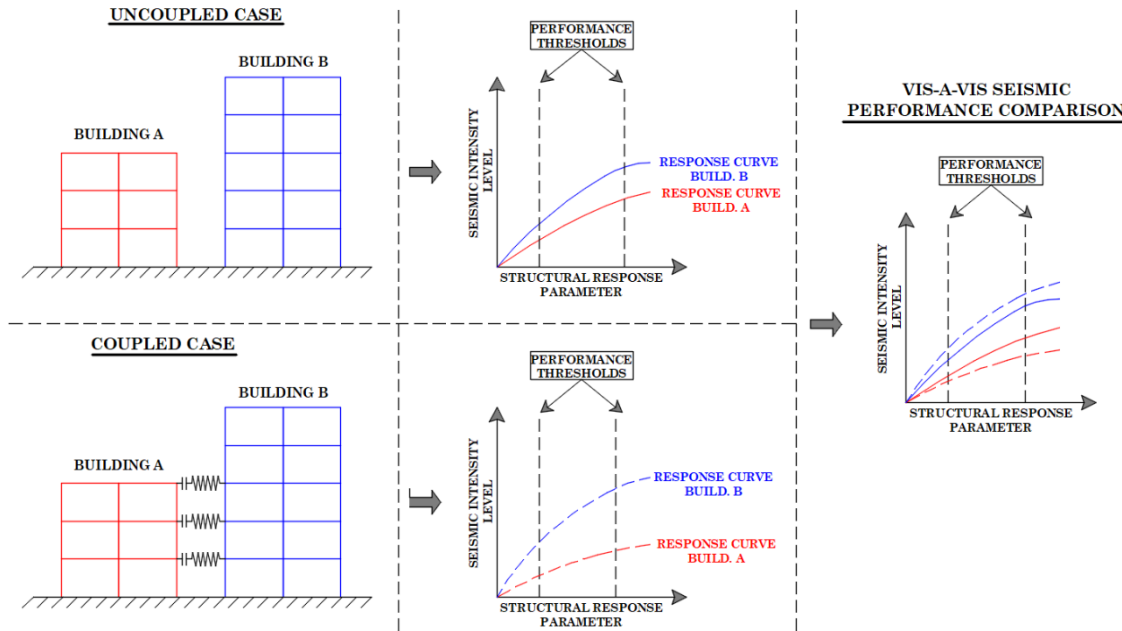


Figure 1.1: Workflow for comparative seismic structural performance quantification of adjacent structures with and without interaction (i.e., slab-to-slab pounding/collisions) denoted as coupled and uncoupled model cases.

A major challenge in applying IDA to examine interaction/collisions of adjacent yielding structures is the onerous computational effort required in modelling accurately seismic pounding forces. This is because such forces are high-amplitude and short-lived and, therefore, necessitate the use of very small time-steps for numerical integration of the underlying nonlinear equations of motion in undertaking NRHA. Therefore, the overarching aim is pursued by judiciously balancing the level of sophistication/complexity of seismic action modelling (i.e., number of recorded ground motions considered in IDA application) and structural modelling (i.e., degrees of freedom). In this regard, three different levels of complexity of seismic/input and structural modelling are considered as specified in the matrix shown in Figure 1.2. The latter matrix delineates the seismic action and structural modelling assumptions adopted in the numerical (IDA) studies undertaken in different chapters.

<b>STRUCTURAL MODELS</b> <b>SEISMIC ACTION MODEL</b>	<b>3D</b>	<b>2D MDOF</b>	<b>SDOF</b>
<b>Single response spectrum compatible GM per horizontal axis</b>	<b>Chapter 4</b>		
<b>25 GMs compatible on average to response spectrum with even distribution on M,R</b>		<b>Chapter 6</b>	
<b>72 GMs</b>			<b>Chapter 5</b>

Figure 1.2: Matrix that illustrates the seismic action and building modelling complexity combinations adopted in this thesis with the corresponding chapters.

Specifically, three different scenarios are examined in this thesis, judicially defined to strike a balance between seismic action and structural complexity, in addressing the following objectives:

- Assessment of inelastic end-member rotation demands to horizontal (beams) and vertical structural members (columns and shear walls) in adjacent multi-storey RC buildings in a typical city-block interacting during seismic events through slab-to-slab collisions.
- Derivation of fragility curves in terms of peak inelastic inter-storey drift ratios of adjacent interacting RC structures accounting for ground motion record-to-record variability and for different limit states.
- Quantification of the influence of pounding model properties to IDR fragility curves (i.e. stiffness and energy dissipation properties assumed during collisions) as well as the separation gap.
- Assess the differences between statistical properties of fragility curves derived from inelastic MDOF frames and the equivalent SDOF inelastic oscillators derived from the MDOF frames through pushover analysis.

The above objectives are set out to fill several gaps of knowledge in the literature that are identified through a detailed literature review undertaken in chapter 2.

### 1.3 Thesis Organisation

This thesis is organised in seven chapters. The current chapter gives a general overview of the EISP phenomenon and sets the overarching aim and objectives pursued in the thesis together with an overview of the methodology adopted to meet the objectives. The chapter concludes with the aims and objectives that are set in this thesis. The Chapter 2 presents an extensive literature review on EISP phenomenon and knowledge gaps that are addressed in this thesis. Further, the chapter discusses past studies on pounding mitigation measures, pounding modelling techniques, studies on the issues related to the computation of MSD and studies on the impact of EISP on the seismic response.

Chapter 3, reviews to some detail the stages of the PEER framework developed by the Pacific Earthquake Engineering Research Centre. This framework serves as the basis for the development of the herein proposed PBSA approach to study the influence of EISP accounting for record-to-record uncertainty. Further, the Chapter discusses in full the IDA method that is adopted throughout this thesis as the analysis to determine the imposed seismic structural demand for various levels of seismic intensity.

Next, Chapter 4 presents a case-study that quantifies the influence of EISP on the inelastic seismic demand distribution adopting a particular configuration of three adjacent RC buildings represented by a three-dimensional (3D) nonlinear FE model. The chapter discusses the characteristics (e.g. geometric, relative positions, materials etc) of the model and presents comprehensive results from application of IDA using a single pair of response spectrum compatible artificial accelerogram. Finally, the chapter discusses the impact of EISP on the inelastic seismic demands of the FE building models.

Chapter 5 develops the PBSA approach to study EISP. The chapter discusses the adopted finite element models and presents the analytical expression of a novel IM. Further, probabilistic EISP models are derived and discussed for two different contact/pounding element models adopting different values for the model parameters.

## Chapter 1 - Introduction

In Chapter 6 probabilistic seismic performance of adjacent RC building frames is derived and discussed. Further, the chapter investigates and discuss on the impact of the adopted modelling complexity of structures to study the influence of EISP in probabilistic terms on the seismic performance of structures.

Finally, chapter 7 summarizes the contribution achieved within this thesis and recommendation for future work.

# Chapter 2

## Interaction of Adjacent Building Structures During Earthquakes

### 2.1 Overview

Damages due to EISP, have been identified in several field investigations carried out in the aftermath of major seismic events. In a survey (*Hall and Beck, 1986*) that followed the 1985 earthquake that struck Mexico City, the authors reported that 40% of the surveyed buildings had structural pounding related damages. Further, 15% of all these reported cases had collapsed, due to pounding. However, later revisited estimates (*Anagnostopoulos and Karamaneas, 2008*) reduced the initial percentage to only 20-30% of the originally identified cases.

Another field survey (*Kasai and Maison, 1997*) carried out in the regions of San Francisco and Monterey Bay that were struck by the 1989 Loma Prieta earthquake, reported extensive damages due to pounding, over a large geographic area, including areas with large epicentral distances. Moreover, during the 2011 earthquake that shocked the densely build Christchurch business district, although pounding was identified as a secondary effect, the authors (*Cole et al., 2011*) observed that 6% of the total surveyed buildings were damaged due to pounding.



Figure 2.1: Severe damages including concrete spalling and column shearing, observed on two adjacent RC buildings in the aftermath of the 2014 Kefalonia earthquake.

Building damages due to EISP can be segregated into five major types (*Jeng and Tzeng, 2000; Cole et al., 2011*).

**Type I:** Pounding between adjacent buildings with unequal floor heights and/or foundation levels.

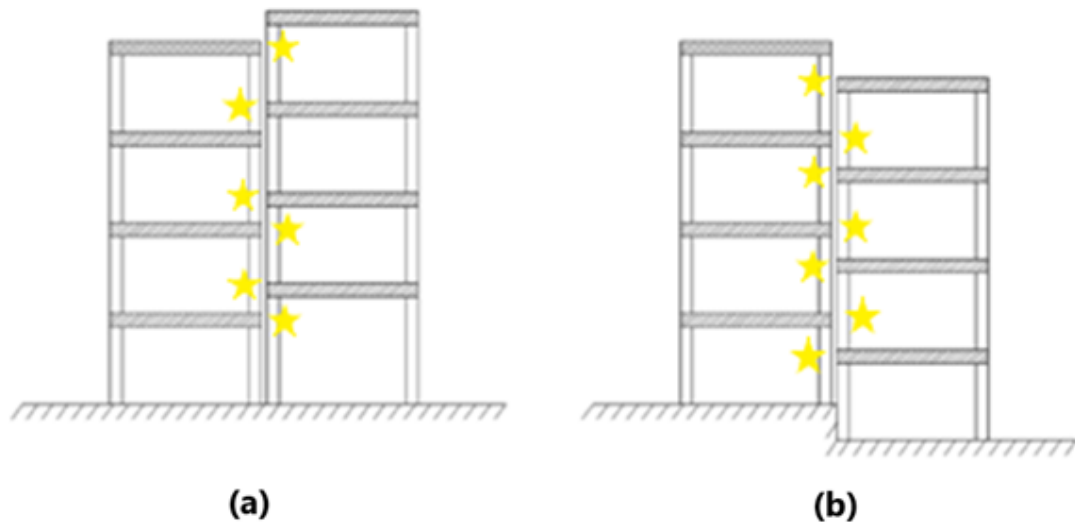


Figure 2.2: Earthquake induced structural pounding between buildings with a) unequal floor heights and/or b) different foundation levels, leads to floor-

---

slab to column collisions with a potential abrupt failure of columns, due to column shearing (Jeng and Tzeng, 2000).

During interactions between adjacent buildings with unequal floor heights and/or dissimilar foundation levels, both buildings experience floor-slab to column collisions. These collisions, may introduce high amplitude shear forces on the columns that are located on the sides that are subjected to pounding. These additional forces may exceed design limits leading to column shearing and a sudden catastrophic collapse (*Jeng and Tzeng, 2000; Karayannis and Favvata, 2004; Anagnostopoulos and Karamaneas, 2008*).

**Type II:** Pounding between adjacent buildings with significantly dissimilar mass properties.

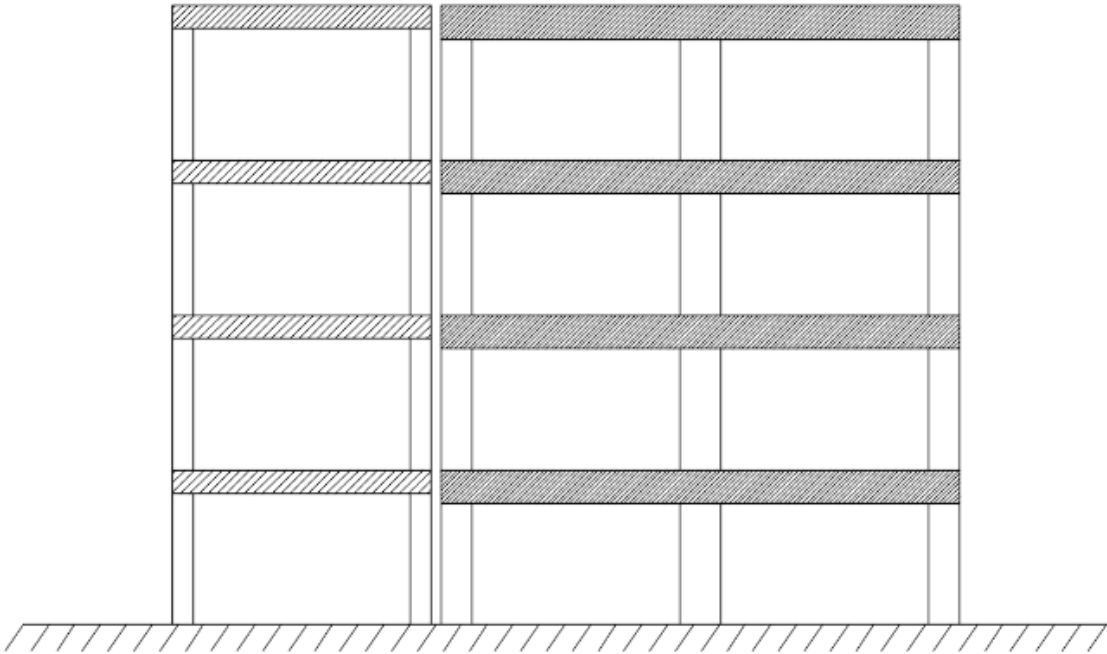


Figure 2.3: Pounding between a stiff and a flexible structure with equal floor heights (Jeng and Tzeng, 2000).

Earthquake induced structural pounding between a massive and a light adjacent building, typically leads to significant amplifications of the structural response of the lighter building and severe local damages at the locations of pounding. In contrast, due to pounding, the lateral floor displacements of the massive building are typically restricted and therefore pounding typically has a beneficial impact on the heavier building (*Anagnostopoulos, 1988*) since the imposed structural demand is reduced.

---

**Type III:** Adjacent buildings with different number of floors.

Tall buildings adjacent to shorter buildings, will experience large displacement amplifications on the floor that is located above the last floor of the lower building (see Figure 2.5). This “*whiplash*” type of response, typically increases ductility demands on the columns of that specific floor and mainly those located on the side that is subjected to pounding (*Karayannis and Favvata, 2004*).

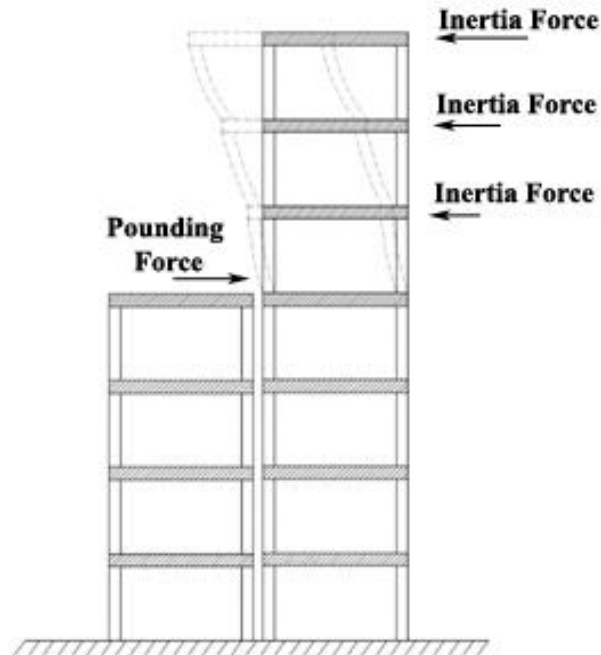


Figure 2.4: Pounding between buildings with different floor elevations (Jeng and Tzeng, 2000).

**Type IV:** Adjacent buildings with in plan eccentricity.

In the case of adjacent buildings that exhibit in plan eccentricity, the developing pounding forces are typically limited at one corner (see Figure 2.6). Therefore, the column located at that corner may fail due to pounding that also causes a torsional movement of the floor slab (*Jeng and Tzeng, 2000*).

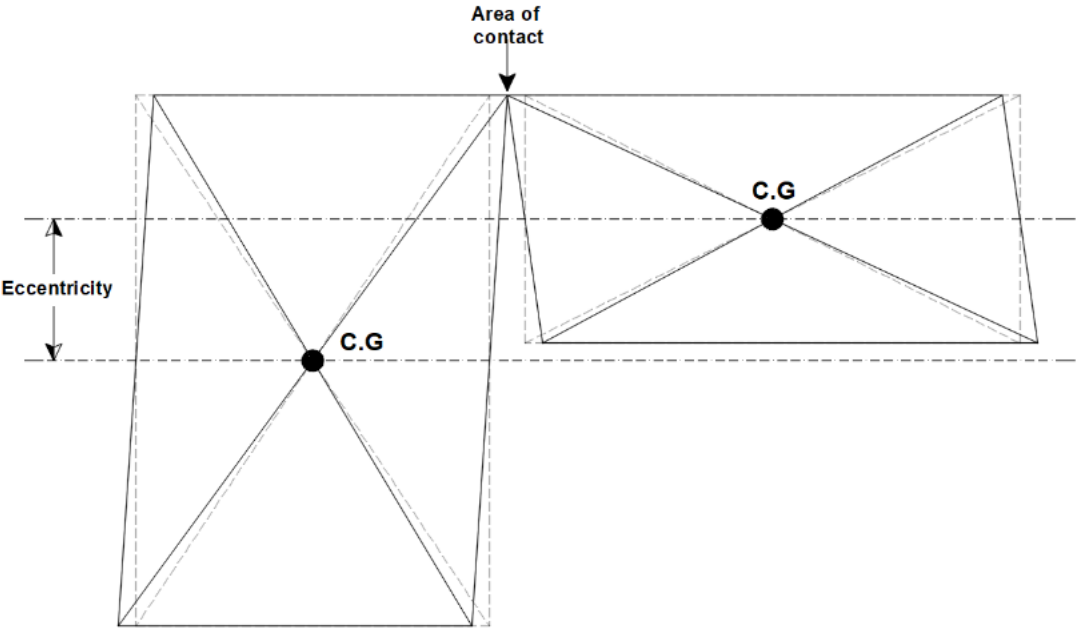


Figure 2.5: Schematic that illustrates the case of pounding between buildings that exhibit in plan eccentricity (Jeng and Tzeng, 2000). Pounding occurs at one corner, typically causing extensive damages to the column that is located at that corner.

**Type V:** Pounding buildings in series.

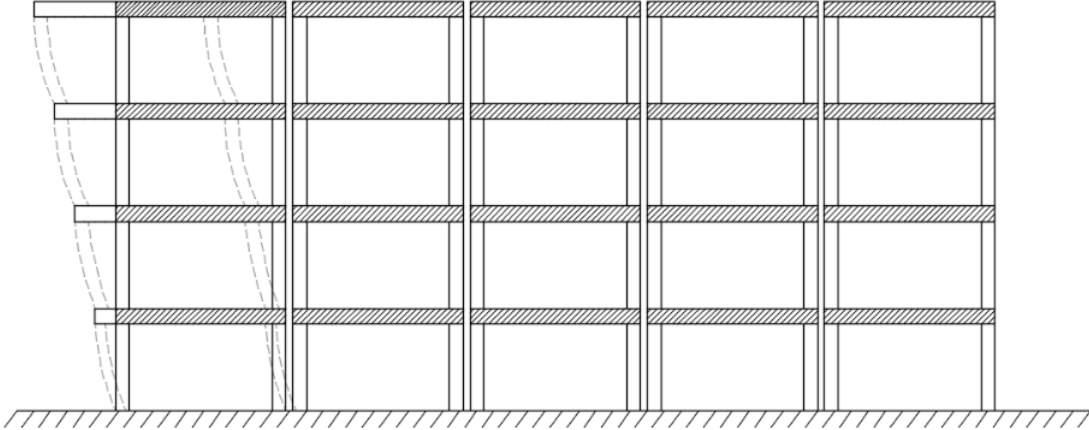


Figure 2.6: Schematic for the case of pounding between buildings in series with equal floor heights (Jeng and Tzeng, 2000). Typically, pounding has a detrimental impact on the structural integrity of the buildings that are located at the ends.

In the case of buildings that are constructed in series, those that are located at the ends, typically suffer significant damages due to pounding

(*Anagnostopoulos and Spiliopoulos, 1992*). Such a configuration, resembles the pendulum effect (*Jeng and Tzeng, 2000*) or alternatively can be interpreted as a massive building colliding on a lighter building. In contrast, buildings that are located at the intermediate locations in the series, tend to be protected during ground motion excitation as their horizontal floor displacements are typically restricted. Still however, all structures will experience high acceleration pulses during collisions that may damage internal sensitive equipment (e.g. machinery, electronic devices etc).

Thus, structural pounding has a detrimental impact on one or more of the adjacent structures and ignoring the phenomenon typically lead to less conservative designs (*Karayannis and Favvata, 2005*). Along these lines as previously noted, most contemporary codes of practice (e.g. *Eurocode 8, CEN2004-8*; the *Uniform Building Code UBC 1993*; *National Building Code of Canada, NBCC, 1990*; *Chinese Seismic Building Code, GBJ11-89*; *National Earthquake Hazards Reduction Program code, NEHRP, 1991*) impose a MSF in order to prevent pounding (*Efraimiadou et al., 2013*). However, in order to protect existing structures that are likely to collide under strong ground motion excitation, several researches investigated and proposed measures, mainly in the form of some type of damping devices, that can mitigate the impact of EISP on their seismic structural response.

## 2.2 Mitigating Pounding

An early study by (*Westermo, 1989*) proposed a link and beam system, to transfer the connection forces to the floors of the interacting structures. The considered scheme was found to effectively reduced the magnitude of the developing pounding forces by limiting the overlapping relative displacements. However, the author observed that the considered coupling mechanism, led to an increase of the base shear of the stiffer structure.

In (*Anagnostopoulos and Karamaneas, 2008*) the authors proposed shear walls, located transversely to the side of the building that is subjected to pounding (figure 2.7). These shear walls, act as absorbers of collisions and provide efficient protection against pounding, especially in the case of adjacent buildings with unequal heights. In such a case, the proposed collision shear walls, represent a low-cost solution to prevent column shearing and a subsequent catastrophic collapse, while sustaining only local and repairable damages and therefore protecting both buildings. However, since pounding is

not prevented, both buildings will experience short acceleration pulses that may harm acceleration sensitive building contents.

The majority however, of the pounding mitigation measures that are proposed in the literature, are based on the inter-connectivity/coupling of the adjacent structures by means of seismic control devices. These devices, under the assumption of optimal tuning, offer the ability to reduce the risk of pounding and improve the overall seismic structural performance of the coupled structures (e.g. *Luco and De Barros, 1998*).

Along these lines, (*Kim et al., 2006*) proposed Visco-Elastic Dampers (VEDs) to be used in seismic joints in order to reduce the earthquake induced structural responses of adjacent structures or in skybridges. The optimal performance of the proposed scheme is achieved when used as a coupling mechanism between structures that exhibit a significant difference in their fundamental frequencies.

In a similar study, (*Xu et al., 1999*) the authors examined the effectiveness of fluid dampers used to link closely spaced structures in terms of reduction in the earthquake induced displacements, accelerations and shear forces. They observed significant reduction in the dynamic responses of both buildings, when the parameters of the dampers are judiciously chosen, typically after a parametric study.

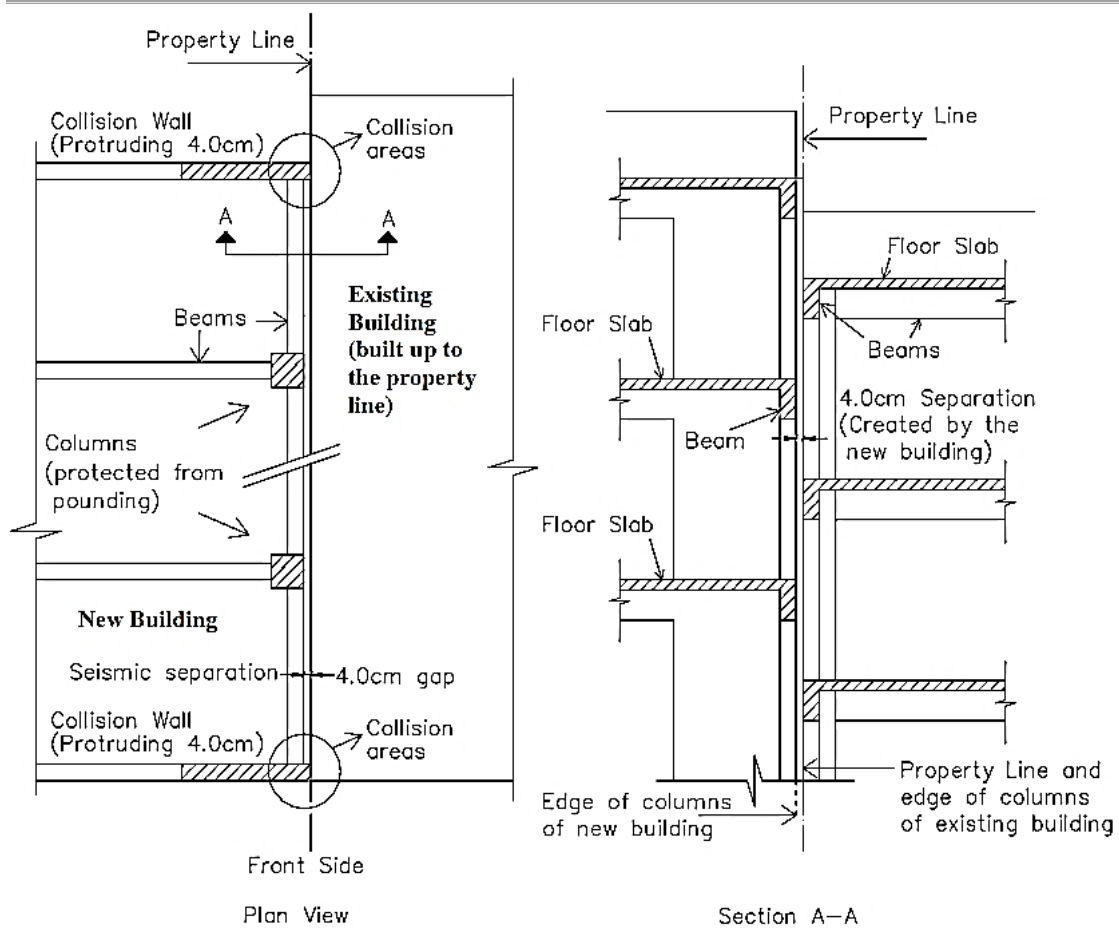


Figure 2.7: Collision shear walls located at the property line in order to prevent column shearing from floor to column collisions (Anagnostopoulos and Karamaneas, 2008).

In (Bharti *et al.*, 2010) the authors examined the effectiveness of Magneto-Rheological Dampers (MRD) to mitigate the seismic response of two coupled adjacent tall buildings. The study considered passive-off, passive-on and semi-active control strategies and found that MR dampers can effectively reduce the response of both short and tall buildings for a wide range of ground motion. However, the optimal determination of the voltages as well as the number of dampers, remains a challenging process. To this extend (Ok *et al.*, 2008) proposed a methodology to define the above parameters based on multi-objective genetic optimization algorithm and the stochastic linearization method.

In another study by (Pratesi *et al.*, 2014) related to an iconic slender RC tower bell with inefficient separation from neighbouring structures, the authors proposed a damped inter-connection retrofit in order to mitigate EISP. In fact,

the authors calculated that the proposed solution reduced by about 50% the developing bending moments, by 30% the axial force and by 50% the shear forces compared to the non-pounding case. Further, it was concluded that pounding has a significant impact on the seismic response of the tower and the neighbouring church.

In (Liolios et al., 2015), the authors studied the efficiency of cable ties in various strengthening schemes in order to enhance the seismic capacity of adjacent RC structures, under the assumptions of environmental degradation and interactions under multiple ground motion excitations. Structural pounding is found to cause higher level of damages under multiple seismic scenarios and that cable strengthening has a significant beneficial impact of the seismic response of the RC structures. Therefore, cable strengthening is found to represent an attractive solution to upgrade existing RC structures, taking also into account the associated low cost when compared to the typically expensive seismic control devices.

Another interesting study from the field of probabilistic performance-based design (*Tubaldi et al.*, 2014), proposed an efficient methodology in order to quantify the seismic risk of adjacent building coupled with linear and nonlinear viscous dampers. The proposed methodology accounts for the inherent uncertainties of the seismic input as well as the system parameters.

Finally, a study within the field of bridge engineering (*Abdel Raheem*, 2009), proposed cable restrainers that tie together the adjacent bridge segments. The study considered three different configurations of the restrainers I) deck to deck II) through the pier and III) through a hinge with a shear key. Configuration I, was found to be effective against deck falling but failed to guard against deck unseating. Configurations II and III were found to be effective in unseating prevention of the bridge decks with the cost of amplified moments and shear forces imposed on the corresponding supporting pier.

The accurate representation of pounding in analytical studies, requires refined modelling coupled with a reliable analytical method in order to capture inelastic deformations, local crushing and fracturing of material.

### **2.3 Contact Modelling for EISP Applications**

In EISP analytical studies contact during RHA is typically simulated either by the theory of stereomechanics or through the use of parametrically defined

---

contact elements. These two modelling approaches are discussed in more detail in this section.

### 2.3.1 Theory of Stereomechanics for Contact Modelling

The representation of contact in pounding numerical simulations based on the theory of stereomechanics, is based on the conservation of momentum to update the velocities of the colliding bodies after their interaction (*Muthukumar and DesRoches, 2006*). In the simple case of two colliding bodies with masses  $m_1$  and  $m_2$  and initial velocities  $v_1$  and  $v_2$  the corresponding updated post-collision velocities  $v'_1$  and  $v'_2$  are given by equations (2.1) and (2.2) respectively (*Goldsmith, 1960*).

$$v'_1 = v_1 - (1 + e) \frac{m_2}{m_1 + m_2} (v_1 - v_2) \quad (2.1)$$

$$v'_2 = v_2 - (1 + e) \frac{m_1}{m_1 + m_2} (v_2 - v_1) \quad (2.2)$$

The parameter  $e$  represents the degree of plasticity between collisions. It is termed in the literature as the *coefficient of restitution*, with a range of possible values between 0 and 1. The two extreme values, represent a perfectly plastic and a perfectly elastic collision correspondingly. The value of the *coefficient of restitution*  $e$  depends on the materials and the relative velocities of the colliding bodies (*Jankowski, 2009*). Given the absence of sufficient experimental data, the value of  $e$  typically ranges between 0.4 and 1.0. However, the vast majority of EISP studies typically adopt values that lie within a range of  $e = 0.50 - 0.65$ .

Several past studies on EISP, have been based on the theory of stereomechanics (e.g. *Papadrakakis, et al., 1991; Athanassiadou, Penelis and Kappos, 1994; Malhotra, 1998; DesRoches and Muthukumar, 2002*). However, the theory assumes instantaneous collisions between colliding bodies. Therefore, the method ignores transient stresses and deformations (*Muthukumar and DesRoches, 2006*) and thus reduces the accuracy of the simulations. In addition, from a practical perspective, the method cannot be easily implemented in structural analysis software packages.

Given these limitations and deficiencies of contact representation by means of the theory of stereo-mechanics, the majority of analytical EISP studies,

adopted a force-based approach i.e. impact/contact elements to model pounding forces during RHA.

### 2.3.2 Contact Elements

Several types of contact elements, with a varying degree of modelling complexity and modelling accuracy have been proposed and implemented in past studies. The four main types of impact elements are a) the linear pounding model (Anagnostopoulos, 1988) b) the non-linear pounding model (Hertz) (Davis, 1992) c) the linear visco-elastic pounding model (Kelvin - Voigt) (Anagnostopoulos, 2004) and d) the non-linear visco-elastic pounding model (Hertz damp) (Jankowski, 2005).

The linear elastic pounding model (figure 2.9) represents the simplest contact model that can be incorporated into structural analysis software. It consists of a linear spring with stiffness  $K$  that is typically proportional to the axial stiffness of the interacting structures (Maison and Kasai, 1990; Maison and Kasai, 1992). The non-linear contact model (figure 2.9), implements a non-linear spring instead in order to model impact based on the Hertz law (Jing and Young, 1991; Davis 1992; Ma and Pantelides, 1998).

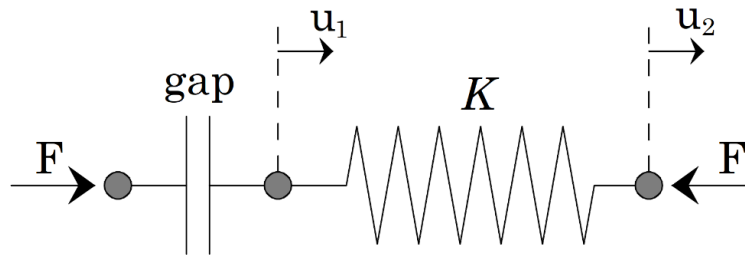


Figure 2.8: The linear and non-linear (Hertz) impact models that consists of a linear spring and a non-linear spring correspondingly with a stiffness  $K$  in series with a gap element. The stiffness  $K$  has typically a value that is proportional to the stiffness of the colliding structures.

The pounding force  $F$  in the case of the linear and non-linear contact models is given by equations 2.3 and 2.4 correspondingly:

$$F = \begin{cases} K\delta, & \delta \leq 0 \\ 0, & \text{otherwise} \end{cases} \quad (2.3)$$

$$F = \begin{cases} K\delta^a, & \delta \leq 0 \\ 0, & \text{otherwise} \end{cases} \quad (2.4)$$

The constituents of the linear visco-elastic and the nonlinear visco-elastic impact elements is depicted in the following figure.

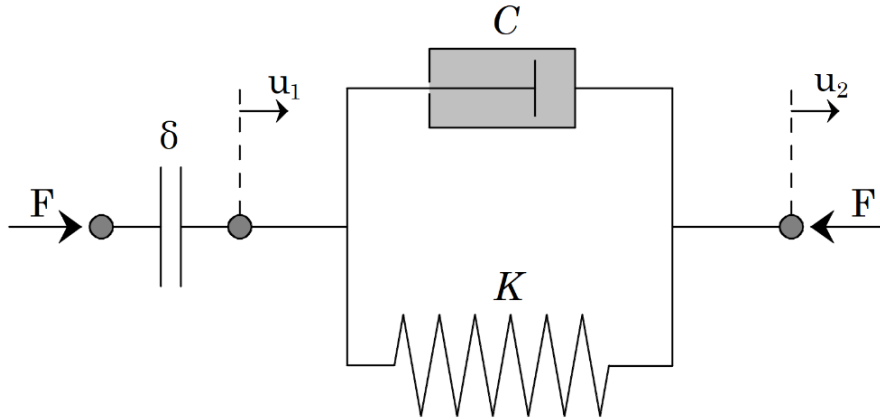


Figure 2.9: Configuration of the linear viscoelastic (Kelvin - Voigt) and non-linear viscoelastic (Hertzdamp) impact models that consists of a linear spring and a non-linear spring correspondingly in parallel with a viscous damper that allows for the modelling of energy losses during impact.

The pounding force  $F$  in the case of the linear viscoelastic and the non-linear viscoelastic contact models is given by equations 2.5 and 2.6 correspondingly:

$$F = \begin{cases} K\delta + C\dot{U}, & \delta \geq 0 \\ 0, & otherwise \end{cases} \quad (2.5)$$

$$F = \begin{cases} K\delta^a + C\dot{U}, & \delta \geq 0 \\ 0, & otherwise \end{cases} \quad (2.6)$$

where,  $\delta$  is defined as:

$$\delta = u_1 - u_2 - gap \quad (2.7)$$

The adopted value of  $a$  is typically 3/2. Further, all contact models are activated when:

$$\delta = u_1 - u_2 - gap \leq 0$$

A significant breakthrough for EISP studies was accomplished in (Anagnostopoulos, 2004). The author, derived an analytical expression between the coefficient of reinstatement and the damping coefficient  $C$ . The analytical expression is:

$$C = 2\xi \sqrt{\kappa \frac{m_1 m_2}{m_1 + m_2}} \quad (2.8)$$

where  $\xi$  is given by:

$$\xi = -\frac{\ln(r)}{\sqrt{\pi^2 + (\ln(r))^2}} \quad (2.9)$$

and  $r$  is the coefficient of restitution given by:

$$r = \frac{u_2 - u_1}{u_{01} - u_{02}} \quad (2.10)$$

As discussed, the problem of EISP was studied early on through analytical investigations (e.g. *Anagnostopoulos*, 1988). However, the validity of the analytical predictions was investigated later on by means of experimental studies. In (*Papadrakakis and Mouzakis*, 1995), shake table tests considering two-storey RC frames with equal floor heights and zero separation distance, were subjected to harmonic and random excitation signals. The data from the shake table tests were found to be in good agreement with the results obtained via numerical simulations of the corresponding analytical models. In simulations, the contact impact problem was treated by means of the Lagrange multiplier method (*Papadrakakis et al.*, 1991) that was found to represent an accurate numerical analysis method for pounding case studies.

Similarly, in (*Filiatrault et al.*, 1995) shake table tests were undertaken in order to study EISP between a three-storey and an eight-storey single bay steel frame. Numerical analysis of the corresponding building arrangement with pounding force modelled in terms of uniaxial elastic gap elements. The authors concluded that displacement and magnitudes of pounding forces were accurately predicted through numerical analysis. However, during contact the relative rotation of the adjacent beam-column hinges caused local damages that cannot be introduced in the analytical solution by means of the uniaxial gap elements.

## 2.4 Studies on the Minimum Safety Distance

The determination of the most suitable methodology for the calculation of the MSD remains a very active research area within the field of EISP. A study by (*Yu et al.*, 2017), proposed a general spectral difference method to calculate the minimum safety distance between building in order to prevent pounding.

The proposed method overcomes the limitation of the proportional damping that is assumed in the traditional response spectrum method. The proposed methodology is found to be more accurate especially in the case where the structures exhibit strong non-proportional damping characteristics (e.g. when dampers are installed).

The accuracy of the Double Difference Combination (DDC) rule was examined in (*Lopez-Garcia and Soong, 2009*) in the prediction of the minimum safe distance considering linear structural systems. The study considered linear 5% damped SDOF systems excited under modulated and filtered Gaussian white noise and the response is evaluated by means of Monte Carlo Simulation. It was found that the accuracy depends on the ratio of the natural periods as well as the relationship between the natural periods of the SDOF systems and the main frequency of excitation.

In a similar study (*Hong et al., 2003*), the authors considered two adjacent buildings modelled as SDOF and MDOF systems and excited under white noise. A parametric investigation was undertaken in order to establish whether the Complete Quadratic Combination (CQC) of the modal responses provides sufficient separation to prevent pounding based on the results from random vibration analysis. The authors concluded that the CQC leads to under and over-estimations of the required minimum separation distance. Similar conclusions were drawn also in the case when the ground motion excitation is characterized by the Kanai-Tajimi power spectral density.

Another study by (*Lopez-Garcia and Soong, 2009*), examined four different criteria that are used in the computation the MSD in order to prevent pounding between hysteretic structural systems. The study was based on adjacent 5% damped bi-linear hysteretic SDOF systems excited by means of non-stationary random process and Monte Carlo simulations. The results showed none of the considered criteria provided consistent predictions in terms of an exact or a conservative MSD.

In (*Favvata, 2107*), the seismic performance of an 8-storey RC frame that collides against a 3-storey RC frame-wall is examined. During seismic excitation, pounding occurs between floors and slabs and the two structures are assumed to be in initial contact. The study considered nine seismic demand levels simulated by mean of 14 suitably scaled accelerograms. The adequacy of the MSD is established based on two criteria a) minimization of

the critical shear demands of the column b) total prevention of pounding. It was found that the provisions of Eurocode 8 for the calculation of the minimum required separation distance to prevent pounding, yielded conservative results for the considered case.

## **2.5 Influence of EISP on the seismic response of adjacent structures**

Several studies, investigated the influence of EISP on the seismic performance of adjacent structures. Typically, the influence of EIPS is quantified in terms of differences between the structural response under the influence of pounding and a benchmark case study that assumes no interaction between the structures. In (*Moustafa and Mahmoud, 2014*), structural damages due to earthquake induced structural pounding between nonlinear SDOF systems, were assessed by means of a variety of damage indices including among other, the ductility, pounding force, input and dissipated energy. These indices, are known to correlate well with structural damage and thus provide useful information on the condition of the structure. The study concluded that the impact of pounding on the seismic response is sensitive to the support conditions as base isolated structures are found to interact more due to their increased flexibility.

Another study (*Madani, et al., 2015*) investigated the impact of pounding and Structure-Soil-Structure Interaction (SSSI) on the nonlinear response of multi-storey structures with an initial separation distance that varies between 0% (initial contact) and 100% of the minimum safety distance as it is required by the design codes. It was found that the resulting pounding forces are sensitive to the support conditions and pounding occurs mainly at the upper floors when the initial separation distance increases. Further, the study concluded that the inflicted damages were mainly attributes to pounding rather than on the SSSI.

A study by (*Jankowski, 2008*) examined the impact of earthquake induced structural pounding between three-dimensional equal height buildings that exhibit substantially differences in their dynamic properties, on their seismic response. Pounding was found to have a significant impact on the response of the lighter and more flexible structure in terms of response amplifications and increase of the inelastic demands. In addition, the seismic behaviour of the lighter building demonstrated increased sensitivity to changes in the values

of the considered structural parameters. In contrast, the heavier and stiffer building was found to be insensitive to changes in the values of structural parameters and effectively unaffected by the collisions.

In the (Agarwal *et al.*, 2007) the authors studied pounding between two degree of freedom systems supported on a variable friction model base isolation. The study showed that when compared to fixed boundary conditions, the adopted base isolation system led to a decrease on the number of impacts. Further, the base isolation system resulted into high magnitude pounding forces. However, under the assumption of a varying stiffness coefficient based on the velocity, the magnitude of the pounding forces was significantly reduced.

Finally, (Komodromos, 2008) studied the impact of pounding on isolated buildings under strong ground motion excitation. The study showed that pounding may excite higher modes and disrupt the typically rigid-body motion that is associated with base isolated buildings.

## 2.6 Research Gaps

In most EISP studies, the influence of seismic pounding to the inelastic demands of 3D structures has only been addressed by examining simplified structural models of mostly academic interest (e.g. Papadrakakis *et al.*, 1991; Jankowski, 2008; Efraimiadou *et al.*, 2013; Madani Behnamfar and Tajmir Riahi, 2015). Such simplified models, are typically products of an idealisation process of more complex structures where the mass of the floors is lumped on one or more structural nodes and the floor stiffness is typically represented by a single structural element. Only a limited number of case studies (e.g. Jankowski, 2009; Jankowski, 2012) adopted detailed/realistic 3D Finite Element (FE) models to assess the influence of seismic pounding on the structural response.

Further, thus far all studies on the influence of EISP on the seismic response of buildings are based on a limited number of artificially generated (e.g. Crozet *et al.*, 2017) or arbitrary selected recorded ground motions (e.g. Moustafa and Mahmoud, 2014) and therefore the record-to-record variability is not rigorously accounted for. In addition, the parameters of the impact model parameters are commonly taken to be fixed to an arbitrary value (e.g. Anagnostopoulos, 1988; Moustafa and Mahmoud, 2014; Madani, Behnamfar and Tajmir Riahi, 2015) and their influence on the seismic performance of structures has not been adequately addressed.

To this extend, the strategy adopted in this thesis (and outlined in figure 1.2) in order to address the identified research gaps consists of the following steps/studies: Firstly, in (§4. Influence of Bi-Directional Pounding on the inelastic Demand Distribution of Three Adjacent Multi-Storey RC Buildings) attention is focused on a real-life configuration of buildings (corner city block) as a case study that allows for the concurrent examination of different scenarios arising in real-life settings. These scenarios include a) pounding between building with significantly different design specifications b) pounding between buildings with unequal number of floors c) pounding between buildings that at least one of them exhibits torsional sensitive behaviour and d) bi-directional pounding of a corner building in an urban building block. The level of sophistication of the three-dimensional nonlinear FE model developed accounting for impact as well as hysteretic structural response renders this study novel in the literature. The seismic excitation is represented by a single pair of artificial accelerograms whose response spectrum matches closely the Eurocode 8 spectrum used in designing the buildings.

Then, in (§5. Fragility Sensitivity of RC Colliding Buildings on the Modelling Parameters of the Linear and Linear Viscoelastic Contact Model) the influence of the impact element stiffness, the initial clearance (gap) and the ability of the pounding model to dissipate energy during collisions (i.e., all three parameters of the adopted linear contact models reviewed in section 2.3.2) on the seismic performance of three pairs of inelastic SDOF systems is undertaken in probabilistic terms accounting for record-to-record variability following a PBSA approach. More specifically, the study adopts a suite of 72 recorded ground motions that are used to excite the SDOF pairs to various (increasing) seismic intensity levels. The influence of the impact model parameters is then quantified in terms of probabilistic seismic performance curves via the vis-à-vis performance comparison workflow outlined in (§ 1.2 Aims and Objectives). It is also noted that the adoption of SDOF oscillators as proxy systems in order to study more complex structures, is a common approach that is typically followed in the field, as it allows to focus on the phenomenon of pounding and speed up computations.

Finally, in (§6. Probabilistic Seismic Performance Assessment of Adjacent RC Building Frames Interacting at Floor Levels), the impact of seismic pounding

on the seismic performance of one of the building pairs that were considered in the previous study, is investigated by means of two-dimensional multi-storey inelastic RC building frames. The seismic performance of the inelastic RC frames is assessed within a PBSA approach by means of fragility models that gauge seismic performance for low and moderate intensity seismic shaking. Then, the derived seismic performance of the same pair of buildings derived for the two cases of a) inelastic SDOF systems and b) inelastic multi-storey building frames is compared in order to assess the impact of modelling complexity on the seismic performance. Notably, the work undertaken in Chapter 6 is novel being the first study to quantify the impact of the structural modelling complexity to the seismic performance of structures represented through fragility curves subjected to floor-to-floor collisions.

# Chapter 3

## The Performance Based Earthquake Engineering Framework

### 3.1 Overview

The Performance Based Earthquake Engineering (PBEE) framework developed within the Pacific Earthquake Engineering Research (PEER) Centre (Porter 2003, Moehle and Deierlein 2004) integrates multidiscipline research knowledge to provide probabilistic descriptions of the seismic hazard associated with a given site and facility in terms of performance metrics (“*Decision Variables*” - DVs). These DVs, can be easily understood and used by stakeholders (e.g. monetary losses, number of casualties, downtime etc.) for better informed risk management decisions. Although a direct probabilistic relationship between decision variables (e.g. monetary losses) and the site-specific seismic risk is highly desirable, the derivation of such relationship is practically intractable.

In this regard, the PBEE (Deierlein *et al.*, 2007) decomposes the process in four distinct stages (figure 3.1). Each stage of the framework is decoupled from the previous one and can be considered independently. The general notation  $G(x|y) = P(x \leq X|Y = y)$  used in Figure 3.1, denotes the cumulative probability distribution of a random variable  $x$  given a specific outcome  $y$  of a random variable  $Y$ .

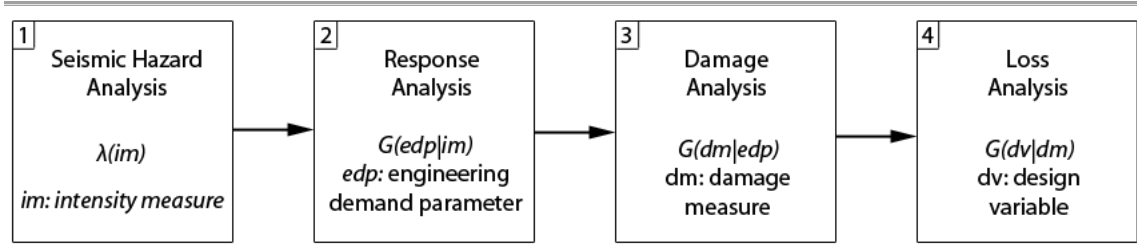


Figure 3.1: The four distinct stages of the performance based earthquake engineering (PBEE) framework (Yang et al, 2009).

Initially, Probabilistic Seismic Hazard Analysis (PSHA) quantifies the site-specific seismic hazard in the form of a seismic hazard curve that is a function of a suitably selected IM and describes mean annual rates of exceedance of various seismic intensity levels. Further, (historical) ground motions of interest (based on criteria like fault characteristics, distance from fault, dynamic structural characteristics etc.) are identified and collected.

Next, in the Probabilistic Seismic Demand Analysis (PSDA), Response History Analyses (RHA) are performed using the pre-compiled collection of ground motions (from stage 1). The responses obtained are functions of the IM selected in PSHA and a strategically selected Engineering Demand Parameter (EDP) that is able to reflect on various structural states and damage accumulation.

In damage analysis (stage three), performance threshold values designated as Limit States (LS) (FEMA, 2000; FEMA, 2009) that are known to correlate well with various damage states, are identified on the IM-EDP response curves. Deriving LS values is a non-trivial procedure that typically involves meticulous laboratory tests, post-earthquake reconnaissance etc. Then statistical analysis provides damage probabilistic descriptions for each LS in terms of curves that express mean annual frequencies of exceedance, also referred in the pertinent literature as fragilities (Celik and Ellingwood, 2010).

Finally, in *loss analysis*, the obtained damage values, are translated in to loss quantities of interest and are again expressed in probabilistic terms (Esteve and Ruiz, 1989). The analytical expression of the PBEE framework is given by the triple integral in following equation (Vamvatsikos and Cornell, 2002).

$$\lambda(dv < DV) = \int_{im} \int_{dm} \int_{edp} G(dv | dm) \cdot |dG(dm | edp)| \cdot |dG(edp | im)| \cdot |d\lambda(im)| \quad (3.1)$$

The various stages/steps of the framework are readily identified in equation 3.1. More specifically  $G(edp|im)$  is the complementary cumulative distribution

of the EDP for the given IM,  $(dm|edp)$  is complementary cumulative distribution of the damage measure given an EDP and  $G(dv|dm)$  is the complementary cumulative distribution of the selected decision variable given a Damage Measure DM. Each of the previously identified complementary cumulative distributions, are products of each of last three stages of the PBEE framework. Then the triple integral (equation 3.1) couples the above distributions with the site-specific seismic hazard information to finally obtain the associated levels of risk  $\lambda(DV)$  expressed in terms of the decision variable  $DV$ .

Thus, in pursuing accurate estimates of the  $\lambda(DV)$ , it is of paramount importance to obtain accurate probabilistic descriptions of the seismic performance of structures (*stage two*). This chapter focuses on IDA (Vamvatsikos and Cornell, 2002) used as a tool to probe into the seismic response of structures is the analysis method of choice in all the numerical studies that are part of this thesis.

### 3.2 Incremental Dynamic Analysis

Incremental Dynamic Analysis (IDA) is a structural analysis procedure aiming to derive a “one to one” mapping of different levels of the input seismic action onto judiciously chosen peak structural response quantities obtained from NRHA (Vamvatsikos and Cornell, 2002). The “level” or “intensity” of the seismic input action is expressed by means of a single scalar intensity measure (IM) or of a collection (vector) of IMs. Commonly used IMs include the peak ground acceleration (PGA) and the (pseudo) spectral acceleration at the fundamental natural period of the structure under analysis  $S_a(T_1)$ .

The IM levels, are defined to force a structure all the way from elastic response to final global dynamic instability (collapse). Further, the peak (inelastic) seismic demand is expressed by means of an EDP, such as the peak lateral displacement measured at a certain point on the structure along the direction of the seismic action. As discussed, IDA can readily account for the inherent uncertainty of the earthquake induced ground motion (GM) by considering a collection of recorded GMs corresponding to specific earthquake scenarios (e.g. moment magnitude, epicentral distance etc.) as input to perform RHAs for various IMs.

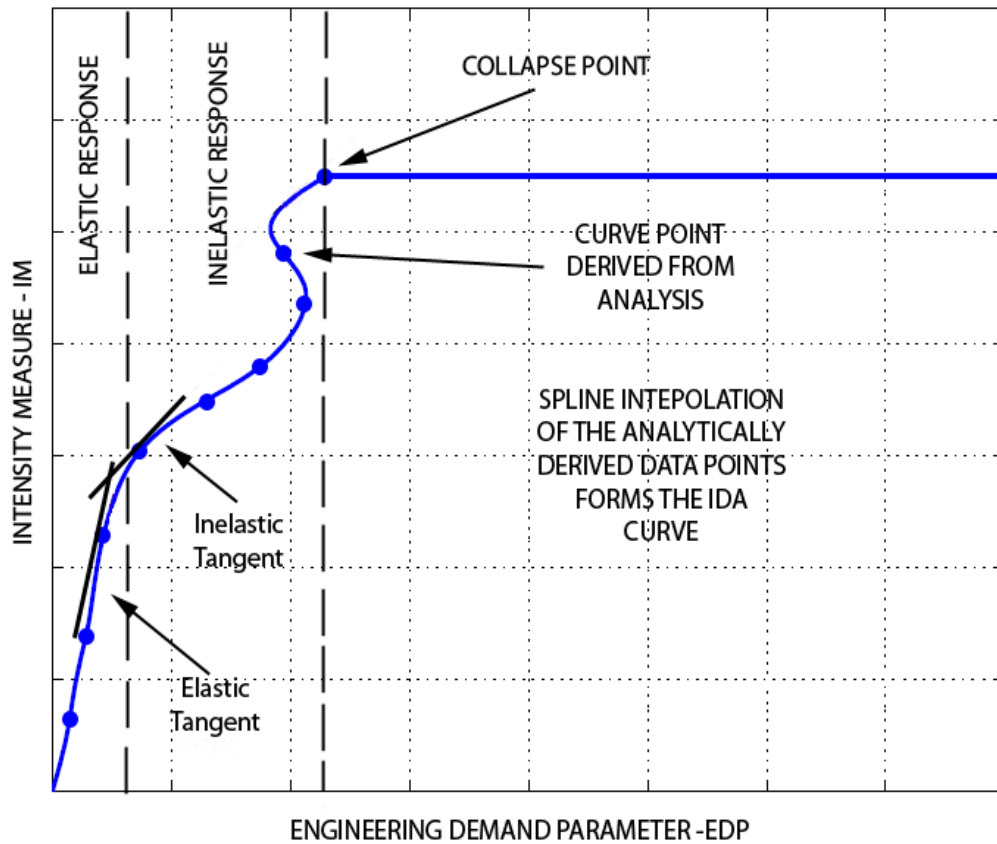


Figure 3.2: Typical observable patterns in an IDA curve (*Skrekas and Giaralis, 2013*).

IDA data results for each GM considered in the analysis are commonly represented in the form of IM versus EDP graphs (IDA curves) (Figure 3.3). In figure 3.2, a typical IDA curve corresponding to a single GM is shown. Each “dot” is derived from a RHA and the IDA curve is constructed via (spline) interpolation (*Vamvatsikos and Cornell, 2002*). In most of the cases, the non-linear response region can be readily identified, while a “stiffening” pattern (EDP reduces from an increased IM as shown in Figure 3.2) and other complex non-linear phenomena may reveal themselves depending on the structure and the properties of the considered GM for specific IM and EDP measures. In this regard, IDA can be viewed as a “dynamic version” of the well-known static inelastic (pushover) analysis widely used by the engineering community for structural design and assessment purposes against (lateral) dynamic loads.

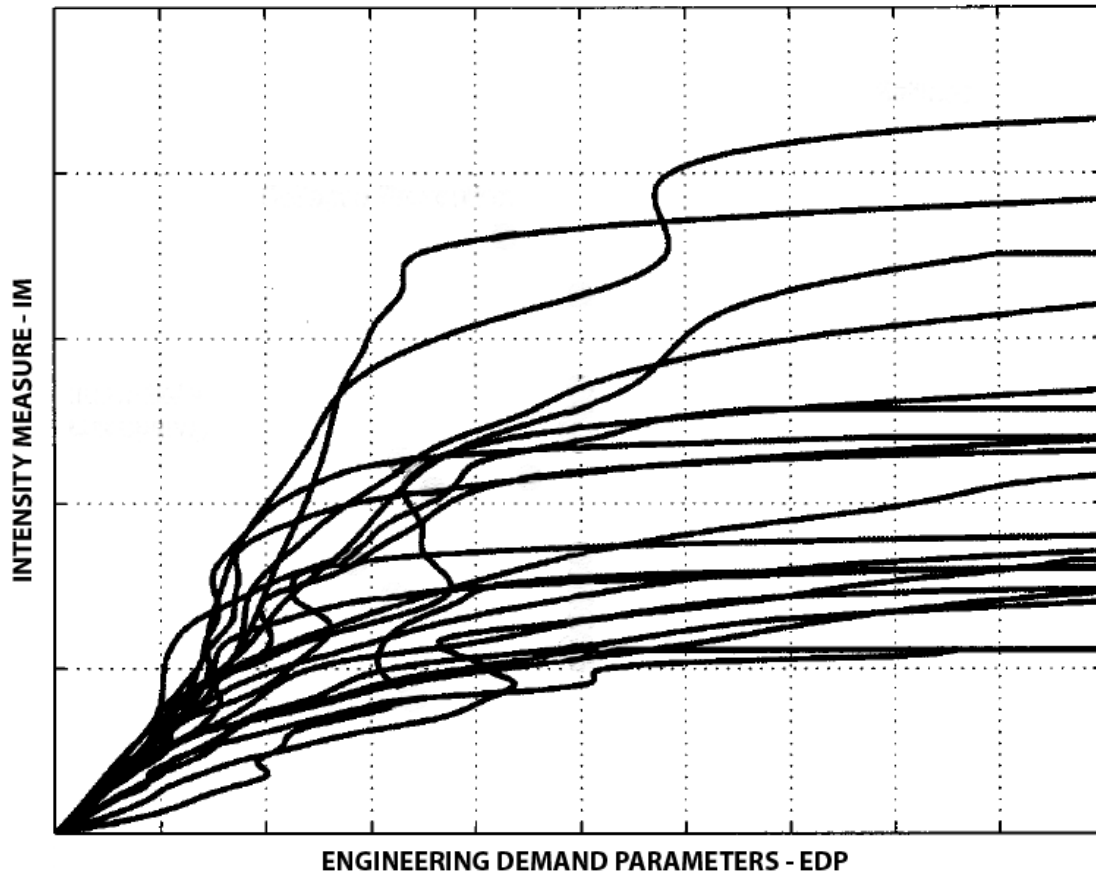


Figure 3.3: IDA curves obtain for a specific structure excited under a collection of ground motions scales to various intensity levels to represent various seismic hazard scenarios (Vamvatsikos and Cornell, 2002).

### 3.3 Statistical Analysis of IDA curves

Statistical analysis of the IDA curves (also known in the relevant literature as “summarization of IDA curves”) involves consideration of their “cross-sectional fractiles” (Vamvatsikos and Cornell, 2004). Cross-sectional fractile values allow the calculation of the 16%, 50% and 84% percentiles for the various levels of the EDP. Using these values, it is possible to obtain the fractile values of EDPs which then in turn can be interpolated to produce IDA fractile curves as those shown in figure 3.4. Then performance thresholds (limit states) are identified on the summarized IDA curves.

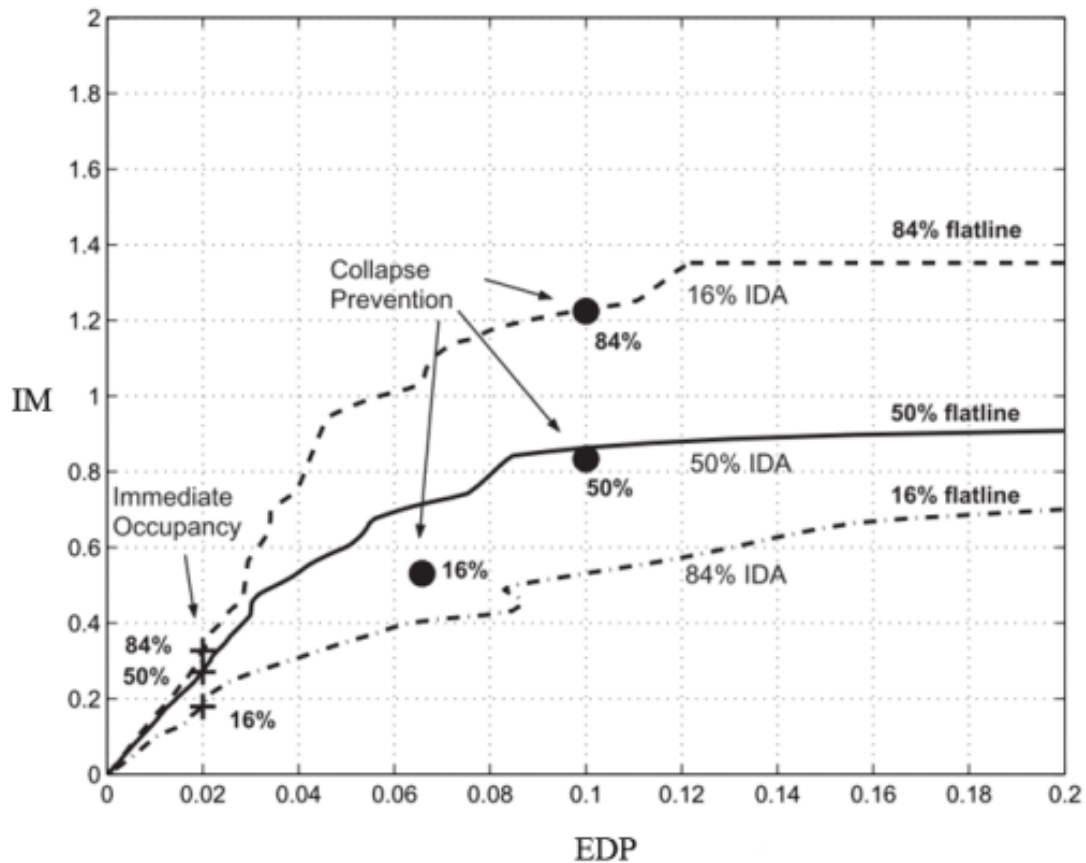


Figure 3.4: Example of summarized IDA curves and corresponding limit states (Vamvatsikos and Cornell, 2002).

IDA has been extensively used in the seismic performance assessment of a variety of structures (e.g. Mander *et al.*, 2007; Chomchuen and Boonyapinyo, 2017; Mahmoudi Moazam, Hasani and Yazdani, 2018) and to test the accuracy of other approximate analysis methods (Vamvatsikos and Cornell, 2002). Being computationally intensive, the method has found application initially into the analysis of two-dimensional structures. However, the method easily expands to three dimensional structures simply by considering the two horizontal orthogonal components of the ground motions in the suite. Then, either the two components of the ground motion are simultaneously considered in the IDA or IDA is performed for each ground motion component separately and the resulting EDPs are combined usually with the well-known SRSS rule

It becomes evident, that the accuracy of the PSDA analysis relates to the efficacy of the adopted IMs and EDPs (termed as IDA parameters) to reflect on the seismic hazard and the structural damages respectively.

---

### 3.4 Selecting IDA parameters

Several metrics to gauge (Cordova *et al.*, 2001) the level/degree of suitability of a candidate IMs have been proposed (Tothong and Cornell, 2007) and are identified as “*efficiency*”, “*sufficiency*”, “*effectiveness*”, “*practicality*”, and “*robustness*” and are discussed in this section.

The “*efficiency*” property is attributed when in the PSDA the selected IM results to reduced dispersion between response curves when compared to the dispersion obtained from another less “*efficient*” IM. “*Efficient*” IMs are highly desirable and the subject of open research since the error in the calculation of the sample mean (e.g. mean IDA response curve) is given by  $\frac{\sigma_{\ln EDP|IM}}{\sqrt{N}}$  (Tothong and Cornell, 2007) and thus is proportional to  $\sigma_{\ln EDP|IM}$ , where  $N$  corresponds to the number of ground motions used in the analysis. An illustrative example demonstrating the impact of a “*more*” efficient IM on the dispersion of IDA curves is presented in figure 3.5.

Note that the number  $N$  of ground motions is rarely larger than 30 since for example in order to reduce the error in half we will have to quadruple the size of the ground motion collection. Given that the number of records of severe (that are by definition rare) seismic historical events stored in relevant databases (e.g. PEER database) and the related additional computational time, the size of the ground motion pool is in most cases restrained below 30.

Furthermore, an IM is “*sufficient*” when the cumulative conditional probability of the EDP,  $G(EDP|IM)$  is only conditionally dependent on the selected IM and independent of any other variables that influence the estimation of the seismic risk (e.g. magnitude). The “*robustness*” term refers to “*scaling robustness*” and associates with the bias introduced in the obtained response curves when scaling ground motions to several intensities, a procedure typical in IDA analyses.

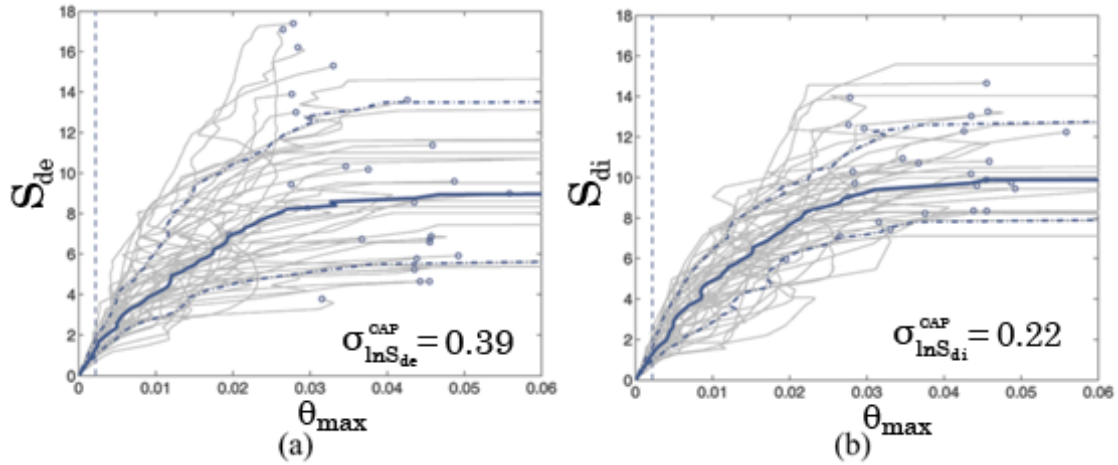


Figure 3.5: Dispersion of IDA curves for two intensity measures in (a) and in (b) demonstrating the efficiency property of the second intensity measure in (b) (Tothong and Cornell, 2007).

The term “*practicality*” correlates with the degree of suitability of the IM for use in the PSHA analysis. Mainly indicates the feasibility and conventionality of a PSHA based on the selected IM. Finally, the “*effectiveness*” property is satisfied when closed form solution of the triple integral in eq. 3.1 can be obtained.

In principle, the suitability of a given IM mainly relates to its ability to correspond to shifts in the modal characteristics of a structure and further to account for the higher mode contributions in the inelastic response range. In this regard, the “*optimal*” IM will always be structure and ground motion specific. However optimal IMs will suffer from the loss of generality and thus unsuitable for use in seismic performance assessment analyses.

Several research efforts attempt to identify/propose IMs that are globally applicable through encoding additional modal information in the IM. For example, in (Shome *et al.*, 1998) the authors demonstrated that the  $S_a(T_1)$  is more efficient compared to Peak Ground Acceleration (PGA) as it relates the IM with the natural structural period. However,  $S_a(T_1)$  is insensitive to changes of the fundamental frequency that occurs in the post-yield response range.

To improve the performance of PSDA, advanced scalar and vector-valued intensity measures were investigated. In (Baker and Cornell, 2008) an IM consisting of  $S_a(T_1)$  in combination with a metric of the spectral shape in terms of  $R_{T_1, T_2} = S_a(T_2)/S_a(T_1)$  where  $T_2$  corresponds to a user selected period,

was proposed. It was found efficient in predicting the maximum inelastic inter-storey drift ratio (IDR) for both ordinary and pulse-like ground motions but the overall performance was dependent on the choice of the  $T_2$ .

Luco and Cornell (2007), proposed an efficient and sufficient scalar  $IM_{1I\&2E}$  that provides estimates of the maximum IDR using two modes and the SRSS rule of modal combination suitable for both ordinary and pulse-like ground motions. Mehanny (2009) proposed a two-parameter scalar IM that account for the spectral shape.  $S_a(T_1)^{1-a}S_a(\sqrt{R}.T_1)^a$ , where R corresponds to the ratio of the lateral strength required for the system to remain elastic over lateral yielding strength.

Furthermore, Sehhati (2011) demonstrated that the Peak Ground Velocity is valid IM for both ordinary and pulse-like ground motions and Yahyaabadi and Tehranizadeh (2011) considered a combination of a wide range of spectral response parameter taking into account period elongation and higher mode effects.

In a more recent study, Zhou *et al.* (2017) studied the efficiency of five vector-based IMs for IDA. Two of the considered vector IMs consider higher structural modes and the other three incorporate the period elongation effect during the inelastic response range. The authors concluded that for first-mode dominant structures it is critical to select an IM that accounts for the period elongation while the number of the selected spectral acceleration has an impact on the efficiency.

In the ensuing numerical work, two different IMs are adopted in applying IDA to pursue performance-based seismic assessment (PBSA) of adjacent building structures within the PBEE framework. The first IM considered in (§4. Influence of Bi-Directional Pounding on the Inelastic Demand Distribution of Three Adjacent Multi-Storey RC Buildings) is the PGA. Although it is an inferior IM in terms of efficiency and sufficient as defined above with respect to, arguably, the most widely used  $S_a(T_1)$  in PBSA studies of non-pounding structures, it does constitute a rationale IM for EISP studies. In fact, PGA is the only IM considered in the open literature for EISP studies [REFs needed here]. This is because EISP studies involve two or more structures and therefore expressing the seismic intensity in terms of spectral acceleration  $S_a(T_1)$  is impractical as it is not obvious which structure's fundamental period  $T_1$  should be used. Further, it is emphasised that the study in Chapter 4 considers only one artificially generated ground motion pair and, therefore,

---

IM efficiency and sufficiency properties of the adopted IM (PGA) are not crucial.

The second IM used is novel to EISP studies involving the interaction of two or more structures with different structural properties. It is termed geometric mean (*avgSa*) and is defined, in the general case of  $K$  interacting structures, as the  $k^{\text{th}}$  square root of the product of the pseudo-spectral accelerations that correspond to the fundamental periods of the  $K$  interacting structures. That is,

$$avgSa = \left( \prod_{i=1}^K S_{a_i, T_i, 5\%} \right)^{\frac{1}{K}} = \sqrt[K]{Sa_{1, T_1, 5\%} \times Sa_{2, T_2, 5\%} \times \dots \times Sa_{K, T_K, 5\%}} \quad (3.2)$$

Note that, whilst it is the first time that *avgSa* is proposed to be used to examine EISP effects to seismic structural performance, this IM has been previously considered, originally by Cordova et al (2000), for PBSA of non-pounding structures. The rationale for its use has been to account for the phenomenological effective period elongation effect exhibited by yielding structures due to structural damage. Recently, Kazantzi and Vamvatsikos (2015) demonstrated that the *avgSa* is more efficient and sufficient than  $Sa(T_1)$  and PGA in PBSA of non-pounding structures. Further, the authors demonstrated that the *avgSa* does not suffer from the lack of sufficiency at high intensity levels (i.e. high scaling factors  $>3$  of the base seismic intensity). To this end, the current consensus is that it represents the most suitable IM for nonlinear RHA studies given its relative simplicity as it requires information containing in the linear response spectrum of a given GM.

Notably, the modular characteristic of the *avgSa* (product of two or more damped spectral accelerations) renders this IM as suitable for ESIP studies in terms of applicability. Expressing the seismic intensity levels in terms of the *AvgSa* during post-processing, adds additional information regarding the fundamental frequencies of the interacting structures. Mathematically, *AvgSa* represents the central tendency of the linear pseudo-spectral acceleration values of the coupled system. Therefore, it can potentially account for shifts in the fundamental frequencies of the interacting structures that occur within their inelastic response range.

In the case of the independent vibration of the adjacent structures that typically serves as a performance benchmark for the coupled case, the GM can be practically introduced during the statistical characterization of the

structural responses by assuming the uncoupled structures as a coupled system that exhibits an initial separation distance that tends to infinity.

Looking away from IMs, the EDPs of choice in the ensuing numerical work are a) the Ductility Ratio (DR) that is defined as the ration between the maximum and yield deformation and b) the Inter-storey Drift Ratio (IDR) that is defined as the ration of the relative displacements between two building floors over the floor height. Both the above EDPs have been found to correlate well with structural damage in non-pounding structures in the literature [REFs needed here] and, therefore, serve well the purpose of quantifying seismic performance of structures subject to pounding.

# Chapter 4

## Influence of Bi-Directional Pounding on the Inelastic Demand Distribution of Three Adjacent Multi-Storey RC Buildings

Adapted from: Skrekas, P., Sextos, A. and Giaralis, A. (2014). Influence of bi-directional seismic pounding on the inelastic demand distribution of three adjacent multi-storey R/C buildings. *Earthquakes and Structures*, 6(1), pp.71-87

### 4.1 Overview

This chapter, presents a realistic case study of EISP between buildings located within a city block. The block consists of a high, newly designed building that is constructed in bi-lateral contact, to two lower and under-designed buildings. The objective is to assess the induced structural damage, in terms of rotational ductility demand at a local and system level, with and without building interaction (pounding), both under the design earthquake and more severe seismic actions.

It is noted that in most real-life cases, pounding of adjacent buildings takes place in a rather complex manner for a number of additional reasons (*Jeng & Tzeng, 2000; Maison et al., 2012*) such as a) buildings are not constructed in series but within blocks, hence, particularly the corner buildings are subject to bi-lateral pounding, and b) due to the lack of available space and the cost of land in modern cities, newer structures are typically higher and slender than older ones, a fact that is commonly associated with the significant contribution of their higher, primarily torsional, modes of vibration.

This is a very common problem nowadays in modern cities and, in fact, it is not yet taken into account by current codes of practice which only prescribe a

minimum separation gap between the constructed building and its immediate built environment (CEN 2004a). This gap is usually determined based on response spectrum analysis in which the expected non-linear behavior of structures is only implicitly accounted for, through the behavior (or force reduction) factor. Field observations have shown that such considerations may not prevent seismic pounding in case of events less frequent than the design earthquake, while it is quite common that “as-built” structures may often have insufficient or no clearance at all for practical reasons.

In the case of adjacent buildings with equal storey floor levels, seismic pounding involves slab-to-slab collisions and, thus, no local loss of stiffness and/or strength to the lateral force resisting structural system takes place. In such cases, the influence of seismic pounding to the global response of structures becomes the issue of concern. In this context, a parametric study was undertaken in (*Jankowski, 2008*) to investigate the influence of slab-to-slab pounding to the seismic response of two 3-storey, double-symmetric in plan, frame buildings considering material non-linearity. The structures were simultaneously subject to the three components of the strong ground motion associated with a specific historical earthquake record and results on the influence of pounding effects with regard to the clearance between the structures, their yielding strength and their inertial and stiffness properties have been reported. The main conclusion was that pounding is more critical for the structure with the lower mass. This conclusion has been further confirmed in (*Jankowski, 2009*) who considered, through a detailed three-dimensional finite element (FE) analyses, the interaction and pounding of a RC building with its significantly lighter, attached, staircase tower of the same total height.

Another historical study of pounding involving under-designed masonry and RC buildings is reported in (*Fiore & Monaco, 2010*). More recently, the influence of pounding to a multi-storey wood frame building located at the corner of a typical building block in San Francisco has been assessed within a PBEE framework (*Maison et al. 2012*). The above conspectus of recent published work reveals that research efforts to assess the influence of seismic pounding have focused either on simplified “academic examples” of structures represented by two-dimensional (2D) or three-dimensional (3D) FE models or on real-life case-studies of under-designed buildings. Still though, the common case of high, newly designed buildings that are constructed in

simultaneous, bi-lateral contact to a number of typically lower and under-designed buildings has not yet been thoroughly studied.

To this extend, this chapter, considers the case of a newly designed, 7-storey, RC building located at the corner of a block in a major metropolitan area, in contact with two adjacent, under-designed, 5-storey buildings. The condition is that for constructional purposes, the first building (hereafter denoted as “K”) is in immediate contact with the other two (identified as “K1” and “K2”), thus, there is practically no separation gap. The assumption is also made that storey levels are at equal heights and that there is no shear slab penetration to the columns in contact (i.e. local damage is only attributed to slab-to-slab pounding).

The condition is that for constructional purposes, the first building (hereafter denoted as “K”) is in immediate contact with the other two (identified as “K1” and “K2”), thus, there is practically no separation gap. The assumption is also made that storey levels are at equal heights and that there is no shear slab penetration to the columns in contact (i.e. local damage is only attributed to slab-to-slab pounding).

## **4.2 Building block case studied**

### **4.2.1 Design considerations**

The adopted case study, is based on a real building block of three adjacent, multi-storey RC buildings bi-laterally interacting as shown in Figure 4.1. The corner building “K” is assumed to be designed according to the European structural design code framework, that is, Eurocode 2 for RC buildings (CEN, 2004b) in conjunction with Eurocode 8 for earthquake resistant design (CEN, 2004a) and the Greek National Annex, for a (design) spectrum assuming peak ground acceleration of 0.16g, soil type “B”, ductility class high (DCH) and behaviour factor “q” equal to 3.0 (CEN, 2004a). Concrete grade was taken as C20/25 (compressive strength equal to 20N/mm<sup>2</sup>) and steel grade as S500 (yielding strength 500Mpa). The modulus of elasticity of the reinforced concrete is taken equal to 29 GPa and its density is 25 kN/m<sup>3</sup>.

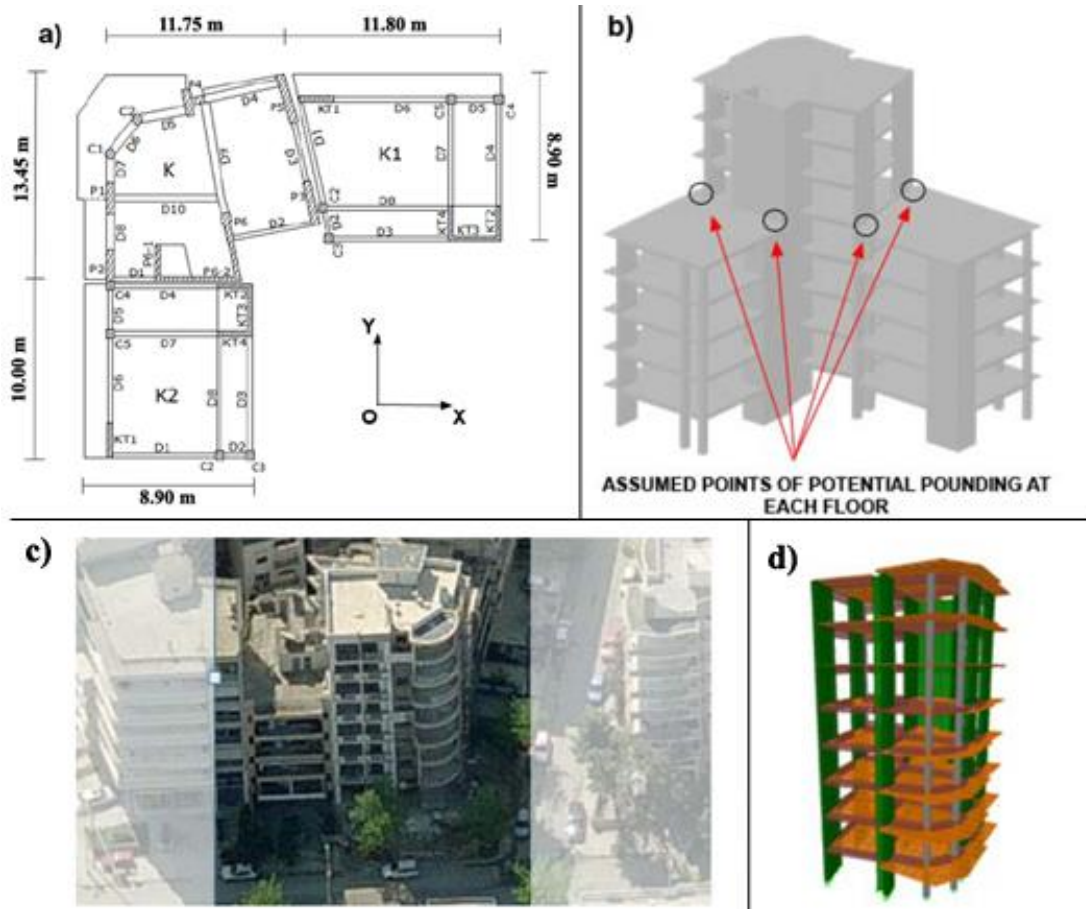


Figure 4.1: The considered three-building complex a) typical floor plan; b) locations of the potential pounding; c) illustration of the real case that is used as a basis of the examined case; and d) 3-Dimensional finite element model of the corner building “K”.

#### 4.2.2 Finite Element (FE) modelling assumptions

Three distinct finite element models have been developed to scrutinize the effect of seismic pounding, i.e., one for “contact-free”, individual, buildings “K”, “K1”, “K2”, and a fourth FE model for the entire interacting complex as shown in Figure 1. The plan views showing the typical sizes of the various structural elements of the corner building K, and buildings K1 and K2 are depicted in figures 4.2 and 4.3 respectively.



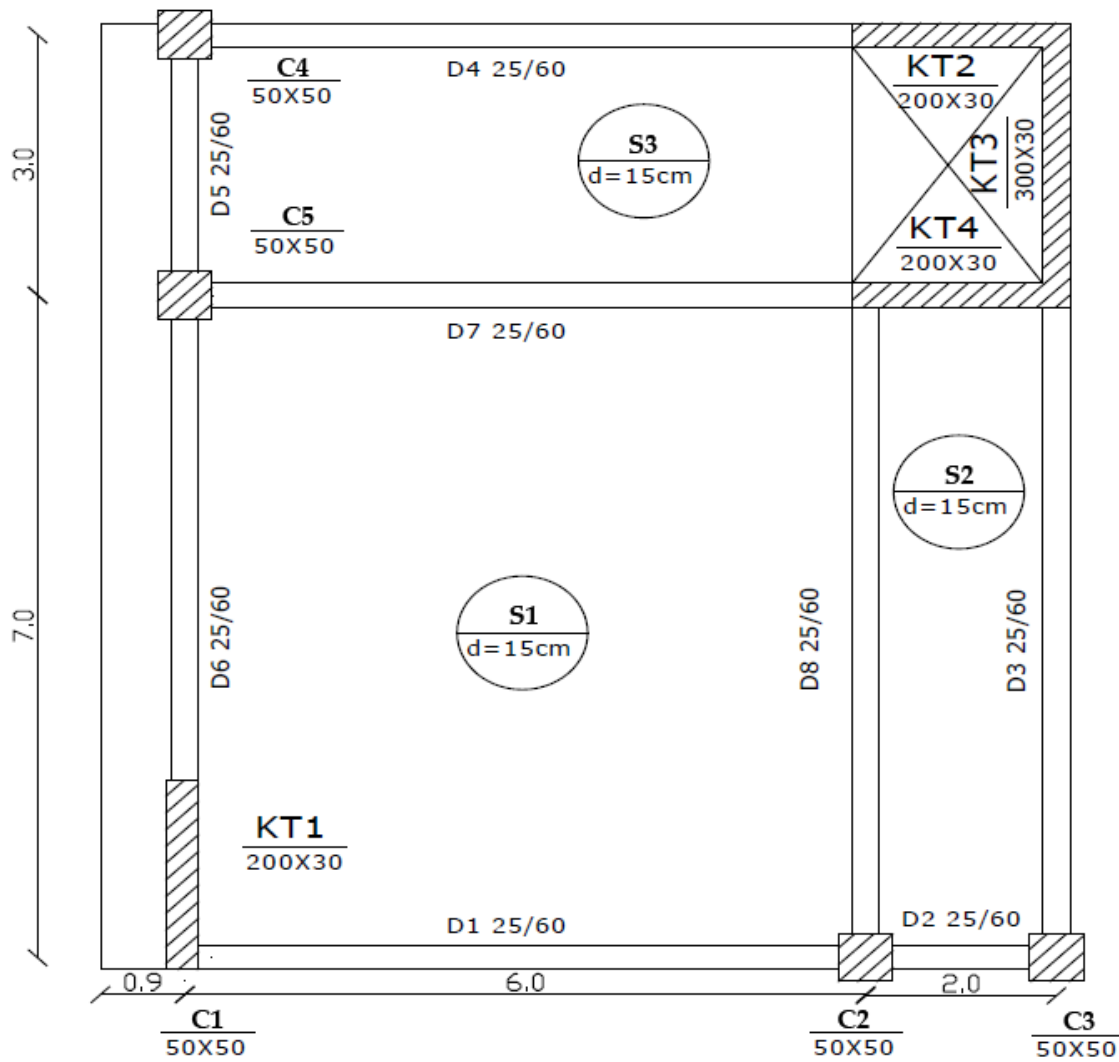


Figure 4.3: Plan view of building K1 and K2 depicting various dimensions (in meters) and structural element sizes (in centimetres).

The commercial FE software SAP2000® (CSI, 2012) has been used for all linear and non-linear analyses. Two-dimensional quadrilateral shell elements were used to model slabs and shear walls, while beams and columns were modelled using linear 1D frame elements (Figure 4.2a).

**Table 4.1:** Natural periods of the considered buildings.

Building	1 <sup>st</sup> Natural period	2 <sup>nd</sup> Natural period	3 <sup>rd</sup> Natural period
K	0.72s (Dominantly translational along x-x axis) $U_x= 50\%$	0.58s (Dominantly translational along y-y axis) $U_y= 70\%$	0.30s (Dominantly rotational) $R_z= 71.5\%$
K1	0.65s (Rotational)	0.43s (Translational)	0.21s (Rotational)
K2	0.58s (Rotational)	0.41s (Translational)	0.21s (Rotational)

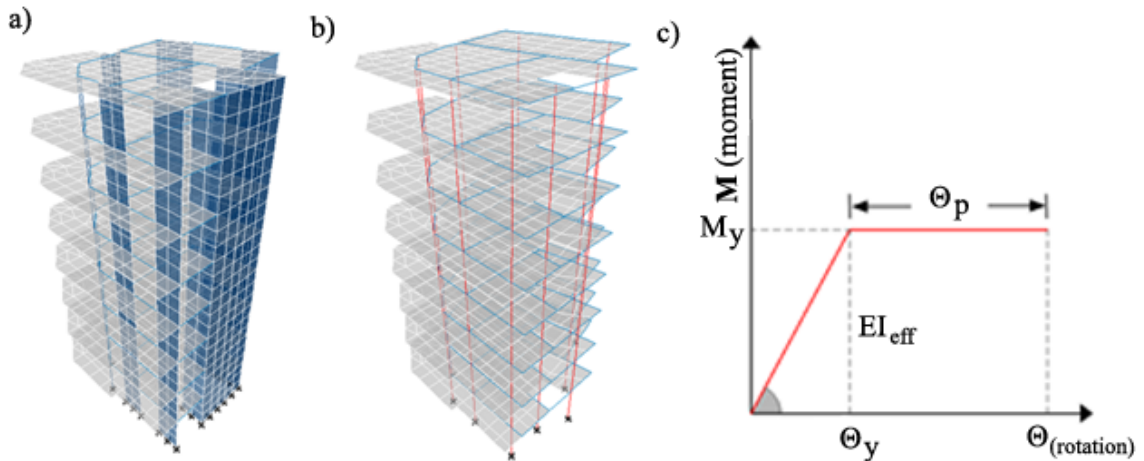


Figure 4.4: Finite Element modelling assumptions for shear walls and cores and considered lumped plasticity moment-rotation law.

Table 4.1 reports the first three natural periods of the three buildings considered along with a qualitative description of the corresponding mode shapes obtained by means of a standard modal analysis to the models for fixed based conditions. It is noted that all structures have a significant torsional mode.

Further, fixed support conditions are adopted for all buildings implying that soil structure interaction (SSI) effects are negligible. This choice is justified: (1) partly by the fact that stiff soil conditions (soil type B according to Eurocode 8) are assumed in the definition of the design spectrum for which

SSI effect is less likely to be severe/important, and (2) partly by the recent work of *Madani et al. (2015)* in which it is concluded that the influence of SSI on storey shears and lateral displacements is significantly less important than pounding.

### 4.2.3 Material Nonlinearity

Inelastic material behaviour in flexure at all critical cross-sections of beams and columns is introduced by assuming lumped plasticity through rotational spring elements assigned at both ends of each frame element. A bilinear perfectly elasto-plastic moment–rotation ( $M-\theta$ ) relationship is assumed for each plastic hinge as shown in Figure 4.2c after appropriate computation of the corresponding moment-curvature ( $M-\varphi$ ) relationships by means of standard fibre analysis with the program RCCOLA (*Kappos, 1993*). The plastic rotation  $\theta_p$  is computed by the equation (*Priestley, Seible and Calvi, 1996*) as follows:

$$\theta_p = L_p(\varphi_\theta - \varphi_y) \quad (4.1)$$

where  $\varphi_u$  and  $\varphi_y$  are the ultimate and yielding curvatures, respectively, determined from fibre analysis and plastic hinge length  $L_p$  is given by:

$$L_p = 0.08L + 0.022f_y d \quad (4.2)$$

In the above equation,  $L$  is the distance from the critical section of the plastic hinge to the point of contraflexure,  $f_y$  is the assumed yielding stress of the longitudinal reinforcement bars, and  $d$  is the radius of the longitudinal reinforcement bars. The yield rotation  $\theta_y$  is evaluated from the corresponding area in the curvature diagram, as  $\theta = \int \varphi dx$ , although the above procedure has been found to underestimate the actual  $\theta_y$ . In fact, the slope of the second branch of the  $M - \theta$  curve is higher than that of the  $M - \varphi$  curve and is dependent on the rotational ductility factor  $\mu_\theta$  (*Kappos and Sextos, 2001*). Nevertheless, the assumption is made that the yield rotation  $\theta_y$  can be evaluated by the curvature diagram, thus, it is estimated as:

$$\theta_y = 0.5\varphi_y L \quad (4.3)$$

The values of each property used in the calculation of the moment-rotation law (see Figure 4.4) derived from the corresponding moment-curvature relationships as described above, for each structural element, are reported in Appendix A. Shear walls and concrete cores are modelled by means of an

“equivalent central column” connected to the beams at the level of each floor using perfectly rigid virtual frame elements. This modelling strategy is necessary to allow for inelastic behaviour at the base of shear walls and cores which is assumed as a critical cross-section in the earthquake resistant design of coupled RC buildings. Bi-linear rotational spring elements, defined in the same manner as detailed above for the case of beams and columns, are introduced at their base to account for the potential formation of plastic hinges. A typical topology of this modelling is juxtaposed with the FE model used in the design phase of the K building in Figure 4.2 for the purpose of comparison. Special attention has been given to calibrate the model with the equivalent central columns to achieve similar modal properties with the FE models used in the design stage where shear walls and cores were explicitly modelled via 2D shell elements.

#### 4.2.4 Geometric Nonlinearity

For the purposes of the present study, pounding is modelled using a uniaxial linear spring which is activated only under compression. To this aim, the built-in “gap” non-linear element of SAP2000 has been incorporated in the FE model combining all three buildings of the considered complex. Impact is assumed to take place at four locations at each floor level as shown in Figure 4.1b. Assuming that the buildings are initially in contact, which is also the case of the actual building block used as the reference for this study (Figure 4.1c), the pounding forces along the local longitudinal degree of freedom of each gap element can be expressed as follows

$$f = \begin{cases} kx, & x \leq 0 \\ 0, & x > 0 \end{cases}, \quad (4.4)$$

where  $k$  is the stiffness of the spring set equal to 107 kN/m and  $x$  is the relative displacement at the spring edges. It is noted that the adopted pounding model does not take into account contact friction and local energy dissipation during pounding (Anagnostopoulos, 2004; Jankowski, 2005; Mouzakis and Papadrakakis, 2004; Muthukumar and DesRoches, 2006), hence, it is assumed that pounding does not contribute to the dissipation of the input seismic (kinetic) energy and subsequently, it is inherently conservative in terms of peak response quantities. This is in alignment with the purposes of this study which seeks to “envelop” the pounding effect in terms of peak ductility demands following common earthquake resistance design

considerations, rather than to explicitly represent and model in absolute terms the complicated phenomenon of seismic pounding.

### 4.3 Representation of seismic input action

Earthquake ground motion is introduced through artificial accelerograms that are compatible with the Eurocode 8 response spectrum for the site of interest and are uniformly scaled for different levels of seismic intensity expressed in terms of PGA (i.e.,  $0 \leq a_g \leq 1.0g$  at a step of  $0.1g$ ), in applying Incremental Dynamic Analysis (*Vamvatsikos & Cornell, 2002*). Given that in this study initially the record-to-record is ignored as previously discussed, the adoption of an artificial accelerogram has been preferred over a recorded one as it is easier to be generated and subsequently modified to match as closely as possible the response spectrum as discussed in *Giaramis and Spanos (2009)*. The latter criterion (i.e., close spectral matching) is deemed more important than the use of a recorded accelerogram whose frequency content may be perhaps more physically meaningful. In subsequent numerical work aiming to study the effect of record-to-record variability onto structural performance under EISP sufficiently large numbers of judiciously selected recorded ground motions are used as opposed to artificially generated ones.

Further, the progressive scaling permits the gradual yielding of the structure with increasing intensity and the investigation of the effect of bi-directional building pounding to the extent and location of the induced damage. It is noted that although the spectral acceleration at the natural period of a structure is a widely used intensity measure (IM), it is PGA that is adopted herein, since the particular study involves three coupled buildings for which the fundamental period is not common. It is also reported that ground motion variability is deliberately not taken into explicit consideration in this study in order to draw some fundamental deterministic conclusions first, based on the Eurocode 8 (uniform hazard) target response spectrum.

Two, equal intensity accelerograms, corresponding to the two principal directions of excitation (x-x, y-y), have been generated for each level of PGA using the wavelet-based stochastic approach detailed in (*Giaramis and Spanos, 2009*) after close spectral matching along the entire period range of interest (Figure 4.3a). The adopted stochastic approach yields non-stationary in amplitude strong ground motion records compatible with a given design displacement (target) spectrum by means of a harmonic wavelet-based iterative procedure and a state-of-the-art baseline correction technique. The

approach does not account for non-stationarity in the frequency content of the ground motion. The latter consideration is addressed in the ensuing chapters by adopting large numbers of recorded GMs in conjunction with reduced complexity structural models.

Pertinent statistical attributes of the inelastic seismic demands to the horizontal (beams) and the vertical (columns and shear walls) members at every floor of each structure are monitored for various scaling factors of the input seismic action. To directly illustrate the effect of pounding on the damage induced at the three buildings, the rotational ductility demand  $\mu_{\theta}$  at all distinct members of the three buildings is adopted as the principal Engineering Demand Parameter (EDP). The time-histories of the considered accelerograms are also shown in Figure 4.3b and 4.3c.

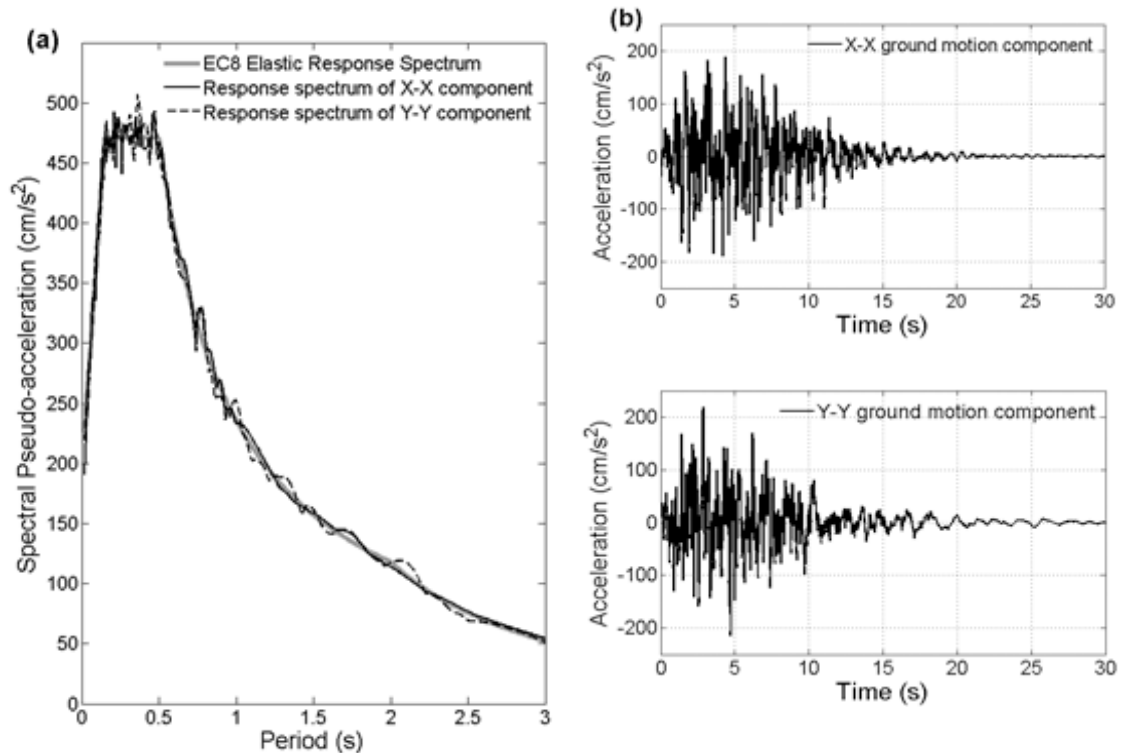


Figure 4.5: a) EC8 spectrum and response spectra of spectrum compatible accelerograms considered. b) Time traces of spectrum compatible accelerograms.

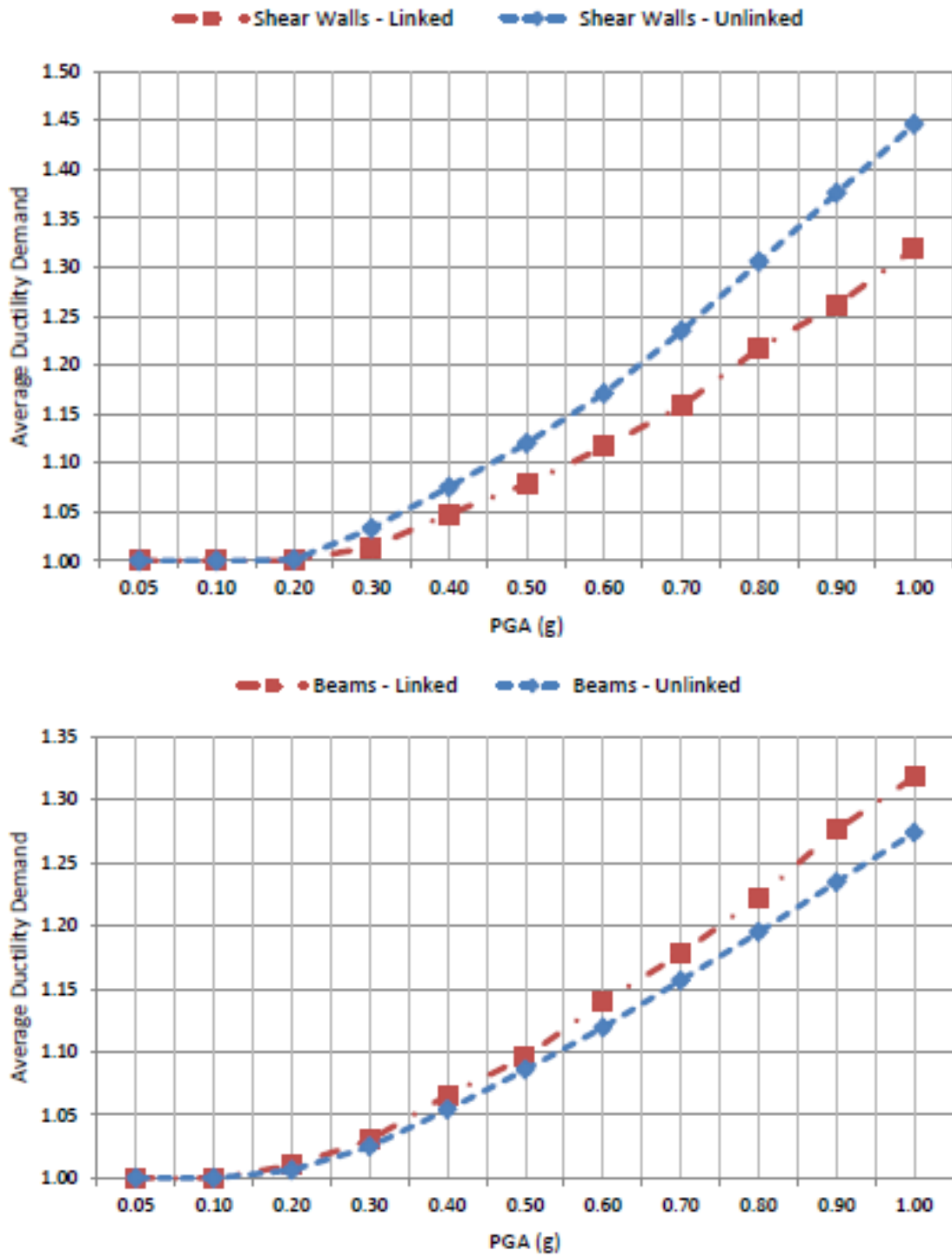
#### **4.4 Effect of bi-directional pounding on the inelastic demand distribution of three coupled buildings.**

Following the development of the 3D, coupled finite element model of the three adjacent buildings comprising the block, a series of 10 non-linear time-history analyses were undertaken studying the dynamic response of both the bi-directionally interacting system and that of each individual building considered entirely uncoupled (i.e., as if the seismic joint was of infinite length). Then, seismic damage, expressed in terms of rotational ductility demand, was predicted for the adopted seismic scenario presented in section 3, for the case of the linked (coupled) and unlinked (uncoupled) buildings, K, K1 and K2.

Figure 4.4 illustrates the variation of the average ductility demand at the base of the shear walls, the edge of the beams and the top and bottom of the columns at the ground floor of the seven-storey corner building “K”, with and without pounding and for increasing seismic intensity (PGA). It is seen that independently of seismic pounding, structural damage at the shear walls and the beams of the ground storey is first initiated approximately at a peak ground acceleration of approximately 0.15g, a fact which is consistent with the capacity design of the “K” building (i.e., beam yielding precedes column failure) and the acceptance of damage for the design earthquake through the adoption of a behaviour factor  $q=3.0$ .

A second reasonable observation that is made is that, the effect of bi-directional pounding to the rotational ductility demand of the ground floor shear walls and beams is increasing with increasing intensity. Furthermore, shear walls of the corner “K” building seem to be relieved at the ground floor due to its multiple pounding with “K1” and “K2”; in particular, the average  $\mu_{\theta}$  is reduced from 1.45 to 1.30 for the extreme case of  $a_g = 1.0g$ . This is not the case though for beams which are critically affected by seismic pounding (Figure 4.4 middle). This effect is even more profound in Figure 4.5 where the detrimental influence on pounding to the beam damage is clearly seen at the 5th, 6th and 7th storey.

# Chapter 4 - Influence of Bi-Directional Pounding on the Inelastic Demand Distribution of Three Adjacent Multi-Storey RC Buildings



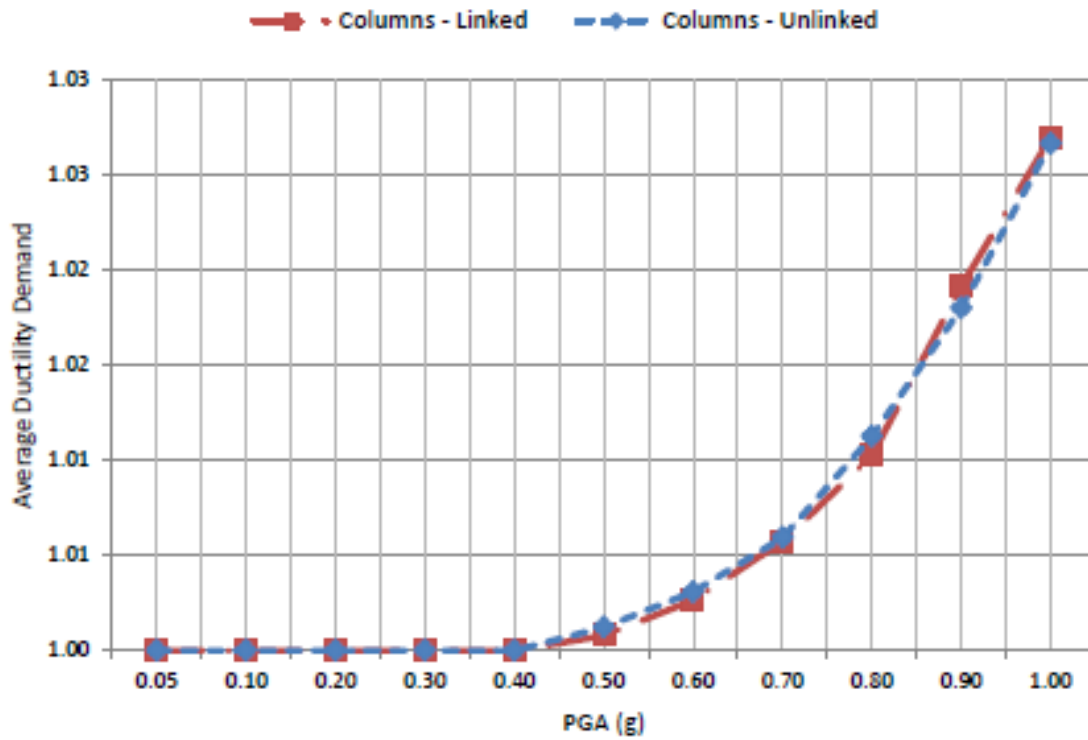
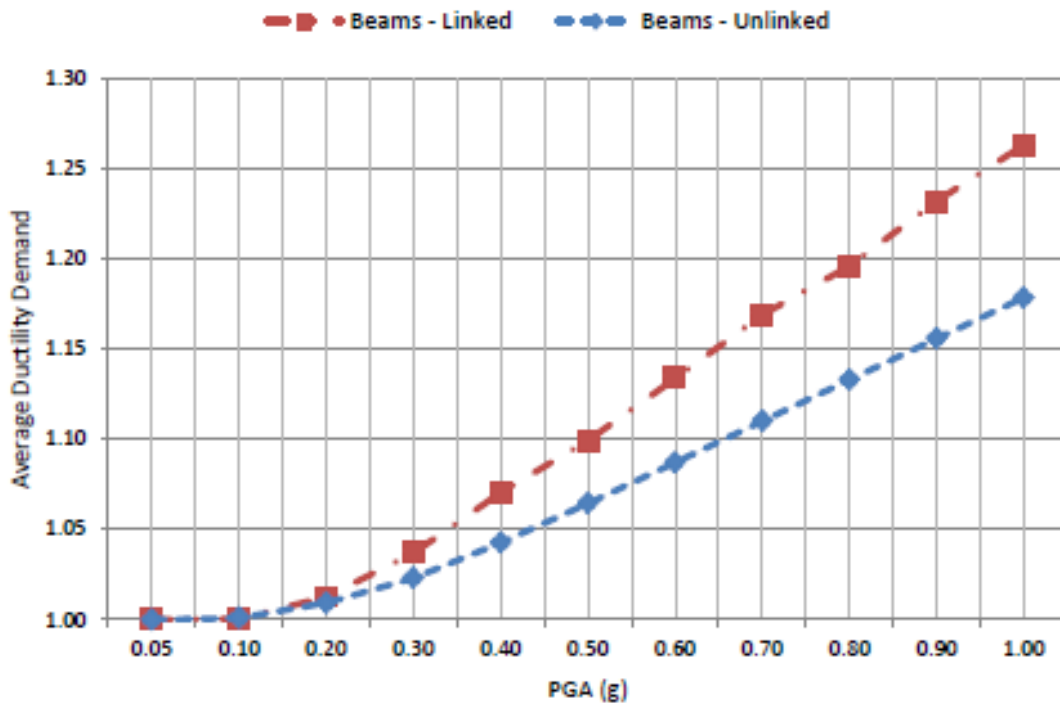
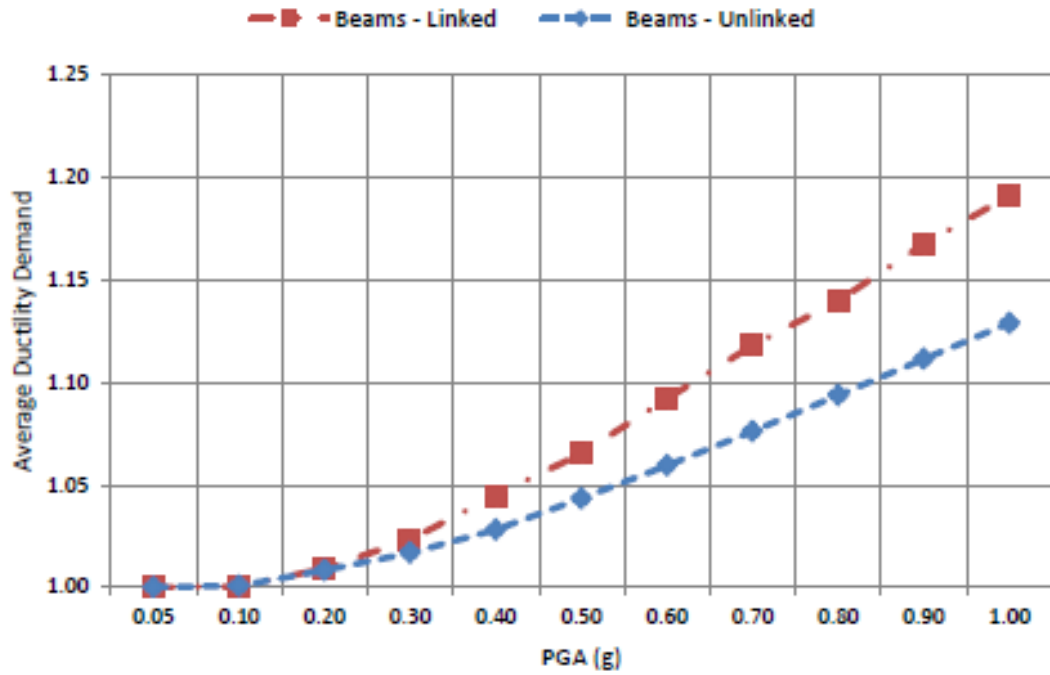


Figure 4.6: Average ductility demand at the base of the shear walls (top), the edge of the beams (middle) and columns (bottom) of the ground floor for the corner building “K” with and without pounding and different levels of seismic intensity (PGA).

Chapter 4 - Influence of Bi-Directional Pounding on the Inelastic Demand Distribution of Three Adjacent Multi-Storey RC Buildings



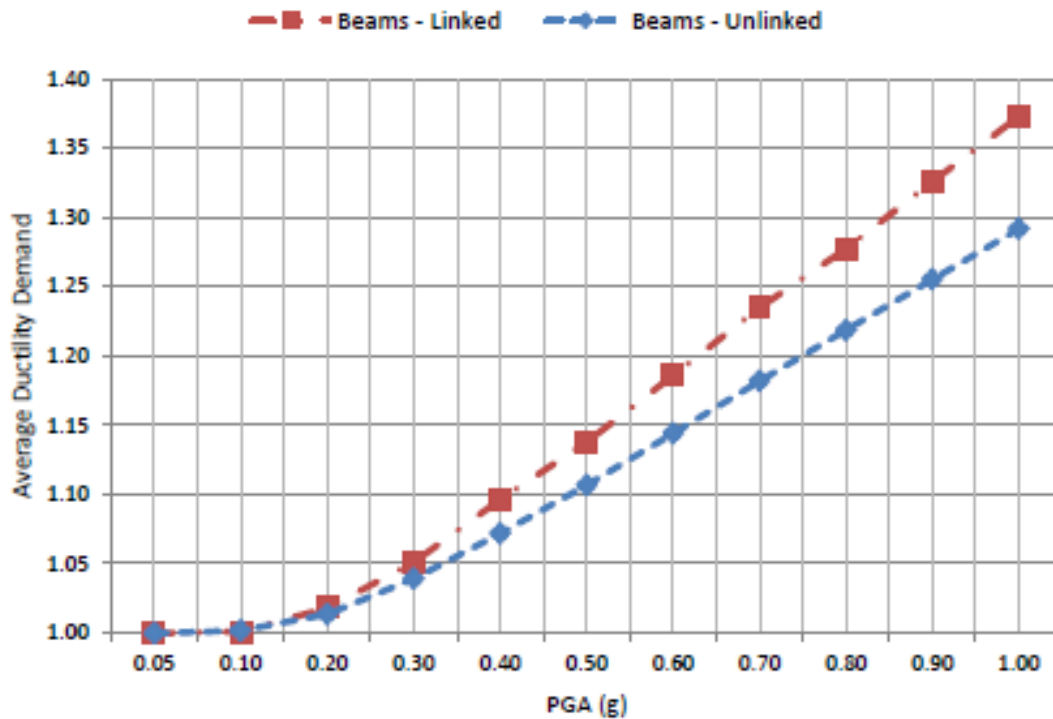


Figure 4.7: Average ductility demand induced at the beams of the fifth (bottom), sixth (middle) and seventh floor(top) for the corner building “K”, with and without pounding and different levels of seismic intensity (PGA).

In general, pounding effects do not significantly affect the seismic demands of the columns but this is primarily because seismic forces are resisted by the shear walls and the columns remain elastic even for high levels of PGA. To better visualize the interaction between the three buildings due to seismic pounding, a series of additional illustrations is presented in Figures 4.6 - 4.9 highlighting the mean of the ductility demand ratio (i.e.,  $E = \mu_{\theta,linked}/\mu_{\theta,unlinked}$ ) as well as the standard deviation of this ratio, in all buildings, with and without pounding and for different levels of ground motion intensity (i.e., 0.5g and 0.9g).

Focusing again on the 7-storey, corner building “K” it is also clearly seen that the vertical elements (Figures 4.6 and 4.8) are generally either relieved *on average* (i.e., ground floor members independently of PGA) or show a negligible increase in ductility demand that does not exceed 1% (ratio  $E < 1.01$ ). It is critical to notice though, that this effect is only observed on average, while the significant variation of the demand in individual structural members is essentially suppressed. For instance, there are many cases where the  $\mu + \sigma$  of the rotational ductility demand ratio ( $\mu_{\theta,linked}/\mu_{\theta,unlinked}$ ) is almost doubled

## Chapter 4 - Influence of Bi-Directional Pounding on the Inelastic Demand Distribution of Three Adjacent Multi-Storey RC Buildings

independently of the storey and the level of PGA examined. Similarly, the  $\mu$ - $\sigma$  of the rotational demand ratio, may well drop below 0.4. This is a clear indication of the significant effect of seismic pounding not only on absolute values of demand but particularly on the damage distribution, even in new buildings that are designed to modern seismic codes.

The same observation is also valid for the beams of the corner building “K” where the discrepancy in ductility demand, with and without pounding, is indeed very high, even though *on average*, again, ductility demand is only increased by a mere 10%.

Studying the side, lower, buildings “K1” and “K2” the above findings are also valid.

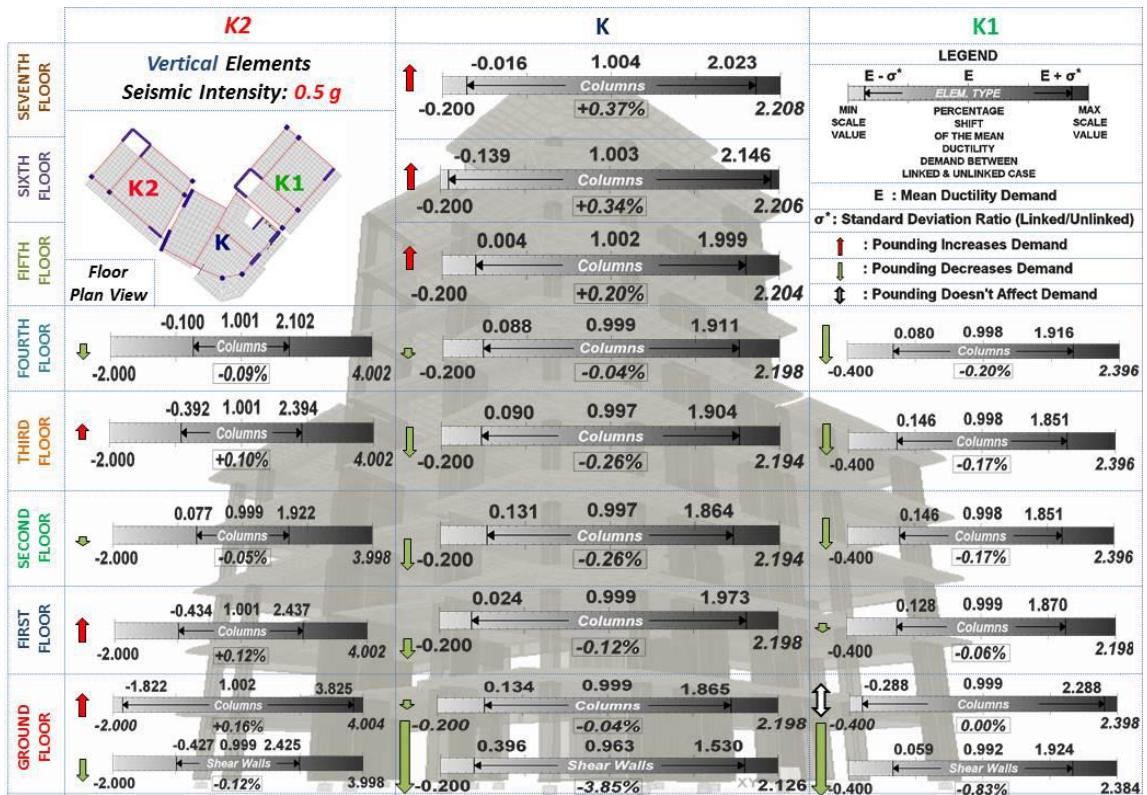


Figure 4.8: Variation of inelastic demand ( $\mu \pm \sigma$ ) due to structural pounding (columns,  $a_g = 0.5 g$ ).

## Chapter 4 - Influence of Bi-Directional Pounding on the Inelastic Demand Distribution of Three Adjacent Multi-Storey RC Buildings

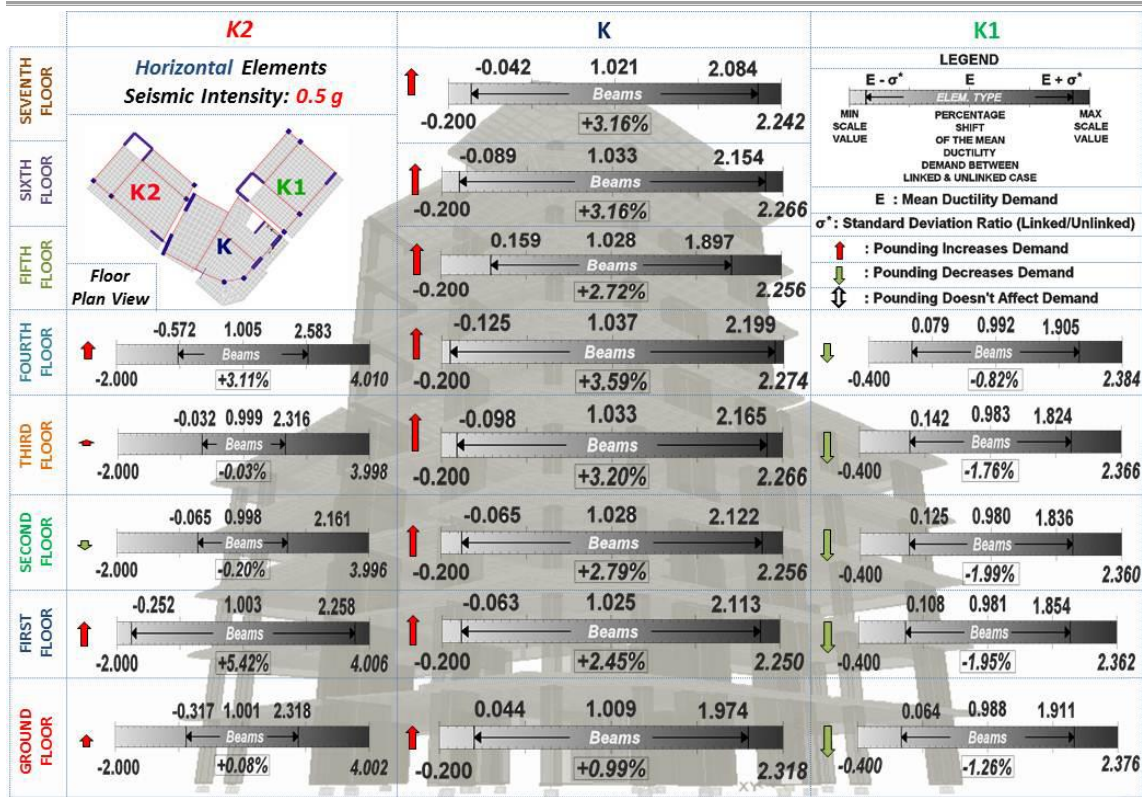


Figure 4.9: Variation of inelastic demand ( $\mu \pm \sigma$ ) due to structural pounding (beams,  $a_g = 0.5 g$ ).

## Chapter 4 - Influence of Bi-Directional Pounding on the Inelastic Demand Distribution of Three Adjacent Multi-Storey RC Buildings

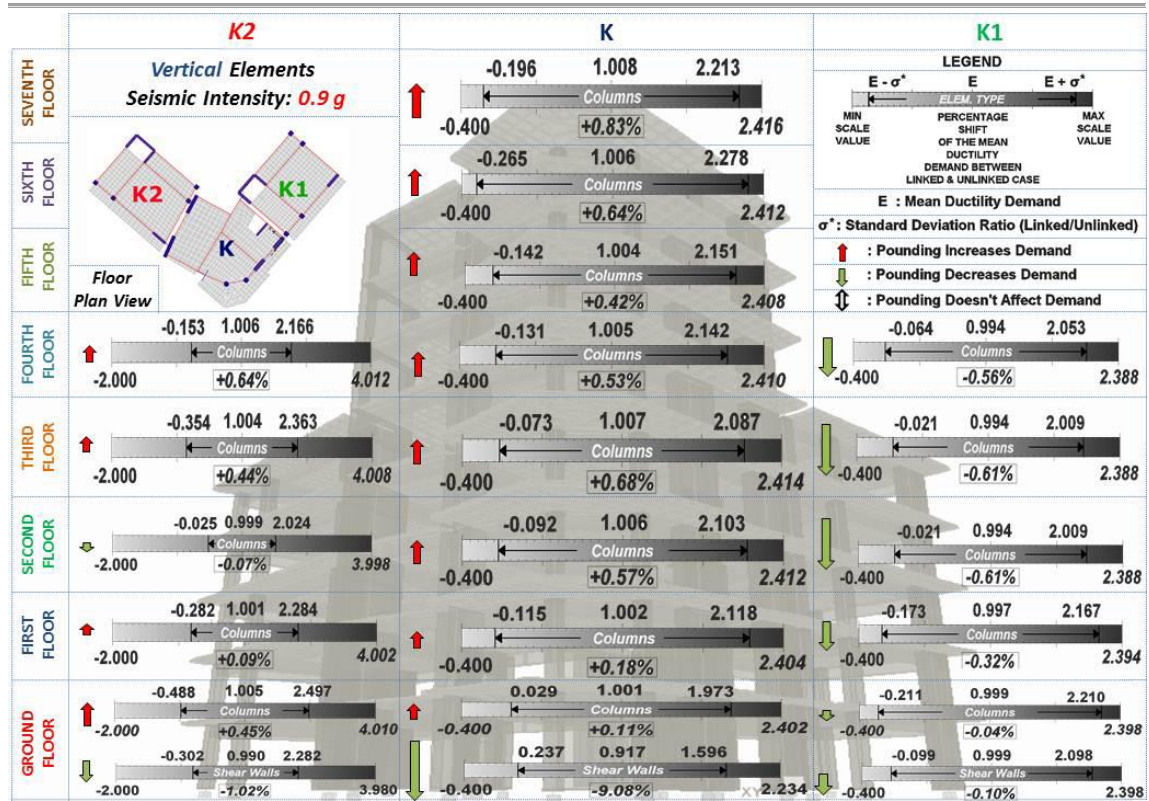


Figure 4.10: Variation of inelastic demand ( $\mu \pm \sigma$ ) due to structural pounding (columns,  $a_g = 0.9 g$ ).

## Chapter 4 - Influence of Bi-Directional Pounding on the Inelastic Demand Distribution of Three Adjacent Multi-Storey RC Buildings

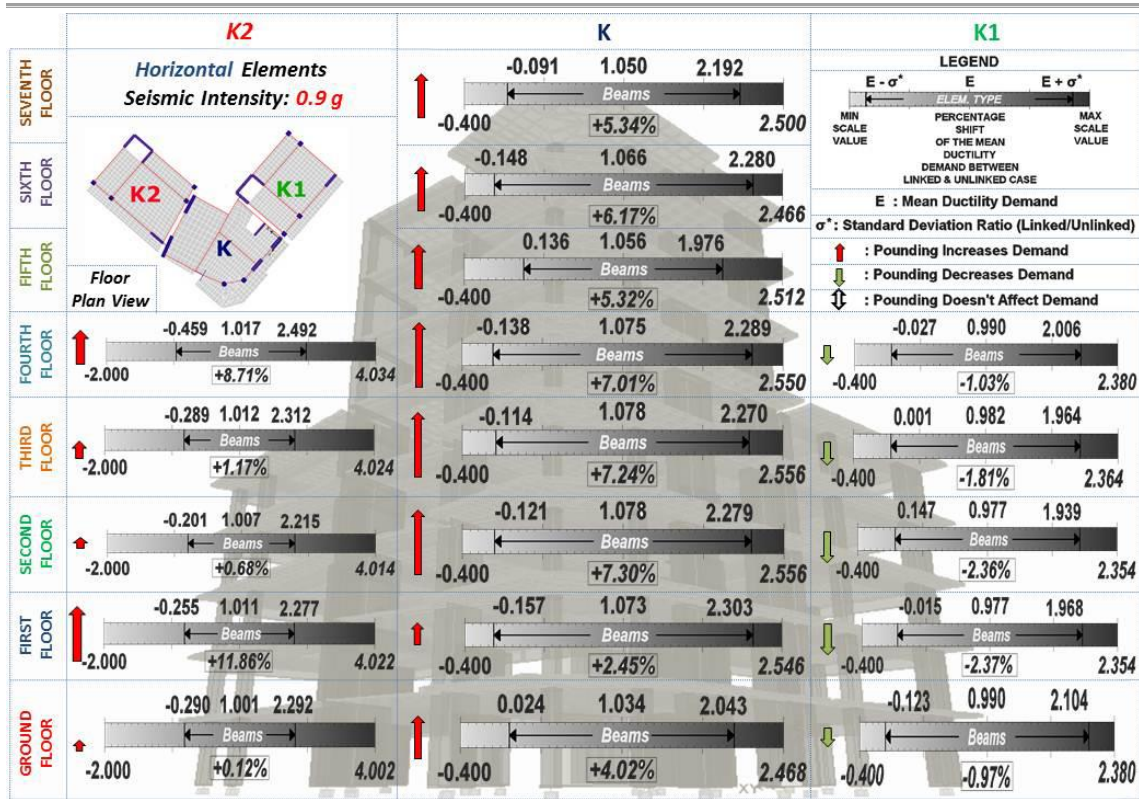


Figure 4.11: Variation of inelastic demand ( $\mu \pm \sigma$ ) due to structural pounding (beams,  $ag = 0.9 g$ ).

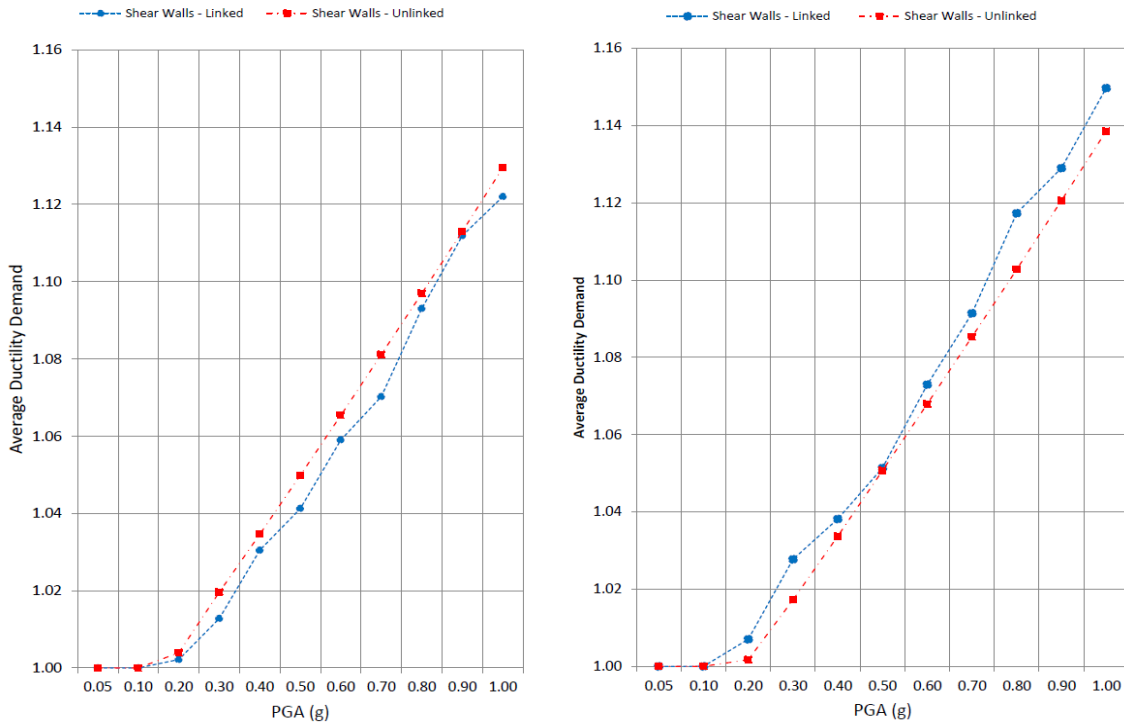
Again, on average, building “K2” is generally relieved (mean ratio  $E < 1.00$ ) in all structural members, in all storeys and independently of ground motion intensity. However, the inelastic demand discrepancy remains substantial and there are numerous structural members where the local ductility demand is either doubled or dropped by more than 50% due to bi-directional pounding with the corner building “K”. A close look at the result of building “K2” confirms once more the general trend of high structural response discrepancy.

What is therefore seen from this analysis is that, in contrast to the simpler cases studied in the literature, where buildings are aligned along a straight line and the lower buildings experience the most critical impact of seismic pounding, the dynamics of a coupled building block in full bi-directional contact is much more complex and difficult to predict. It is also seen that there is no clear trend which can be attributed to the different height of the buildings, since the torsional coupled behavior of the three interacting buildings can critically affect both the high-rise and the lower buildings simultaneously and to the same extent.

#### **4.5 Influence of strong ground motion severity**

It can be deduced from Figures 4.6 - 4.9 that, on average, pounding reduces ductility demands for all structural members and floors of the “K1” building, while it has a mixed effect for structural members of the of the “K2” building. Given that these two buildings are dominated by torsional response (see Table 4.1) and that they experience “single-sided” pounding, an additional series of non-linear time-history analysis within the same IDA context as before have been performed to investigate the effect of directionality of the considered input ground motion. Specifically, a full set of results have been obtained having the strong ground motion component along X-X direction reversed. In Figure 4.10 representative results for the “K1” building are presented indicating that the directivity of the strong ground motion affects considerably the seismic demands of single-sided pounding. In particular, reversing the direction of the X-X ground motion component imposes higher ductility demands for the “K1” building when pounding occurs. This result further reinforces the previous remark on the complexity of the effects of pounding in considering adjacent buildings interacting in 3-D within a complex building block.

## Chapter 4 - Influence of Bi-Directional Pounding on the Inelastic Demand Distribution of Three Adjacent Multi-Storey RC Buildings



X-X component of Fig. 3(b) acting along the “positive” O-X axis of Figure 4.1a

X-X component of Fig. 3(b) acting along the “negative” O-X axis of Fig. 1(a)

Figure 4.12: Average ductility demand of shear walls at the ground floor of building “K1”, with pounding (linked) and without pounding (un-linked) for different levels of seismic intensity (PGA).

### 4.6 Closure

A judiciously chosen case study has been considered to illustrate the complex non-linear response of realistic building blocks, involving code-compliant RC buildings which are a) constructed in contact to under-designed, lower-rise, existing structures in metropolitan areas, b) located at the corner of a building stock, and c) are subject to bi-directional pounding due to torsion. Pertinent numerical data have been furnished to provide an insight as to what difference in terms of inelastic seismic demands (and consequently in terms of detailing) pounding would make in the design of new code-compliant RC buildings.

## Chapter 4 - Influence of Bi-Directional Pounding on the Inelastic Demand Distribution of Three Adjacent Multi-Storey RC Buildings

---

Specifically, a detailed numerical model of the coupled 3D, interactive building block was developed and the inelastic demand distribution (expressed in terms of rotational ductility demand  $\mu_{\theta}$ ) was computed for all members of all buildings, with and without pounding and for different levels of seismic intensity. These results demonstrate a general average trend of reduced inelastic demands of vertical structural members in the lower floors of the 7-story building and relatively higher demands in the upper storeys when interaction between adjacent buildings takes place. The same is also seen on average for one of the two side buildings (“K1”) which shows a minor decrease in inelastic demand of both beams and columns. What is important to notice though, is that the discrepancy of the inelastic demand induced by seismic forces, with and without pounding, is significant: the mean plus one standard deviation of the ratio  $\mu_{\theta,linked}/\mu_{\theta,unlinked}$  is greater than 2.0 almost in all cases of buildings and members examined. This is deemed to be interesting evidence that the trends observed in the literature with respect to the pounding of buildings aligned in series are not necessarily visible in the case of complex blocks of buildings colliding bi-directionally.

Nevertheless, it is noted that, purposely, due to the complexity of the adopted structural models, the influence of record-to-record variability of the strong ground motion to seismic pounding inelastic demands has not been accounted for. This issue is addressed systematically in the following two chapters within a PBEE framework.

# Chapter 5

## Fragility Sensitivity of RC Colliding Buildings on the Modelling Parameters of the Linear and Linear Viscoelastic Contact Model

### 5.1 Overview

This chapter, presents an analytical study based on the probabilistic framework described in Chapter 3, to assess the impact of EISP on the seismic performance of adjacent non-linear SDOF systems used as proxies of yielding building structures. More specifically, the study considers two impact models, namely a) the linear and b) the linear viscoelastic (*Anagnostopoulos, 1988*), to model the associated pounding forces during collisions. Then, a sensitivity study is performed by perturbing the impact element parameters (gap and impact element stiffness) in order to assess, the sensitivity of structural seismic performance on the contact element type and the perturbed parameters.

The motivation of the herein study is presented in section 5.2, while section 5.3 presents the characteristics and the properties of the considered building stock. Section 5.4 discusses the details of the adopted parametric study for the two considered impact element types. Further, section 5.5 presents the characteristics of the accelerograms of the ground motion suite and the mathematical formulation of the adopted novel IM that is used express the seismic intensity levels. Section 5.6 presents an analytical discussion on the results of the PSDA. Finally, section 5.7 presents a summary of the conclusion derived in this chapter.

## 5.2 Related Work and Motivation

In EISP analytical case studies, the parameters of the selected contact models, adopt values that lie within “reasonable” ranges, established on the basis of numerical sensitivity studies (e.g. *Anagnostopoulos*, 1998; *Anagnostopoulos and Spiliopoulos*, 1992; *Chau and Wei*, 2001) or numerical iterations (*Jankowski*, 2005) and a limited number of experimental studies (e.g. *Papadrakakis and Mouzakis*, 1995, *Filiatrault and Wagner*, 1995; *Chau et al.*, 2003). The later, confirmed that there is a sufficient agreement between analytical studies and experimental tests.

Several past studies, investigated on the sensitivity of the seismic response on the impact element modelling parameters. In an early study (*Anagnostopoulos*, 1988) that assessed the impact of structural pounding between SDOF systems in a series configuration, pounding forces were introduced into the analysis by means of the linear viscoelastic pounding model. The SDOF systems were excited using five arbitrary selected recorded ground motions. It was reported that the displacement response was insensitive to changes in the stiffness and damping of the impact element. Therefore, he suggested that pounding between buildings can be studied without the need of an accurate knowledge of the impact element parameters. Further, based on the results of the sensitivity study, the author suggested that reasonable values for the stiffness and damping of the impact element are 20 times the stiffness of the stiffer adjacent SDOF system and a damping coefficient that is calculated based on a coefficient of restitution  $r = 0.65$  and Equations 2.8, 2.9 and 2.10 (Chapter 2, §2.3.1.3 Contact Elements).

In a similar study, *Anagnostopoulos and Spiliopoulos*, (1992) using the same collection of recorded ground motions, investigated the impact of structural pounding, modelled by the linear viscoelastic model on the seismic response of adjacent MDOF systems. It was concluded that the responses are more sensitive to the damping property of the impact element rather than its stiffness. However, the influence of the damping of the impact element on the displacement responses was negligible under the assumption of a reasonable adopted level of damping. In, (*Chau and Wei*, 2001) the authors studied a non-linear Hertzian impact model to express collisions between two SDOF systems under harmonic base excitation. The authors reported that the maximum pounding velocity was very sensitive to the adopted contact law.

More recently, a comprehensive sensitivity study on the impact of EISP between two inelastic SDOF oscillators was undertaken utilising Monte Carlo simulations and Sobol's method to derive sensitivity indexes (*Crozet et al.*, 2017). Further the adopted excitation was based on a wide band of artificially generated ground motions. It was found that the most influential parameters affecting the structural response were the frequency ratio and mass ratio between the two oscillators.

Thus far, all sensitivity studies on the influence of EISP on the impact element parameters are based on a limited number of ground motions with an unknown seismic hazard level. To this extend, the study presented in this chapter adopts a probabilistic PBSA approach to establish the influence of the gap and the impact element stiffness and the energy dissipation on the seismic performance of two non-linear SDOF systems. Further, this study presents a comparison between the derived probabilistic models (fragility curves) that describe the structural vulnerability as a function of the seismic intensity. The objective is to quantify the degree of difference in the derived probabilistic models for the two adopted impact models.

### **5.3 Adopted benchmark Structural models**

This study considers five Eurocode 8 compliant RC building frames shown in Figure 5.1. They were developed by Fardis (1994) as part of a calibration and assessment exercise of the current Eurocode 8 and extensively used in the literature as benchmark structures to study the potential of different seismic analysis tools (*e.g. Mwafy and Elnashai*, 2001; *Papanikolaou and Elnashai*, 2005; *Katsanos, et. al*, 2014) as well as the response of contemporary code-compliant buildings (*e.g. Katsanos et al.*, 2014). The RC building frames represent different real-life seismic resistance systems (frame, shear wall and frame) with high and low ductility levels (based on the Eurocode 8 classification) as well as different number of stories and overall height. They therefore observe significantly different dynamic properties (*e.g. fundamental natural periods, mode shapes, etc*).

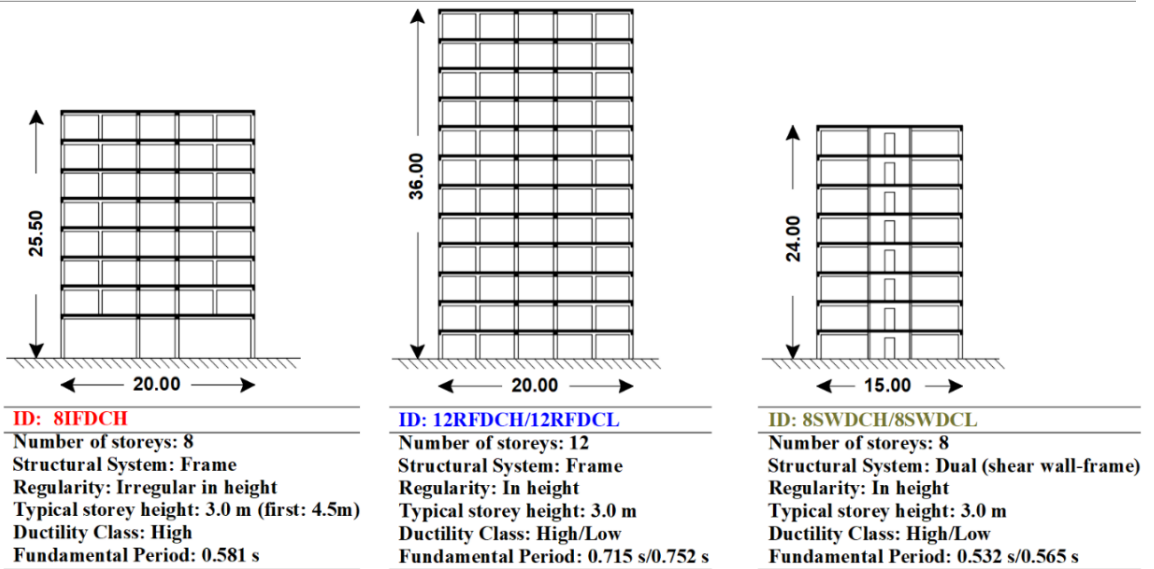


Figure 5.1: Properties and geometric characteristics of the five adopted RC buildings frames.

In (Katsanos, *et. al.*, 2014), the N2 method (Fajfar and Gasperic, 1996) relying on static inelastic (pushover) analysis has been considered to derive equivalent SDOF systems (Table 5.1) with a bilinear backbone curve (Figure 5.2). The herein study, adopts the derived equivalent non-linear SDOF systems, in order to significantly reduce the computational time that is required to perform IDA based PSDA. The properties of the equivalent nonlinear SDOF systems are shown in Table 5.1.

**Table 5.1:** Properties of the equivalent five non-linear SDOF systems (source: *Katsanos, Sextos and Elnashai, 2014*).

	<i>12RFDCH</i>	<i>12RFDCL</i>	<i>8SWDCH</i>	<i>8SWDCL</i>	<i>8IFDCH</i>
Yield Displacement ( <i>m</i> )	0.356	0.357	0.282	0.248	0.287
Ultimate Displacement ( <i>m</i> )	1.801	1.881	1.202	0.822	1.276
Yield Base Shear ( <i>kN</i> )	6505.62	5501.93	8333.64	6489.67	4578.75
Ultimate Base Shear ( <i>kN</i> )	6615.62	5612.26	8653.99	6900.92	4712.67
Elastic Stiffness ( <i>kN/m</i> )	18259.49	15422.24	29564.88	26156.20	15978.59
Post-Elastic Stiffness ( <i>kN/m</i> )	76.17	72.42	348.10	716.52	135.32
Period ( <i>sec</i> )	0.966	1.038	0.707	0.723	0.804
Mass ( <i>Kg</i> )	432.39X10 <sup>3</sup>	421.03X10 <sup>3</sup>	374.55X10 <sup>3</sup>	346.84X10 <sup>3</sup>	261.49X10 <sup>3</sup>

The equivalent five non-linear SDOF systems were modelled in OpenSEES (*McKenna et al, 2000*) using a non-linear zero-length spring that follows a bi-linear moment - rotation law and an elastic element (figure 5.2). Further, a 5% Rayleigh damping is implemented.

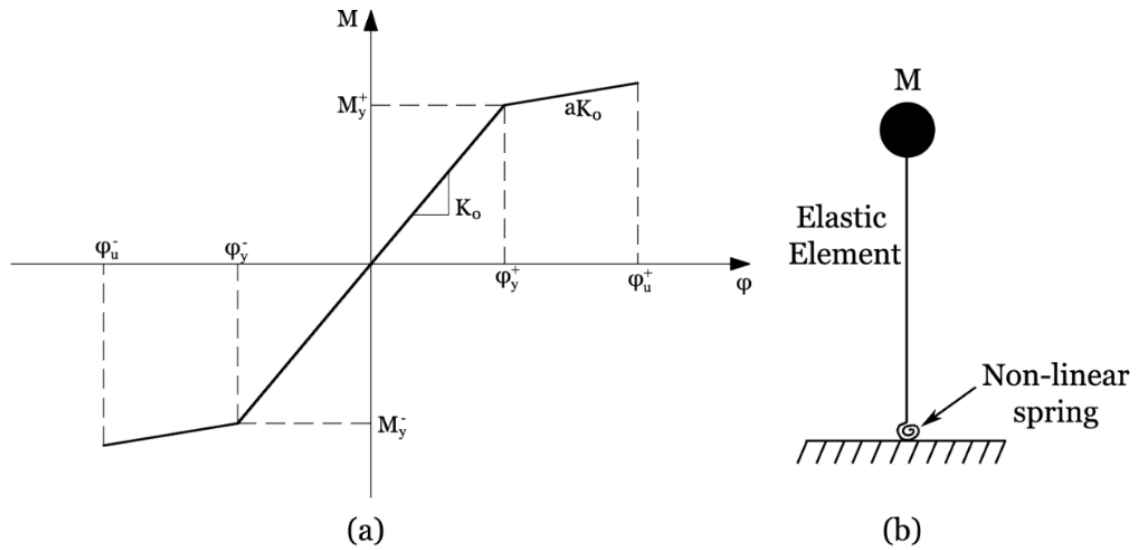


Figure 5.2: a) Moment - Rotation bilinear backbone curve and b) non-linear SDOF systems modelled in OpenSEES with an elastic element and a zero-length non-linear spring with a bi-linear Moment - Rotation law.

The (bi-linear) pushover curves of the five non-linear SDOF systems are depicted in figure 5.3.

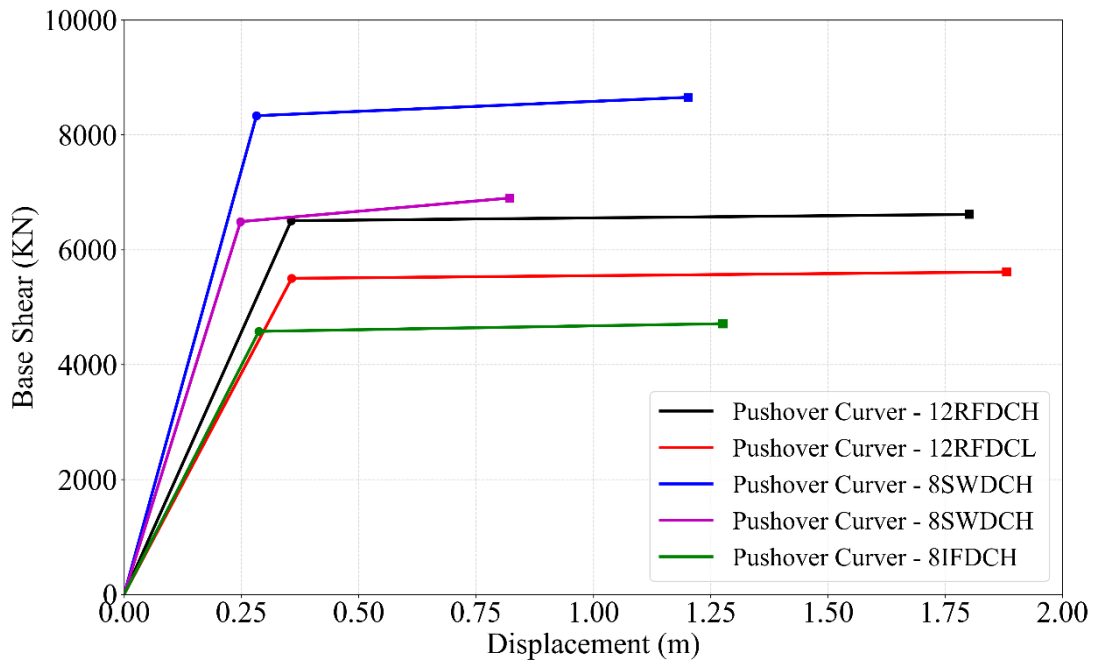


Figure 5.3: Pushover curves of the five adopted non-linear SDOF systems.

## 5.4 Cases of Pounding Model Parameters Considered

The adopted cases of pounding model parameters are based on three pairs of two nonlinear SDOF systems (see Figure 5.4). The coupling always involves a non-linear SDOF system that correspond to a 12-storey RC building frame and a non-linear SDOF system that corresponds to an 8-storey RC building frame. The selection intends to couple systems with out-of-phase oscillations in order to study EISP. The fundamental period ratios, the mass ratios and the elastic stiffness ratios for each considered pair of non-linear SDOF systems are depicted in Table 5.2.

**Table 5.2:** Period, mass and elastic stiffness ratios for the three adopted pairs of non-linear SDOF systems that are considered in this study.

Building Pair	12RFDCH and 8SWDCH	12RFDCH and 8SWDCL	12RFDCL and 8IFDCH
Period Ratio $T_{12\text{-storey}} / T_{8\text{-storey}}$	1.37	1.34	1.29
Mass Ratio $M_{12\text{-storey}} / M_{8\text{-storey}}$	1.15	1.25	1.61
Elastic Stiffness Ratio $K_{el,12\text{-storey}} / K_{el,8\text{-storey}}$	0.62	0.70	0.97

The value of the initial separation distance (gap) is let to vary for both pounding/impact models considered, i.e., linear and linear viscoelastic pounding models as shown in Figures 5.4a and 5.4b, taking on values [0%, 1%, 5%, 10%, 25%, 50%, 75% and 100%] of the Eurocode 8 compliant Separation Distance (SD) (Equation 5.1) that is defined as the SRSS of the maximum inelastic displacements of the two oscillators.

$$SD = \sqrt{D_{oscil.1,max,inelastic}^2 + D_{oscil.2,max,inelastic}^2} \quad (5.1)$$

Further, the impact element stiffness  $K_p$  is let to take two different values for both pounding models considered, treated as the two extremes in order to investigate the influence of  $K_p$  to the seismic response of the structures and to their fragilities. Following recommendations in Anagnostopoulos (1988), the highest value of the impact element stiffness,  $K_p^H$ , is set equal to 20 times the pre-yielding stiffness of the stiffer SDOF system, while the lowest value is given as  $K_p^L = K_p^H / 10$ .

The damping coefficient  $C$ , of the linear viscoelastic impact model as well as the stiffness of the secondary spring  $K'_p$  (see figure 5.4b) are kept constant. The damping coefficient  $C$  is set constant since this study focuses on the influence of the presence or not, of energy dissipation in RHA and its exact value is not deemed important (Anagnostopoulos, 1988). The value of  $K'_p$  is set as  $K'_p = K_p \times 10^3$  and it is derived via sensitivity analysis that showed no impact on the RHA results for a  $K'_p$  up to this value.

The adopted value of the damping coefficient  $C$  is derived based on a coefficient of restitution of  $r = 0.5$  and equations 2.8, 2.9 and 2.10. The value of the coefficient of restitution that is typically adopted in the literature, ranges between 0.5 (e.g. Anagnostopoulos and Spiliopoulos, 1992) and 0.65 (e.g. Anagnostopoulos, 1988).

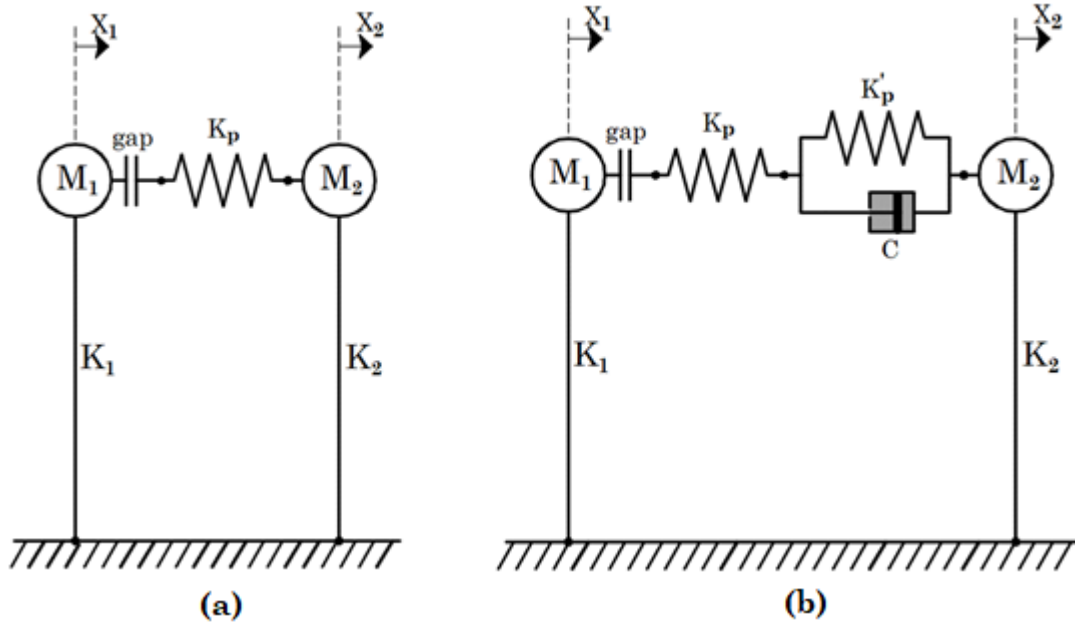


Figure 5.4: Modelling pounding forces by means of the a) linear contact model and b) linear viscoelastic pounding model, for pounding between two bodies with masses  $M_1$  and  $M_2$  and corresponding stiffnesses  $K_1$  and  $K_2$ .

The parameter combinations (gap and  $K_p$ ) for the case of modelling pounding forces via the linear pounding model are shown in Table 5.3.

**Table 5.3:** List of the considered cases with the adopted values of the parameters of the linear contact model for each building pair.

Adopted gap range	12RFDCH and 8SWDCH	12RFDCH and 8SWDCL	12RFDCL and 8IFDCH
Gap = [0%, 1%, 5%, 10%, 25%, 50, 100% of SD]	$K_p^H = 591297.6 \text{ kN}$	$K_p^H = 523124.1 \text{ kN}$	$K_p^H = 319573.8 \text{ kN}$
	$K_p^L = 59129.76 \text{ kN}$	$K_p^L = 52312.41 \text{ kN}$	$K_p^L = 31957.38 \text{ kN}$

The parameter combinations (gap and  $K_p$ ) for the case of modelling pounding forces via the linear visco-elastic pounding model are shown in Table 5.4.

**Table 5.4:** List of the considered cases with the adopted values of the parameters of the linear contact model for each building pair.

Adopted gap range	12RFDCH and 8SWDCH	12RFDCH and 8SWDCL	12RFDCL and 8IFDCH
Gap = [0%, 1%, 5%, 10%, 25%, 50, 100% of SD]	$K_p^H = 591297.6 \text{ kN}$ $C = 4357477 \text{ Ns/m}$ $K_p' = 591297.6 \times 10^3 \text{ kN}$	$K_p^H = 523124.1 \text{ kN}$ $C = 4013580 \text{ Ns/m}$ $K_p' = 523124.1 \times 10^3 \text{ kN}$	$K_p^H = 319573.8 \text{ kN}$ $C = 2871917 \text{ Ns/m}$ $K_p' = 319573.8 \times 10^3 \text{ kN}$
	$K_p^L = 59129.76 \text{ kN}$ $C = 4357477 \text{ Ns/m}$ $K_p' = 591297.6 \times 10^3 \text{ kN}$	$K_p^L = 52312.41 \text{ kN}$ $C = 4013580 \text{ Ns/m}$ $K_p' = 523124.1 \times 10^3 \text{ kN}$	$K_p^L = 31957.38 \text{ kN}$ $C = 2871917 \text{ Ns/m}$ $K_p' = 319573.8 \times 10^3 \text{ kN}$

For each combination in Table 5.3 and Table 5.4, a PSDA based on IDA and a suite of 72 accelerograms is performed, summing a total of 77760 non-linear RHAs. As discussed in Chapter 3 (§3.2 Incremental Dynamic Analysis), the adjacent non-linear SDOF systems, are driven along their full response range (from elastic, to inelastic up until their ultimate displacement (see Table 5.1)). The adopted scaling scheme is based on the track and fill algorithm described in (Vamvatsikos and Cornell, 2004). The algorithm increases geometrically the intensity scaling factor to rapidly detect the collapse intensity range (tracking phase). Then through iteration, the collapse seismic intensity is bracketed with higher accuracy (bracketing phase). Finally, the algorithm “fills” the response curve through multiple RHA at lower seismic intensity levels. Herein, the algorithm terminates under the condition that one of the two oscillators has reached its ultimate displacement limit. In that case, both oscillators are assumed to have failed.

Further, as discussed in Chapter 3 the third stage of the PBEE framework (stage three damage analysis) requires suitably selected performance metrics

(limit states) that correlate well with damage. In this study, the full response range in terms of static pushover curves for each non-linear SDOF system is known. To this extend, this study adopts two limit states that relate to light and severe damage levels. The light damage limit state is defined as the 120% of the yield displacement. The severe damage limit state is defined as the 80% (near collapse) of the ultimate displacement. Both the limit states lie within the non-linear response range of the non-linear SDOF systems.

**Table 5.5:** Adopted displacement limit states for each considered pair of SDOF systems corresponding to light and severe damage.

	Displacement Limit State corresponding to light damage (m)		Displacement Limit State corresponding to severe damage (m)	
12RFDCH & 8SWDCH	12RFDCH	8SWDCH	12RFDCH	8SWDCH
	0.427	0.338	1.441	0.962
12RFDCH & 8SWDCL	12RFDCH	8WDCL	12RFDCH	8WDCL
	0.427	0.298	1.441	0.658
12RFDCL & 8IFDCH	12RFDCL	8IFDCH	12RFDCL	8IFDCH
	0.428	0.344	1.505	1.021

## 5.5 Selected IM and Ground Motion Suite

### 5.5.1 Record selection and scaling

Typically, structural design scenarios involve a collection of ground motions scaled to a site-specific seismic hazard scenario or the structures are excited under a limited number of ground motions (e.g. EC8 guidelines requires seven accelerograms) (*Katsanos et. al., 2014*). However, given that this study essentially corresponds to a sensitivity analysis on the initial separation distance and the stiffness of the impact model, the selected accelerograms are selected in order to represent a collection with a broad range of seismological criteria such as the magnitude, rapture mechanism, amplitude and the frequency content. (see Figure 5.5). The adopted accelerograms are listed in table B.1 of Appendix B. Figure 5.5 depicts the magnitude versus the distance

of the considered accelerograms in the ground motion suite. It can be seen that the points on the  $M_w$ , R plane are sufficiently spread.

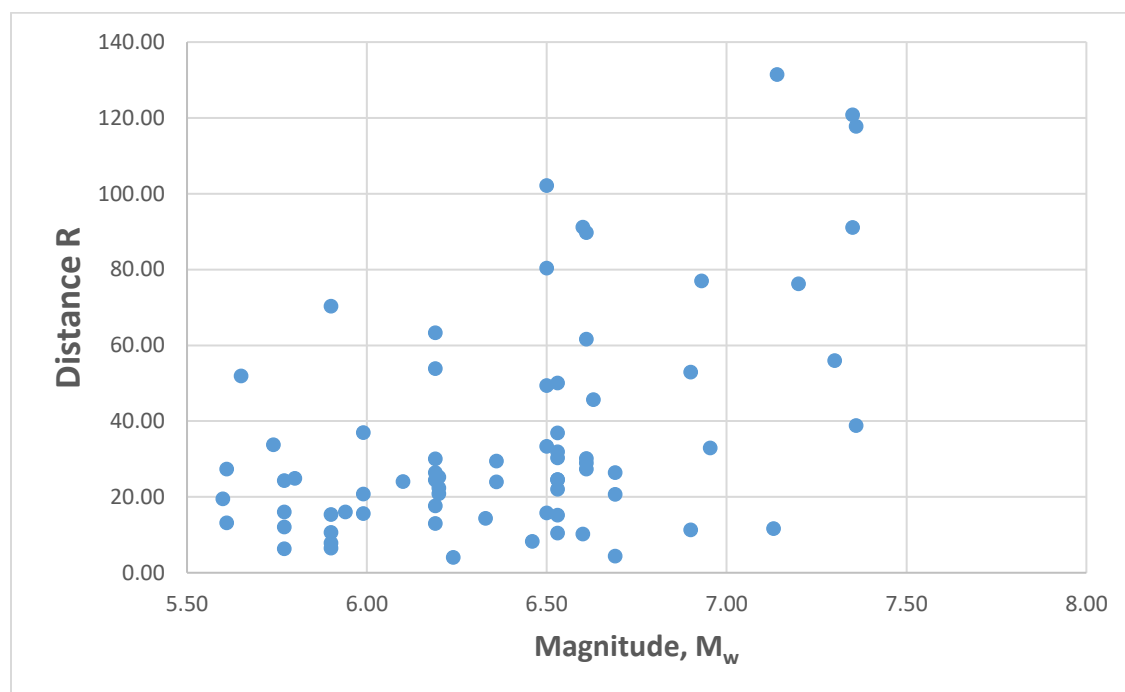


Figure 5.5: Plots of the a) Magnitude  $M_w$  vs the Distance R for the all the accelerograms in the adopted ground motion suite.

### 5.5.2 A proposed IM for EISP case studies

In EISP studies, the seismic intensity is typically expressed in terms of the PGA (e.g. Polycarpou and Komodromos, 2010; Efraimiadou et al., 2013). This is because the most commonly used structure-specific IM which is well known to be more efficient than PGA, namely the  $Sa(T_1)$  is not well-defined for a system of two or more structures with different  $Sa(T_1)$ s that interact. In this regard, the geometric mean ( $AvgSa$ ) is herein proposed to be used as structure-specific IM for K interacting structures.

It is noted that the latter IM has been shown to be more efficient than the  $Sa(T_1)$  for seismic performance assessment of single (non-pounding) structures especially in near collapse limit states (see e.g. Vamvatsikos and Cornell, 2005 and Kohrangi et al., 2017 and references therein) as it accounts for higher modes of vibration as well as apparent period elongation phenomena of MDOF yielding structures (see e.g. Katsanos et al. 2014; Kohrangi et al., 2016).

Thus, this study adopts the geometric mean which in the case of two interacting structures is expressed as:

$$AvgSa = \sqrt{Sa_{1,T_1,5\%} \times Sa_{2,T_2,5\%}} \quad (5.2)$$

Expressing the seismic intensity levels in terms of the *AvgSa* during post-processing, adds additional information regarding the fundamental frequencies of the interacting structures. Mathematically, the *AvgSa* represents the central tendency of the linear pseudo-spectral acceleration values of the coupled system. Therefore, it can potentially account for shifts in the fundamental frequencies of the interacting structures that occur within their inelastic response range.

In the case of the independent vibration of the adjacent structures that typically serves as a performance benchmark for the coupled case, the *AvgSa* can be practically introduced during the statistical characterization of the structural responses by assuming the uncoupled structures as a coupled system that exhibits an initial separation distance that tends to infinity.

## 5.6 Numerical Results and Discussion

This section, presents the results of the IDA based PSDA and discusses on the derived fragility curves for all three considered pairs of non-linear SDOF systems.

### 5.6.1 Uncoupled Response

Figures 5.6 to 5.7 depict the IDA curves and the distributions of the seismic intensity levels at which the exceedance of the two adopted limit states occurs, for the case of the uncoupled response of the 12RFDCH and 8SWDCH SDOF systems. The presented figures are indicative of the general trends observed. The complete set of figures that consider all three pairs of inelastic SDOF systems is included in Appendix C.

## Chapter 5 - Fragility Sensitivity of RC Colliding Buildings on the Modelling Parameters of the Linear and Linear Viscoelastic Contact Model

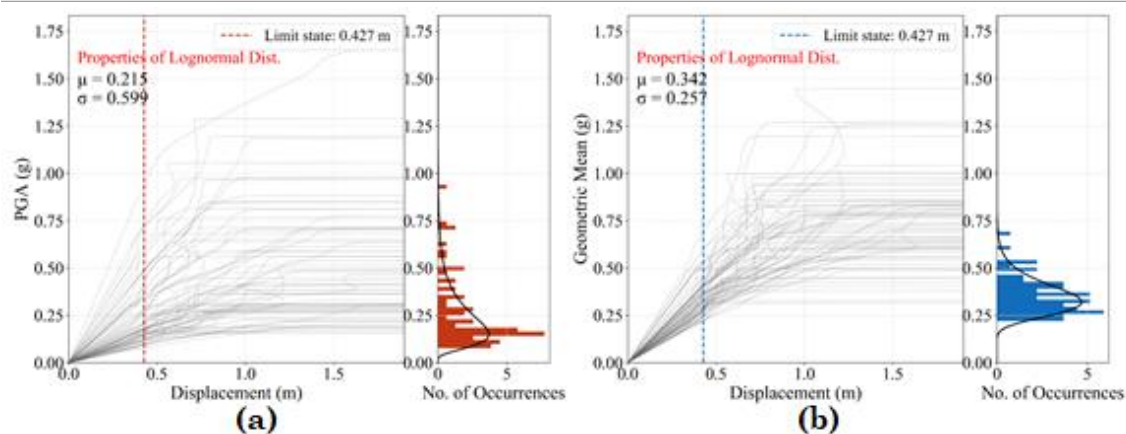


Figure 5.6: IDA curves and distributions of the seismic intensity levels at which the exceedance of the 0.427 (m) displacement limit state (light damage) occurs - Uncoupled response of the 12RFDCH SDOF system -  $\mu$  and  $\sigma$  are the mean and the standard deviation of the lognormal distribution that corresponds to the best fit a) IM = PGA and b) IM = GM.

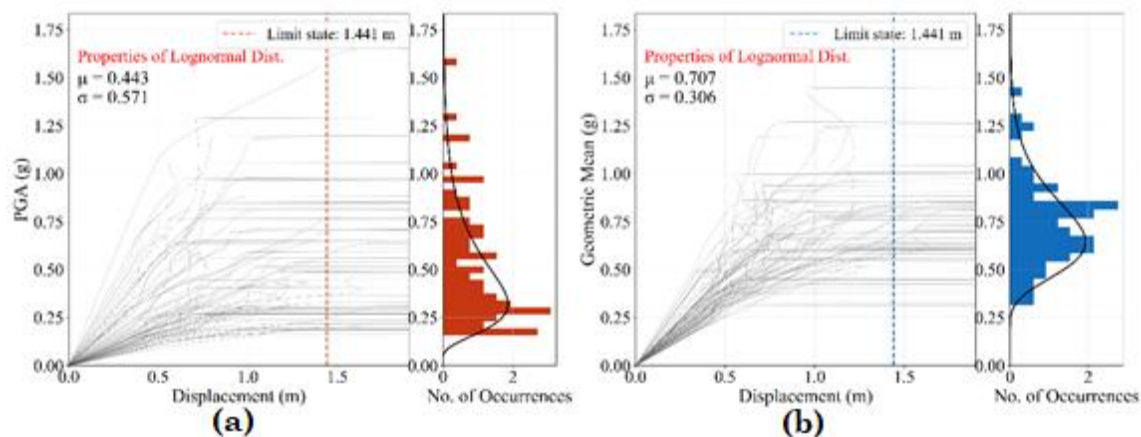


Figure 5.7: IDA curves and distributions of the seismic intensity levels at which the exceedance of the 1.441 (m) displacement limit state (severe damage) occurs - Uncoupled response of the 12RFDCH SDOF system -  $\mu$  and  $\sigma$  are the mean and the standard deviation of the lognormal distribution that correspond the best fit a) IM = PGA and b) IM = GM.

Figure 5.8, shows the fragility curves for the uncoupled response of all non-linear SDOF oscillators for the two considered limit states. It is noted that for all fragility models that are presented in this study, the seismic intensity is expressed in terms of the *AvgSa* since it is found to reduce the spread of the IDA curves for all the cases considered in this study (see Figures in Appendix C). Further, the parameters ( $\mu$  and  $\sigma$ ) of the lognormal fit that are reported presented in the figures is derived via the Matlab software package.

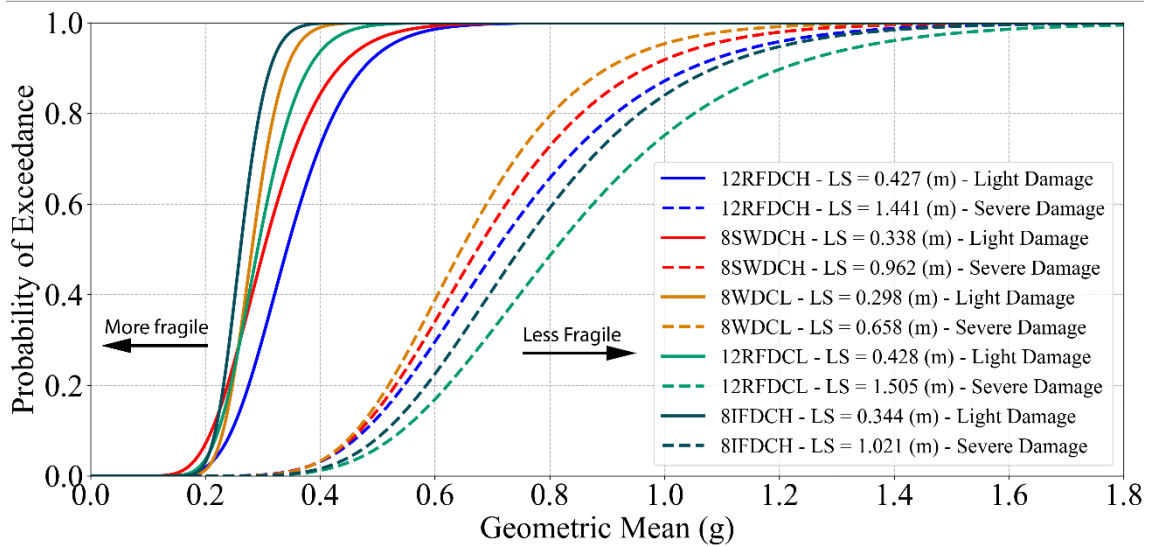


Figure 5.8: Fragility curves for the uncoupled response of the five non-linear SDOF systems for the two limit states that correspond to light and severe damage.

The 12RFDCH SDOF system (classified as high ductility) presents lower fragility levels than the 12RFDCL (classified as low ductility) for the light damage limit state (0.427 m and 0.428 m correspondingly). The opposite is observed for the severe damage limit state due to the differences in the value of the limit state for the two oscillators (1.441 m and 1.505 m).

Fragility curves that are associated with the 8-storey equivalent SDOF systems present a mixed picture, due to significant differences in their limit state values. However, it can be easily observed that the 8WDCL system corresponds to the most fragile SDOF system. Although the fragility curve of the 8IFDCH SDOF systems for the light damage limit state is located to the right of the fragility curve of the 8SWDCH SDOF system, the limit state value (for light damage) of the 8WDCL SDOF system is significantly higher than the corresponding limit state of the 8IFDCH (0.658 m vs 0.344m).

### 5.6.2 Coupled Response Time Histories

### 5.6.3 IDA Curves of Interacting Oscillators with Zero Gap

Figures 5.9 and 5.10 depict the IDA curves and the distributions of the seismic intensity levels at which the exceedance of the two adopted limit states, indicative only for the 8SWDCH inelastic oscillator for the case of pounding between 12RFDCH and 8SWDCH with zero initial separation and maximum

value of the linear impact element stiffness. The full set of plots for the coupled response for all the considered case studies is shown in Appendix C.

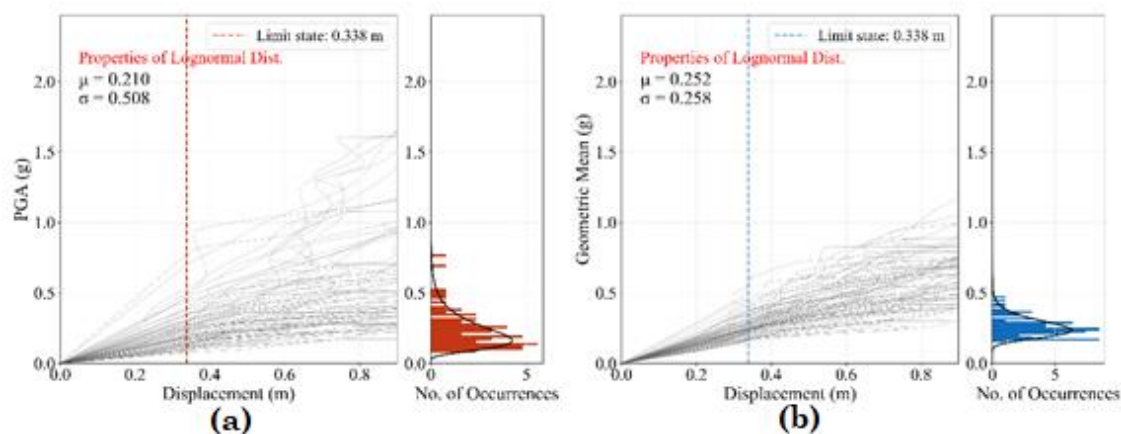


Figure 5.9: Pounding between 12RFDCH and 8SWDCH SDOF systems - Distribution of the seismic intensity levels at which the exceedance of the 0.338 (m) displacement limit state occurs - Coupled response of the 8SWDCH building with gap = 0.00 (m) - Contact forces are modelled via the linear contact model with  $K_p = \text{High}$  -  $\mu$  and  $\sigma$  are the mean and the standard deviation of the lognormal distribution that corresponds to the best fit a) IM = PGA and b) IM = GM.

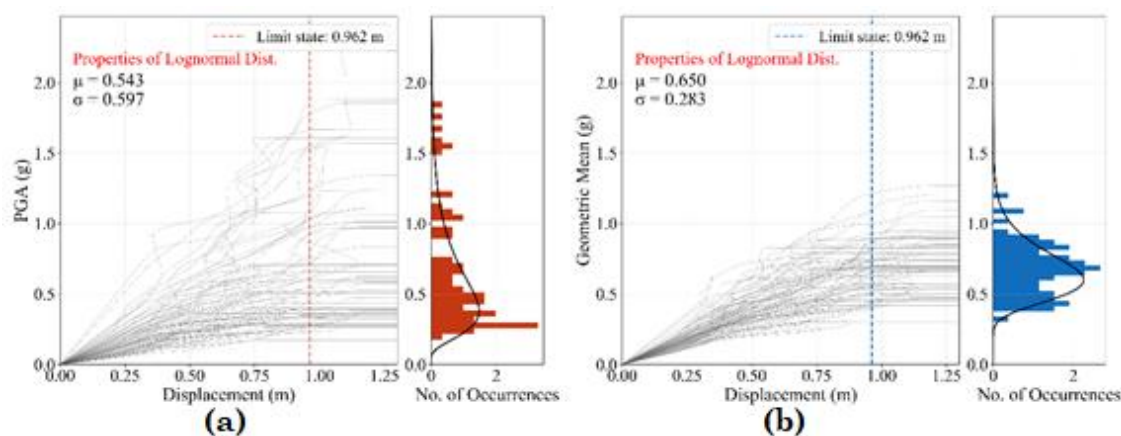


Figure 5.10: Pounding between 12RFDCH and 8SWDCH SDOF systems - Distribution of the seismic intensity levels at which the exceedance of the 0.962 (m) displacement limit state occurs - Coupled response of the 8SWDCH building with gap = 0.00 (m) - Contact forces are modelled via the linear contact model with  $K_p = \text{High}$  -  $\mu$  and  $\sigma$  are the mean and the standard deviation of the lognormal distribution that corresponds to the best fit a) IM = PGA and b) IM = GM.

It can be readily observed that the expressing the seismic intensity in terms of  $AvgSa$  results in a significant reduction on the spread of the IDA curves.

### 5.6.4 Impact of Gap on Fragility Curves of Interacting Oscillators

Figure 5.11 and 5.12 depict indicative the fragility curves for pounding between 12RFDCH and 8SWDCH inelastic SDOF systems for various gap sizes.

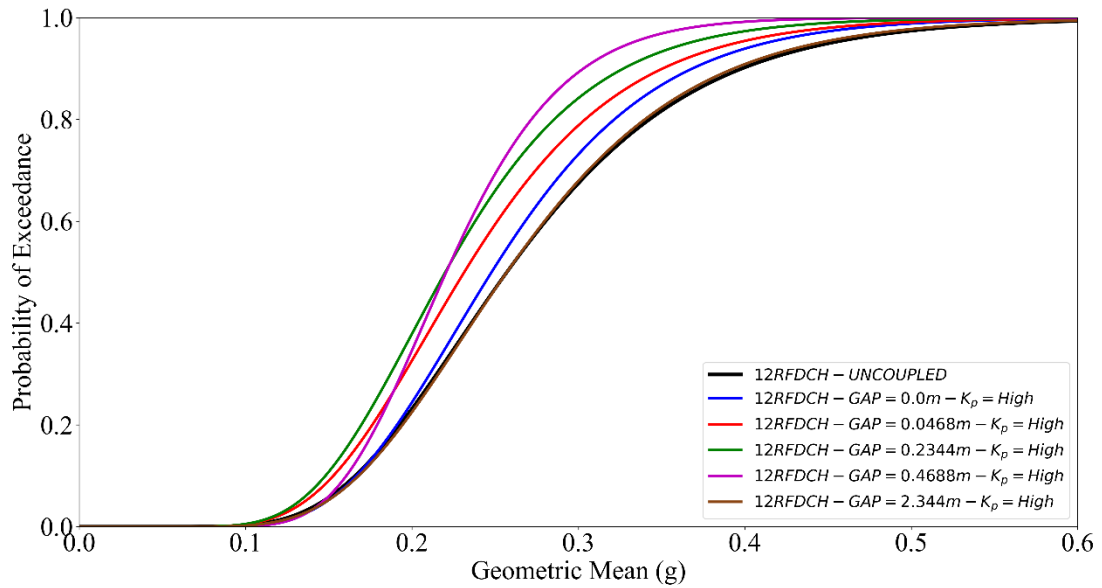


Figure 5.11: Fragility curves of the 12RFDCH inelastic oscillator for various gap sizes and light damage LS - Pounding between 12RFDCH and 8SWDCH - Pounding forces modelled in terms of the linear pounding model.

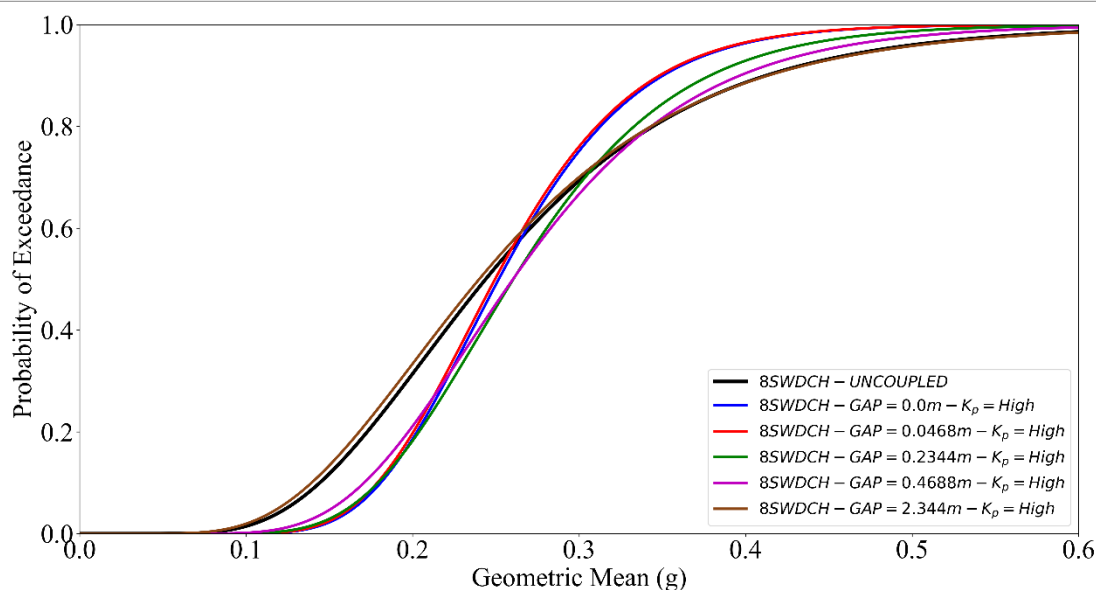


Figure 5.12: Fragility curves of the 8SWDCH inelastic oscillator for various gap sizes and light damage LS - Pounding between 12RFDCH and 8SWDCH - Pounding forces modelled in terms of the linear pounding model.

It can be observed, that as the gap size increases from zero up to 0.46 m (10% of SD), the fragility of the 12RFDCH oscillator increases as well (see Figure 5.11). The opposite is observed for the stiffer 8SWDCH oscillator (see Figure 5.12) where the fragility of the oscillator decreases as the size of the gap increases for up to a value of 0.46 m (10% of SD). In fact, for gap sizes larger than 25% of the SD, fragility curves of both oscillators gradually convergence to the benchmark fragility curve (that corresponds to the uncoupled response).

Thus, pounding has an increasingly detrimental impact on the more flexible 12RFDCH oscillator and an increasingly beneficial impact on the stiffer 8SWDCH for gap sizes up to 25% of SD. Therefore, the case of initial contact between the two oscillators does not represent the worst-case scenario. This is due to the larger magnitude of the pounding forces (see figures 5.13 and 5.14) for as the gap increases for up to 25% of SD despite the fact that the two oscillators tend to collide fewer times (see Figures 5.15 and 5.16).

Chapter 5 - Fragility Sensitivity of RC Colliding Buildings on the Modelling Parameters of the Linear and Linear Viscoelastic Contact Model

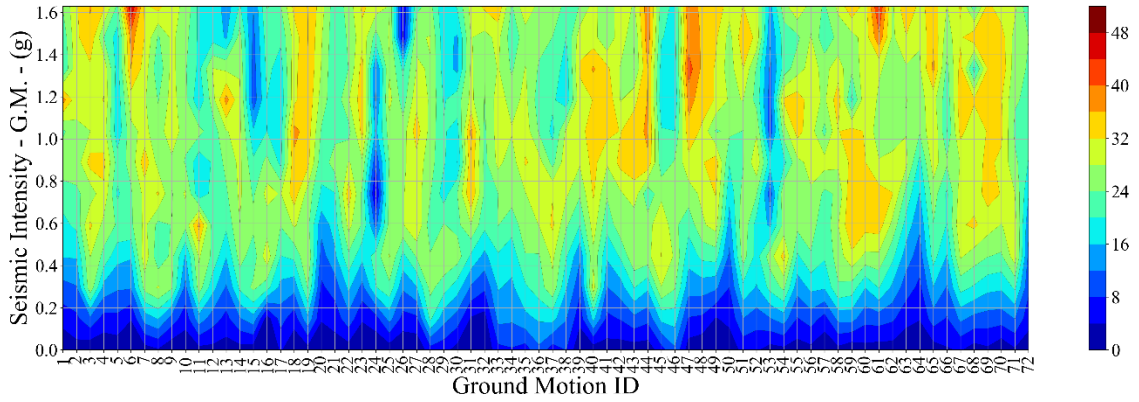


Figure 5.13: Contour plot of the magnitude of pounding forces (units MN) per ground motion and seismic intensity. Pounding between 12RFDCH and 8SWDCH SDOF oscillators with gap = 0% of SD.

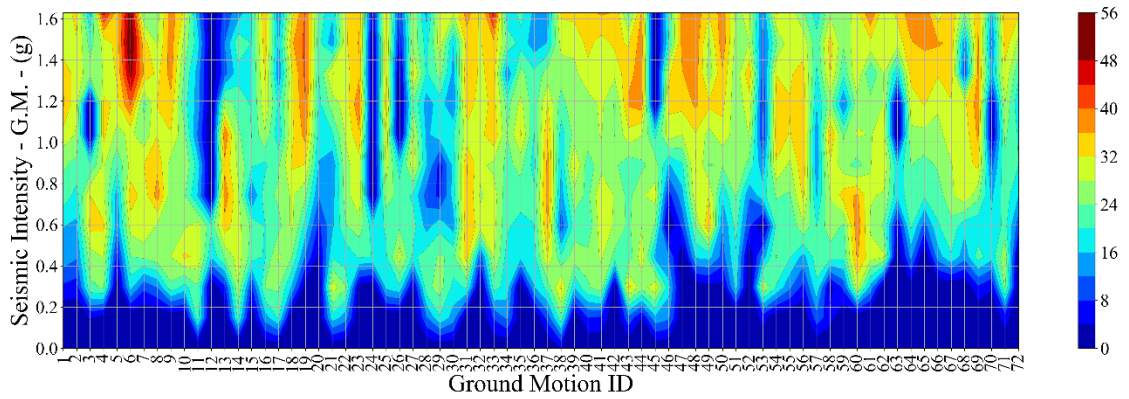


Figure 5.14: Contour plot of the magnitude of pounding forces (units MN) per ground motion and seismic intensity. Pounding between 12RFDCH and 8SWDCH SDOF systems with gap = 10% of SD.

## Chapter 5 - Fragility Sensitivity of RC Colliding Buildings on the Modelling Parameters of the Linear and Linear Viscoelastic Contact Model

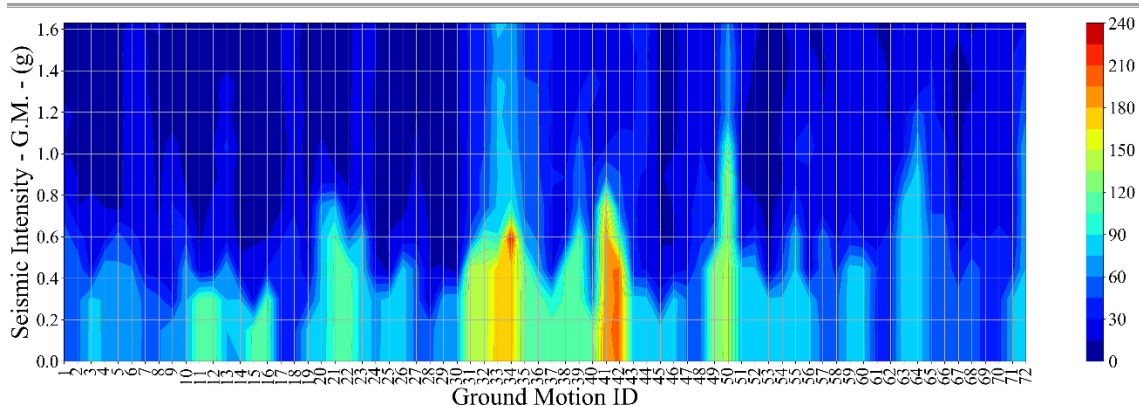


Figure 5.15: Contour plot of the number of pounding events per ground motion and seismic intensity. Pounding between 12RFDCH and 8SWDCH SDOF systems with gap = 0% of SD.

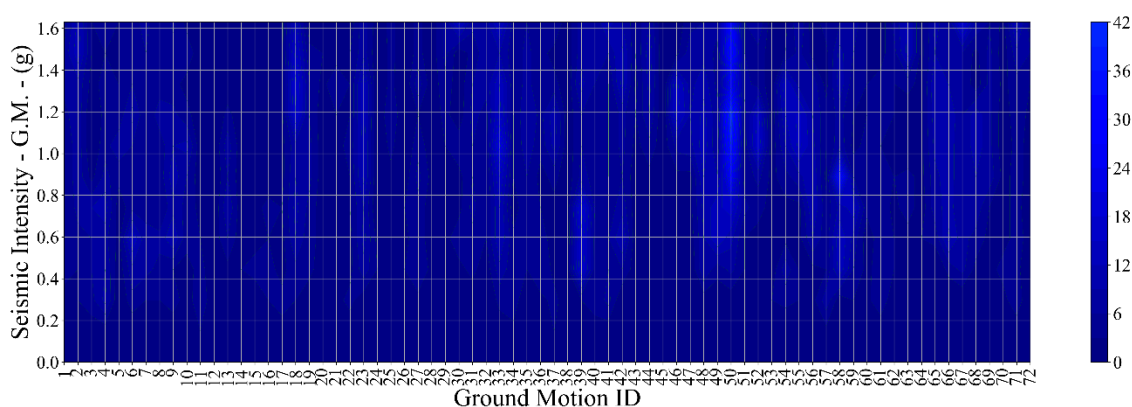


Figure 5.16: Contour plot of the number of pounding events per ground motion and seismic intensity. Pounding between 12RFDCH and 8SWDCH SDOF systems with gap = 10% of SD.

Figures 5.17 and 5.18 depict indicative the Fragility Curves for the severe damage limit state for the 12RFDCH and 8SWDCH oscillators. It is shown that at higher intensity levels, fragility curves follow the same trends.

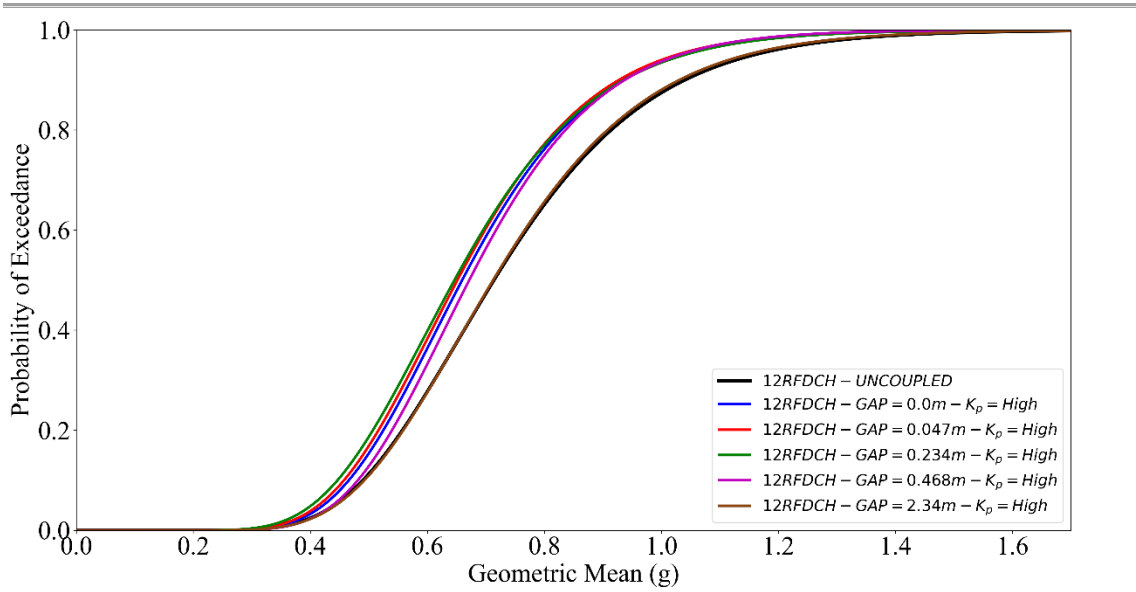


Figure 5.17: Fragility curves of the 12RFDCH inelastic oscillator for various gap sizes and severe damage LS - Pounding between 12RFDCH and 8SWDCH - Pounding forces modelled in terms of the linear pounding model.

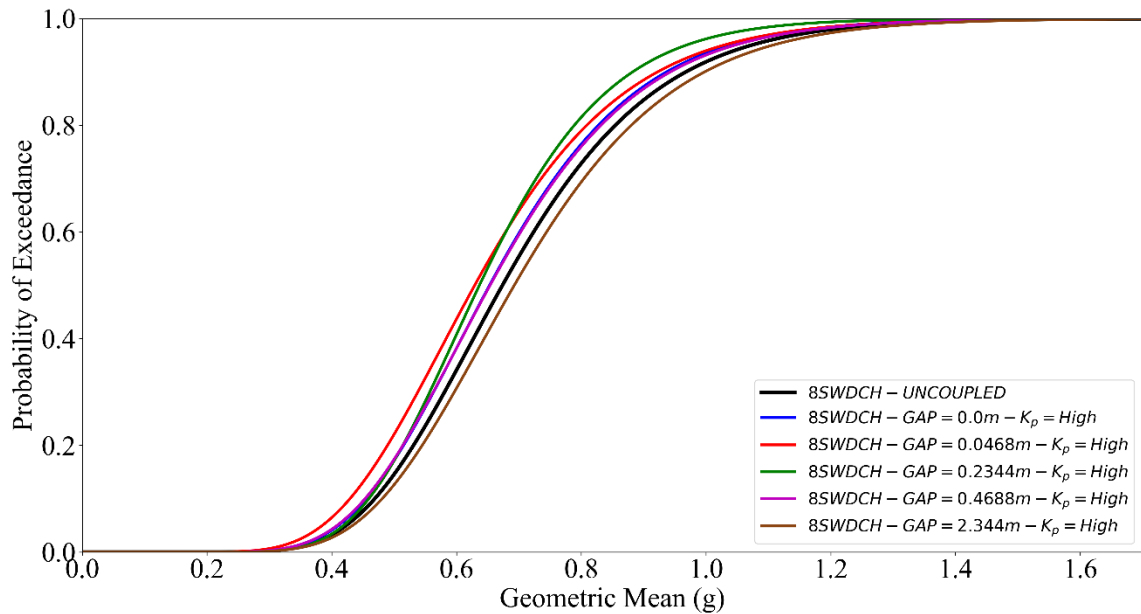


Figure 5.18: Fragility curves of the 8SWDCH inelastic oscillator for various gap sizes and severe damage LS - Pounding between 12RFDCH and 8SWDCH - Pounding forces modelled in terms of the linear pounding model.

### 5.6.5 Impact of $K_p$ on Fragility Curves

Figures 5.19 and 5.20, show the fragility curves for the 12RFDCL and 8IFDCH inelastic oscillators for the case of the third pair of SDOF systems with pounding forces modelled by means of the linear pounding model and considering the light damage LS. In addition, Figures 5.21 and 5.22, show the fragility curves for the same case studies but considering the severe damage LS. The value of  $K_p$  takes both maximum and minimum values for the various gap sizes in order to assess the influence of the  $K_p$  parameter.

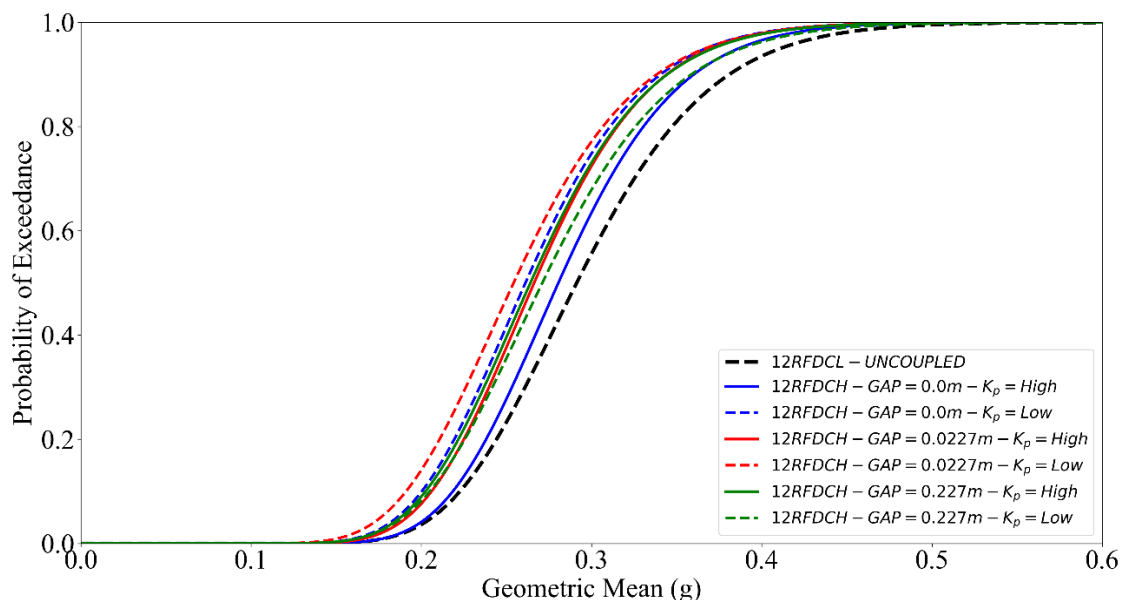


Figure 5.19: Fragility curves of the 12RFDCL inelastic oscillator for various gap sizes and light damage LS - Pounding between 12RFDCL and 8IFDCH - Pounding forces modelled in terms of the linear pounding model.

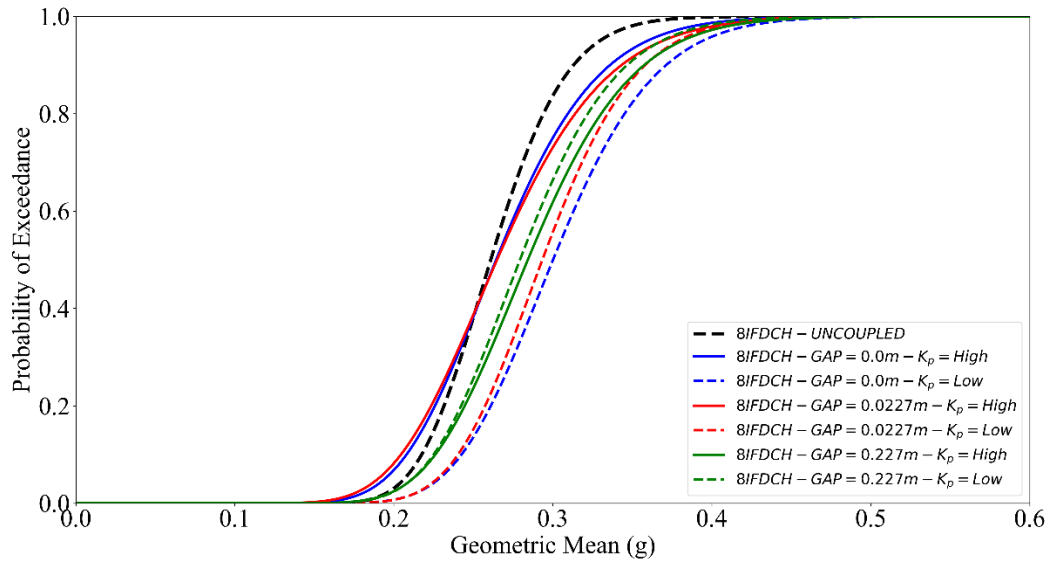


Figure 5.20: Fragility curves of the 8IFDCH inelastic oscillator for various gap sizes and light damage LS - Pounding between 12RFDCL and 8IFDCH - Pounding forces modelled in terms of the linear pounding model.

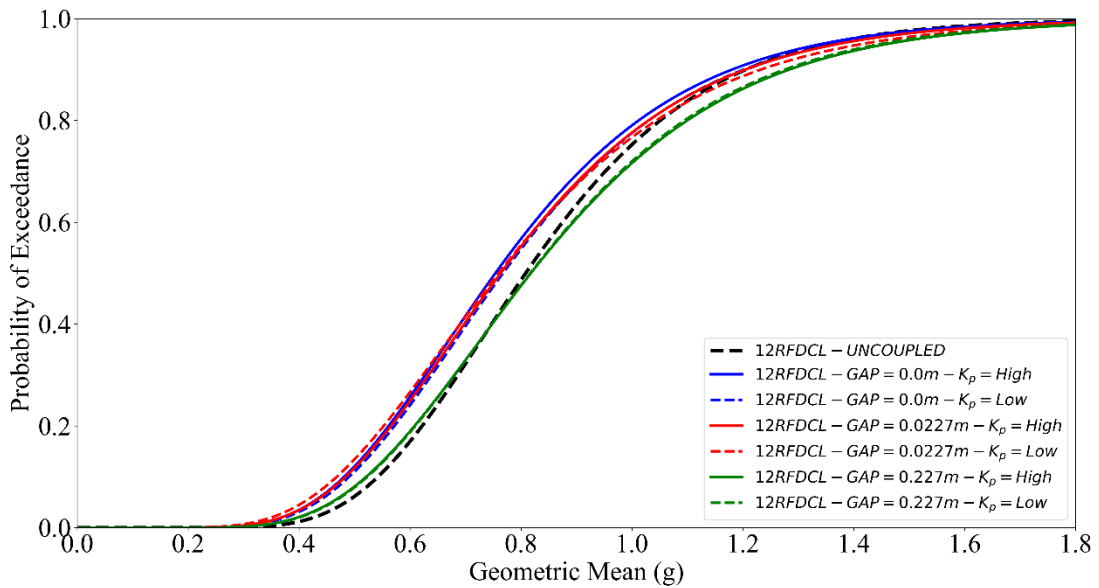


Figure 5.21: Fragility curves of the 12RFDCL inelastic oscillator for various gap sizes and severe damage LS - Pounding between 12RFDCL and 8IFDCH - Pounding forces modelled in terms of the linear pounding model.

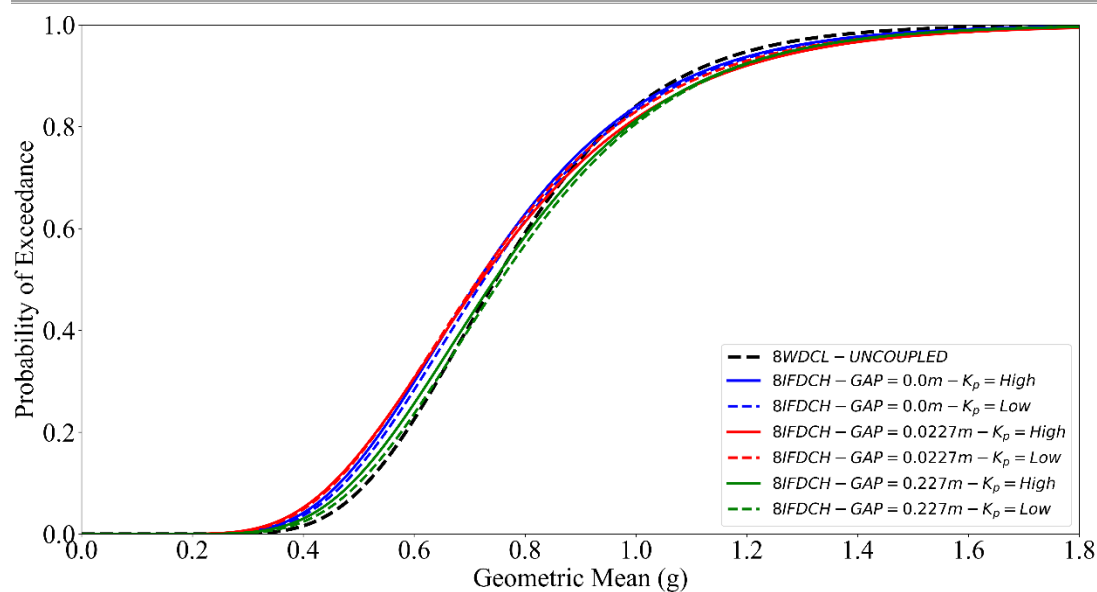


Figure 5.22: Fragility curves of the 8IFDCH inelastic oscillator for various gap sizes and light damage LS - Pounding between 12RFDCL and 8IFDCH - Pounding forces modelled in terms of the linear pounding model.

It is observed that for the light damage limit state the  $K_p$  parameter has a greater impact on the fragility of both oscillators (see Figures 5.19 and 5.20). In contrast, the impact of the  $K_p$  parameter on the fragility curves that correspond to the severe damage LS is less significant (see figures 5.21 and 5.22). The insignificance of  $K_p$  at higher intensity levels seems initially counter-intuitive. However, as it is shown in Figure 5.23 and 5.24, the interaction/pounding between the two oscillators is much more frequent at lower intensity levels.

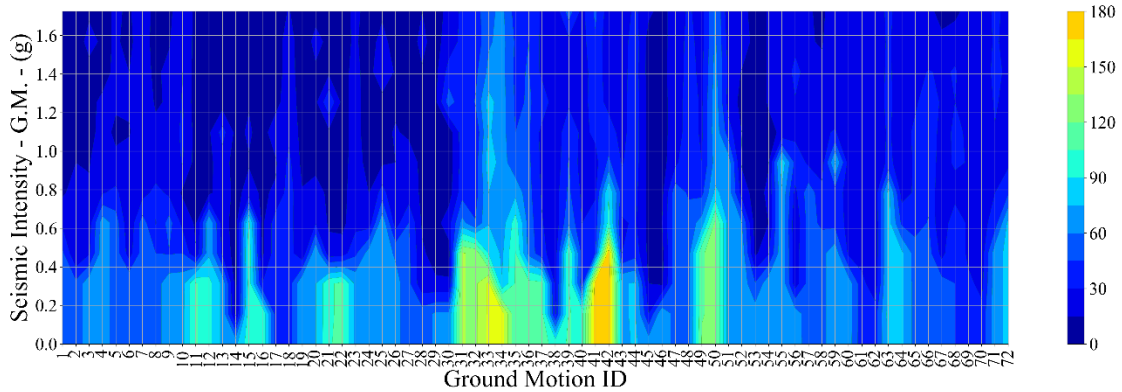


Figure 5.23: Contour plot of the number of pounding events per ground motion and seismic intensity. Pounding between 12RFDCL and 8IFDCH SDOF systems with gap = 0% of SD.

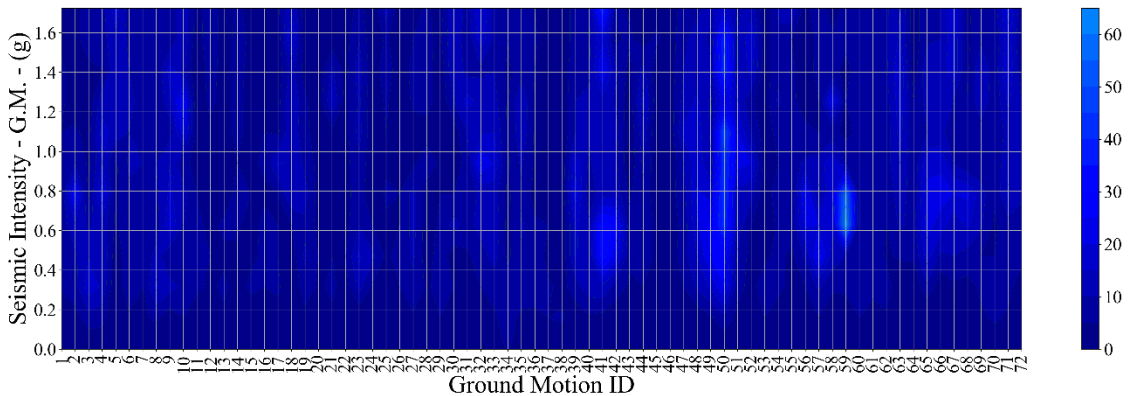


Figure 5.24: Contour plot of the number of pounding events per ground motion and seismic intensity. Pounding between 12RFDCL and 8IFDCH SDOF systems with gap = 5% of SD.

This observed phenomenon of the more frequent interactions at lower seismic intensity levels, is attributed to the fact that interactions at high seismic intensity levels between the non-linear SDOF systems, lead to the shift of the equilibrium of one or both oscillators. Therefore, the oscillations after that shift occur about the new equilibrium. This is illustrated in Figure 5.25 that shows the displacement response histories of the 12RFDCL and 8IFDCH non-linear SDOF oscillator subjected to pounding for a low and a high seismic intensity level. It is clear (figure 5.25b) that both oscillators after about 7 seconds of interaction oscillate about new equilibriums and the interaction is lost.

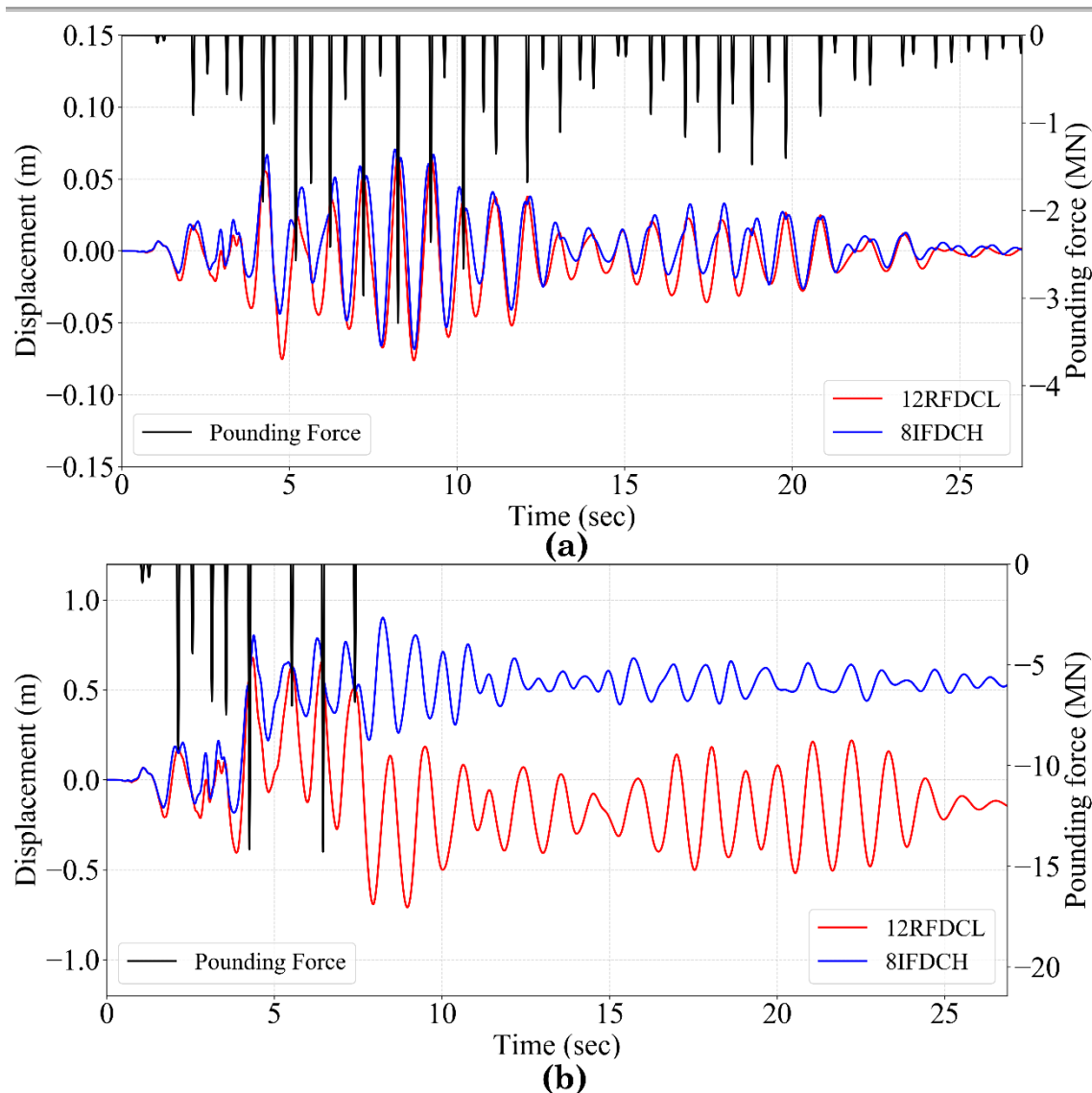


Figure 5.25: Pounding between 12RFDCL and 8IFDCH. Displacement response histories for both oscillators with zero initial separation distance and  $K_p$ =high. a) seismic intensity at 0.12 g (GM) and b) seismic intensity at 0.87 g (GM).

After a visual inspection of the above fragility curves, the following conclusions can be drawn:

**a) Light damage limit state**

- For initial separation distances below 25% of the code defined separation distance, the impact element stiffness significantly affects the SDOF fragilities of both oscillators. That can be attributed to the

increase of the number of collisions due to a smaller initial stand-off distance.

- In contrast, initial separation distances above 25% of the code defined separation distance, results in fragility curves that lie within the proximity of the fragility curve that corresponds to the uncoupled response.
- The fragility of the stiffer oscillator is reduced. In contrast, the fragility of the more flexible oscillator is increased.
- The value of the  $K_p$  parameter of the herein considered pounding models has a significant impact on the fragility curves for low to moderate seismic intensity levels.
- Energy dissipation during impact does not significantly affect the shape of the fragility curves.
- All fragility curves, show a strong tendency to converge to the benchmark fragility curve that corresponds to the uncoupled response as the initial separation distance is increased.

**b) Severe damage limit state**

- Fragility curves for the various initial separation distances lie on both sides of the benchmark fragility curve (uncoupled response). However, the location of the fragility curve at an initial separation distance lies at the opposite side of the corresponding fragility curve of the other oscillator. Therefore, if pounding has a beneficial impact on one oscillator, then it has a detrimental impact on the other one.
- The impact element stiffness ( $K_p = high$  and  $K_p = low$ ) parameter has an impact on the shape of the fragility curves. This is due to the higher magnitude of the pounding forces due to the increased seismic intensity levels.
- The type of the impact element has a visible impact on the shape of the fragility curves for the severe damage limit state. However, the impact will be quantified in detail in the next section.
- Fragility curves show a weaker tendency to convert to the benchmark fragility curve that corresponds to the uncoupled response.

### 5.6.6 Influence of Energy Dissipation During Collisions

In this section, the impact of the dissipation of energy during collisions on the seismic fragility of the non-linear SDOF systems, is quantified by means of percentage differences between the parameters of the derived seismic fragility

models. The percentage differences between the mean and the standard deviation reported hereafter are defined as:

$$\text{Mean Difference} = \frac{\text{mean}_{frag. linear} - \text{mean}_{frag, viscoelastic}}{\text{mean}_{frag. linear}} \times 100 \quad (5.3)$$

$$\text{Std Difference} = \frac{\text{std}_{frag. linear} - \text{std}_{frag, viscoelastic}}{\text{std}_{frag. linear}} \times 100 \quad (5.4)$$

where  $\text{mean}_{frag. linear}$ ,  $\text{std}_{frag. linear}$ ,  $\text{mean}_{frag, viscoelastic}$ ,  $\text{std}_{frag, viscoelastic}$  are the mean ( $\mu$ ) and standard deviation ( $\sigma$ ) parameters of the lognormal fit of the linear and linear viscoelastic pounding models correspondingly. The  $\mu$  and  $\sigma$  parameters are reported in the figures of Appendix C.

Figure 5.26 depict indicative for the case of pounding between 12RFDCH and 8WDCL, the percentage differences of the mean and standard deviation of the lognormal distributions as a function of the initial separation distance. The percentage differences are calculated and compared for the two considered impact models (linear and linear visco-elastic) and for the upper and lower bound values of the impact element stiffness  $K_p$  ( $K_p = High$  and  $K_p = low$ ).

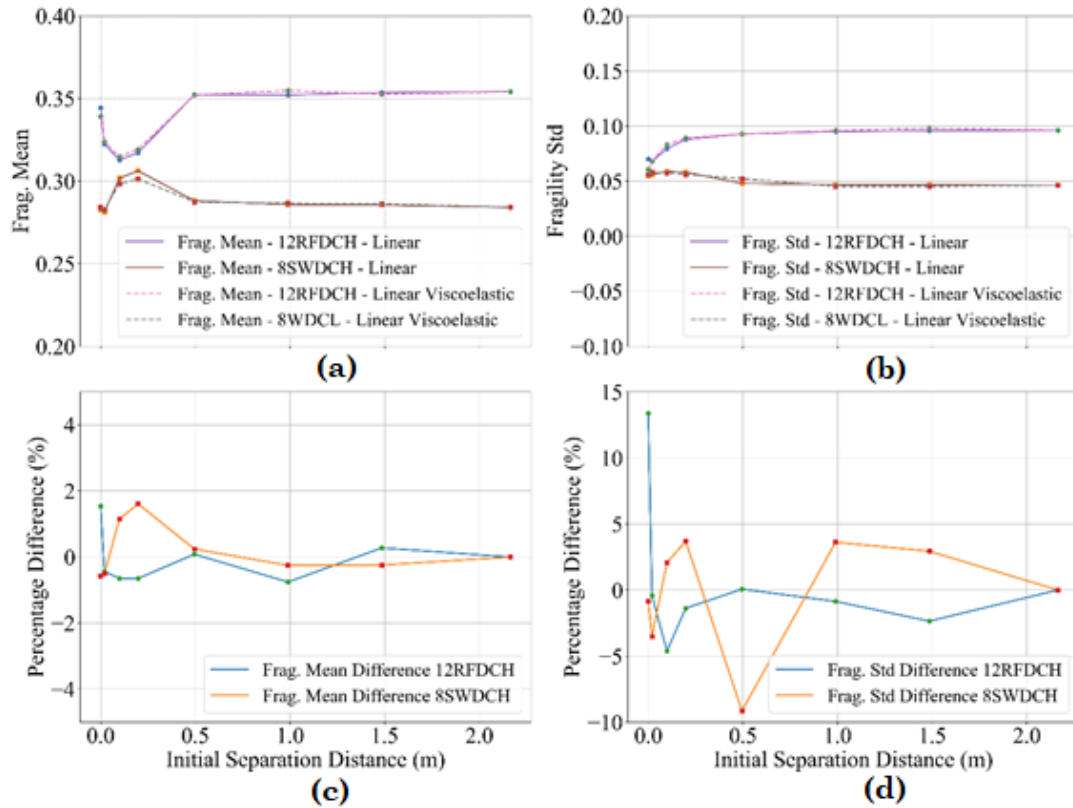


Figure 5.26: Pounding between 12RFDCH and 8WDCL SDOF systems - light damage limit state and  $K_p = High$  a) mean values of the fragility models of the two adopted contact models as a function of the initial separation distance b) standard deviation values of the fragility models for the two adopted contact models as a function of initial separation distance c) percentage difference between the mean values of the two adopted contact models as a function of the initial separation distance and b) percentage difference between the standard

Table 5.6 summarizes the upper and lower bounds of the percentage differences for the mean and the standard deviation values for the two adopted limit states.

Chapter 5 - Fragility Sensitivity of RC Colliding Buildings on the Modelling Parameters of the Linear and Linear Viscoelastic Contact Model

Table 5.6: Summary of the upper and lower bounds (max and min) of the percentage differences of the mean and the standard deviation values for the two adopted limit states (light damage/severe damage).

			Mean		Standard Deviation	
			Light Limit State/Severe Limit state		Light Limit State/Severe Limit state	
			12RFDCH	8SWDCH	12RFDCH	8SWDCH
12RFDCH and 8SWDCH	K <sub>p</sub> = High	Upper Bound	0.8%/0.6%	0.4%/0.0%	8.9%/14.2%	2.2%/13.8%
		Lower bound	-0.5%/-2.9%	-0.91%/-2.76	-0.2%/-13.9%	-3.8%/-8.2%
	K <sub>p</sub> = Low	Upper Bound	+1.4%/+1.8%	+0.9%/+2.1%	6.2%/3.8%	2.32%/1.6%
		Lower bound	-1.0%/-2.6%	-1.0%/-2.3%	-8.8%/-5.2%	-8.7%/-6.0%
12RFDCH and 8WDCL	K <sub>p</sub> = High	Upper Bound	1.5%/1.5%	1.6%/2.4%	13.4%/7.0%	3.7%/5.2%
		Lower bound	-0.8%/-3.6%	-0.6%/-1.6%	-4.6%/-17.4%	-9.1%/-11.8%
	K <sub>p</sub> = Low	Upper Bound	1.7%/1.9%	0.7%/2.3%	18.4%/8.0%	5.1%/6.0%
		Lower bound	-1.8%/-3.7%	-0.7%/-2.9%	-5.5%/-9.5%	-12.2%/-4.8%
12RFDCL and 8IFDCH	K <sub>p</sub> = High	Upper Bound	1.4%/2.9%	2.1%/1.9%	5.6%/5.1%	10.2%/6.7%
		Lower bound	-1.3%/-2.4	-0.6%/-1.9%	-6.5%/5.1%	-8.3%/-1.9%
	K <sub>p</sub> = Low	Upper Bound	0.6%/3.8%	1.6%/1.2%	6.2%/19.1%	13.1%/7.8%
		Lower bound	-0.2%/-4.5%	-0.6%/-4.1%	-2.0%/-5.9%	-3.9%/-5.9%

The percentage difference for the mean shape parameter of the fragility curves for all oscillators and for all initial separation distances remains bounded between +2.1% and -1.8% for the light damage limit state and +3.8% and -4.5% for the severe damage limit state. The corresponding bounds for the standard deviation are +18.4% and -12.2% and +19.1% and -17.4% for the

light and severe damage limit states correspondingly. Thus, it can be concluded that the impact of the contact element type is more significant at high seismic intensity levels, however the difference remains relatively low.

### 5.6.7 Impact of Energy Dissipation on The Number of Pounding Events and Magnitude of Pounding Forces

This section, presents indicative a contour plot of the number of pounding events and the magnitudes of the developing pounding forces for each ground motion and seismic intensity levels for the case of pounding between 12RFDCH and 8SWDCH SDOF systems with zero gap and pounding forces modelled via the linear pounding model with  $K_p^H$ . The contour plots are generated via linear interpolation between the data points. The full set of contour plots for all three pairs of inelastic SDOF systems for the case of zero initial separation distance is shown in Appendix F.

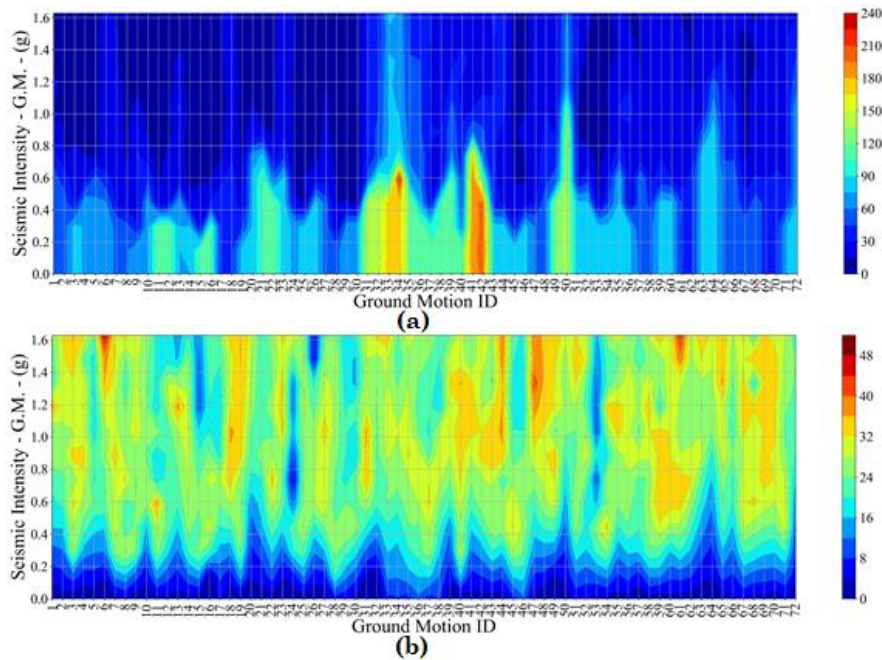


Figure 5.27: Pounding between 12RFDCH and 8SWDCH - Linear pounding model - Gap = 0.00 (m) and  $K_p = \text{High}$  a) Contour plot of the number of pounding events per ground motion and intensity level b) Contour plot of the magnitude of the pounding forces per ground motion and intensity level.

The durations of the ground motions are depicted in Figure 5.28. It can be readily observed that there is a good correlation between the duration of the ground motions and the number of pounding events.

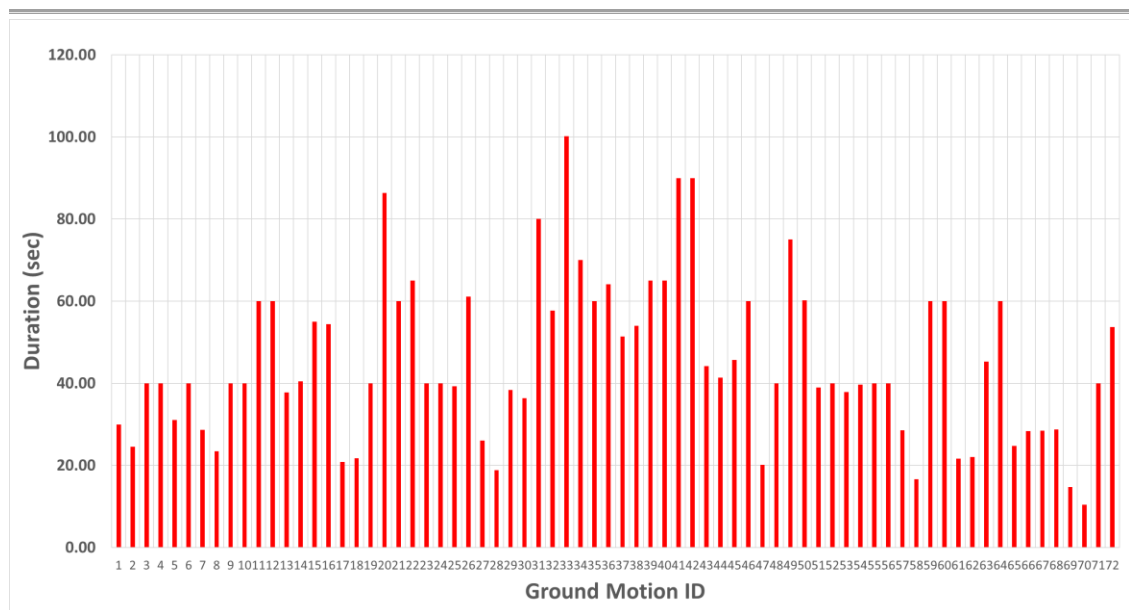


Figure 5.28: Duration of the 72 ground motions considered in this study.

A visual inspection of the contour plots that depicts the information on the number of pounding events and the magnitudes of the pounding forces, leads to the following conclusions:

- Pounding forces modelled by means of the linear pounding model exhibit higher magnitudes than those modeled by the linear visco-elastic pounding model. This is due to the energy that is dissipated during collisions via the viscous damper of the linear visco-elastic pounding model.
- Contour plots of both the pounding force magnitude and the number of pounding events follow similar trends for the two considered impact models. Therefore, the impact element type does not have a significant impact on the distribution of the number of collisions and the magnitude of the developing pounding forces.
- The number of pounding events have a good correlation with the duration of ground motions.

## 5.7 Closure

This study, considered a building stock of five code-compliant inelastic RC building frames to assess the influence of the impact element stiffness, the initial separation distance and the dissipation of energy on their seismic performance. The seismic performance is assessed within the context of PBEE that readily accounts for the record-to-record variability, which has not been

addressed thus far in the literature for seismic pounding case studies. Five computationally efficient, and equivalent to the five code-compliant RC building frames are used in three pairs in order to perform PSDA for the various combinations considered herein. The PSDA analysis is based on IDA and a suite of 72 far-field ground motions. Seismic intensity is expressed in terms of a proposed IM termed as *avgSa*, that is found to be more efficient than the PGA that is typically used in EISP studies. The proposed IM, can account for shift and elongation phenomena of the fundamental periods observed within the inelastic response.

In this study, it is shown that:

- Pounding has a significant impact on the shape of the fragility curves for an initial separation distance up to 25% of the code specified (Eurocode 8) minimum required distance.
- The impact element stiffness is more influential at high intensity levels. However, the difference on the shape parameters of the fragility curves for the two herein considered extreme values, is very low.
- The adoption of the linear visco-elastic pounding model for the modelling of pounding forces results in differences in the shape parameters of the fragility curves. However, to the opinion of the author these differences are small and therefore, the linear pounding model represents an attractive pounding modelling technique, especially for lower seismic intensity levels
- The number of pounding events at higher intensity levels is reduced as one or both of the SDOF systems oscillate about a new point of equilibrium. Therefore, at high levels of seismic intensity, the two systems tend to collide within the first few seconds of the seismic excitation and then experience very few or zero pounding events. Thus, severe damages at high intensity levels are more likely to occur due to the capacity exceedance of elements rather than on the increase of the seismic demand due to pounding.
- The number of pounding events depends mainly on the duration of the ground motion excitation.
- The magnitude and the number of the pounding events depends mainly on the value of the impact element stiffness rather than on the type of the adopted pounding model type.

## Chapter 5 - Fragility Sensitivity of RC Colliding Buildings on the Modelling Parameters of the Linear and Linear Viscoelastic Contact Model

---

The results presented in this study, are based on simple SDOF systems and therefore this work does not cover all aspects of structural pounding which is a highly complex phenomenon. Adopting higher complexity models will allow to consider factors such as the spatial distribution of the pounding forces along the building heights as well as the inelastic demand distributions due to pounding across all structural elements.

# Chapter 6

## Probabilistic Seismic Performance Assessment of Adjacent RC Building Frames Interacting at Floor Levels.

### 6.1 Overview

In this chapter, the PBSA approach introduced in Chapter 5 is further implemented to study the impact of EISP on the seismic performance of two RC planar building frames.

One contribution of this chapter is the utilization of PBSA to assess the influence of structural pounding on the seismic performance of inelastic multi-storey structures modelled as nonlinear MDOF systems in the context of PBEE framework. More specifically, the adopted approach considers multiple seismic hazard scenarios and derives probabilistic predictions by means of fragility curves derived by using 25 recorded GMs. These curves can be readily combined with seismic hazard curves in conducting seismic risk/vulnerability analysis of adjacent buildings subject to pounding (see e.g., *Rossetto and Elnashai, 2005*). Herein, the proposed IM in Eq. (5.2) is adopted to develop fragility curves and limit states away from collapse are considered being more representative for the case of modern code-compliant structures.

Note that most studies of EISP addressing code-compliant structures modelled as inelastic MDOF systems consider a single level of seismic performance (e.g. ultimate design limit) and adopt code-specific uniform-hazard response spectrum (e.g., *Efraimiadou et al 2013*). In this context, seismic action is often represented through considering spectrum compatible response-histories corresponding to a single IM/seismic hazard level which does not provide accurate estimates of seismic risk in colliding structures as discussed in *Barbato and Tubaldi (2013)*. Further, even in cases where multiple seismic hazard levels are considered in examining EISP effects to inelastic response of multi-storey structures, a limited number of GMs are considered and neither statistical characterisation of

record-to-record variability is pursued nor fragility curves are developed (e.g. *Favvata*, 2017).

Importantly, the herein presented study is based on two of the 5 RC building frames considered in Chapter 5 (§5.2 *Structural Modelling Assumptions*). Thus, the availability of the equivalent non-linear SDOF systems provides the opportunity to quantify the influence of the adopted modelling complexity on the accuracy of the derived probabilistic seismic performance assessment of the adjacent structures subjected to pounding. The comparison of statistics of inelastic response demands of equivalent nonlinear SDOF systems with nonlinear MDOF systems is a second major contribution of this chapter.

## 6.2 Structural modeling assumptions

The two adopted RC buildings frames (Figure 6.1) have been studied in the past in (*Fardis*, 1994), (*Mwafy and Elnashai*, 2001), (*Papanikolaou and Elnashai*, 2005) and (*Katsanos et al.*, 2014). They represent modern seismic resistance systems (frame and shear wall - frame systems for the twelve and eight storey buildings correspondingly) with equivalent levels of seismic safety (high ductility class - EC8 classification).

Each frame is modelled in OpenSEES (*McKenna et al*, 2000) using nonlinear force-based distributed plasticity elements for all structural elements. Shear walls are modelled by means of equivalent column elements. Material non-linearity for concrete, reinforcement steel and contact elements, is introduced by means of OpenSEES built-in uniaxial material models. The force-deformation laws of these uniaxial materials are depicted in Figure 6.2, and the range of values of the material model parameters, are reported in table 6.1. The mass is lumped at the structural nodes that exhibit three degrees of freedom. Permanent and live loads are considered to be 2.0 *KN/m* and the buildings are assumed to be supported on soil class B.

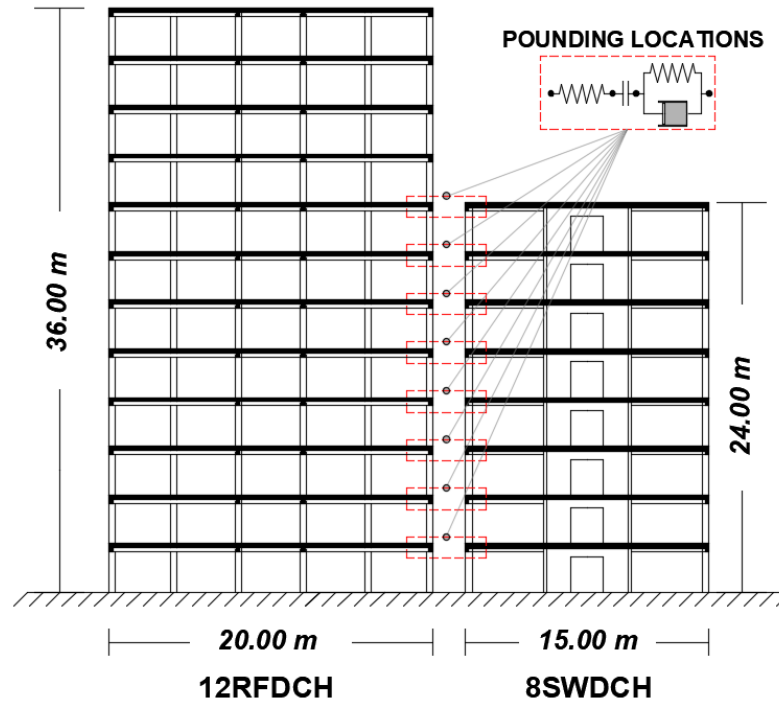


Figure 6.1: Designations and dimensions of the two herein adopted RC buildings, assumed to be in initial contact. Slab to slab pounding is modelled by means of the linear visco-elastic pounding model.

The OpenSEES numerical models were calibrated against the corresponding static pushover curves reported in (Katsanos *et al.*, 2014). Model transfer between FEA software and the subsequent calibration process is a non-trivial task that depends on many parameters (e.g. element and material formulations, numerical integration techniques etc). The derived static pushover curves from the herein developed nonlinear distributed plasticity models are compared to those reported in Figure 6.3 (Katsanos *et al.*, 2014). Note that the latter have been derived using lumped plasticity model in Zeus (Elnashai *et al.*, 2002) and were the ones used in defining the equivalent SDOF systems used in the previous Chapter. Overall, a reasonably close approximation of the two sets of pushover curves is achieved which, further establishes a fair comparison between fragilities derived from pounding/interacting equivalent SDOF systems in Chapter 5 and the MDOF ones considered in this chapter.

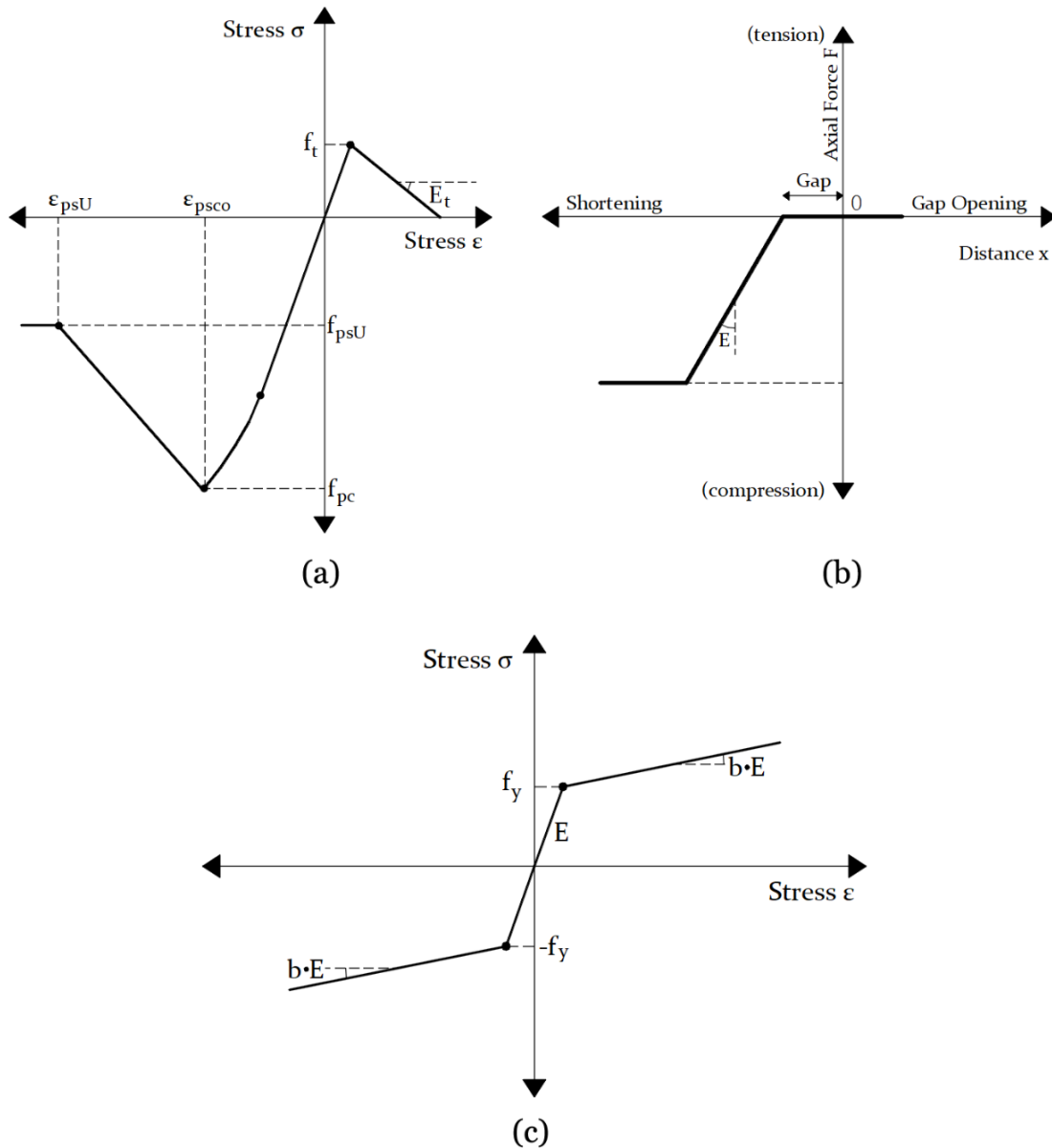


Figure 6.2: a) Force deformation model for RC beams, columns and shear walls (OpenSEES concrete02 uniaxial material) b) Force - deformation relationship for the contact element (OpenSEES ElasticPPGap uniaxial material) c) Force deformation model for the reinforcement steel (OpenSEES Steel01 uniaxial material).

Table 6.1 Values of the various material properties used in the modelling of the two inelastic MDOF systems.

OpenSEES Concrete02						
	$f_{pc}$ (MPa)	$\epsilon_{psc0}$	$f_{psU}$ (MPa)	$\epsilon_{psU}$	$f_t$ (MPa)	$E_t$ (MPa)
12RFDCH	33-37	0.0067	12 - 25	0.020 - 0.035	2.6	$2.0 \times 10^3$
8SWDCH	35	0.009	13	0.08	2.6	$2.0 \times 10^3$
OpenSEES Steel01						
	$F_y$ (MPa)	$E$ (MPa)		$b$		
12RFDCH	585 - 2000	200		0.0085 - 0.017		
8SWDCH	585 - 1500	200		0.0085 - 0.017		

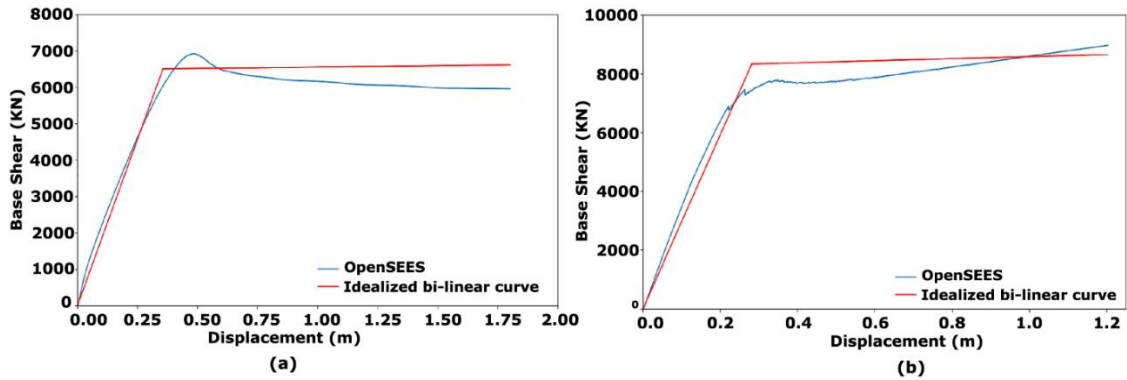


Figure 6.3: Static pushover curves of the 2D RC buildings frames juxtaposed the target prototype idealized bi-linear pushover curve a) 12RFDCH and b) 8SWDCH building.

Both buildings are regular in height with a constant floor height of 3.0 m. To this extent, pounding is assumed to occur only between floor slabs. Further, pounding forces are modelled by means of the linear viscoelastic pounding elements initially proposed in (*Anagnostopoulos, 1988*). This contact element accounts for energy dissipation during collisions and is activated only when the relative distance between each floor is zero. An adaptive time step that varies between  $5 \times 10^{-4}$  sec up to  $1 \times 10^{-5}$  sec is adopted as a compromise between performance and accuracy. Further, test runs indicated that a smaller time-step has an insignificant impact on the imposed seismic demands.

The adopted values for the stiffness of the linear spring is based on the floor stiffnesses calculated based on (*Caterino et al., 2013*) and its values is

$K = 3.92 \times 10^9$  N (parameter E in Figure 6.2 b) (Anagnostopoulos, 1988). The damping coefficient  $C$  is calculated based on Equations 7.3 and eq.4 (Anagnostopoulos, 2004) with a value of  $745142.8$  N s/m.

## 6.3 Selected IM and ground motion suite

### 6.3.1 Record selection and scaling

Eurocode 8 compliant assessment of inelastic structural response of code-compliant structures involves the use of a small number of accelerograms (usually 7) scaled to match the linear Eurocode 8 response spectrum (see e.g., Giaralis and Spanos 2009). The average inelastic demands is used to quantify seismic performance. In this regard, most EISP studies addressing code-compliant adjacent interacting multi-storey buildings modelled as nonlinear MDOF structures represent the seismic action by means of small suites of spectrum compatible GMs either artificial as discussed in section 4.3 (e.g., Efraimiadou et al. 2013 uses 6 artificial spectrum compatible accelerograms) or recorded (e.g., Favvata 2017 considers 7 recorded GMs). In the latter work, the spectrum compatible recorded GMs are scaled to three different intensities to span different seismic hazard levels. In other cases, (e.g., Abdel Raheem 2014), small number of non-spectrum compatible GMs are considered.

Nevertheless, representation of the seismic action using such a small number of GMs can only adequately quantify the mean inelastic demands, while higher number of GMs is required to capture record-to-record variability (see e.g., Vega et al. 2009). To this aim, herein a subset of 25 far-field recorded GMs out of the 72

used in Chapter 6 in conjunction with nonlinear SDOF pounding structures, are utilized (see section 5.5.1). This subset spans a broad range of seismological parameters such as the magnitude, rupture mechanism, amplitude, and frequency content as shown in Figure 6.4. As discussed in section 1.2, the reason for adopting a reduced number of GMs in performing NRHA for MDOF pounding structures is to contain computational time within reasonable scales. IDA is undertaken with GM scaling limit of  $1.0 g$  ( $PGA$ ) as the main focus herein is on light damage limit states away from collapse of practical interest to code-compliant structures.

Chapter 6 - Probabilistic Seismic Performance Assessment of Adjacent RC Building Frames Interaction at Floor Levels

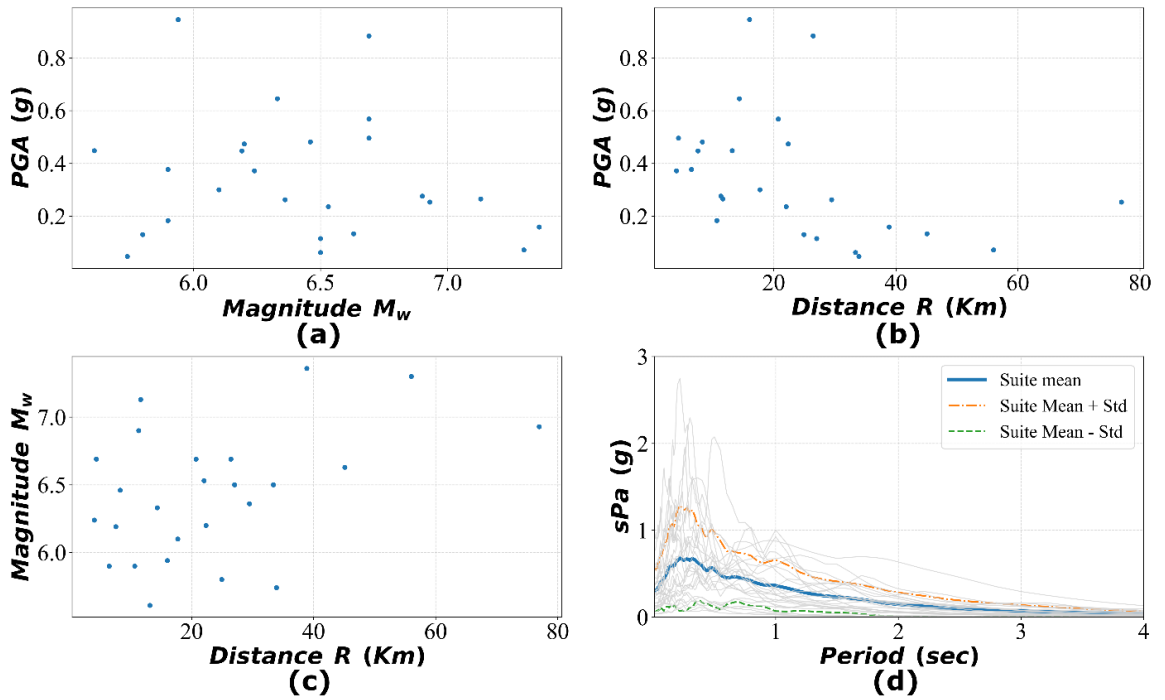


Figure 6.4: Distribution of ground motions in a) PGA -  $M_w$  space (b) PGA -  $R$  space (c)  $M_w$  -  $R$  space and (d) the pseudo spectral accelerations of the adopted ground motion suite (table 6.1).

**Table 6.2:** Ground motions used in the study and related information (PEER-NCA, Chiou et al).

<i>ID</i>	<i>Event</i>	<i>Station</i>	<i>Mag. <math>M_w</math></i>	<i><math>V_{s,30}</math> (m/s)</i>	<i><math>R_{rup}</math> (Km)</i>	<i>PGA (g)</i>	<i>Site Class<sup>a</sup></i>
1	Coyote Lake (1979.08.06)	Halls Valley	5.74	281.61	33.83	0.047	D
2	Livermore (1980.01.24)	Del Valle Dam	5.80	403.37	24.95	0.130	C
3	Mammoth Lakes (1980.05.25)	Long Valley Dam	5.94	537.16	16.03	0.945	C
4	Northern California (1954.12.21)	Ferndale City	6.50	219.31	27.02	0.115	D
5	Big Bear (1992.06.28)	Big Bear Lake Civic Center	6.46	430.36	8.30	0.481	C
6	Chalfant Valley (1986.07.20)	Zack Brothers Ranch	6.19	316.19	7.58	0.447	D
7	Chi-Chi, Taiwan-2 (1999.09.20)	TCU073	5.90	476.65	10.68	0.183	C
8	Coalinga (1983.05.02)	Parkfield-Fault -Zone #14	6.36	246.07	29.48	0.262	D

Chapter 6 - Probabilistic Seismic Performance Assessment of Adjacent  
RC Building Frames Interaction at Floor Levels

9	Taiwan (1986.11.14)	Taiwan1 C00	7.30	309.41	56.01	0.072	D
10	Northwest China (1997.04.11)	Jiashi	6.1	240.09	17.73	0.3	D
11	Sierra Madre (1991.06.28)	Altadena Eaton Canyon	5.61	375.16	13.17	0.448	C
12	Erzican, Turkey (1992.03.13)	Erzincan	6.69	352.05	4.38	0.496	D
13	Kern County (1952.07.21)	Taft Lincoln School	7.36	385.43	38.89	0.159	C
14	Borrego Mountain (1968.04.09)	El Centro Array #9	6.63	213.44	45.12	0.133	D
15	Friuli, Italy (1976.05.06)	Codroipo	6.50	249.28	33.4	0.062	D
16	Northridge (1994.01.17)	Castaic-Old Ridge Route	6.69	450.28	20.72	0.568	C
17	Managua, Nicaragua (1972.12.23)	Managua	6.24	288.77	4.06	0.372	D
18	Imperial Valley (1979.10.15)	Delta	6.53	242.05	22.03	0.236	D
19	Victoria, Mexico (1980.10.15)	Cerro Prieto	6.33	471.53	14.37	0.645	C
20	Westmorland (1981.04.26)	Westmorland Fire Station	5.90	193.67	6.5	0.377	D
21	Loma Prieta (1989.10.18)	Emeryville	6.93	198.74	76.97	0.253	D
22	Kobe (1995.01.16)	Amagasaki	6.90	256.0	11.34	0.276	D
23	Chi-Chi, Taiwan-2 (1999.09.20)	CHY080	6.20	496.21	22.37	0.474	C
24	Northridge (1994.01.17)	Santa Monica City Hall	6.69	336.2	26.45	0.883	D
25	Hector Mine (1999.10.16)	Hector	7.13	726.0	11.66	0.265	C

<sup>a</sup> According to the NEHRP site classification: Site class A ( $v_{s,30} \geq 1500$  m/s), Site class B ( $760$  m/s  $\leq v_{s,30} < 1500$  m/s), Site class C ( $360$  m/s  $\leq v_{s,30} < 760$  m/s), Site class D ( $180$  m/s  $\leq v_{s,30} < 360$  m/s)

## 6.4 Numerical results and discussion

As discussed, pounding occurs between floor slabs and therefore there is no risk of column shearing. In this case, pounding forces can cause local damages at the areas of contact and high acceleration pulses at floor levels. Figure 6.5, depicts such acceleration pulses for the 8<sup>th</sup> floor of both buildings under seismic excitation of the #3 ground motion of table 6.1. The magnitude of the acceleration pulses that are inflicted on the lower 8SWDCH building are significant higher than those experienced by the taller 12RFDCH building.

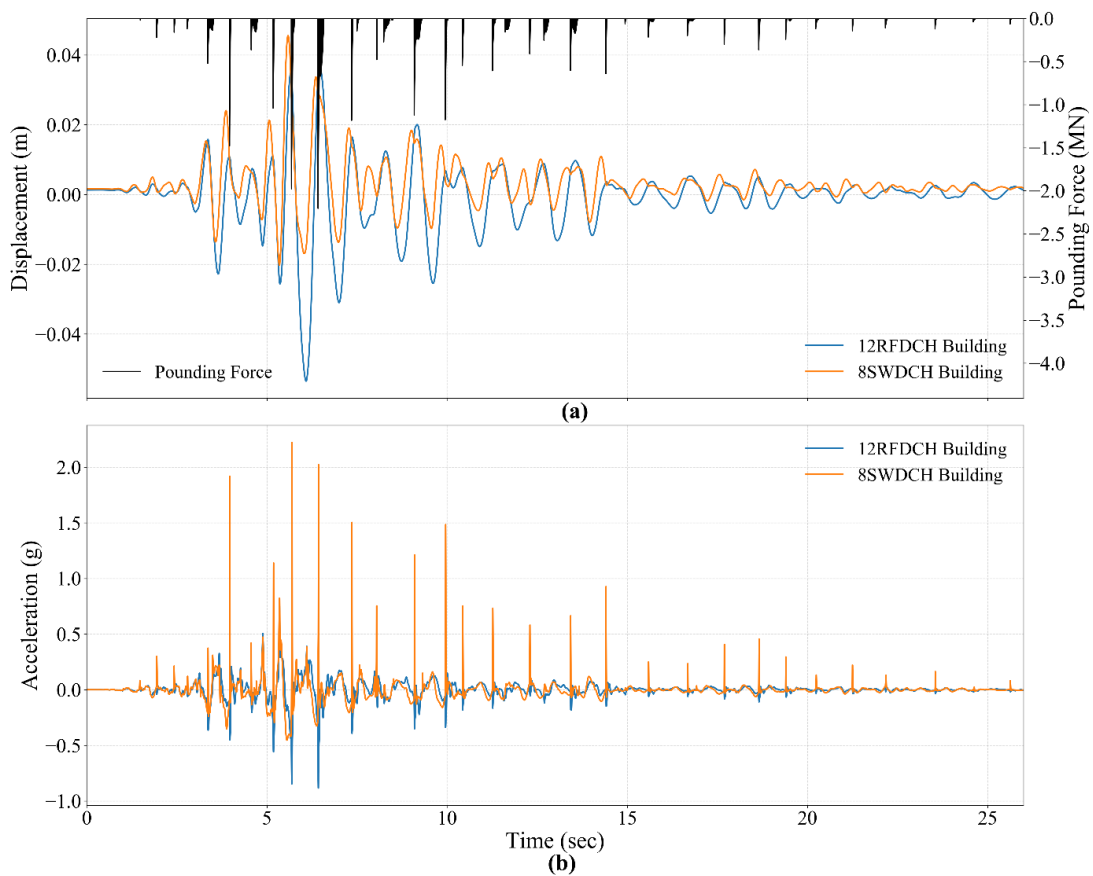


Figure 6.5: Displacement and acceleration response histories for both buildings excited with ground motion #3 scaled at 0.5g (PGA) a) 8th floor displacements and pounding forces b) 8th floor acceleration response history with the distinct acceleration pulses.

Herein, structural damage is expressed by means of the IDR that represents a macroscopic engineering demand parameter that correlates well with global damage. In the case of the 12RFDCH building, the maximum IDR for the lower eight floors where pounding occurs and the upper four floors are assessed separately. The average IDR values and their spread per building floor considering all ground motions in the suite

for scales 0.5g (PGA) and 1.0g (PGA) are depicted in Figures 6.6 and 6.7 correspondingly.

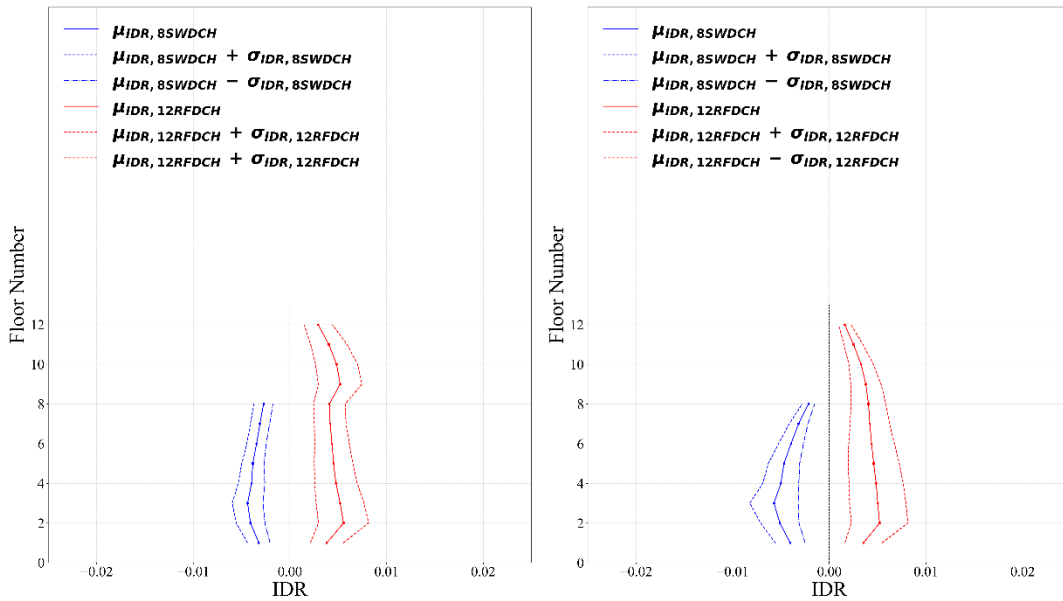


Figure 6.6: Average IDR values and their spread considering all ground motions in the suite scaled to 0.5g (PGA) a) with pounding and b) without pounding.

It can be readily observed that the 9<sup>th</sup> floor of the 12RFDCH building experiences a sudden increase of the average IDR value due to the whiplash effect. Moreover, pounding increases the spread of the IDR values for the upper 4 floors of the 12RFDCH building.

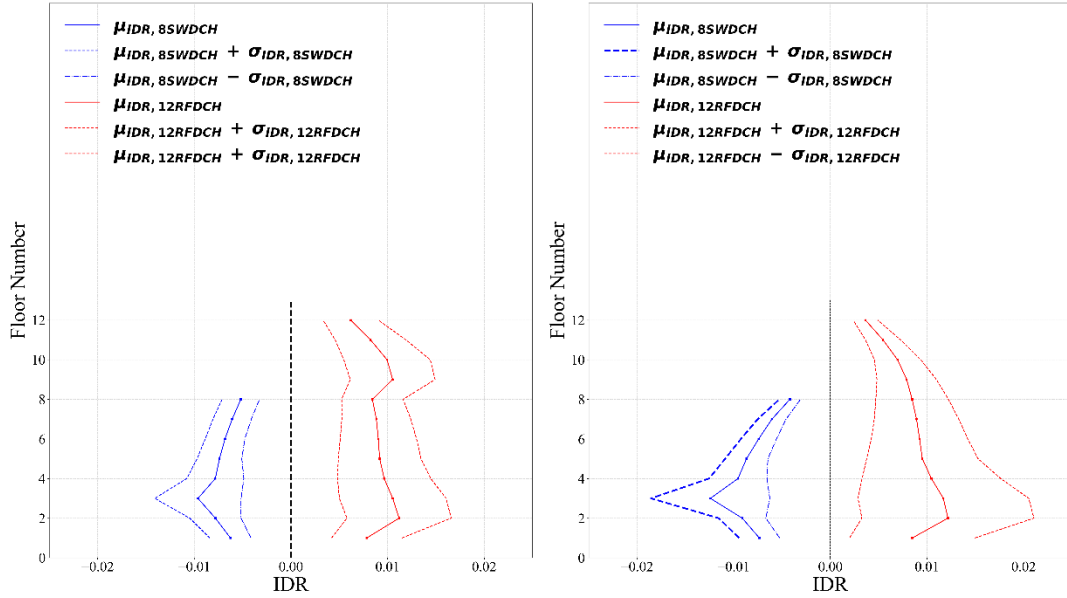


Figure 6.7: Average IDR values and their spread considering all ground motions in the suite scaled to 1.0g (PGA) a) with pounding and b) without pounding.

Herein, the 1% of  $\theta_{max}$  (Immediate Occupancy, *Vamvatsikos and Cornell, 2002*) is considered as a LS that is well-known to correspond to light is damage.

### 6.4.1 IDA curves

The IDA curves presented in this section are derived based on the following steps:

- Initially, IDA curves are derived based on a scaling scheme that limits the seismic intensity to 1.0g in terms of the PGA (see Figure 6.8 a. and c.).
- Then the intensity (vertical) axis of the IDA curves is renormalized/rescaled based on the avgSa IM. The second step transforms the IDA curves as it is illustrated in figures 6.8 b and d.

Following the above two steps, the derived IDA curves for the two RC frame buildings are shown in figures 6.8. As discussed, for each IDA curve, the seismic intensity is expressed both in terms of the PGA and the *AvgSa*.

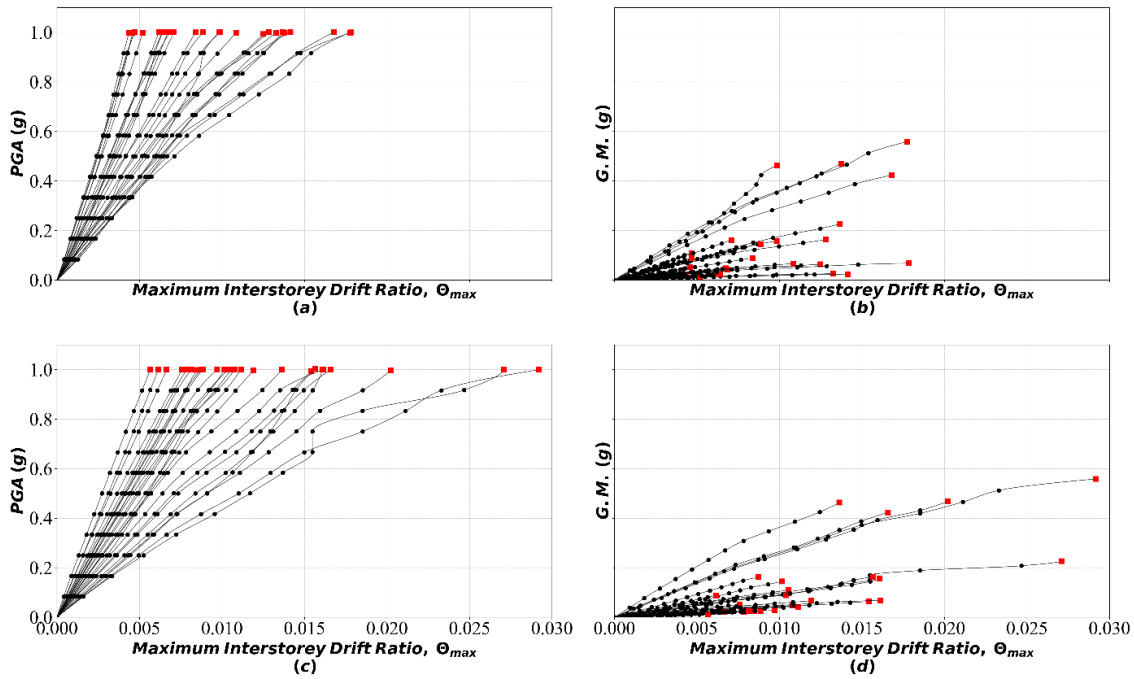


Figure 6.8: IDA curves for the 8SWDCH building a) coupled with 0.0 m initial separation distance and IM=PGA b) coupled with 0.0 m initial separation distance and IM=AvgSa c) uncoupled and IM=PGA d) uncoupled and IM=AvgSa.

It can be readily observed that pounding restricts the maximum interstorey drifts for both RC frames at the floors where pounding occurs. However, the opposite behavior is observed for the upper floors of the 12RFDCH building where pounding tends to increase the maximum interstorey drifts. This whiplash type of response has been repeatedly observed in the past (e.g. *Skrekas et al.*, 2014, *Favvata*, 2017)

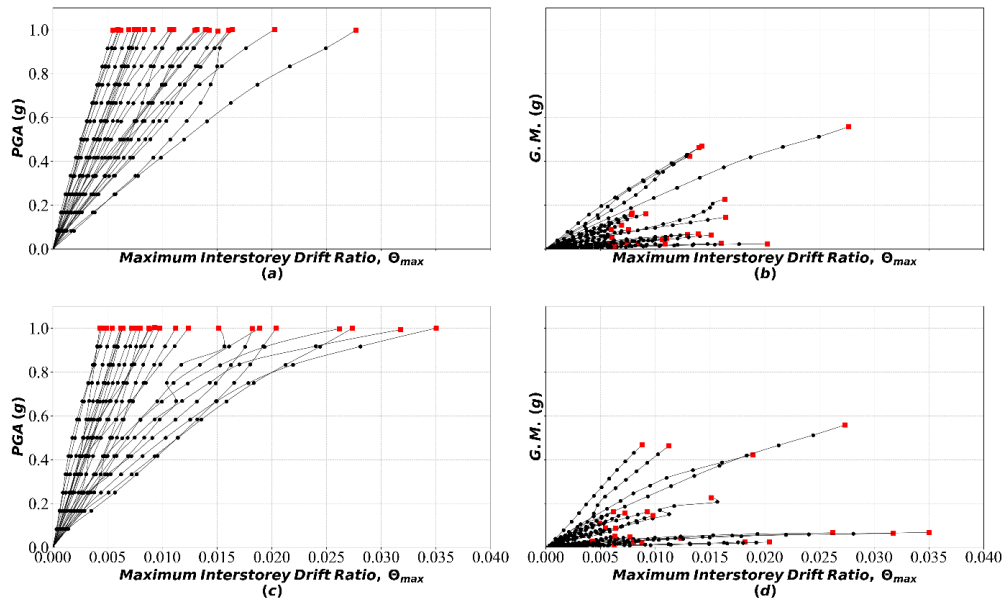


Figure 6.9: IDA curves for the lower eight floors of 12RFDCH building a) coupled with 0.0 m initial separation distance and IM=PGA b) coupled with 0.0 m initial separation distance and IM= *AvgSa* c) uncoupled and IM=PGA d) uncoupled and IM= *AvgSa*

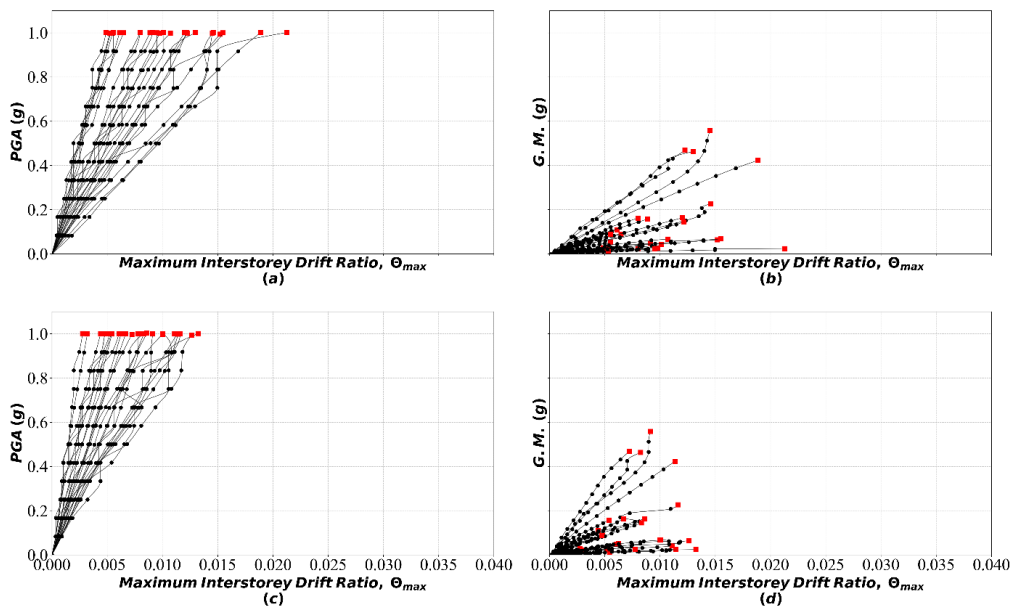


Figure 6.10: IDA curves for the upper four floors of the 12RFDCH building a) coupled with initial separation distance and IM=PGA b) coupled with initial separation distance and IM= *AvgSa* c) uncoupled and IM=PGA d) uncoupled and IM= *AvgSa*.

### 6.4.2 Fragility curves

The following plots, depict the distributions of the seismic intensity levels where the exceedance of the considered limit state occurs and the corresponding fragility models.

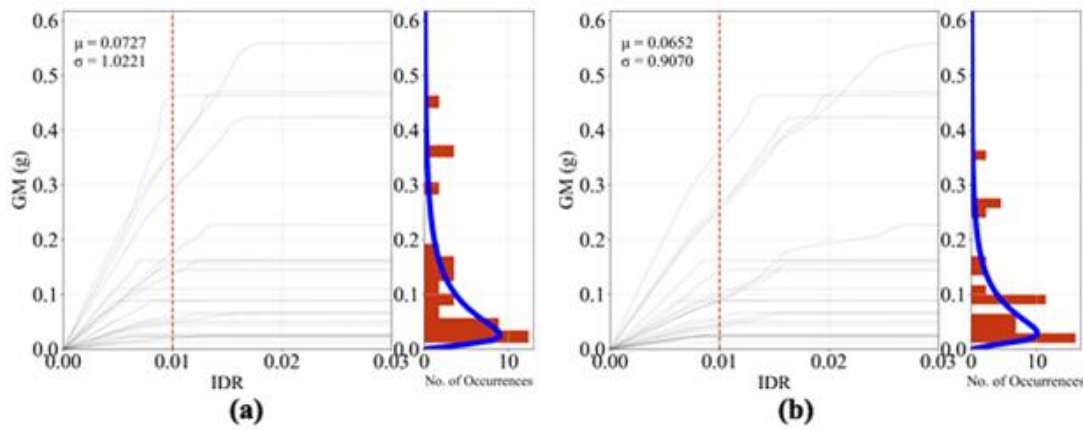


Figure 6.11: Parameters of the lognormal fit for the 1% IDR limit state - 8SWDCH building a) coupled b) uncoupled.

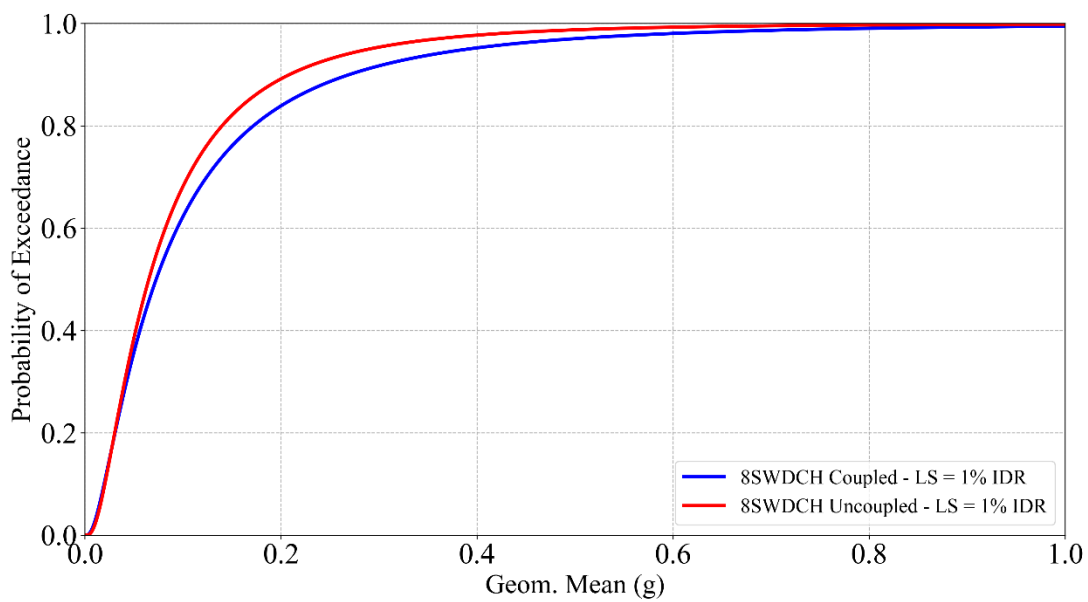


Figure 6.12: Fragility curves for the 8SWDCH building for the coupled and uncoupled case.

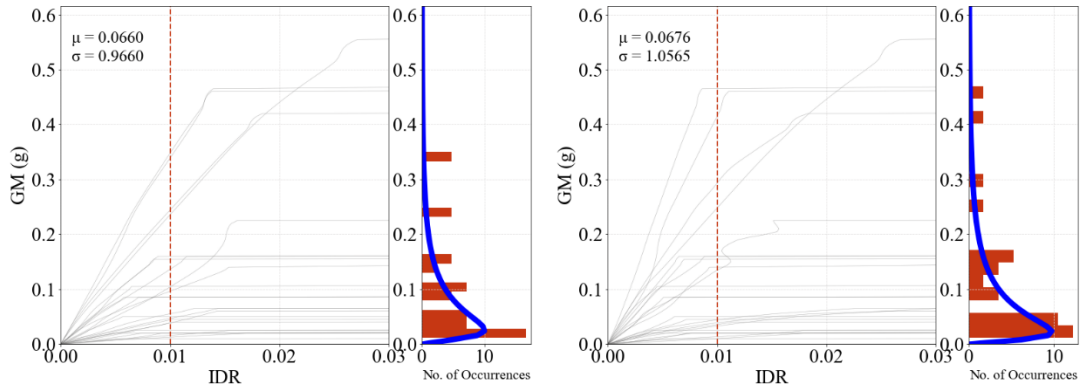


Figure 6.13: Parameters of the lognormal fit for the 1% IDR limit state - 12RFDCH building a) coupled b) uncoupled.

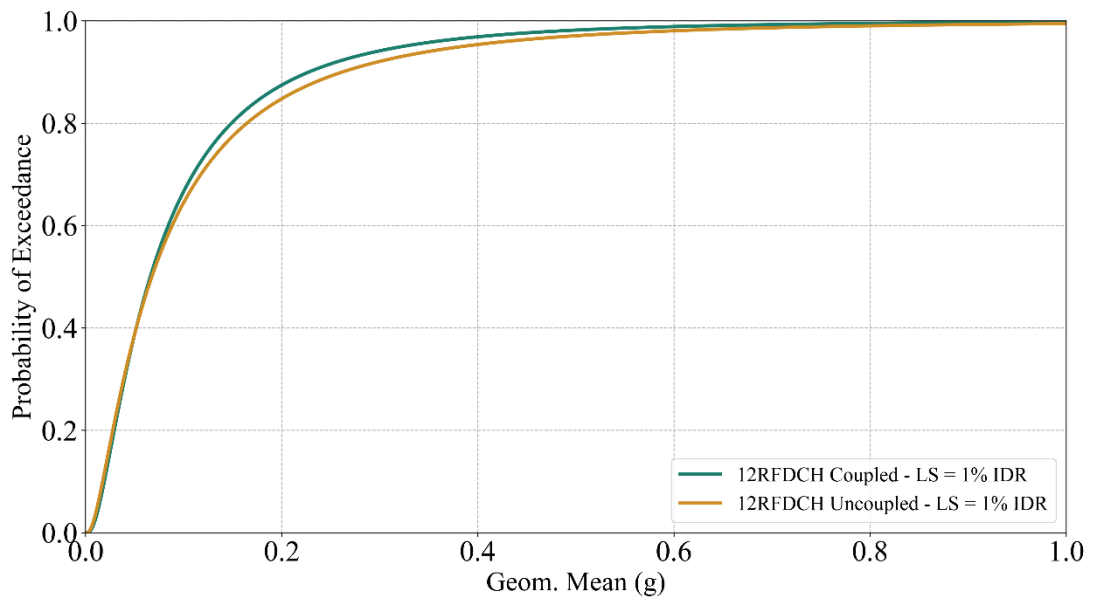


Figure 6.14: Fragility curves for the lower 8 floors of the 12RFDCH building for the coupled and uncoupled case.

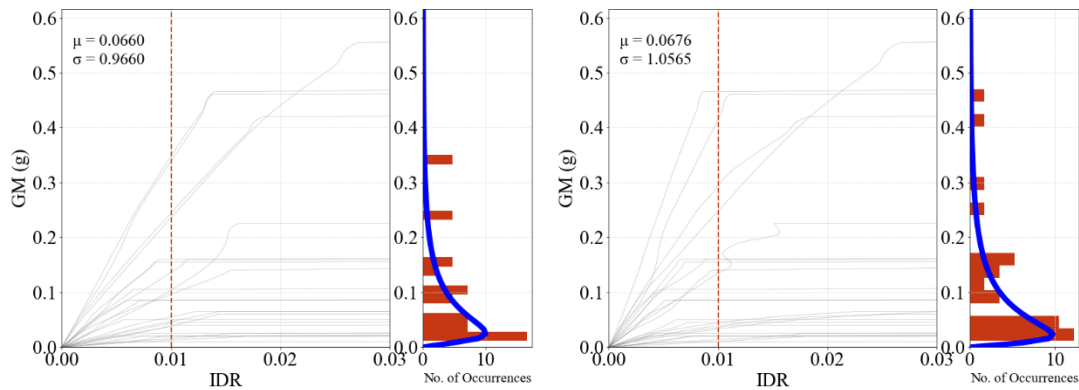


Figure 6.15: Parameters of the lognormal fit for the 1% IDR limit state - 12RFDCH building a) coupled b) uncoupled.

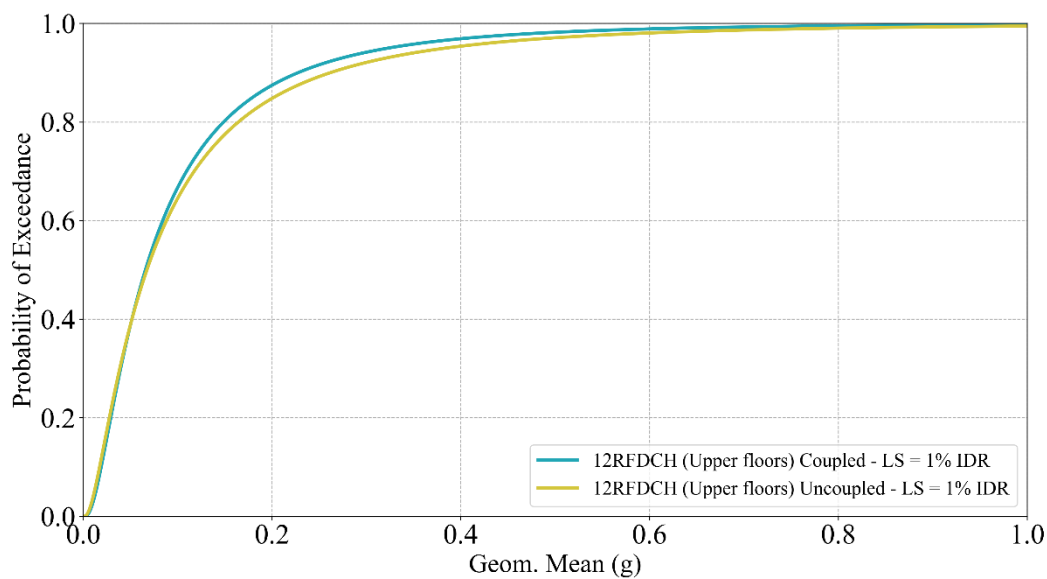


Figure 6.16: Fragility curves for the upper 4 floors of the 12RFDCH building for the coupled and uncoupled case.

It can be easily observed that for the 1% IDR limit state, pounding has a detrimental impact (an amplification of floor displacements) on the more flexible 12RFDCH building for both the lower and upper floors. In contrast, pounding has a beneficial effect on the stiffer and lower 8SWDCH building.

It is noted in passing that the influence of EISP to IDRs confirm trends previously reported in the literature but mostly discussed in the average (deterministic) context. Specifically, *Anagnostopoulos and Spiliopoulos, (1992)* examined EISP between MDOF systems for a suite of 5 GMs reported that EISP can reduce or increase the response of a structure based on the relative dynamic characteristics of the colliding buildings. In addition, pounding increased the spread of the derived inelastic response quantities. These previous findings based on a small number of GMs are herein confirmed as it is found that the mean fragility curves are shifted either left or right, compared to the fragility curve corresponding to the

uncoupled structure indicating that IDR increases or reduces, respectively. Further the shape of the fragility curves becomes more inclined indicating that EISP increases the spread of the obtained inelastic response quantities, especially at higher levels of the seismic intensity.

Further, *Efrimiadou et. al* (2013) studied the response of a 5-storey and 8-storey interacting inelastic RC frames and reported that EISP decreased the average IDR values from 2.44% to 2.3% (on average considering all floors) of the 5-storey structure. In contrast, pounding increased the average IDR values of the 8-storey building from 1.97% to 2.11% (on average considering all floors). Similar average trends are found herein (see e.g., figure 6.7) as pounding tends to restrict the average IDR values from 0.81% to 0.71% (on average considering all floors) of the (lower) 8-storey building and decrease the average IDR values from 0.91% to 0.85% (on average considering all floors) for the (higher) 12-storey building.

#### **6.4 Comparing probabilistic predictions based on SDOF and MDOF building frames**

As discussed in Chapter 2, pounding represents a very complex and computational expensive dynamic phenomenon. In this section, probabilistic seismic performance predictions derived based on the RC building frames are compared with predictions derived based on the equivalent SDOF models. The objective is to assess the ability of the SDOF for accurate spatial representation of the dynamic properties of the two structures, load paths as well as the spatial distribution of the pounding forces along the building floors. In this case however in order to produce comparable probabilistic predictions the adopted EDP is the maximum top floor displacement.

The SDOF models build in OpenSEES, exhibit the bilinear response curve shown Figure 6.3 (red line) and are excited under the same ground motion suite with an identical scaling procedure. Moreover, pounding is modelled by means of the linear viscoelastic model and a similar calibration procedure is adopted as discussed in section §6.2 . The calibrated pounding model parameters are 52312.4 *KN* for the stiffness *K* of the linear pounding spring and 2590193 *N s/m* for the damping coefficient *C*.

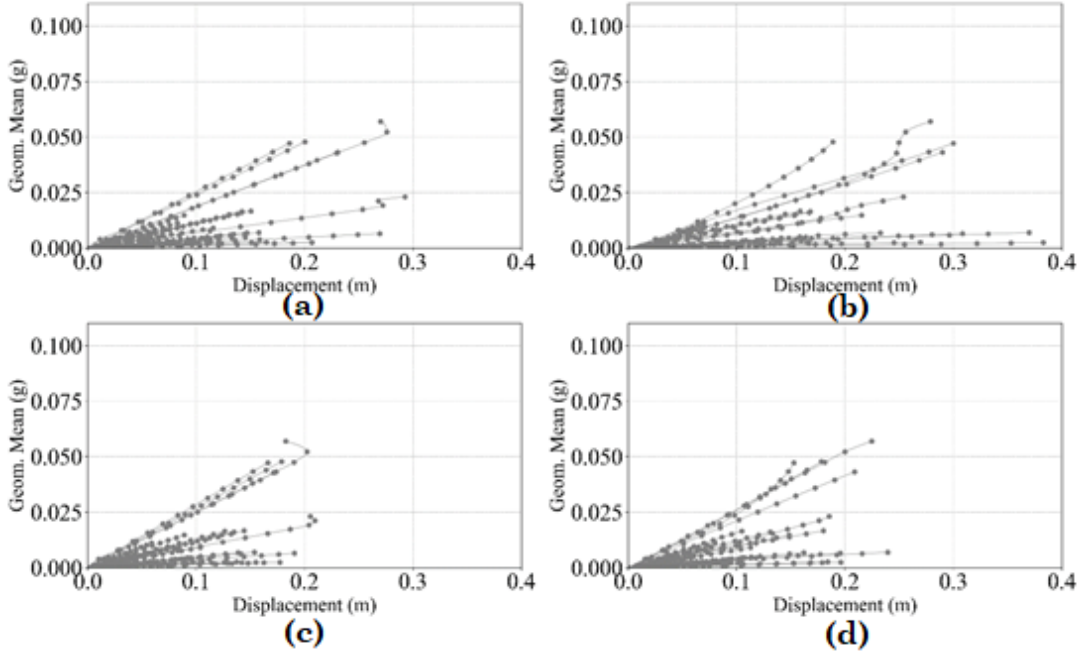


Figure 6.17: IDA curves for a) 12RFDCH - SDOF model b) 8SWDCH - SDOF model c) 12RFDCH - Frame d) 8SWDCH - Frame.

Next, percentage differences between the parameters of the fitted lognormal distributions derived for the MDOF systems and equivalent SDOF for the cases of the uncoupled and coupled response are calculated as

$$\text{Mean Difference} = \frac{\text{mean}_{frag.SDOF} - \text{mean}_{frag.MDOF}}{\text{mean}_{frag.SDOF}} \times 100 \quad (6.1)$$

$$\text{Std Difference} = \frac{\text{std}_{frag.SDOF} - \text{std}_{frag.MDOF}}{\text{std}_{frag.SDOF}} \times 100 \quad (6.2)$$

where  $\text{mean}_{frag.SDOF}$ ,  $\text{std}_{frag.SDOF}$ ,  $\text{mean}_{frag.MDOF}$ ,  $\text{std}_{frag.MDOF}$  are the mean and the standard deviation parameters of the fitted lognormal distribution for the cases of pounding between SDOF and MDOF systems respectively.

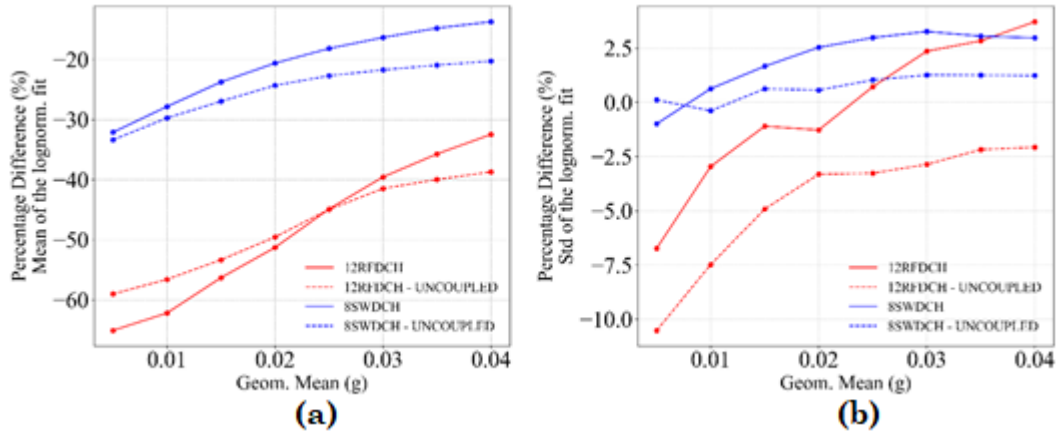


Figure 6.18: Percentage difference of parameters of the lognormal distributions for the two building frames vs the SDOF models.

Figure 6.18 plots percentage differences in Eqs. (6.1) and (6.2) as function of the seismic intensity. The mean parameter of the fragility models of the SDOF systems is 32% to 66% lower for the 12RFDCH building and 12% to 32% lower for the 8SWDCH building depending on the level of seismic intensity. Therefore, overall, probabilistic performance assessments based on the SDOF proxies leads to a significant underestimation of the seismic pounding hazard in the mean sense. Interestingly, it is seen that percentage mean differences reduce with increasing intensity but at a decreasing rate. The fact that the SDOF proxy predicts more accurately the mean response of the MDOF system for the lower (8-storey) building frame compared to the taller (12-storey) is readily attributed to the less importance that higher-order dynamics have in the case of shorter structures. On the antipode, record to record variability for the various seismic intensity levels expressed through the standard deviation parameters of the fragility models exhibit significant lower percentage differences compared to the mean values. In fact, the equivalent SDOF proxy captures well peak inelastic response variability of the short (8-storey) MDOF frame as well as of the tall (12-storey) MDOF frame for intensity levels above  $\text{avgSa} = 0.02g$ .

## 6.5 Closure

In this Chapter, a procedure for the probabilistic seismic performance assessment of two adjacent RC building frames with equal floor heights subjected to pounding was presented. These predictions were compared with probabilistic predictions derived under the assumption that the two RC frames vibrate independently and with predictions based on equivalent, computationally efficient SDOF models. It was found that:

- Probabilistic seismic performance assessments of adjacent structures with insufficient separation can present a powerful tool for accurate probabilistic predictions especially suitable for structures of high value.
- Pounding restricts the maximum IDR for the 8SWDCH building and the lower 8 floors of the 12RFDCH building.
- Pounding increases the maximum IDR for the upper 4 floors of the 12RFDCH building. This is consistent with the whiplash phenomenon observed during pounding between building with unequal number of floors.
- Fragility models derived for the adopted limit states indicate that pounding has mostly a detrimental impact rather than a beneficial one.
- Comparisons between the probabilistic seismic performance assessments based on 2D frames and the equivalent SDOF models, indicate that predictions based on the SDOF models significantly underestimate peak inelastic demands in the mean sense but capture accurately record-to-record variability expressed through the standard deviation of fitted log-normal distributions to IDA curves.
- Equivalent SDOF model corresponding to the shorter 2D frame provides more accurate probabilistic seismic performance predictions than the equivalent SDOF model of the taller 2D frame.

# Chapter 7

## Conclusions

### 7.1 Summary and Main Contributions

This thesis has focused on the quantification of slab-to-slab interaction/pounding to inelastic demands of new (i.e. code-compliant) RC building structures under increasing seismic intensity. The main research contributions of this thesis are:

- *Contribution 1:* Detailed inelastic lumped plasticity three-dimensional FE models corresponding to real-life case-study structures with unequal number of floors are studied and ductility demands of horizontal and vertical members are examined separately and quantified for different floors, buildings and seismic intensity level.

Thus far, the influence of pounding to inelastic demands on 3D structures has been addressed via simplified models of academic interest. Therefore, in this thesis (§4. Influence of Bi-Directional Pounding on the Inelastic Demand Distribution of Three Adjacent Multi-Storey RC Buildings) the influence of seismic pounding on the inelastic seismic demands of three, code-compliant RC buildings that represent a realistic building block is examined. The considered case, involved a code-compliant RC structure that is constructed in contact with under-designed lower structures in a corner building-block configuration. Attention was focused on examining pounding influence to peak inelastic demands at critical sections of different structural members (beams, columns and shear walls) a) between buildings with unequal number of floors, b) between a code-compliant and adjacent under-design structures, c) under bi-directional seismic excitation capturing the influence of earthquake directivity in three-dimensions (i.e., accounting for torsional effects).

By examining average trends of the inelastic demands, it is found that pounding has significant detrimental impact for all buildings and structural members. These trends, do not necessarily align with results from case studies that considered buildings in a series configuration. This indicates that pounding between structures in real-life complex building blocks can be far more complex and should be accounted for, during the assessment/design phase where applicable.

- *Contribution 2:* A PBSA approach has been put forward, inspired from modern PBEE concepts, to quantify the influence of EISP to peak inelastic demands of adjacent structures probabilistically accounting for record-to-record variability. The proposed PBSA relies on undertaking IDA and, in this context, a novel IM is established, namely the geometric mean of the spectral acceleration at the fundamental natural period of the pounding/interacting structures, avgSa, which is shown to be much more efficient than the PGA commonly used in EISP studies and, therefore, expedites computationally PBSA of pounding structures.

Application of performance-based approaches accounting for record-to-record variability to the global response of adjacent interacting/colliding structures has been quite limited, if existent, to date. With the exception of Vega *et al* (2009), who applied full-fledged PBSA to study EISP for a bridge deck interacting with the two abutments modelled as a linear SDOF oscillator subject to double rigid-barrier pounding, all studies of EISP for adjacent inelastic structures consider a small number of GMs to represent the seismic action and quantify mean seismic demands (e.g., Jankowski 2008, Efraimiadou *et al.* 2013, Abdel Raheem 2014, Favvata 2017). This gap in the literature has been herein attributed partly to the high computational cost of conducting IDA in inelastic models accounting for pounding and partly due to the lack of an efficient IM applicable to pounding/interacting structures that can reduce peak inelastic seismic demand variability. In this regard, the PBSA approach presented in Chapter 5 along with the novel IM proposed, avgSa, effectively addresses this gap in the literature facilitating rendering the use of probabilistic PBEE tools practically applicable to the study of EISP.

To this end, it has been numerically shown in Chapter 5 that avgSa is a much more efficient IM than PGA which has been exclusively used in all EISP studies found in the literature. Specifically, it has been found that avg Sa reduces significantly the spread of IDA curves compared to PGA in a series of inelastic models comprising pounding inelastic SDOF structures used as proxies to 5 different RC multi-storey frame structures subject to a suite of 72 GMs. The reduction of IDA curves spread has been examined at different limit states and quantified in terms of standard deviation of log-normal distributions fitted to the IDA curves data following standard PBEE approaches. This reduction is attributed to the fact that avgSa brings in relevant damage potential information from the interacting structures (i.e.,  $S_a(T_1)$  of each structure) as opposed to PGA which is non-structure specific IM.

- *Contribution 3:* Derivation of probabilistic models in terms of fragility curves of adjacent/pounding structures represented by inelastic SDOF oscillators using the herein proposed PBSA approach. These fragility models can be readily coupled with suitably selected decision variables and seismic hazard curves to provide full-fledged seismic risk analysis accounting for EISP. Moreover, sensitivity study that quantifies the influence of gap size, pounding stiffness, and energy dissipation during collision on the shape of the fragility curves has also been conducted. This is the first of its kind numerical study to assess EISP parameters in a statistical/probabilistic context accounting for record-to-record variability as captured by the fragility curves pinned to different limit states.

Chapter 5 considered five RC code-compliant inelastic building frames in order to assess the influence of the separation distance (gap), the impact element stiffness and the energy dissipation on their seismic response within the context of PBSA. The five inelastic building frames were replaced by equivalent proxy non-linear SDOF systems and their seismic performance was assessed for the various considered parametric combinations by means of IDA using a suite of 72 GMs.

It was found that both the gap (up to 25% of the code compliant separation distance) and the impact element stiffness have a significant impact on the shape of the fragility curves mainly for the light damage limit state (low-to-moderate seismic intensity). Although counter-intuitive, this is due to the increased number of interactions at low seismic intensity levels since at higher intensities the two systems oscillate about new equilibrium points that significantly reduces or prevents pounding. It is also noted that these results are not in agreement with past sensitivity studies that are based on results from RHA typically based on a few recorded accelerograms. These studies reported that the influence of the impact element stiffness has an insignificant impact on the structural response.

Further, it is shown that at low-to-moderate seismic intensity levels, the energy dissipation during collisions has an insignificant impact. The influence of energy dissipation increases at higher seismic intensity levels. However, it remains marginal and therefore modelling pounding forces with less complex and computationally more efficient pounding models, that do not account for the energy dissipation during collisions (e.g. linear and nonlinear elastic impact elements) are recommended, especially for low-to-moderate seismic intensities. Also, pounding was found to have a detrimental impact on the more flexible oscillator for all the considered cases and in most cases, beneficial for the stiffer oscillator.

- *Contribution 4:* Comparison of EISP probabilistic model parameters derived by application of PBSA to adjacent multi-storey RC building frames subject to slab-to-slab pounding modelled as inelastic MDOF systems and as inelastic SDOF oscillators. This is the first study of its kind to quantify the influence of structural modelling complexity to the inelastic demand predictions of slab-to-slab colliding buildings and it did so by examining fragility curves as well as mean and standard deviation of IDA curves data accounting for record-to-record variability as captured by a suite of 25GMs

A review of the relevant literature has revealed that numerous slab-to-slab EISP studies (e.g., Chau and Wei 2001, Barbato and Tubaldi 2013, Moustafa and Mahmoud 2014) consider inelastic SDOF interacting oscillators used as proxies of planar multi-storey structures which are widely used to predict peak inelastic seismic demands in structures where no pounding occurs (e.g., Miranda and Ruiz-Garcia 2002, Katsanos et al . 2014). This is primarily done in studies aiming to quantify the effects of EISP to global seismic demands in order to reduce the computational cost of NRHA to MDOF systems. However, the issue of whether such simplified SDOF oscillators can indeed capture the influence EISP vis-à-vis more detailed inelastic MDOF systems has not been systematically addressed in the literature.,. This is an important issue since pounding introduces local additional external forces that directly affects nearby structural elements (e.g., at the specific floor where collision occurs). Therefore, modelling complexity (i.e., MDOF systems as opposed to equivalent inelastic SDOF oscillators) becomes more delicate in EISP studies than in structures with no pounding is not present.

To address this issue, Chapter 6 (§6. Probabilistic Seismic Performance Assessment of Adjacent RC Building Frames Interacting at Floor Levels) investigated the influence of floor-to-floor pounding on the probabilistic seismic performance of inelastic building frames with unequal number of floors and their equivalent inelastic SDOF systems. The influence of pounding is quantified against the benchmark case study where there are no pounding/interactions using PBSA that accounts for the record-to-record variability and is expressed in terms of fragility curves derived by considering 25 far-field GMs and using the efficient avgSa IM. Attention was focused on a light damage limit state (1% of  $\theta_{\max}$ ) that corresponds to low/moderate seismic intensity levels that are of practical importance. To this extend the scaling of the 25 GMs considered was limited to 1.0g (PGA).

Comparisons between fragility curves derived for the inelastic building frames and their equivalent inelastic SDOF systems, indicate that

predictions based on the SDOF models tend to underestimate peak inelastic demands in the mean sense but capture accurately record-to-record variability expressed through the standard deviation of fitted log-normal distributions to IDA curves.

### **7.2 Recommendations for Future Work**

The herein proposed PBSA framework can be extended and applied to several different EISP scenarios to quantify the influence of EISP in the statistics of peak inelastic demands of adjacent colliding structures and, ultimately, to the seismic risk and seismic vulnerability assessment of adjacent structures.

At first instance, further research work is warranted to quantify the influence of record-to-record variability as well as to seismic action directionality in interacting/colliding structures accounting for torsional effects/response. Such a consideration requires the extension and application of the PBSA framework developed in Chapter 5 of this thesis to three-dimensional FE models, as those considered in Chapter 4 of this thesis, using multicomponent IDA (Lagaros 2010). Moreover, additional research is required to apply the developed PBSA framework to study slab to column pounding in adjacent structures with unequal floor levels. This consideration requires adopting detailed inelastic FE models capturing local failure due to collisions (mostly shear failure) of columns as those considered in Favvata (2017).

Notably, the above extensions and future work necessitate considerable computational resources. However, through adopting the avgSa as the IM of choice in conducting IDA, it is hoped that satisfactory accuracy to peak inelastic response statistics of pounding adjacent structures can be obtained by considering a relatively small number of GMs. The latter consideration is yet another open research question requiring further investigation.

Another important path for future work is to study the effect of structure-soil-structure interaction (SSSI) to EISP of adjacent structures using the probabilistic PBSA approach. To date, this effect has only been studied within a deterministic context (e.g., Mahmoud et al. 2013 and Madani et al. 2015) which demonstrated that SSSI may be important for stiff adjacent structures founded on relatively soft soil.

More importantly, given that EISP influence depends significantly on the dynamic properties of the structures colliding, a further promising course for future research is the extension of the herein developed PBSA approach

to account for uncertainty to the structural properties following the lines of Vamvatsikos and Fragiadakis (2010).

In all the above cases, the developed PBSA framework and its extensions, supported by the efficient avgSa, can be used to study the effects of EISP to site-specific seismic risk assessment through integration with pertinent seismic hazard curves. It is thus envisioned that, with the advent of ever-more advanced computational resources, seismic risk analysis in congested urban environments will be accounting for EISP phenomena to improve the accuracy of seismic loss predictions. The tools developed in this thesis and their future extensions herein listed pave the way to fulfil this vision and to account for EISP which was found to be an important contributor to seismic loss in several reconnaissance reports in the aftermath of major seismic events in metropolitan areas but, which are not currently accounted for in seismic risk and vulnerability analyses.

---

## Bibliography

Abdel Raheem, S. (2009). Pounding mitigation and unseating prevention at expansion joints of isolated multi-span bridges. *Engineering Structures*, 31(10), pp.2345-2356.

Abdel Raheem, S. (2014). Mitigation measures for earthquake induced pounding effects on seismic performance of adjacent buildings. *Bulleting of Earthquake Engineering*, 12(4), pp.1705-1724.

Agarwal, V., Niedzwecki, J. and van de Lindt, J. (2007). Earthquake induced pounding in friction varying base isolated buildings. *Engineering Structures*, 29(11), pp.2825-2832.

Anagnostopoulos, S. (1988). Pounding of buildings in series during earthquakes. *Earthquake Engineering & Structural Dynamics*, 16(3), pp.443-456.

Anagnostopoulos, S. (2004). Equivalent viscous damping for modelling inelastic impacts in earthquake pounding problems. *Earthquake Engineering & Structural Dynamics*, 33(8), pp.897-902.

Anagnostopoulos, S. and Karamaneas, C. (2008). Use of collision shear walls to minimize seismic separation and to protect adjacent buildings from collapse due to earthquake-induced pounding. *Earthquake Engineering & Structural Dynamics*, 37(12), pp.1371-1388.

Anagnostopoulos, S. and Spiliopoulos, K. (1992). An investigation of earthquake induced pounding between adjacent buildings. *Earthquake Engineering & Structural Dynamics*, 21(4), pp.289-302.

Athanassiadou C., Penelis G., Kappos A. (1994). Seismic response of adjacent buildings with similar or different dynamic characteristics. *Earthquake Spectra*, 10, pp193-317

Baker, J. and Cornell, C. (2008). Vector-valued intensity measures for pulse-like near-fault ground motions. *Engineering Structures*, 30(4), pp.1048-1057.

Barbato, M. and Tubaldi, E. (2013). A probabilistic performance-based approach for mitigating the seismic pounding risk between adjacent buildings. *Earthquake Engineering & Structural Dynamics*, 42(8), pp.1203-1219.

## Bibliography

---

- Benjamin, J. and Cornell, C. (1970). Probability, statistics, and decision for civil engineers. New York [u.a.]: McGraw-Hill.
- Bharti, S., Dumne, S. and Shrimali, M. (2010). Seismic response analysis of adjacent buildings connected with MR dampers. *Engineering Structures*, 32(8), pp.2122-2133.
- Caterino, N., Cosenza, E and Azmoodeh, B. (2013). Approximate methods to evaluate storey stiffness and interstorey drift of RC buildings in seismic area. *Structural Engineering and Mechanics*, 46(2), pp.245-267.
- Celarec, D. and Dolsek, M. (2013). The impact of modelling uncertainties on the seismic performance assessment of reinforced frame buildings. *Engineering Structures*, 52, pp.340-354.
- Celik, O.C. & Ellingwood, B.R. (2010). Seismic fragilities for non-ductile reinforced concrete frames – role of aleatoric and epistemic uncertainties. *Structural Safety*; 32, 1–12.
- CEN (2004a), European Standard EN 1998-1:2004 Eurocode 8: Design of structures for earthquake resistance, Part 1: General rules, seismic actions and rules for buildings”, Comité Européen de Normalisation, Brussels. Design (Vol. 3). Brussels, Belgium: European Committee for Standardization.
- CEN (2004b), European Standard EN 1992-1-1:2004 Eurocode 2: Design of concrete structures, Part 1-1: General rules and rules for buildings, Comité Européen de Normalisation, Brussels.
- CEN. Eurocode 8 (2004): Design of Structures for Earthquake Resistance - Part 1: General Rules, Seismic Actions and Rules for Buildings, EN 1998-1: 2004, Comité Européen de Normalisation, Brussels.
- Chase, J., Boyer, F., Rodgers, G., Labrosse, G. and MacRae, G. (2014). Probabilistic risk analysis of structural impact in seismic events for linear and nonlinear systems. *Earthquake Engineering & structural Dynamics*, 43(10), pp.1565-1580.
- Chau, K. and Wei, X. (2001). Pounding of structures modelled as non-linear impacts of two oscillators. *Earthquake Engineering and Structural Dynamics*, 30(5), pp.633-651.
- Chopra, A.K. (2001), “Theory and Applications to Earthquake Engineering”, second ed., *Dynamics of Structures*, Prentice-Hall, New Jersey.

- Chopra, A.K. and Chintanapakdee, C. (2004), "Inelastic deformation ratios for design and evaluation of structures: Single-degree-of-freedom bilinear systems", *Journal of Structural Engineering*, 130(9), 1309-1319.
- Cole, G., Dhakal, R. and Turner, F. (2011). Building pounding damage observed in the 2011 Christchurch earthquake. *Earthquake Engineering & Structural Dynamics*, 41(5), pp.893-913.
- Cordova PP, Deierlein GG, Mehanny SS, Cornell CA. Development of a two-parameter seismic intensity measure and probabilistic assessment procedure. Proceedings of the 2nd US–Japan Workshop on Performance-based Earthquake Engineering Methodology for RC Building Structures, Sapporo, Hokkaido, 2000.
- Crozet, V., Politopoulos, I., Yang, M., Martinez, J. and Erlicher, S. (2017). Sensitivity analysis of pounding between adjacent structures. *Earthquake Engineering and Structural Dynamics*, 47(1), pp.219-235.
- Davis, R. (1992). Pounding of buildings modelled by an impact oscillator. *Earthquake Engineering & Structural Dynamics*, 21(3), pp.253-274.
- Deierlein, G. G., Liel, A. B., Haselton, C. B., & Kircher, C. A. (2007). Assessing Building System Collapse Performance and Associated Requirements for Seismic Design, *In:SEAOC convetion proceedings*, 1–14.
- DesRoches R., Muthukumar S., (2002). Effect of pounding and restrainers on seismic response of multiple-frame bridges. *Journal of Structural Engineering* (ASCE), 127, pp.860-869
- Dimitrakopoulos, E., Makris, N. and Kappos, A. (2009). Dimensional analysis of the earthquake-induced pounding between adjacent structures. *Earthquake Engineering & Structural Dynamics*, 38(7), pp.867-886.
- Efraimiadou, S. Hatzigeorgiou, G. D.. and Beskos , D.E. (2012), “Structural pounding between adjacent buildings: The effects of different structures configurations and multiple earthquakes”, *Proceedings of '15 WCEE*, Lisbon, September
- Efraimiadou, S., Hatzigeorgiou, G. and Beskos, D. (2013). Structural pounding between adjacent buildings subjected to strong ground motions. Part I: The effect of different structures arrangement. *Earthquake Engineering & Structural Dynamics*, 42(10), pp.1509-1528.
- Elnashai AS, Papanikolaou VK, Lee D. Zeus NL. A system for inelastic analysis of structures. Univ. of Illinois at Urbana-Champaign; 2002.
- Esteva, L., & Ruiz, S. (1989). Seismic failure rates of multi-story frames. *Journal of Structural Engineering*, 115(2), 268–84.

Fajfar, P. and Gaspersic P. (1996). The N2 method for the seismic damage analysis of RC buildings. *Earthquake Engineering and Structural Dynamics*, 25(1), pp.31-46.

Fardis, M. (1994). Analysis and design of reinforced concrete buildings according to Eurocodes 2 and 8, Configurations 3, 5 and 6. *Reports on Prenormative Research in Support of Eurocode 8*.

Favvata, M. (2017). Minimum required separation gap for adjacent RC frames with potential inter-storey seismic pounding. *Engineering Structures*, 152, pp.643-659.

Federal Emergency Management Agency (FEMA) 350. (2000). Recommended seismic design criteria for new steel moment-frame buildings.

Federal Emergency Management Agency (FEMA). (2009). Effects of strength and stiffness degradation on seismic response. *FEMA-P440A*, Washington D.C.

Filiatrault, A., Wagner, P. and Cherry, S. (1995). Analytical prediction of experimental building pounding. *Earthquake Engineering & Structural Dynamics*, 24(8), pp.1131-1154.

Fiore, A. and Monaco, P. (2010). Earthquake-induced pounding between the main buildings of the “Quinto Orazio Flaco” school. *Earthquake and Structures*, 1(4), pp.371-390.

Ge, P. and Zhou, Y. (2018). Investigation of efficiency of vector-valued intensity measures for displacement-sensitive tall buildings. *Soil Dynamics and Earthquake Engineering*. (in Press)

Giaralis A and Spanos PD. (2009). Wavelets based response spectrum compatible synthesis of accelerograms- Eurocode application (EC8). *Soil Dynamics and Earthquake Engineering*, **29**: 219-235.

Giaralis A and Spanos PD. (2011). A response spectrum based stochastic approach to estimate the peak response of structures subject to seismic pounding. *11<sup>th</sup> International Conference on Applications of Statistics and Probability in Civil Engineering*, Switzerland, August.

Goldsmith W. (1960). *The Theory and Physical Behaviour of Colliding Solids*. 1<sup>st</sup> edn, Edward Arnold: London, U.K.

Gulkan, et. al. (1974), "INELASTIC RESPONSES OF REINFORCED CONCRETE STRUCTURES TO EARTHQUAKE MOTIONS.", *Journal of the American Concrete Institute*, **71**(12), 604-610.

Hadi, M.N.S., Uz, M.E. (2011), "Seismic modal response histories of two-way asymmetric adjacent buildings with soil-structure interaction effects subject to Earthquake excitations", *Proceedings of the 13th International Conference on Civil, Structural and Environmental Engineering Computing*, Chania, September

Hahn, G. and Valenti, M. (1997). Correlation of Seismic Responses of Structures. *Journal of Structural Engineering*, **123**(4), pp.405-413.

Hall, J. and Beck, J. (1986). Structural damage in Mexico City. *Geophysical Research Letters*, **13**(6), pp.589-592.

Hao, H. and Chouw, N. (2007), "Design of bridges with modular expansion joints for prevention of earthquake-induced girder poundings", *Proceedings of the Australian Earthquake Engineering Society*, Wollongong, November

Hong, H., Wang, S. and Hong, P. (2003). Critical building separation distance in reducing risk under earthquake excitation. *Structural Safety* (**25**), pp.287-303.

Jankowski, R. (2005), Non-linear viscoelastic modeling of earthquake-induced structural pounding. *Earthquake Engineering and Structural Dynamics*, **34**(6), 595-611.

Jankowski, R. (2008). Earthquake-induced pounding between equal height buildings with substantially different dynamic properties. *Engineering Structures*, **30**(10), pp.2818-2829.

Jankowski, R. (2009), Experimental study on earthquake-induced pounding between structural elements made of different building materials. *Earthquake Engineering and Structural Dynamics*, **39**:343-354

Jankowski, R. (2012). Non-linear FEM analysis of pounding-involved response of buildings under non-uniform earthquake excitation. *Engineering Structures*, **37**, pp.99-105.

Jankowski, R., Wilde and K., Fujino, Y. (2000), "Reduction of pounding effects in elevated bridges during earthquakes", *Earthquake Engineering and Structural Dynamics*, **29**(2), 195-212.

## Bibliography

---

- Jankowski, R., Wilde, K. and Fujino, Y. (1998), "Pounding of superstructure segments in isolated elevated bridge during earthquakes", *Earthquake Engineering and Structural Dynamics*, vol. **27**(5), 487-502.
- Jeng, V. and Tzeng, W. (2000). Assessment of seismic pounding hazard for Taipei City. *Engineering Structures*, **22**(5), pp.459-471.
- Jeng, V. and Tzeng, W.L. (2010), "Pounding-involved response of isolated and non-isolated buildings under earthquake excitation", *Earthquake and Structures*, **1**(3), 231-252.
- Jeong, S.H. Mwafy, M. and Elnashai, A. (2012), "Probabilistic seismic performance assessment of code-compliant multi-story RC buildings", *Engineering Structures*, **34**, 527-537.
- Jing, H. and Young, M. (1991). Impact interactions between two vibration systems under random excitation. *Earthquake Engineering and Structural Dynamics*, **20**(7), pp.667-681.
- Karayannis, C. and Favvata, M. (2004). Earthquake-induced interaction between adjacent reinforced concrete structures with non-equal heights. *Earthquake Engineering & Structural Dynamics*, **34**(1), pp.1-20.
- Kasai, K. and Maison, B. (1997). Building pounding damage during the 1989 Loma Prieta earthquake. *Engineering Structures*, **19**(3), pp.195-207.
- Kasai, K., Jagiasi, A. and Jeng V. (1996). Inelastic vibration phase theory for seismic pounding mitigation. *Journal of Structural Engineering*, **122**(10), pp.1136-1146.
- Katsanos, E., Sextos, A. and Elnashai, A. (2014). Prediction of inelastic response periods of buildings based on intensity measures and analytical model parameters. *Engineering Structures*, **71**, pp.161-177.
- Khatiwada, S., Chow, N. and Butterworth, J. (2013). Evaluation of numerical pounding models with experimental validation. *Bulletin of the New Zealand society for earthquake engineering*. **46**(3).
- Kim, J., Ryu, J. and Chung, L. (2006). Seismic performance of structures connected by viscoelastic dampers. *Engineering Structures*, **28**(2), pp. 183-195.
- Kohrangi M, Bazzurro P, Vamvatsikos D, Spillatura A (2017). Conditional spectrum-based ground motion record selection using average spectral acceleration, *Earthquake Engineering and Structural Dynamics*, **46**, pp.667-1685.

Kohrangi M, Bazzurro P, Vamvatsikos D. (2016). Vector and scalar IMs in structural response estimation: part II–building demand assessment. *Earthquake Spectra* 32(3), pp.1525–1543.

Komodromos, P. (2008), "Simulation of the earthquake-induced pounding of seismically isolated buildings", *Computers and Structures*, **86**(7-8), pp.618-626.

Komodromos, P. et. al. (2007), "Response of seismically isolated buildings considering poundings", *Earthquake Engineering and Structural Dynamics*, **36**(12), pp.1605-1622.

Lagaros ND (2010), "Multicomponent incremental dynamic analysis considering variable incident angle", *Structure and Infrastructure Engineering*, **6**(1-2), pp. 77-94.

Liolios, A., Karabinis, A., Liolios, A., Radev, S., Georgiev, K. and Georgiev, I. (2015). A computational approach for the seismic damage response under multiple earthquake excitations of adjacent RC structures strengthened by ties. *Computers and Mathematics with Applications*, 70(11), pp.2742-2751.

Lopez-Garcia, D. and Soong, T. (2009). Assessment of the separation necessary to prevent seismic pounding between linear structural systems. *Probabilistic Engineering Mechanics*, 24(2), pp.210-223.

Luco, J. and De Barros, F. (1998). Optimal damping between two adjacent elastic structures. *Earthquake Engineering and Structural Dynamics*, 27(7), pp.649-659

Luco, N. and Cornell, C. (2007). Structure-specific Scalar Intensity Measures for Near-Source and Ordinary Earthquake Ground Motions. *Earthquake Spectra*, 23(2), pp.357-392.

Madani, B., Behnamfar, F. and Tajmir Riahi, H. (2015). Dynamic response of structures subjected to pounding and structure-soil-structure interaction. *Soil Dynamics and Earthquake Engineering*, 78, pp.46-60.

Mahmoud, S. and Jankowski, R. (2010). Pounding-involved response of isolated and non-isolated buildings under earthquake excitation. *Earthquakes and Structures*, 1(3), pp.231-252.

Mahmoud, S., Abd-Elhamed, A. and Jankowski, R. (2013). Earthquake-induced pounding between equal height multi-storey buildings considering soil-structure interaction. *Bulletin of Earthquake Engineering*, 11(4), pp.1021-1048.

## Bibliography

---

- Mahmoudi Moazam, A., Hasani, N. and Yazdani, M. (2018). Incremental dynamic analysis of small to medium spans plain concrete arch bridges. *Engineering Failure Analysis*, 91, pp.12-27.
- Maison, B. and Kasai, K. (1990). Analysis for type of structural pounding. *Journal of Structural Engineering (ASCE)*, 116(4), pp.957-977.
- Maison, B. and Kasai, K. (1992). Dynamics of pounding when two buildings collide. *Earthquake Engineering and Structural Dynamics*, 21(9), pp.771-786.
- Malhotra P. (1998). Dynamics of seismic pounding at expansion joints of concrete bridges. *Journal of Engineering Mechanics (ASCE)*, 124, pp.794-802.
- Mander, J.B., Dhakal, R.P., Mashiko, N. & Solberg, K.M. (2007). Incremental dynamic analysis applied to seismic financial risk assessment of bridges. *Engineering structures*, 29, pp.2662 - 2672.
- Maragakis, E. and Jennings, P. (1987). Analytical models for the rigid body motions of skew bridges. *Earthquake Engineering and Structural Dynamics*, 15(8), pp.923-944.
- McKenna F., Fenves G.L., Jeremic B. Scott M. H., (2000), "Open system for Earthquake Engineering", <http://opensees.berkeley.edu>.
- Mehanny, S. (2009). A broad-range power-law form scalar-based seismic intensity measure. *Engineering Structures*, 21(7), pp.1354-1368.
- Miranda, E. and Ruiz-Garcia, J. (2002), "Evaluation of approximate methods to estimate maximum inelastic displacement demands", *Earthquake Engineering and Structural Dynamics*, 31(3), pp.539-560.
- Moehle, J., Deierlein, G. A framework methodology for the performance-based earthquake engineering. 13<sup>th</sup> world conference on Earthquake Engineering (2004), Vancouver, Canada.
- Moustafa, A. and Mahmoud, S. (2014). Damage assessment of adjacent buildings under earthquake loads. *Engineering Structures*, 61, pp.153-165.
- Mwafy, A. and Elnashai, A. (2001). Static pushover versus dynamic collapse analysis of RC buildings. *Engineering Structures*, 23(5), pp.407-424.
- Ok, S., Song, J. and Park, K. (2008). Optimal design of hysteretic dampers connecting adjacent structures using multi-objective genetic algorithm and stochastic linearization method. *Engineering Structures*, 30(5), pp.1240-1249

Pantelides, C.P. and Ma, X. (1998), "Linear and nonlinear pounding of structural systems", *Computers and Structures*, 66(1), pp.79-92.

Papadrakakis, M. and Mouzakis, H. (1995). Earthquake simulator testing of pounding between adjacent buildings. *Earthquake Engineering & Structural Dynamics*, 24(6), pp.881-834.

Papadrakakis, M., Mouzakis, H., Plevris N. and Bitzarakis S. (1991). A Lagrange multiplier solution for pounding of buildings during earthquakes. *Earthquake Engineering and Structural Dynamics*, 20(11), pp.981-998.

Papanikolaou, V. and Elnashai, A. (2005). Evaluation of conventional and adaptive pushover analysis. I: methodology. *Journal of Earthquake Engineering*, 9(6), pp.923-941

Polycarpou, P. and Komodromos, P. (2010). Earthquake-induced poundings of a seismically isolated building with adjacent structures. *Engineering Structures*, 32, pp.1937-1951

Polycarpou, P and Komodromos, P. (2012), "A methodology for an efficient three-dimensional (3D) numerical simulation of earthquake-induced pounding of buildings", *Proceedings of 15<sup>th</sup> WCEE*, Lisbon, September

Polycarpou, P. and Komodromos, P. (2010), "On poundings of a seismically isolated building with adjacent structures during strong earthquakes", *Earthquake Engineering and Structural Dynamics*, 39(8), pp.933-940.

Polycarpou, P. and Komodromos, P. (2011), "Numerical investigation of potential mitigation measures for poundings of seismically isolated buildings", *Earthquake and Structures*, 2(1), pp.1-24. Porter, K.A. (2003). An overview of PEER's Performance-based earthquake engineering methodology, ICASP9, Civil Engineering Risk and Reliability Association (CERRA), San Francisco, CA, July 6-9.

Pratesi, F., Sorace, S. and Terenzi, G. (2014). Analysis and mitigation of seismic pounding of a slender R/C bell tower. *Engineering Structures*, 71, pp.23-34.

Rossetto, T. and Elnashai, A. (2005). A new analytical procedure for the derivation of displacement-based vulnerability curves for populations of RC structures. *Engineering Structures*, 27(3), pp.397-409.

Sehhati, R., Rodriguez-Marek, A., ElGawady, M., Cofer, W.F. (2011). Effects of near-fault ground motions and equivalent pulses on multi-story structures. *Engineering Structures*, 33, pp.767-779.

## Bibliography

---

- Shome, N., Cornell, C.A., Bazzurro, P., and Carballo, J.E. (1998). Earthquakes, records, and nonlinear responses. *Earthquake Spectra*, 14(3), pp.469–500.
- Skrekas, P., and Giaralis, A. (2013) , “Influence of near-fault effects and of incident angle of earthquake waves on the seismic inelastic demands of a typical Jack-Up platform.”, *The Jack-Up conference*, City University London.
- Skrekas, P., Giaralis, A. (2012). On the use of incremental dynamic analysis for evaluating the seismic performance of off-shore jack-up platforms. In: *Proceedings of the 6th International ASRANet Conference for Integrating Structural Analysis Risk and Reliability*, London, paper #35.
- Skrekas, P., Sextos, A. and Giaralis, A. (2014). Influence of bi-directional seismic pounding on the inelastic demand distribution of three adjacent multi-storey R/C buildings. *Earthquakes and Structures*, 6(1), pp.71-87
- Tothong, P, Cornell, C. A. (2007). Probabilistic seismic demand analysis using advanced ground motion intensity measures, attenuation relationships and near-fault effects. *PEER report*. University of California, Berkeley.
- Tubaldi, E., Barbato, M. and Dall’Asta, A. (2014). Performance-based seismic risk assessment for buildings equipped with linear and nonlinear viscous dampers. *Engineering Structures*, 78, pp.90-99.
- Tubaldi, E., Barbato, M. and Ghazizadeh, S. (2012). A probabilistic performance-based risk assessment approach for seismic pounding with efficient application to linear systems. *Structural Safety*, 36-37, pp.14-22
- Vamvatsikos, D. & Cornell, C.A. (2002). Incremental dynamic analysis. *Earthquake Engineering and Structural Dynamics*, 31, pp.491-514.
- Vamvatsikos, D. and Cornell, C. (2004). *Applied Incremental Analysis*. *Earthquake Spectra*, 20(2), pp.523-553.
- Vamvatsikos, D. and Fragiadakis, M. (2010). Incremental dynamic analysis for estimating seismic performance sensitivity and uncertainty *Earthquake Engineering and Structural Dynamics*, 39(2), pp.141-163
- Vega, J., Del Rey, I. and Alarcon, E. (2009). Pounding force assessment in performance-based design of bridges. *Earthquake Engineering & Structural Dynamics*, 38(13), pp.1525-1544.

- Westermo, B. (1989). The dynamics of interstructural connection to prevent pounding. *Earthquake Engineering & Structural Dynamics*, 18(5), pp.687-699.
- Xu, Y., He, Q. and Ko, J. (1999). Dynamic response of damper-connected adjacent buildings under earthquake excitation. *Engineering Structures*, 21(2), pp.135-148.
- Yahyaabadi, a., & Tehranizadeh, M. (2011). New scalar intensity measure for near-fault ground motions based on the optimal combination of spectral responses. *Scientia Iranica*, 18(6), pp.1149–1158.
- Yang, T.Y., Moehle, J., Stojadinovic, B. & Kiureghian, A. D., (2009). Seismic performance evaluation of facilities: Methodology and implementation”, *ASCE*
- Yu, Z., Liu, H., Guo, W. and Liu, Q. (2017). A general spectral difference method for calculating the minimum safety distance to avoid the pounding of adjacent structures during earthquakes. *Engineering Structures*, 150, pp.645-655.
- Zhou, Y., Ge, P. Han, J. and Zu, Z. (2017). Vector-valued intensity measures for incremental dynamic analysis. *Soil Dynamics and Earthquake Engineering*, 100, pp.380-388.

## Appendix A - Parameters of Inelastic Elements

Parameters of all inelastic elements of buildings used in Chapter 4.

Table A.1: Properties of inelastic elements for horizontal of building K.

Element	$M_y$	$M_u$	$\varphi_y$	$\varphi_u$	$\theta_y$	$\theta_p$	$\theta_u$	$\mu_\varphi$	Post Yield Slope	$EI_{eff}/EI$
D1-25/60	129	141	0.006326	0.161064	0.005181	0.041009	0.046190	25.46	2.86E-05	0.16
D2-25/60	129	141	0.006326	0.161064	0.010107	0.060289	0.070396	25.46	1.95E-05	0.16
D3-25/70	155	169	0.005280	0.149747	0.006486	0.047752	0.054239	28.36	3.08E-05	0.14
D4-45/50	139	151	0.007508	0.173683	0.011825	0.082087	0.093912	23.13	1.37E-05	0.14
D5-50/50	179	193	0.007588	0.135460	0.007014	0.038492	0.045505	17.85	3.57E-05	0.16
D6-50/50	179	193	0.007588	0.135460	0.006719	0.037697	0.044416	17.85	3.64E-05	0.16
D7-50/50	179	193	0.007588	0.135460	0.003984	0.030321	0.034305	17.85	4.53E-05	0.16
D8-50/50	179	193	0.007588	0.135460	0.005511	0.034438	0.039949	17.85	3.99E-05	0.16
D9-55/55	202	220	0.006718	0.143497	0.015213	0.070501	0.084714	21.36	2.55E-05	0.14
D10-45/50	139	151	0.007507	0.173683	0.015555	0.077355	0.092909	23.14	1.46E-05	0.14

Table A.2: Properties of inelastic elements for shear walls of building K.

Element	$M_y$	$M_u$	$\varphi_y$	$\varphi_u$	$\theta_y$	$\theta_p$	$\theta_u$	$\mu_\varphi$	Post Yield Slope	$EI_{eff}/EI$
P1	3781	4084.4	0.002184	0.015195	0.026208	0.027222	0.053430	6.96	1.114E-05	0.27
P2	3365	3777.6	0.002810	0.027373	0.033720	0.051392	0.085112	9.74	8.026E-06	0.19
P3	9868	10522	0.001990	0.018494	0.023880	0.035636	0.059516	9.29	1.834E-05	0.37
P4-vert	2527	2674.1	0.002612	0.022655	0.031344	0.041935	0.073279	8.67	3.498E-06	0.24
P4-hor	1670	1781.6	0.003119	0.024758	0.037428	0.045274	0.082702	7.94	2.454E-06	0.32
P5	17732	19082	0.001651	0.013349	0.019812	0.025259	0.045071	8.09	5.345E-05	0.42
P6-1	2205	2358.8	0.002142	0.056875	0.026775	0.113468	0.140243	26.55	1.357E-06	0.21
P6-2-hor	9117	9386.7	0.000942	0.021585	0.011304	0.042795	0.054099	22.91	6.308E-06	0.16
P6-2-vert	7635	8008.2	0.001110	0.025372	0.013320	0.050298	0.063618	22.86	7.414E-06	0.20

Table A.3 Properties of inelastic elements for columns of building K.

Element	$M_y$	$M_u$	$\varphi_y$	$\varphi_u$	$\theta_y$	$\theta_p$	$\theta_u$	$\mu_\varphi$	Post Yield Slope	$EI_{eff}/EI$
C60 N=1.368	<b>388</b>	413	0.007199	0.062413	0.010799	0.016137	0.026935	8.67	1.605E-04	0.29
C60 N=0.912	<b>333</b>	369	0.007740	0.074105	0.011610	0.019396	0.031006	9.57	1.856E-04	0.23
C60 N=0.0	<b>271</b>	305	0.008947	0.156750	0.006710	0.043197	0.049907	17.52	7.771E-05	0.16

## Appendix A

Table A.4 Properties of inelastic elements for beams of building K1 and K2.

Element	$M_y$	$M_u$	$\varphi_y$	$\varphi_u$	$\theta_y$	$\theta_p$	$\theta_u$	$\mu_\varphi$	Post Yield Slope	$EI_{eff}/EI$
D1-25/60	<b>130</b>	140	0.006215	0.166677	0.011964	0.070921	0.082885	26.82	1.52E-05	0.16
D2-25/60	<b>130</b>	140	0.006215	0.166677	0.003263	0.034978	0.038240	26.82	3.08E-05	0.16
D3-25/60	<b>130</b>	140	0.006215	0.166677	0.014683	0.082153	0.096836	26.82	1.31E-05	0.10
D4-25/60	<b>130</b>	140	0.006215	0.166677	0.012508	0.079265	0.091773	26.82	1.36E-05	0.15
D5-25/60	<b>130</b>	140	0.006215	0.166677	0.005438	0.047035	0.052473	26.82	2.29E-05	0.14
D6-25/60	<b>165</b>	182	0.006301	0.101232	0.014335	0.049091	0.063425	16.07	3.53E-05	0.17
D7-25/60	<b>130</b>	140	0.006215	0.166677	0.012508	0.076239	0.088746	26.82	1.42E-05	0.14
D8-25/60	<b>130</b>	140	0.006215	0.166677	0.014683	0.085225	0.099908	26.82	1.27E-05	0.14

Table A.5 Properties of inelastic elements for columns and shear walls of building K1 and K2.

Element	$M_y$	$M_u$	$\varphi_y$	$\varphi_u$	$\theta_y$	$\theta_p$	$\theta_u$	$\mu_\varphi$	Post Yield Slope	$EI_{eff}/EI$
C50X50 N0	<b>312</b>	349.1	0.009754	0.156710	0.007316	0.042949	0.050265	16.07	7.41E-05	0.21
C50X50 N08	<b>397</b>	445.3	0.008222	0.079106	0.006167	0.020717	0.026883	9.62	1.81E-04	0.32
C50X50 N12	<b>458</b>	457.7	0.008608	0.067631	0.006456	0.017250	0.023706	7.86	0.00E+00	0.35
C50X50 F10N08	<b>413</b>	454.7	0.009042	0.102025	0.006782	0.027175	0.033957	11.28	1.22E-04	0.30
C50X50 F10N12	<b>475</b>	528	0.008460	0.077472	0.006345	0.020169	0.026514	9.16	2.01E-04	0.37
KT1-2m	<b>2683</b>	2938	0.002040	0.022402	0.015300	0.027163	0.042463	10.98	6.01E-06	0.23
KT2-2m	<b>2346</b>	2675	0.002111	0.044257	0.015833	0.057029	0.072861	20.96	4.52E-06	0.19
KT3-3m	<b>2559</b>	3053	0.001474	0.027543	0.011055	0.035274	0.046329	18.69	1.07E-05	0.09

## Appendix B - Ground Motions Catalogue

Catalogue of recorded ground motion components used in Chapter 5.

**Table B.1:** Ground motions used in chapter 5 and related information (PEER-NCA).

ID	Event	Mag. $M_w$	$R_{rup}$ (Km)	$V_{s,30}$ (m/s)	Site Class <sup>a</sup>
1	Parkfield (1966.06.28)	6.19	63.34	493.50	C
2	Victoria, Mexico (1980.06.09)	6.33	14.37	471.53	C
3	Northwest California (1941.02.09)	6.60	91.22	219.31	D
4	Chalfant Valley (1986.7.21)	5.77	6.39	316.19	D
5	Livermore (1980.01.24)	5.80	24.95	403.37	C
6	Chalfant Valley (1986.7.21)	5.77	24.33	370.94	C
7	Whittier Narrows (1987.10.01)	5.99	20.79	245.06	D
8	Friuli, Italy (1976.05.06)	6.50	102.15	356.39	D
9	Sierra Madre (1991.06.28)	5.61	27.40	349.43	D
10	Friuli, Italy (1976.05.06)	6.50	33.40	249.28	D
11	Big Bear (1992.6.28)	6.46	8.30	430.36	C
12	Northwest China (1997.04.11)	6.10	24.06	240.09	D
13	Whittier Narrows (1987.10.01)	5.99	15.64	339.06	D
14	Hollister (1961.04.09)	5.60	19.56	198.77	D
15	Taiwan (1986.11.14)	7.30	56.01	309.41	D
16	Kern County (1952.07.21)	7.36	38.89	385.43	C
17	Erzican, Turkey (1992.03.13)	6.69	4.38	352.05	D
18	Coalinga (1983.7.22)	5.77	16.05	257.38	D
19	Northridge (1994.01.17)	6.69	26.45	336.20	D
20	Imperial Valley (1979.10.15)	6.53	31.92	242.05	D
21	Coyote Lake (1979.08.06)	5.74	33.83	281.61	D
22	Coalinga (1986.11.14)	6.36	29.48	246.07	D
23	Sierra Madre (1991.06.28)	5.61	13.17	375.16	C

Appendix B

24	Northridge (1994.01.17)	6.69	20.72	450.28	C
25	Loma Prieta (1989.10.18)	6.93	76.97	198.74	D
26	San Fernando (1971.02.09)	6.61	30.19	634.33	C
27	Mammoth Lakes (1980.5.27)	5.94	16.03	537.16	C
28	Imperial Valley (1979.10.15)	6.53	30.33	316.64	D
29	Friuli, Italy (1976.05.06)	6.50	80.41	352.05	D
30	Friuli, Italy (1976.05.06)	6.50	15.82	505.23	C
31	Borrego Mountain (1968.04.09)	6.63	45.66	213.44	D
32	San Fernando (1971.02.09)	6.61	28.99	452.86	C
33	Imperial Valley (1979.10.15)	6.53	22.03	242.05	D
34	Kern County (1952.07.21)	7.36	117.75	316.46	D
35	Chi-Chi Taiwan (1999.09.20)	6.20	20.91	473.64	C
36	Chi-Chi Taiwan (1999.09.20)	5.9	70.33	665.20	C
37	Duzce, Turkey (1999.11.12)	7.14	131.45	523.00	C
38	Kobe (1995.01.16)	6.90	11.34	256.00	D
39	Coalinga (1983.05.02)	6.36	24.02	274.73	D
40	Westmorland (1981.04.26)	5.90	6.50	193.37	D
41	Chi-Chi Taiwan (1999.09.20)	5.90	10.68	473.65	C
42	Chi-Chi Taiwan (1999.09.20)	6.20	25.30	258.89	D
43	Parkfield (1966.06.28)	6.19	17.64	408.93	C
44	Corinth, Greece (1981.02.24)	6.60	10.27	361.40	C
45	Managua, Nicaragua (1972.12.23)	6.24	4.06	288.77	D
46	Morgan Hill (1984.04.24)	6.19	24.49	239.69	D
47	Chalfant Valley (1986.7.21)	6.19	30.11	359.23	D
48	Chalfant Valley (1986.7.21)	5.65	51.98	467.62	C
49	Chi-Chi, Taiwan-2 (1999.09.20)	6.20	22.37	496.21	C
50	San Fernando (1971.02.09)	6.61	27.40	425.34	C
51	Tabas, Iran (1978.09.16)	7.35	120.81	377.56	C

## Appendix B

52	Tabas, Iran (1978.09.16)	7.35	91.14	302.64	D
53	Imperial Valley (1979.10.15)	6.53	10.45	231.23	D
54	Imperial Valley (1979.10.15)	6.53	24.60	205.78	D
55	Imperial Valley (1979.10.15)	6.53	36.92	212.00	D
56	Imperial Valley (1979.10.15)	6.53	15.25	193.67	D
57	Imperial Valley (1979.10.15)	6.53	50.10	336.49	D
58	Friuli, Italy (1976.05.06)	6.50	49.38	496.46	C
59	Morgan Hill (1984.04.24)	6.19	53.89	116.35	B
60	Morgan Hill (1984.04.24)	6.19	13.02	349.85	D
61	Coalinga (1983.07.22)	5.77	12.13	458.09	C
62	Trinidad (1980.11.08)	7.20	76.26	311.75	D
63	Hector Mine (1999.10.16)	7.13	11.66	726.00	C
64	Morgan Hill (1984.04.24)	6.19	26.43	215.54	D
65	Irpinia (1980.11.23)	6.90	52.94	612.78	C
66	Imperial Valley (1979.10.15)	6.53	24.61	362.38	C
67	Westmorland (1981.04.26)	5.90	15.41	208.71	D
68	Westmorland (1981.04.26)	5.90	7.83	191.14	D
69	San Fernando (1971.02.09)	6.61	89.72	813.48	B
70	San Fernando (1971.02.09)	6.61	61.64	394.18	C
71	Whittier Narrows (1987.10.01)	5.99	36.97	297.71	D
72	Imperial Valley (1940.05.19)	6.95	32.98	213.44	D

## Appendix C - IDA Curves

IDA curve plots produced in the parametric analysis of chapter 5 adopting the PGA (left panels of figures B.1-B34) and Geometric Mean AvgSa (right panels of figures B.1-B34) as IMs.

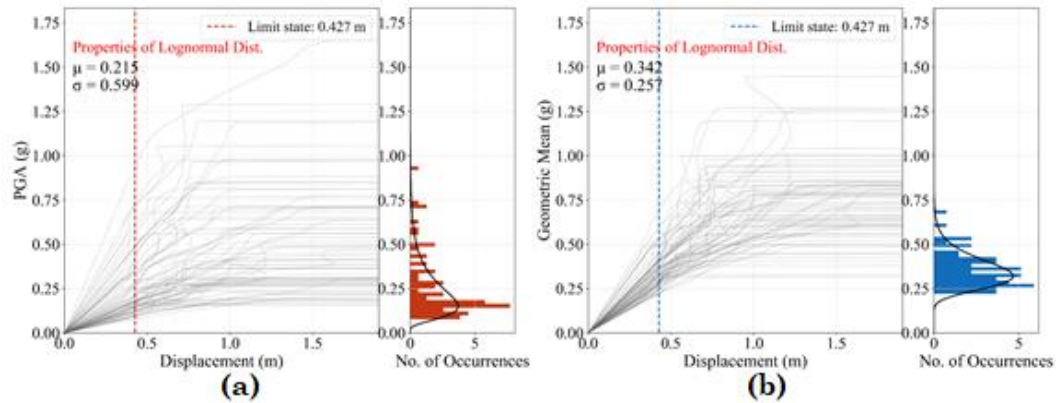


Figure C 1: Distribution of the seismic intensity levels at which the exceedance of the 0.427 (m) displacement limit state (light damage) occurs - Uncoupled response of the 12RFDCH SDOF system -  $\mu$  and  $\sigma$  are the mean and the standard deviation of the lognormal distribution that corresponds to the best fit a) IM = PGA and b) IM = *AvgSa*.

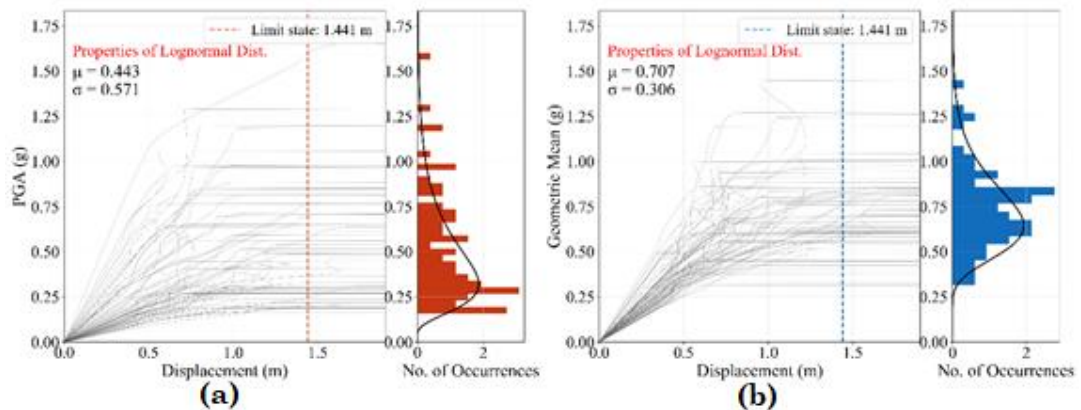


Figure C.2: Distribution of the seismic intensity levels at which the exceedance of the 1.441 (m) displacement limit state (severe damage) occurs - Uncoupled response of the 12RFDCH SDOF system -  $\mu$  and  $\sigma$  are the mean and the standard deviation of the lognormal distribution that correspond the best fit a) IM = PGA and b) IM = *AvgSa*.

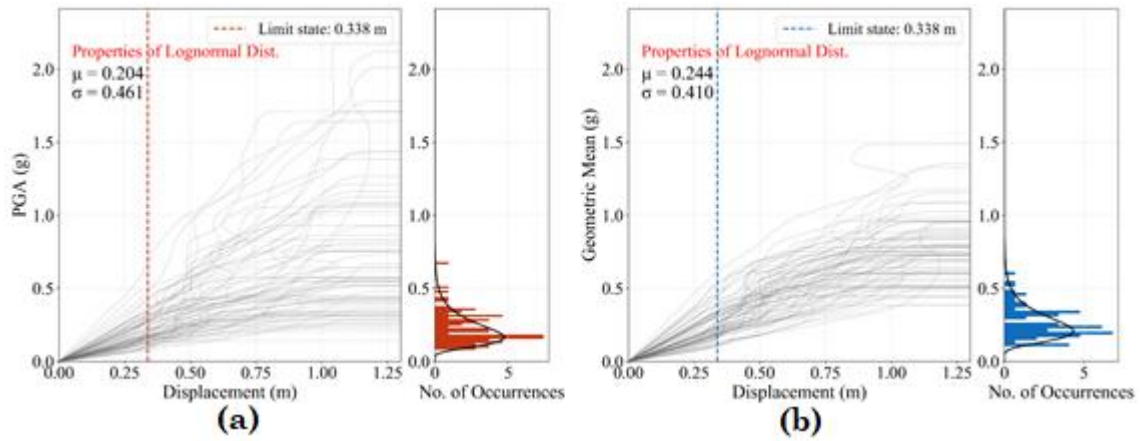


Figure C.3: Distribution of the seismic intensity levels at which the exceedance of the 0.338 (m) displacement limit state (light damage) occurs - Uncoupled response of the 8SWDCH SDOF system -  $\mu$  and  $\sigma$  are the mean and the standard deviation of the lognormal distribution that corresponds to the best fit a) IM = PGA and b) IM = *AvgSa*.

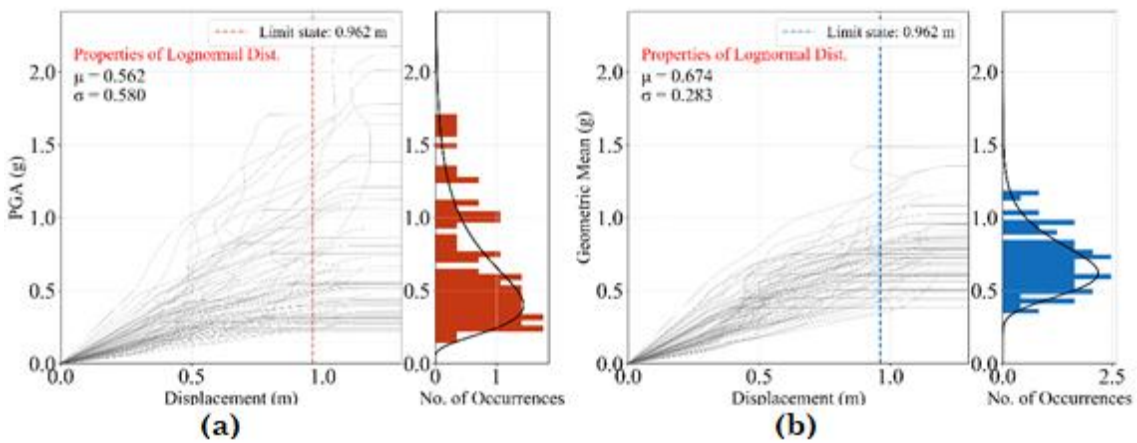


Figure C.4: Distribution of the seismic intensity levels at which the exceedance of the 0.962 (m) displacement limit state occurs - Uncoupled response of the 8SWDCH building -  $\mu$  and  $\sigma$  are the mean and the standard deviation of the lognormal distribution that corresponds to the best fit a) IM = PGA and b) IM = *AvgSa*.

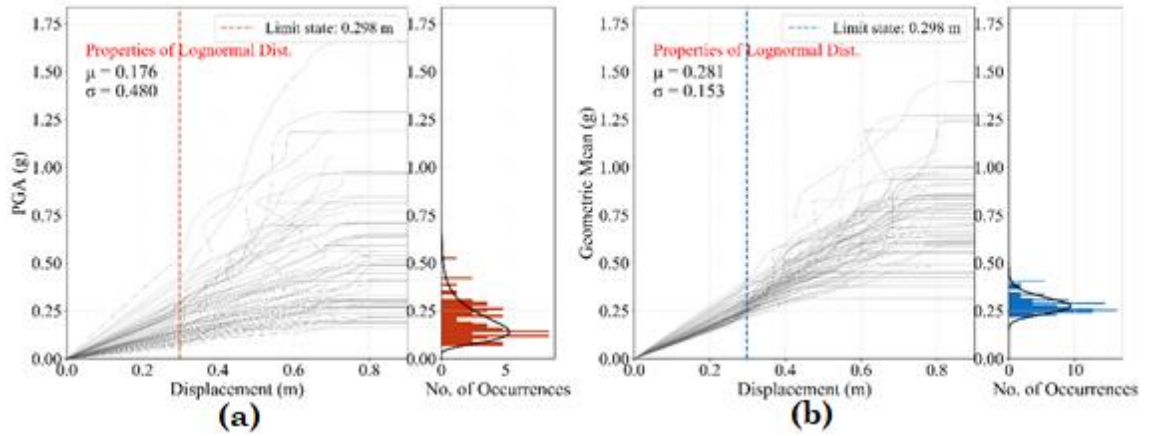


Figure C.5: Distribution of the seismic intensity levels at which the exceedance of the 0.298 (m) displacement limit state occurs - Uncoupled response of the 8WDCL building -  $\mu$  and  $\sigma$  are the mean and the standard deviation of the lognormal distribution that correspond to the best fit a) IM = PGA and b) IM =  $AvgSa$ .

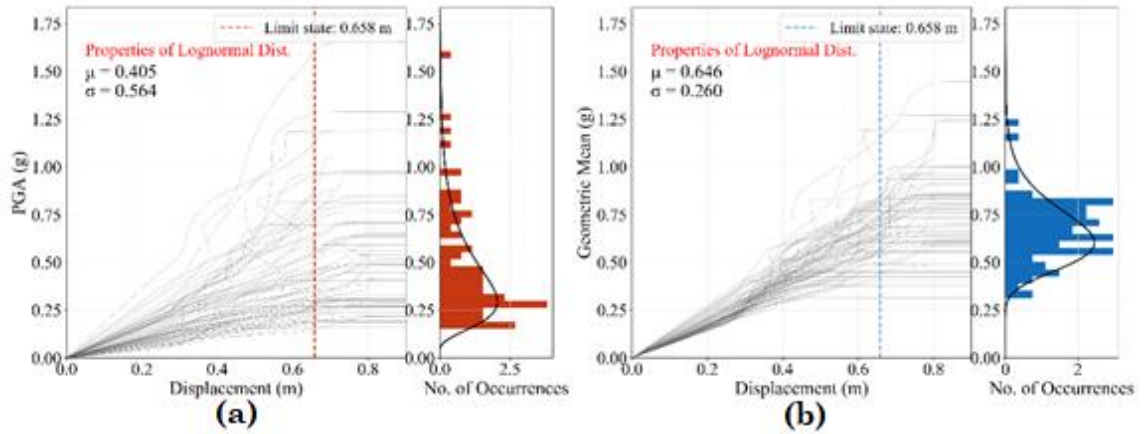


Figure C.6: Distribution of the seismic intensity levels at which the exceedance of the 0.658 (m) displacement limit state occurs - Uncoupled response of the 8WDCL building -  $\mu$  and  $\sigma$  are the mean and the standard deviation of the lognormal distribution that correspond to the best fit a) IM = PGA and b) IM =  $AvgSa$ .

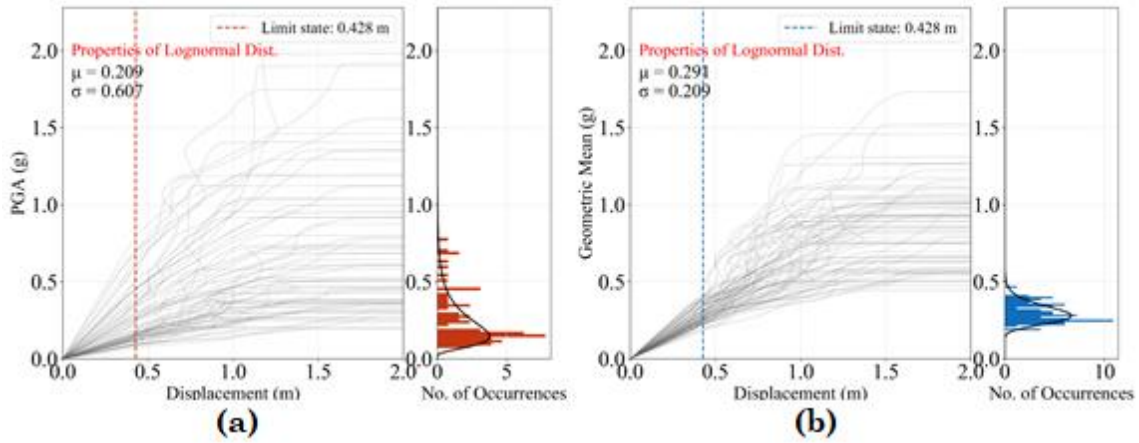


Figure C.7: Distribution of the seismic intensity levels at which the exceedance of the 0.428 (m) displacement limit state occurs - Uncoupled response of the 12RFDCL SDOF system -  $\mu$  and  $\sigma$  are the mean and the standard deviation of the lognormal distribution that corresponds to the best fit a) IM = PGA and b) IM = *AvgSa*.

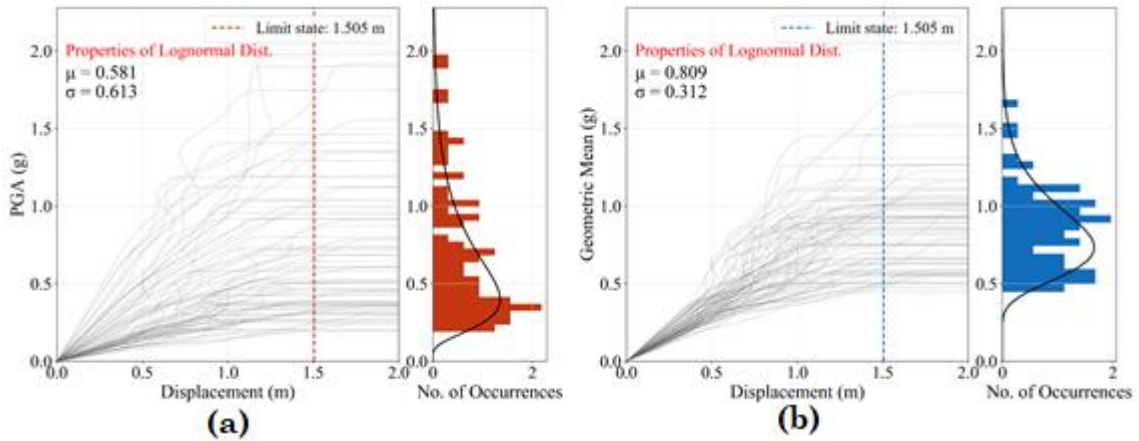


Figure C.8: Distribution of the seismic intensity levels at which the exceedance of the 1.505 (m) displacement limit state occurs - Uncoupled response of the 12RFDCL building -  $\mu$  and  $\sigma$  are the mean and the standard deviation of the lognormal distribution that corresponds to the best fit a) IM = PGA and b) IM = *AvgSa*.

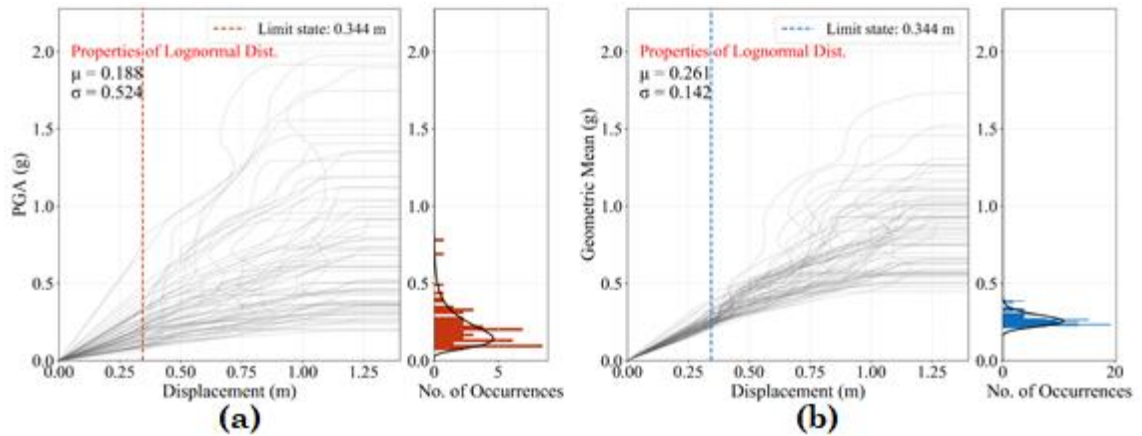


Figure C.9: Distribution of the seismic intensity levels per ground motion at which the exceedance of the 0.344 (m) displacement limit state occurs - Uncoupled response of the 8IFDCH building -  $\mu$  and  $\sigma$  correspond to the mean and the standard deviation of the lognormal distribution that represents the best fit a) IM = PGA and b) IM = *AvgSa*.

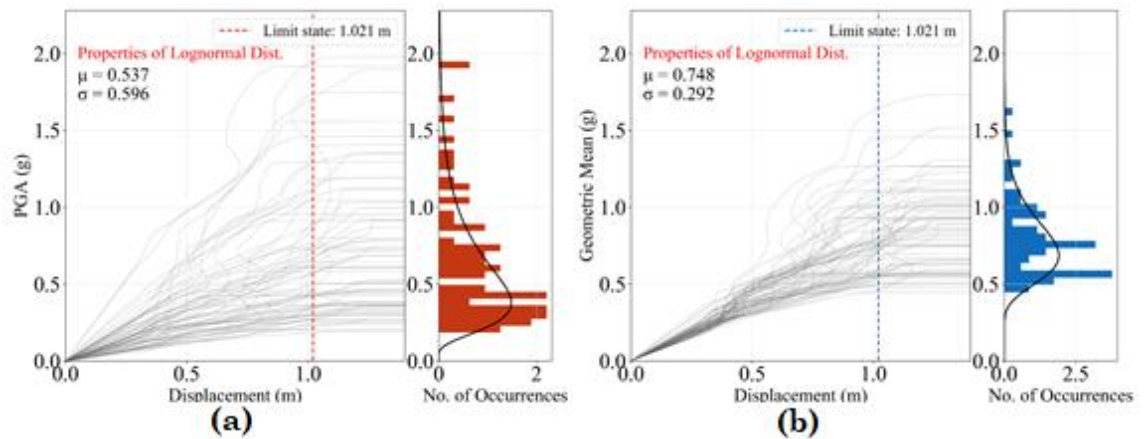


Figure C.10: Distribution of the seismic intensity levels at which the exceedance of the 1.021 (m) displacement limit state occurs - Uncoupled response of the 8IFDCH building -  $\mu$  and  $\sigma$  are the mean and the standard deviation of the lognormal distribution that corresponds to the best fit a) IM = PGA and b) IM = *AvgSa*.

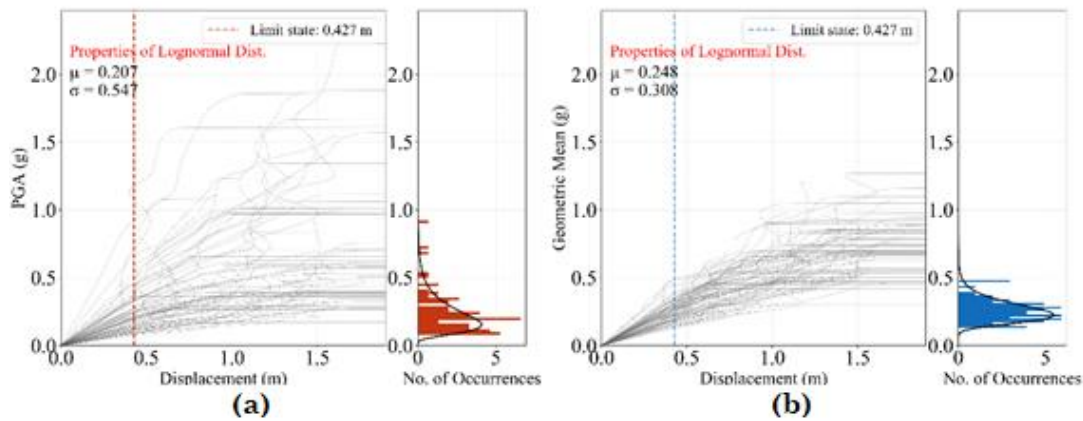


Figure C.11: Pounding between 12RFDCH and 8SWDCH SDOF systems - Distribution of the seismic intensity levels at which the exceedance of the 0.427 (m) displacement limit state occurs - Coupled response of the 12RFDCH building with gap = 0.00 (m) - Contact forces are modelled via the linear contact model with  $K_p = \text{High}$  -  $\mu$  and  $\sigma$  are the mean and the standard deviation of the lognormal distribution that corresponds to the best fit a) IM = PGA and b) IM = *AvgSa*.

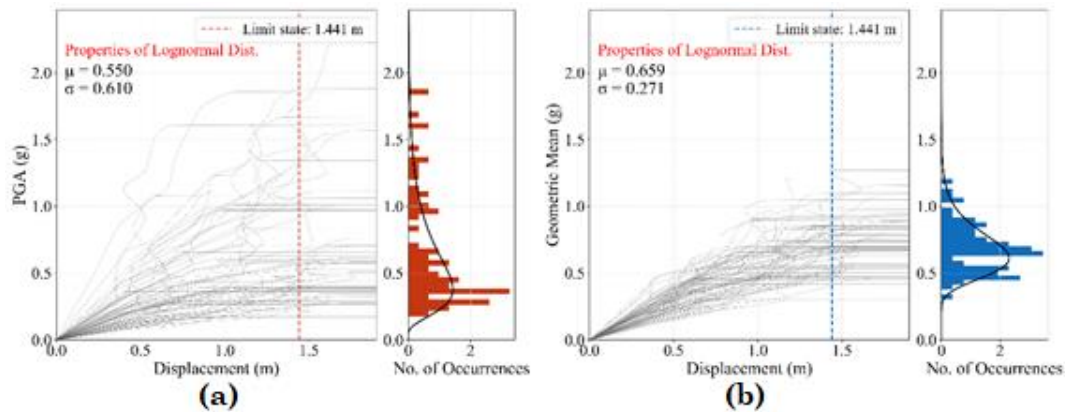


Figure C.12: Pounding between 12RFDCH and 8SWDCH SDOF systems - Distribution of the seismic intensity levels at which the exceedance of the 1.441 (m) displacement limit state occurs - Coupled response of the 12RFDCH building with gap = 0.00 (m) - Contact forces are modelled via the linear contact model with  $K_p = \text{High}$  -  $\mu$  and  $\sigma$  are the mean and the standard deviation of the lognormal distribution that corresponds to the best fit a) IM = PGA and b) IM = *AvgSa*.

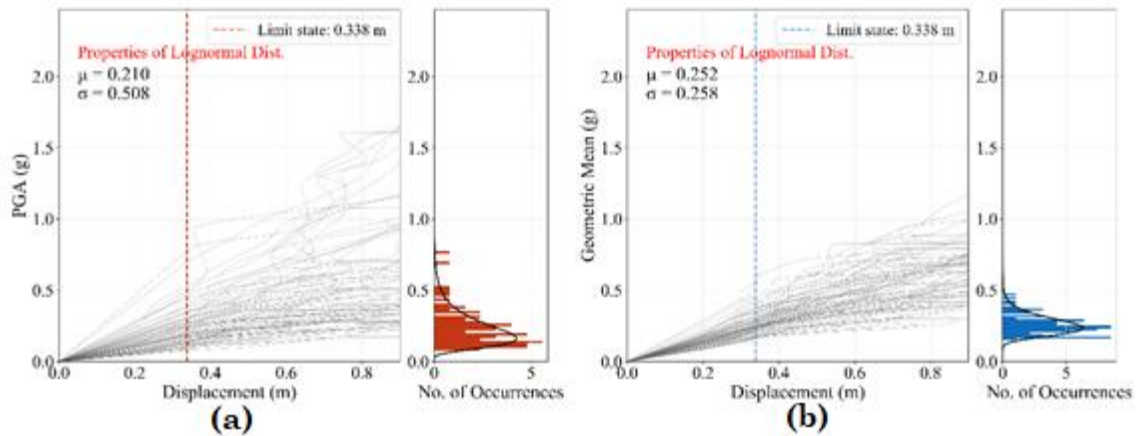


Figure C.13: Pounding between 12RFDCH and 8SWDCH SDOF systems - Distribution of the seismic intensity levels at which the exceedance of the 0.338 (m) displacement limit state occurs - Coupled response of the 8SWDCH building with gap = 0.00 (m) - Contact forces are modelled via the linear contact model with  $K_p = \text{High}$  -  $\mu$  and  $\sigma$  are the mean and the standard deviation of the lognormal distribution that corresponds to the best fit a) IM = PGA and b) IM = *AvgSa*.

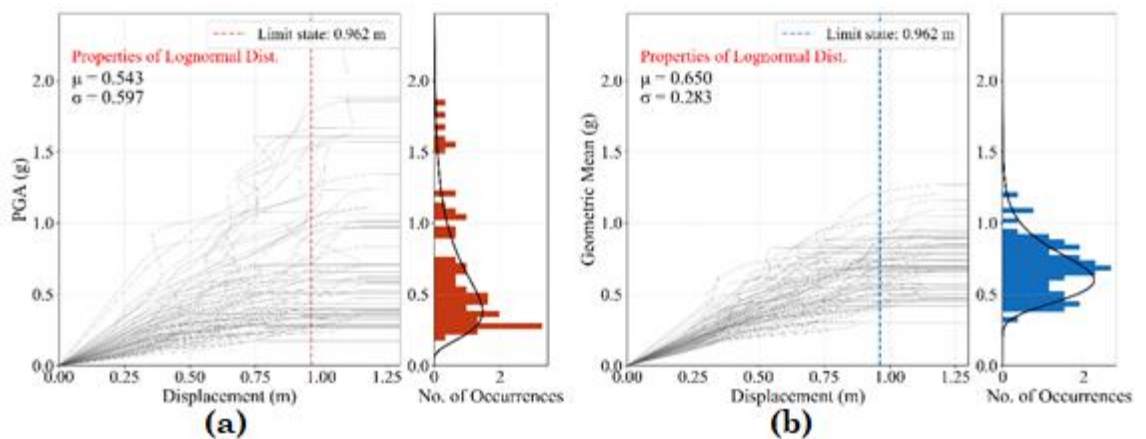


Figure C.14: Pounding between 12RFDCH and 8SWDCH SDOF systems - Distribution of the seismic intensity levels at which the exceedance of the 0.962 (m) displacement limit state occurs - Coupled response of the 8SWDCH building with gap = 0.00 (m) - Contact forces are modelled via the linear contact model with  $K_p = \text{High}$  -  $\mu$  and  $\sigma$  are the mean and the standard deviation of the lognormal distribution that corresponds to the best fit a) IM = PGA and b) IM = *AvgSa*.

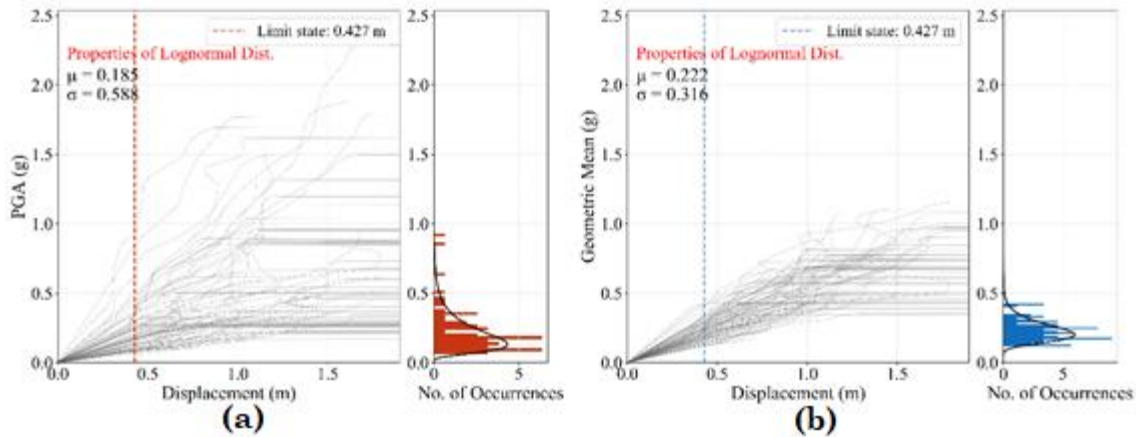


Figure C.15: Pounding between 12RFDCH and 8SWDCH SDOF systems - Distribution of the seismic intensity levels at which the exceedance of the 0.427 (m) displacement limit state occurs - Coupled response of the 12RFDCH building with gap = 0.00 (m) - Contact forces are modelled via the linear contact model with  $K_p = \text{Low}$  -  $\mu$  and  $\sigma$  are the mean and the standard deviation of the lognormal distribution that corresponds to the best fit a) IM = PGA and b) IM = *AvgSa*.

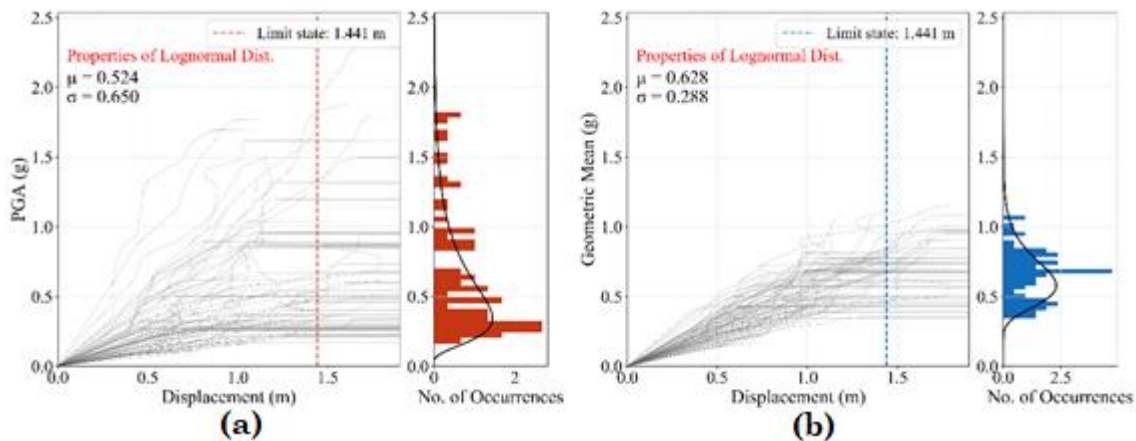


Figure C.16: Pounding between 12RFDCH and 8SWDCH SDOF systems - Distribution of the seismic intensity levels at which the exceedance of the 1.441 (m) displacement limit state occurs - Coupled response of the 12RFDCH building with gap = 0.00 (m) - Contact forces are modelled via the linear contact model with  $K_p = \text{Low}$  -  $\mu$  and  $\sigma$  are the mean and the standard deviation of the lognormal distribution that corresponds to the best fit a) IM = PGA and b) IM = *AvgSa*.

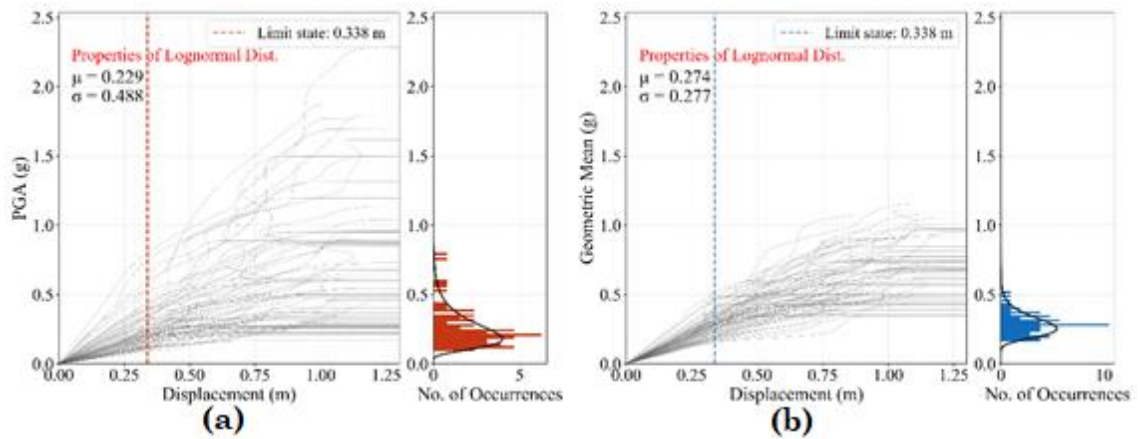


Figure C.17: Pounding between 12RFDCH and 8SWDCH SDOF systems - Distribution of the seismic intensity levels at which the exceedance of the 0.338 (m) displacement limit state occurs - Coupled response of the 8SWDCH building with gap = 0.00 (m) - Contact forces are modelled via the linear contact model with  $K_p = \text{Low}$  -  $\mu$  and  $\sigma$  are the mean and the standard deviation of the lognormal distribution that corresponds to the best fit a) IM = PGA and b) IM = *AvgSa*.

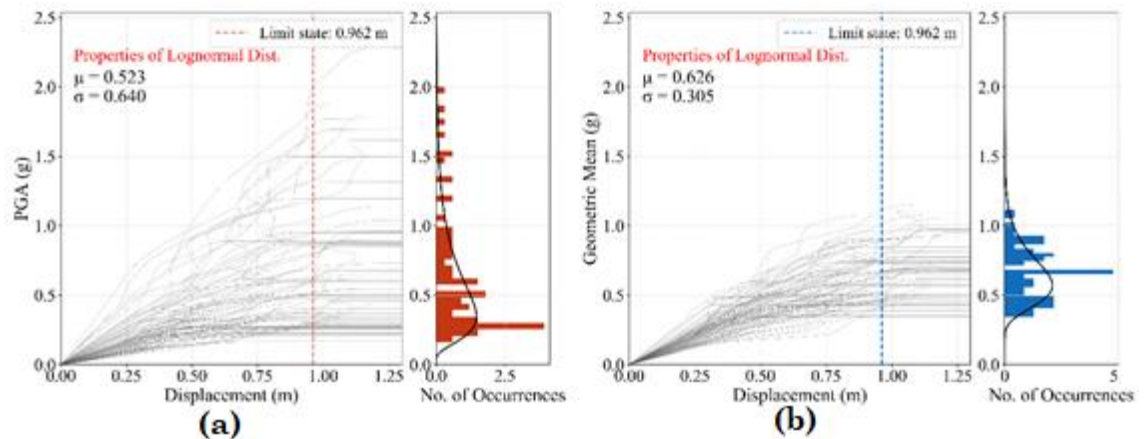


Figure C.18: Pounding between 12RFDCH and 8SWDCH SDOF systems - Distribution of the seismic intensity levels at which the exceedance of the 0.962 (m) displacement limit state occurs - Coupled response of the 8SWDCH building with gap = 0.00 (m) - Contact forces are modelled via the linear contact model with  $K_p = \text{Low}$  -  $\mu$  and  $\sigma$  are the mean and the standard deviation of the lognormal distribution that corresponds to the best fit a) IM = PGA and b) IM = *AvgSa*.

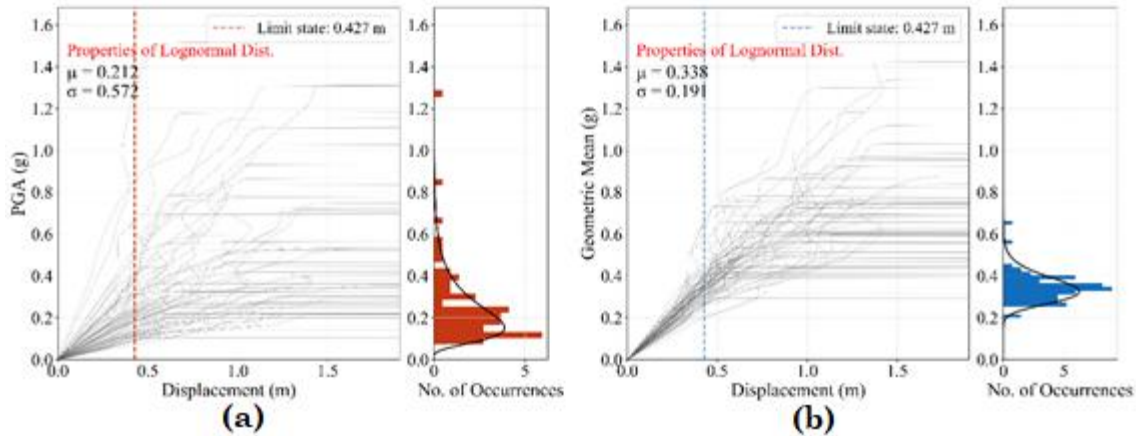


Figure C.19: Pounding between 12RFDCH and 8WDCL SDOF systems - Distribution of the seismic intensity levels at which the exceedance of the 0.427 (m) displacement limit state occurs - Coupled response of the 12RFDCH building with gap = 0.00 (m) - Contact forces are modelled via the linear contact model with  $K_p = \text{High}$  -  $\mu$  and  $\sigma$  are the mean and the standard deviation of the lognormal distribution that corresponds to the best fit a) IM = PGA and b) IM = *AvgSa*.

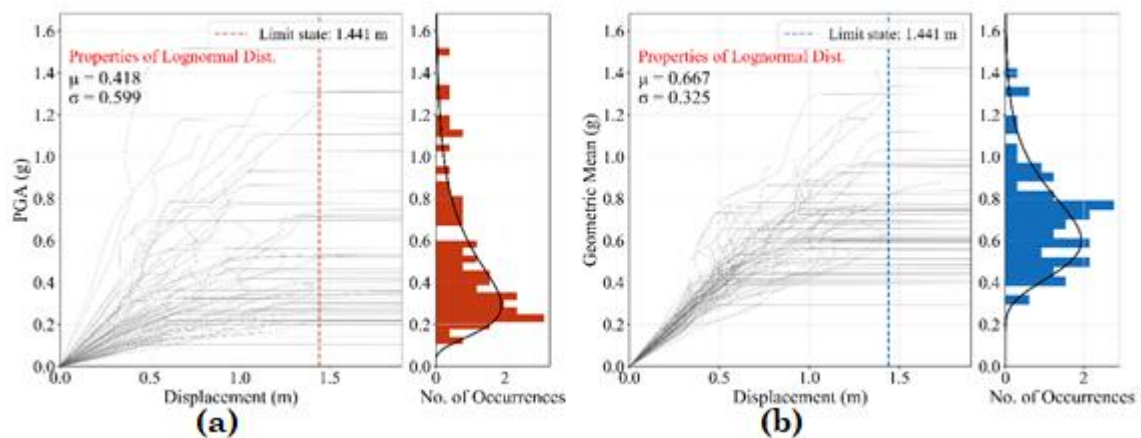


Figure C.20: Pounding between 12RFDCH and 8WDCL SDOF systems - Distribution of the seismic intensity levels at which the exceedance of the 1.441 (m) displacement limit state occurs - Coupled response of the 12RFDCH building with gap = 0.00 (m) - Contact forces are modelled via the linear contact model with  $K_p = \text{High}$  -  $\mu$  and  $\sigma$  are the mean and the standard deviation of the lognormal distribution that corresponds to the best fit a) IM = PGA and b) IM = *AvgSa*.

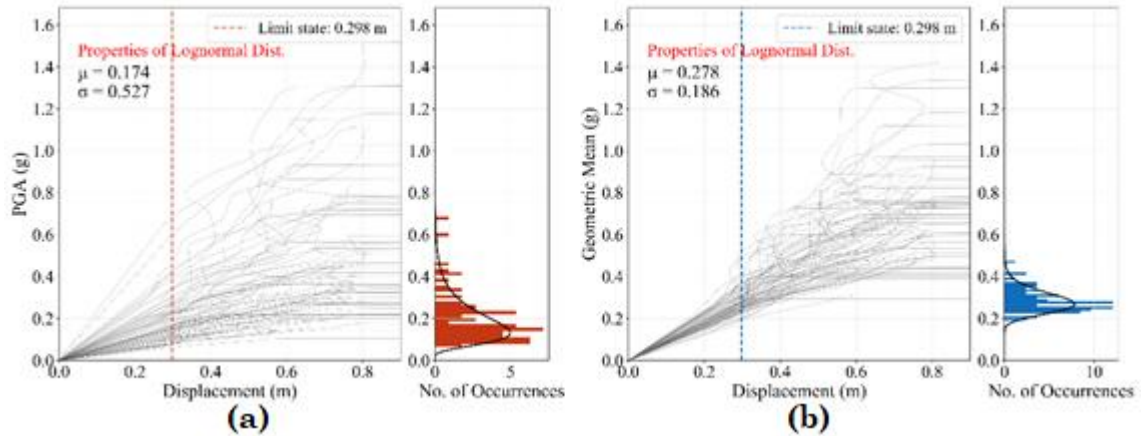


Figure C.21: Pounding between 12RFDCH and 8WDCL SDOF systems - Distribution of the seismic intensity levels at which the exceedance of the 0.298 (m) displacement limit state occurs - Coupled response of the 8WDCL building with gap = 0.00 (m) - Contact forces are modelled via the linear contact model with  $K_p = \text{High}$  -  $\mu$  and  $\sigma$  are the mean and the standard deviation of the lognormal distribution that corresponds to the best fit a) IM = PGA and b) IM = *AvgSa*.

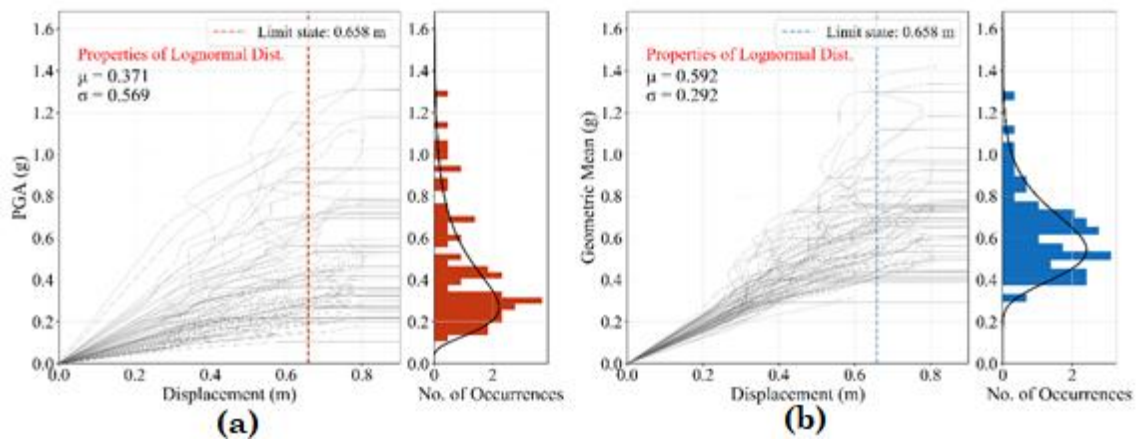


Figure C.22: Pounding between 12RFDCH and 8WDCL SDOF systems - Distribution of the seismic intensity levels at which the exceedance of the 0.658 (m) displacement limit state occurs - Coupled response of the 8WDCL building with gap = 0.00 (m) - Contact forces are modelled via the linear contact model with  $K_p = \text{High}$  -  $\mu$  and  $\sigma$  are the mean and the standard deviation of the lognormal distribution that corresponds to the best fit a) IM = PGA and b) IM = *AvgSa*.

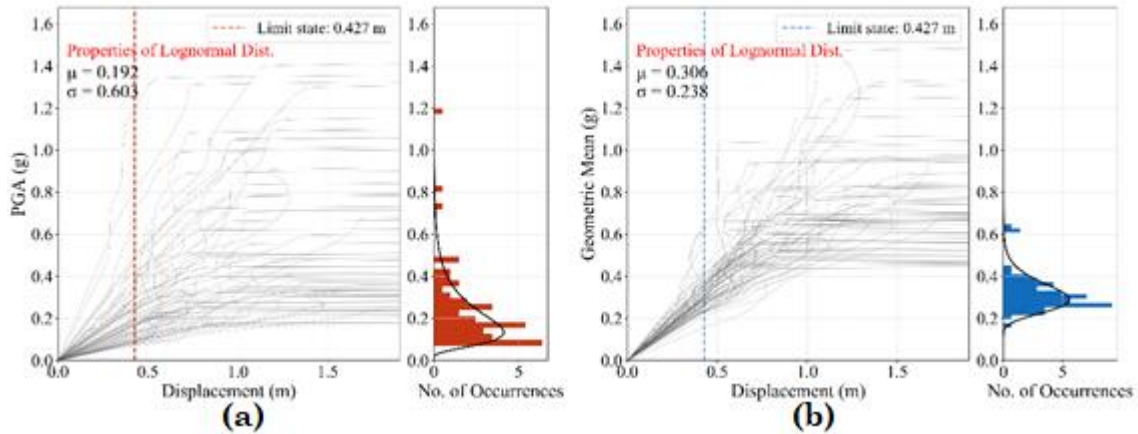


Figure C.23: Pounding between 12RFDCH and 8WDCL SDOF systems - Distribution of the seismic intensity levels at which the exceedance of the 0.427 (m) displacement limit state occurs - Coupled response of the 12RFDCH building with gap = 0.00 (m) - Contact forces are modelled via the linear contact model with  $K_p = \text{Low}$  -  $\mu$  and  $\sigma$  are the mean and the standard deviation of the lognormal distribution that corresponds to the best fit a) IM = PGA and b) IM = *AvgSa*.

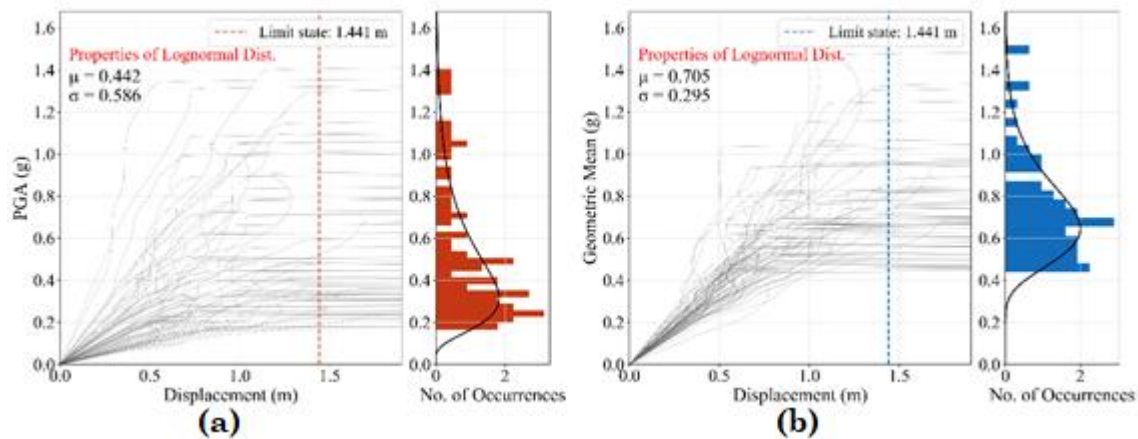


Figure C.24: Pounding between 12RFDCH and 8WDCL SDOF systems - Distribution of the seismic intensity levels at which the exceedance of the 1.441 (m) displacement limit state occurs - Coupled response of the 12RFDCH building with gap = 0.00 (m) - Contact forces are modelled via the linear contact model with  $K_p = \text{Low}$  -  $\mu$  and  $\sigma$  are the mean and the standard deviation of the lognormal distribution that corresponds to the best fit a) IM = PGA and b) IM = *AvgSa*.

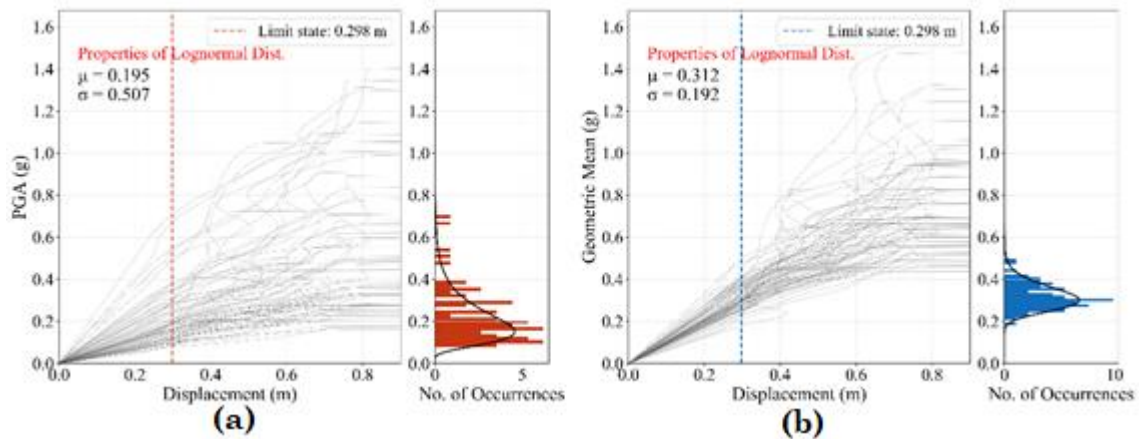


Figure C.25: Pounding between 12RFDCH and 8WDCL SDOF systems - Distribution of the seismic intensity levels at which the exceedance of the 0.298 (m) displacement limit state occurs - Coupled response of the 8WDCL building with gap = 0.00 (m) - Contact forces are modelled via the linear contact model with  $K_p = \text{Low}$  -  $\mu$  and  $\sigma$  are the mean and the standard deviation of the lognormal distribution that corresponds to the best fit a) IM = PGA and b) IM = *AvgSa*.

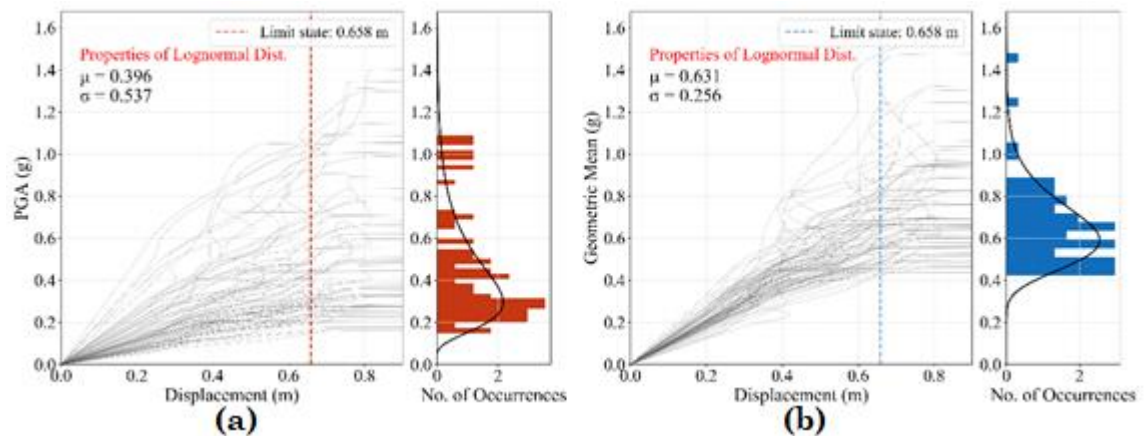


Figure C.26: Pounding between 12RFDCH and 8WDCL SDOF systems - Distribution of the seismic intensity levels at which the exceedance of the 0.658 (m) displacement limit state occurs - Coupled response of the 8WDCL building with gap = 0.00 (m) - Contact forces are modelled via the linear contact model with  $K_p = \text{Low}$  -  $\mu$  and  $\sigma$  are the mean and the standard deviation of the lognormal distribution that corresponds to the best fit a) IM = PGA and b) IM = *AvgSa*.

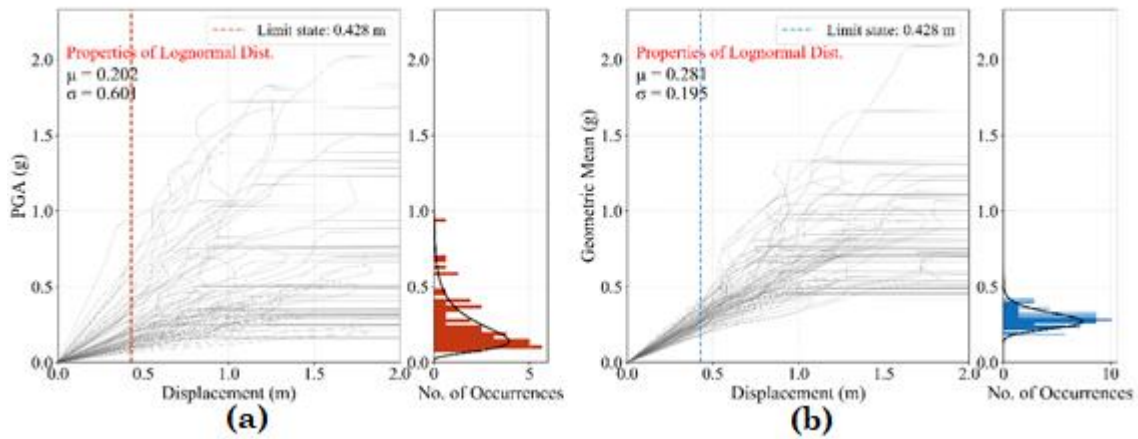


Figure C.27: Pounding between 12RFDCL and 8IFDCH SDOF systems - Distribution of the seismic intensity levels at which the exceedance of the 0.428 (m) displacement limit state occurs - Coupled response of the 12RFDCL building with gap = 0.00 (m) - Contact forces are modelled via the linear contact model with  $K_p = \text{High}$  -  $\mu$  and  $\sigma$  are the mean and the standard deviation of the lognormal distribution that corresponds to the best fit a) IM = PGA and b) IM = GM.

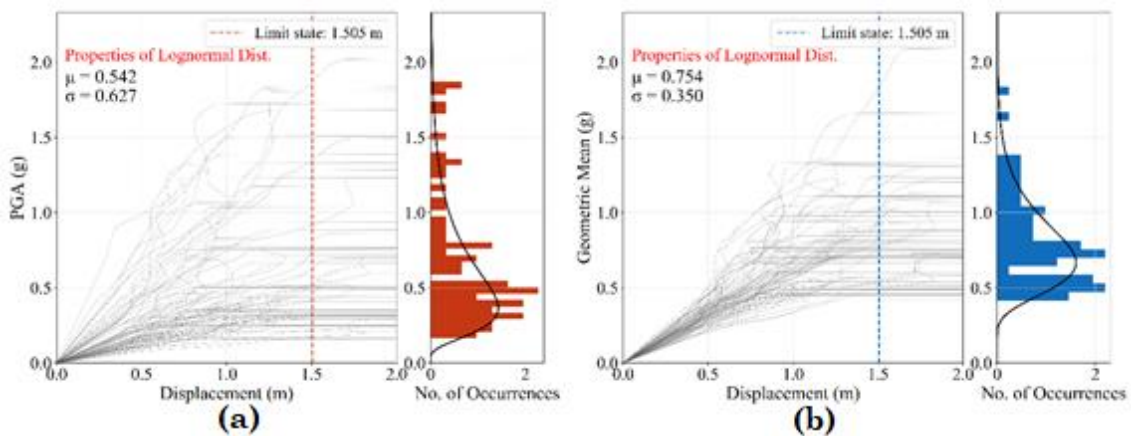


Figure C.28: Pounding between 12RFDCL and 8IFDCH SDOF systems - Distribution of the seismic intensity levels at which the exceedance of the 1.505 (m) displacement limit state occurs - Coupled response of the 12RFDCL building with gap = 0.00 (m) - Contact forces are modelled via the linear contact model with  $K_p = \text{High}$  -  $\mu$  and  $\sigma$  are the mean and the standard deviation of the lognormal distribution that corresponds to the best fit a) IM = PGA and b) IM = AvgSa.

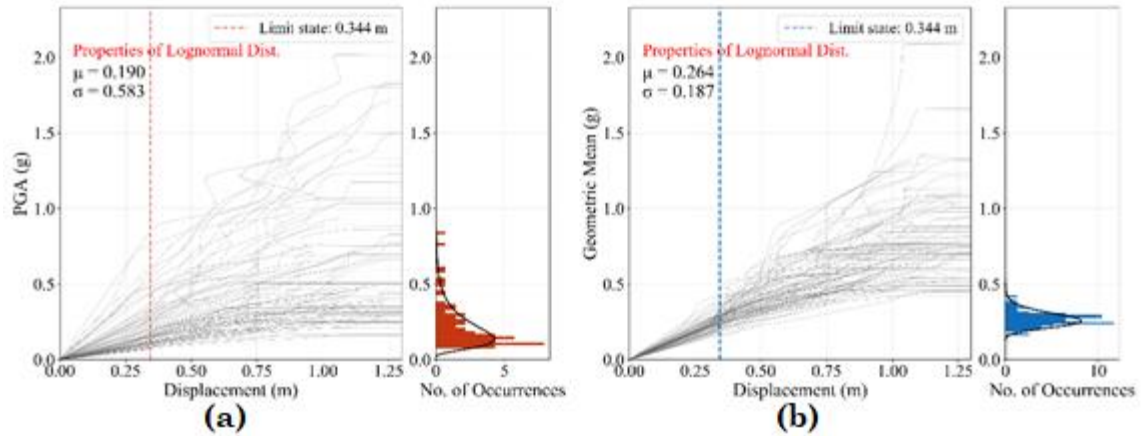


Figure C.29: Pounding between 12RFDCL and 8IFDCH SDOF systems - Distribution of the seismic intensity levels at which the exceedance of the 0.344 (m) displacement limit state occurs - Coupled response of the 8IFDCH building with gap = 0.00 (m) - Contact forces are modelled via the linear contact model with  $K_p = \text{High}$  -  $\mu$  and  $\sigma$  are the mean and the standard deviation of the lognormal distribution that corresponds to the best fit a) IM = PGA and b) IM = *AvgSa*.

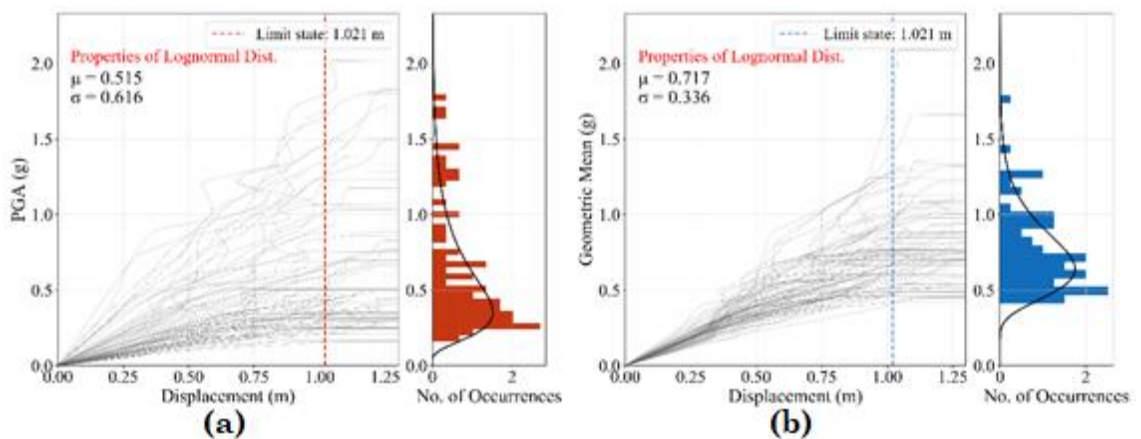


Figure C.30: Pounding between 12RFDCL and 8IFDCH SDOF systems - Distribution of the seismic intensity levels at which the exceedance of the 1.021 (m) displacement limit state occurs - Coupled response of the 8IFDCH building with gap = 0.00 (m) - Contact forces are modelled via the linear contact model with  $K_p = \text{High}$  -  $\mu$  and  $\sigma$  are the mean and the standard deviation of the lognormal distribution that corresponds to the best fit a) IM = PGA and b) IM = *AvgSa*.

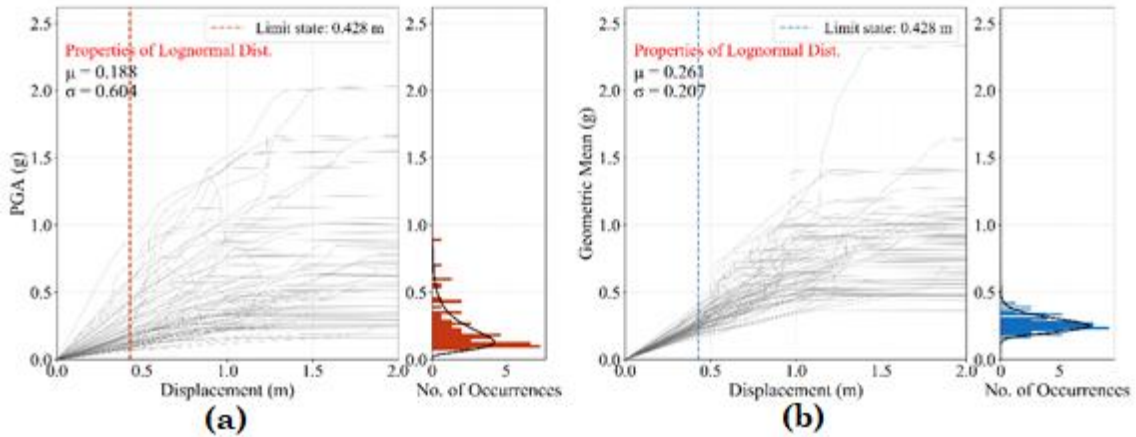


Figure C.31: Pounding between 12RFDCL and 8IFDCH SDOF systems - Distribution of the seismic intensity levels at which the exceedance of the 0.428 (m) displacement limit state occurs - Coupled response of the 12RFDCL building with gap = 0.00 (m) - Contact forces are modelled via the linear contact model with  $K_p = \text{Low}$  -  $\mu$  and  $\sigma$  are the mean and the standard deviation of the lognormal distribution that corresponds to the best fit a) IM = PGA and b) IM = *AvgSa*.

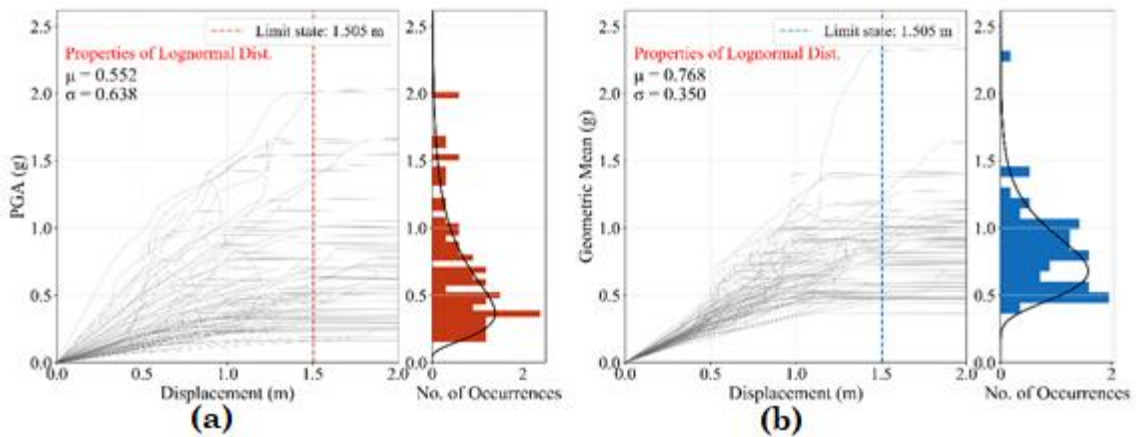


Figure C.32: Pounding between 12RFDCL and 8IFDCH SDOF systems - Distribution of the seismic intensity levels at which the exceedance of the 1.505 (m) displacement limit state occurs - Coupled response of the 12RFDCL building with gap = 0.00 (m) - Contact forces are modelled via the linear contact model with  $K_p = \text{Low}$  -  $\mu$  and  $\sigma$  are the mean and the standard deviation of the lognormal distribution that corresponds to the best fit a) IM = PGA and b) IM = *AvgSa*.

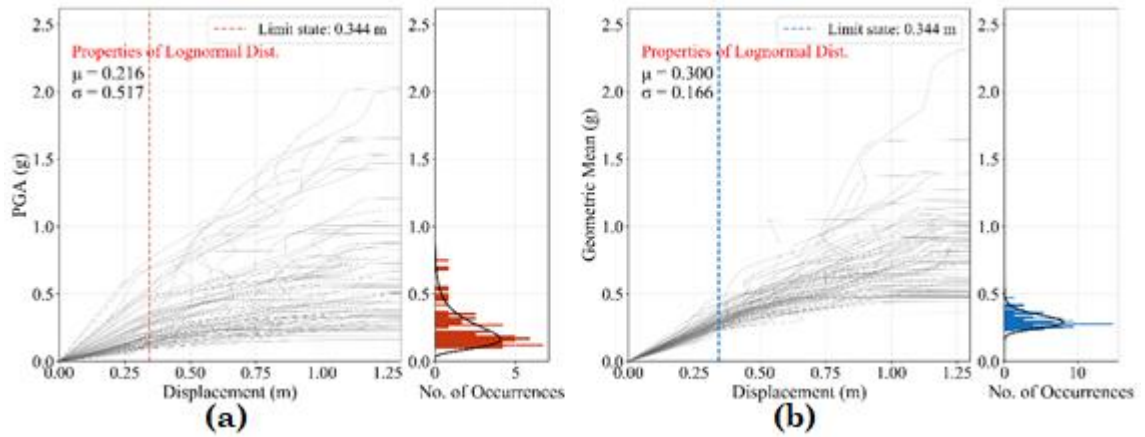


Figure C.33: Pounding between 12RFDCL and 8IFDCH SDOF systems - Distribution of the seismic intensity levels at which the exceedance of the 0.344 (m) displacement limit state occurs - Coupled response of the 8IFDCH building with gap = 0.00 (m) - Contact forces are modelled via the linear contact model with  $K_p = \text{Low}$  -  $\mu$  and  $\sigma$  are the mean and the standard deviation of the lognormal distribution that corresponds to the best fit a) IM = PGA and b) IM = *AvgSa*.

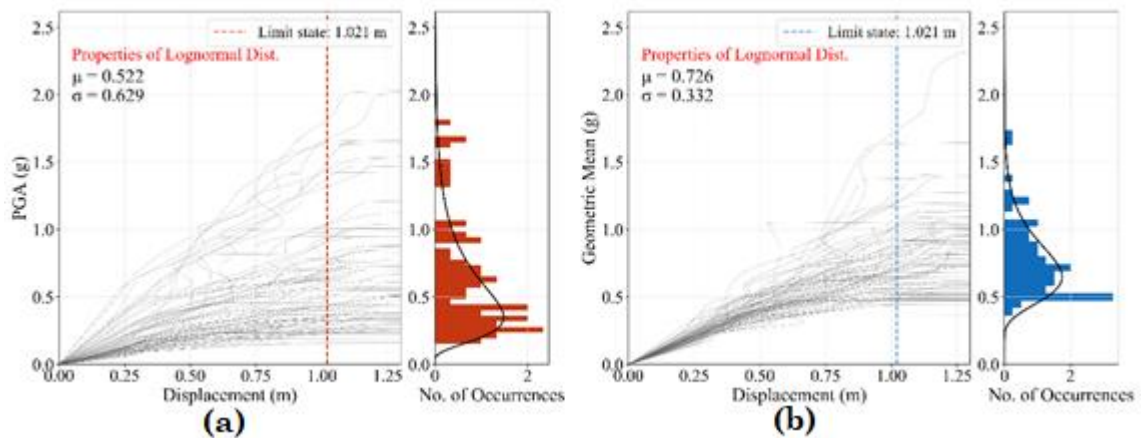


Figure C.34: Pounding between 12RFDCL and 8IFDCH SDOF systems - Distribution of the seismic intensity levels at which the exceedance of the 1.021 (m) displacement limit state occurs - Coupled response of the 8IFDCH building with gap = 0.00 (m) - Contact forces are modelled via the linear contact model with  $K_p = \text{Low}$  -  $\mu$  and  $\sigma$  are the mean and the standard deviation of the lognormal distribution that corresponds to the best fit a) IM = PGA and b) IM = *AvgSa*.

## Appendix D - Fragility Curves

Plots all fragility curves produced in the parametric numerical work of chapter 6.

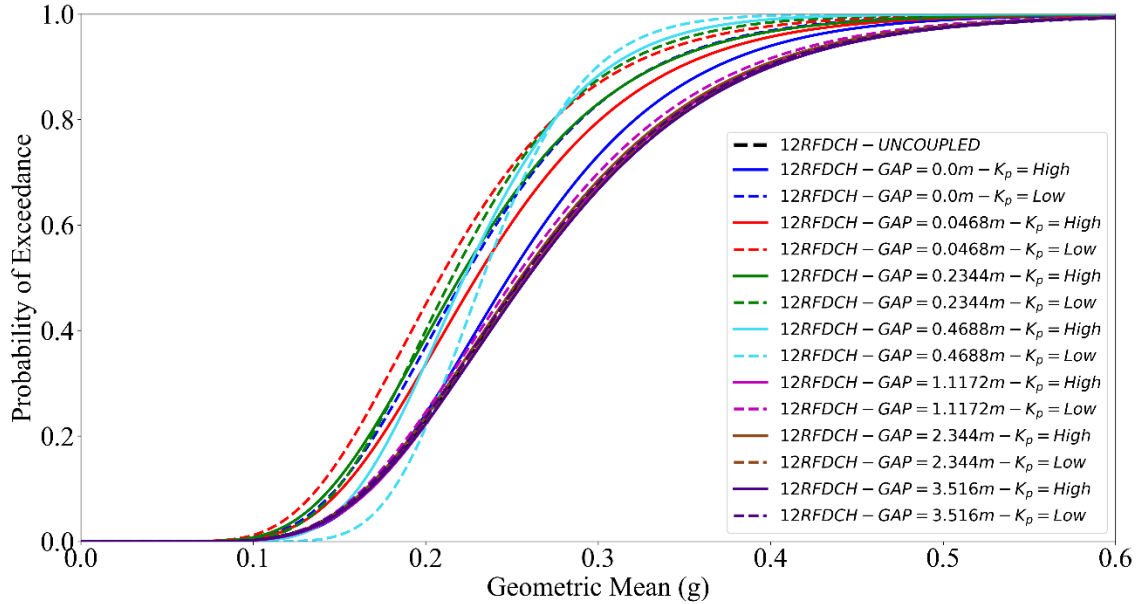


Figure D.1: Fragility curves for the 12RFDCH non-linear SDOF system. Pounding between 12RFDCH and 8SWDCH is modelled using the linear pounding model. Fragility curves are derived for all considered gap and  $K_p$  values for the light damage limit state (0.427 m).

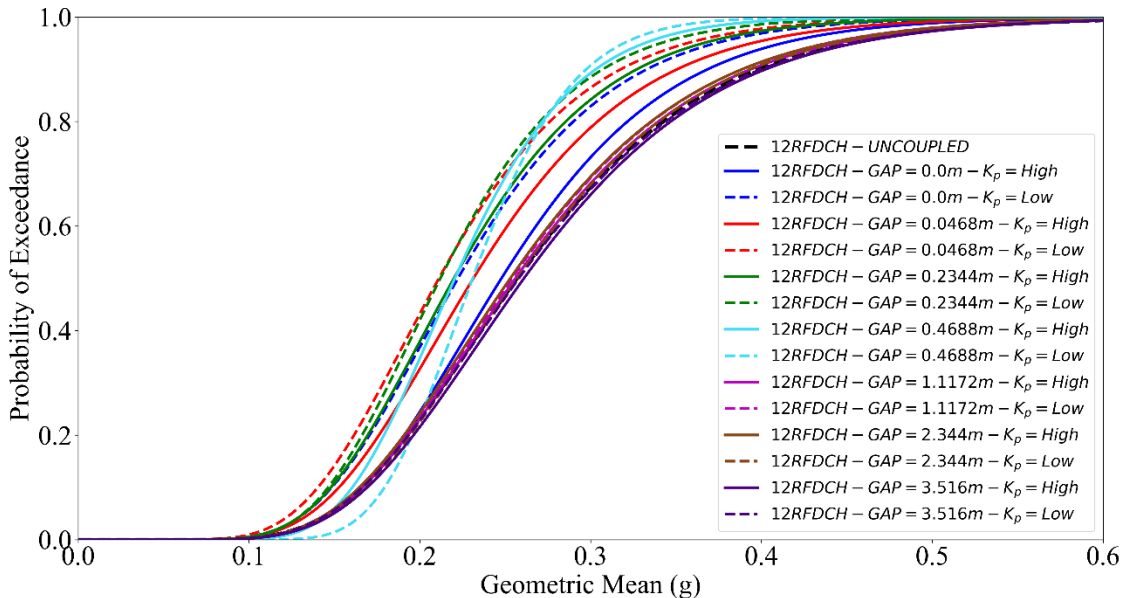


Figure D.2: Fragility curves for the 12RFDCH non-linear SDOF system. Pounding between 12RFDCH and 8SWDCH is modelled using the linear visco-elastic pounding model. Fragility curves are derived for all considered gap and  $K_p$  values for the light damage limit state (0.427 m).

## Appendix D

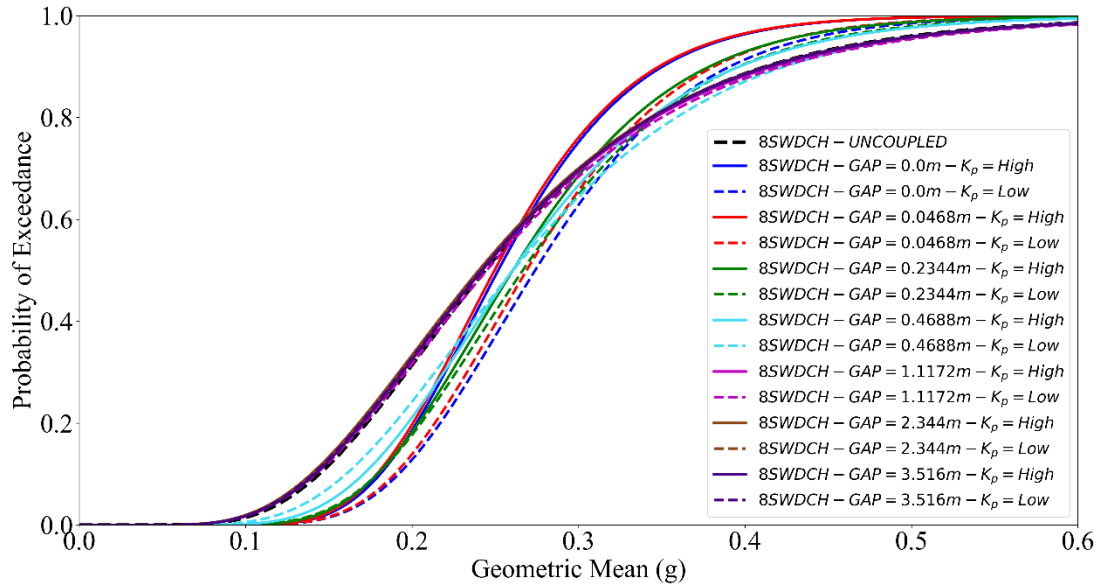


Figure D.3: Fragility curves for the 8SWDCH non-linear SDOF system. Pounding between 12RFDCH and 8SWDCH is modelled using the linear pounding model. Fragility curves are derived for all considered gap and  $K_p$  values for the light damage limit state (0.338 m).

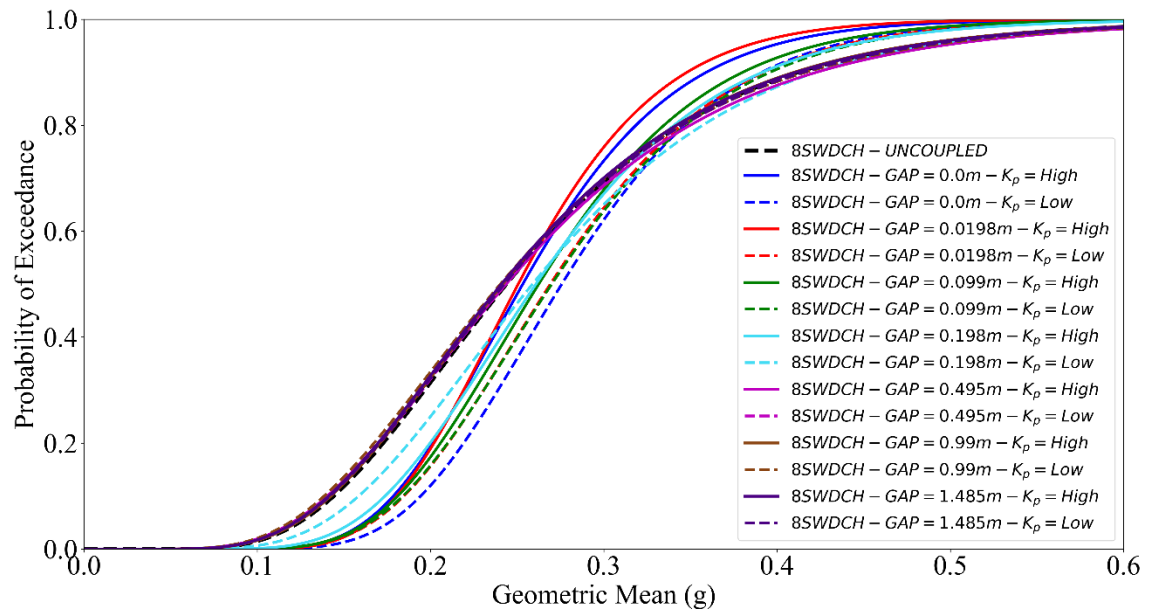


Figure D.4: Fragility curves for the 8SWDCH non-linear SDOF system. Pounding between 12RFDCH and 8SWDCH is modelled using the linear visco-elastic pounding model. Fragility curves are derived for all considered gap and  $K_p$  values for the light damage limit state (0.338 m).

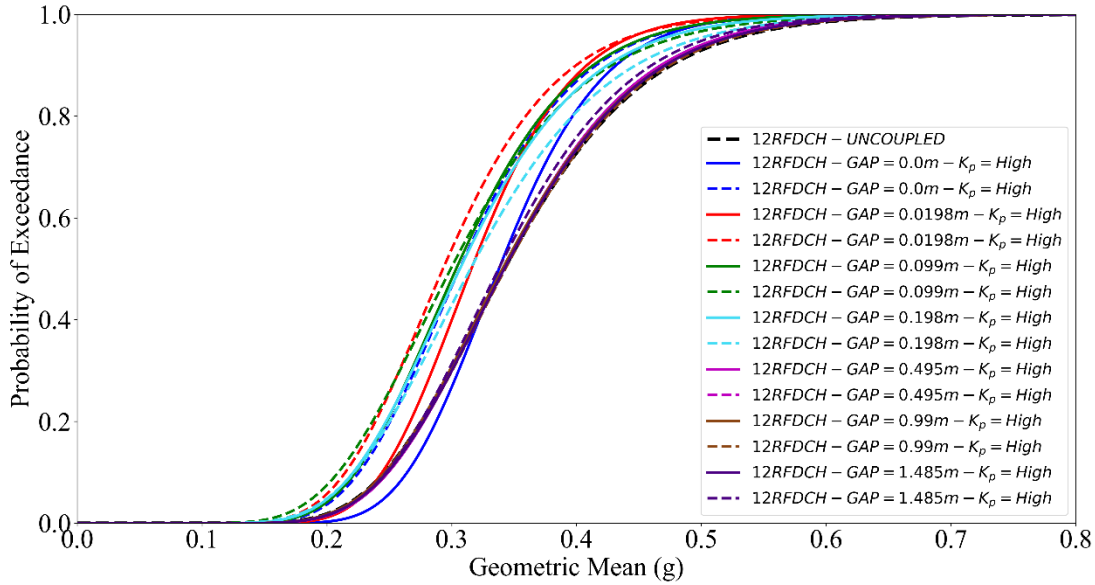


Figure D.5: Fragility curves for the 12RFDCH non-linear SDOF system. Pounding between 12RFDCH and 8WDCL is modelled using the linear pounding model. Fragility curves are derived for all considered gap and  $K_p$  values for the light damage limit state (0.427 m).

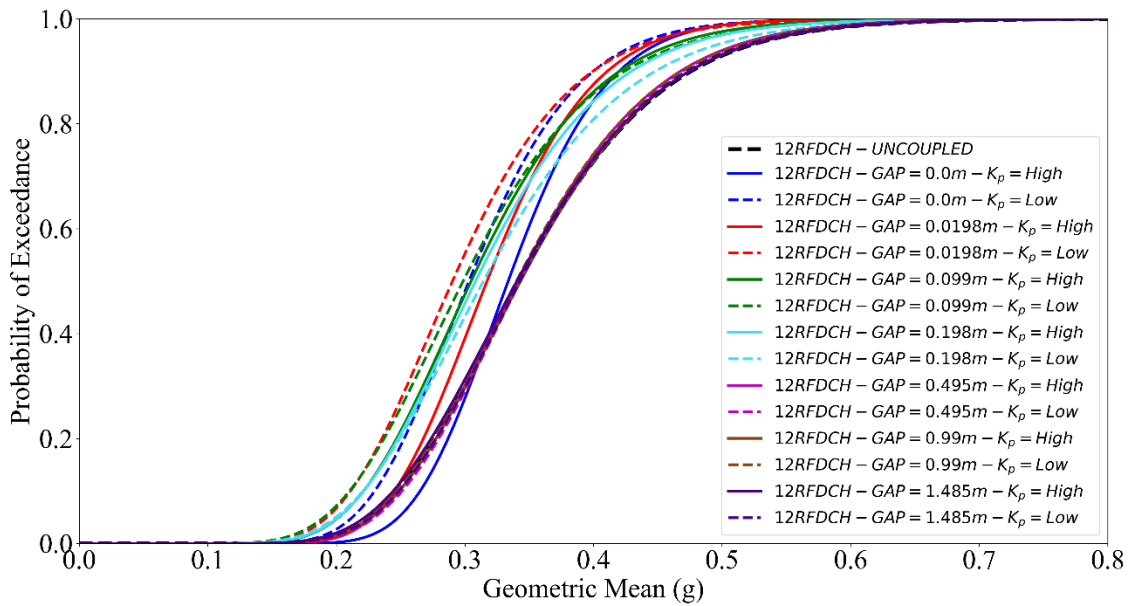


Figure D.6: Fragility curves for the 12RFDCH non-linear SDOF system. Pounding between 12RFDCH and 8WDCL is modelled using the linear visco-elastic pounding model. Fragility curves are derived for all considered gap and  $K_p$  values for the light damage limit state (0.427 m).

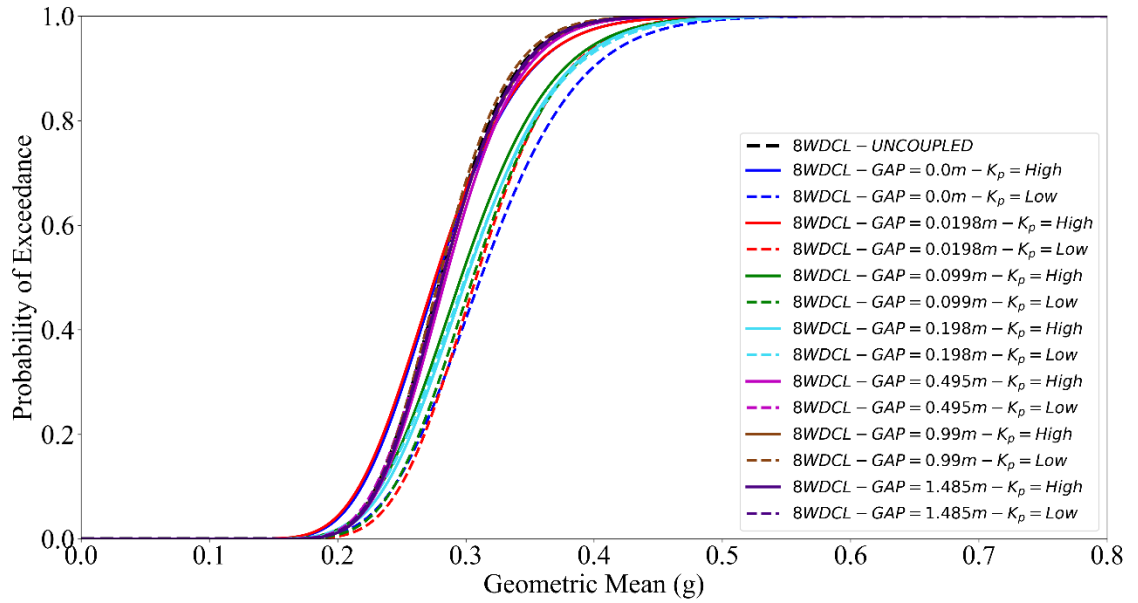


Figure D.7: Fragility curves for the 8SWDCL non-linear SDOF system. Pounding between 12RFDCH and 8WDCL is modelled using the linear pounding model. Fragility curves are derived for all considered gap and  $K_p$  values for the light damage limit state (0.298 m).

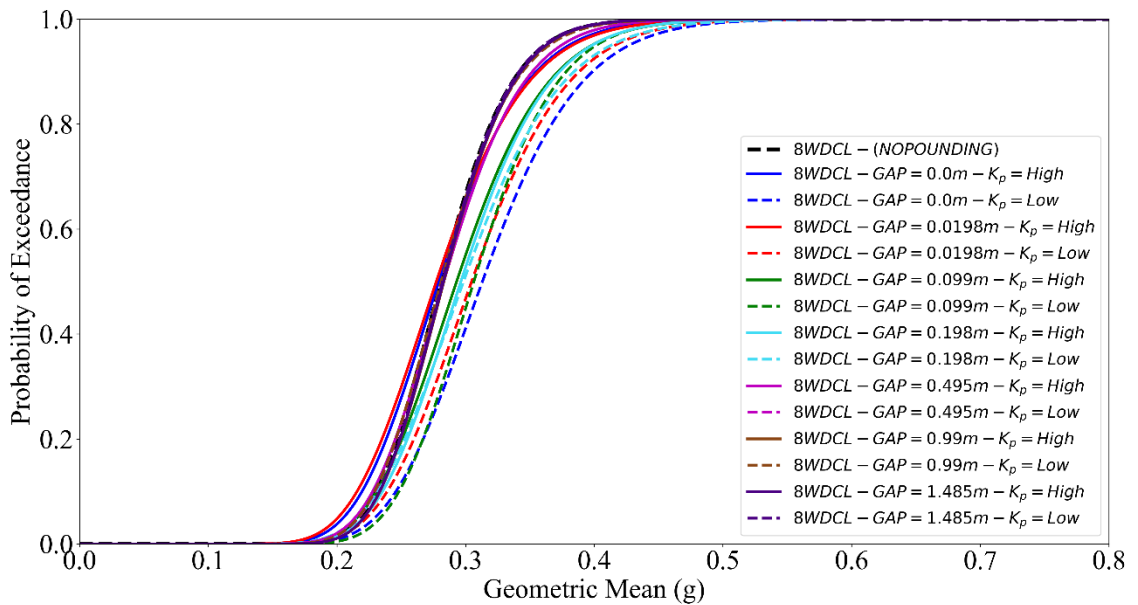


Figure D.8: Fragility curves for the 8SWDCL non-linear SDOF system. Pounding between 12RFDCH and 8WDCL is modelled using the linear visco-elastic pounding model. Fragility curves are derived for all considered gap and  $K_p$  values for the light damage limit state (0.298 m).

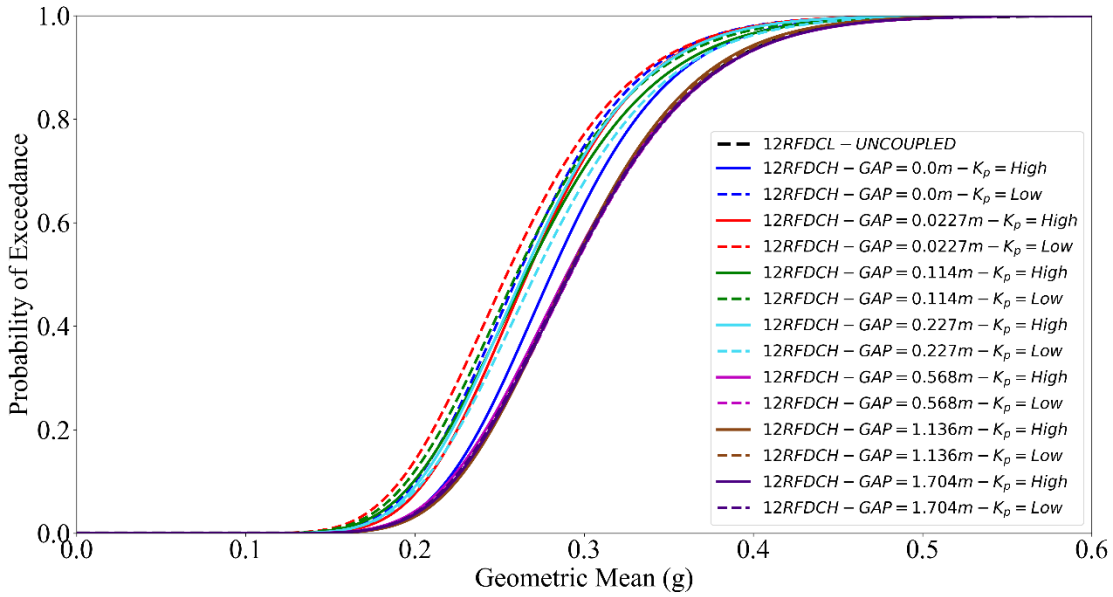


Figure D.9: Fragility curves for the 12RFDCL non-linear SDOF system. Pounding between 12RFDCL and 8IFDCH is modelled using the linear pounding model. Fragility curves are derived for all considered gap and  $K_p$  values for the light damage limit state (0.428 m).

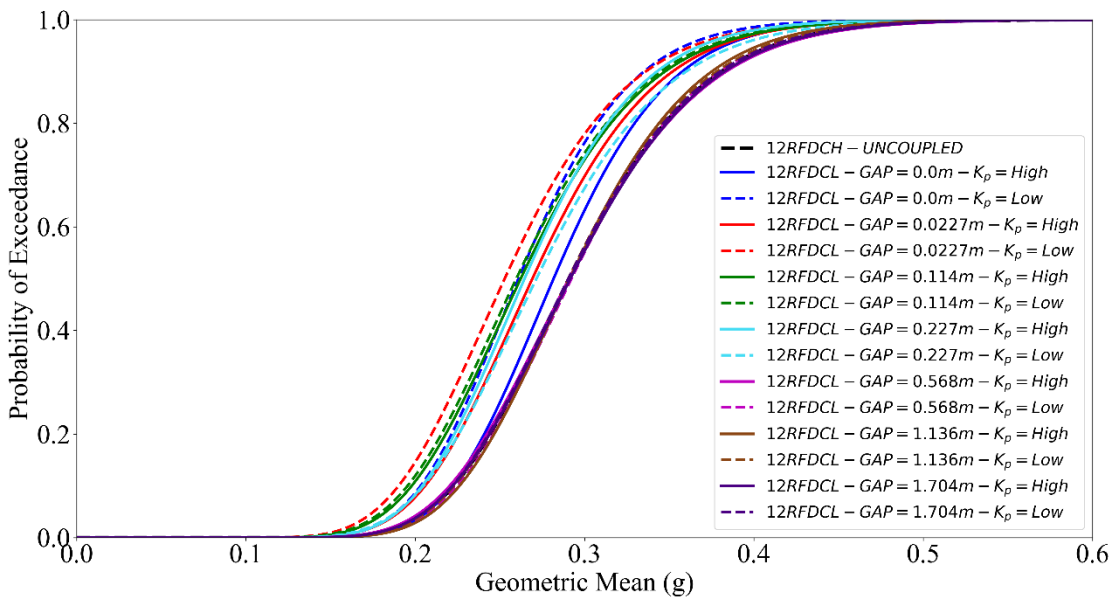


Figure D.10: Fragility curves for the 12RFDCL non-linear SDOF system. Pounding between 12RFDCL and 8IFDCH is modelled using the linear visco-elastic pounding model. Fragility curves are derived for all considered gap and  $K_p$  values for the light damage limit state (0.428 m).

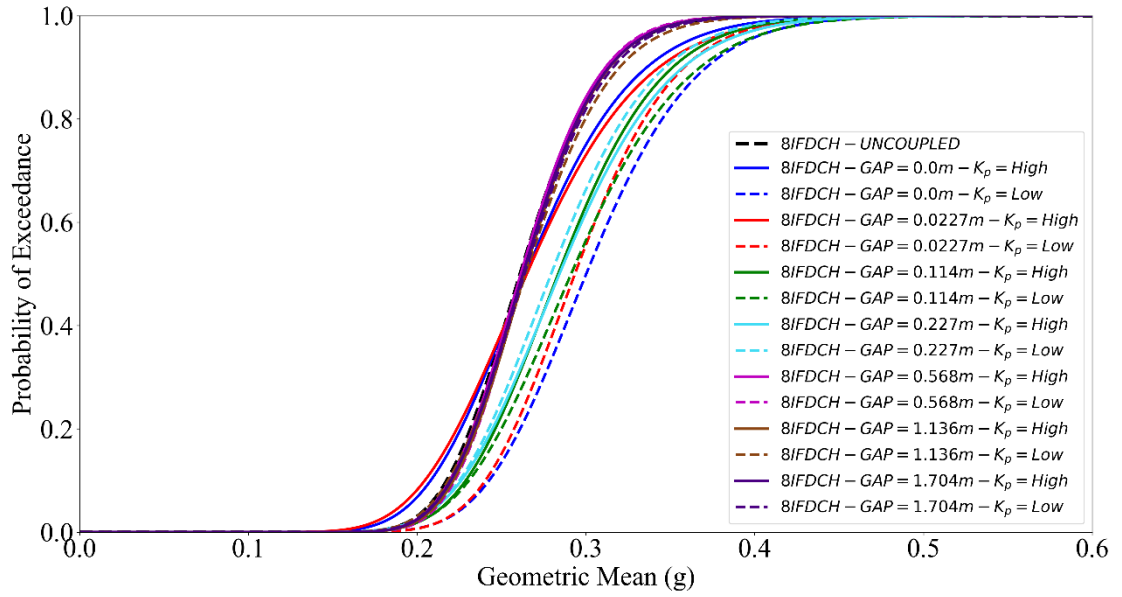


Figure D.11: Fragility curves for the 8IFDCH non-linear SDOF system. Pounding between 12RFDCL and 8IFDCH is modelled using the linear pounding model. Fragility curves are derived for all considered gap and  $K_p$  values for the light damage limit state (0.344 m).

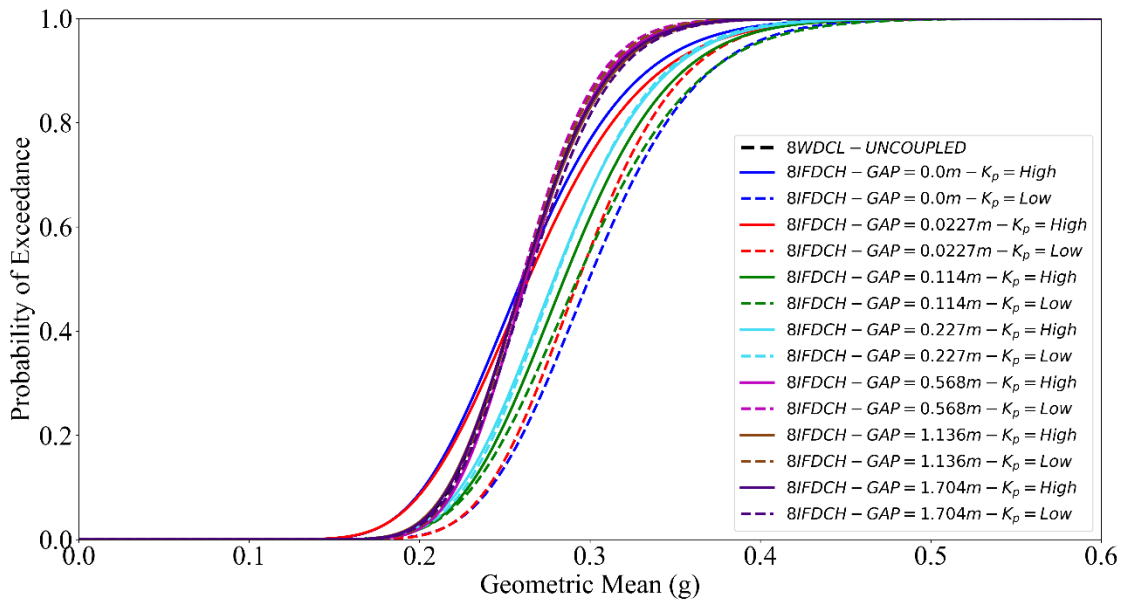


Figure D.12: Fragility curves for the 8IFDCH non-linear SDOF system. Pounding between 12RFDCL and 8IFDCH is modelled using the linear visco-elastic pounding model. Fragility curves are derived for all considered gap and  $K_p$  values for the light damage limit state (0.344 m).

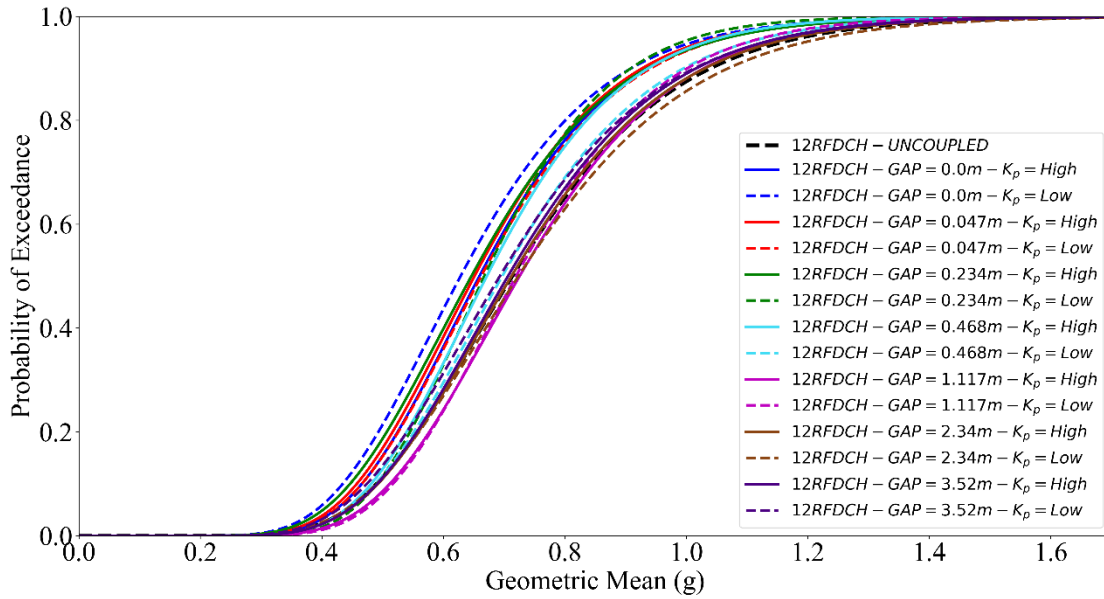


Figure D.13: Fragility curves for the 12RFDCH non-linear SDOF system. Pounding between 12RFDCH and 8SWDCH is modelled using the linear pounding model. Fragility curves are derived for all considered gap and  $K_p$  values for the severe damage limit state (1.441 m).

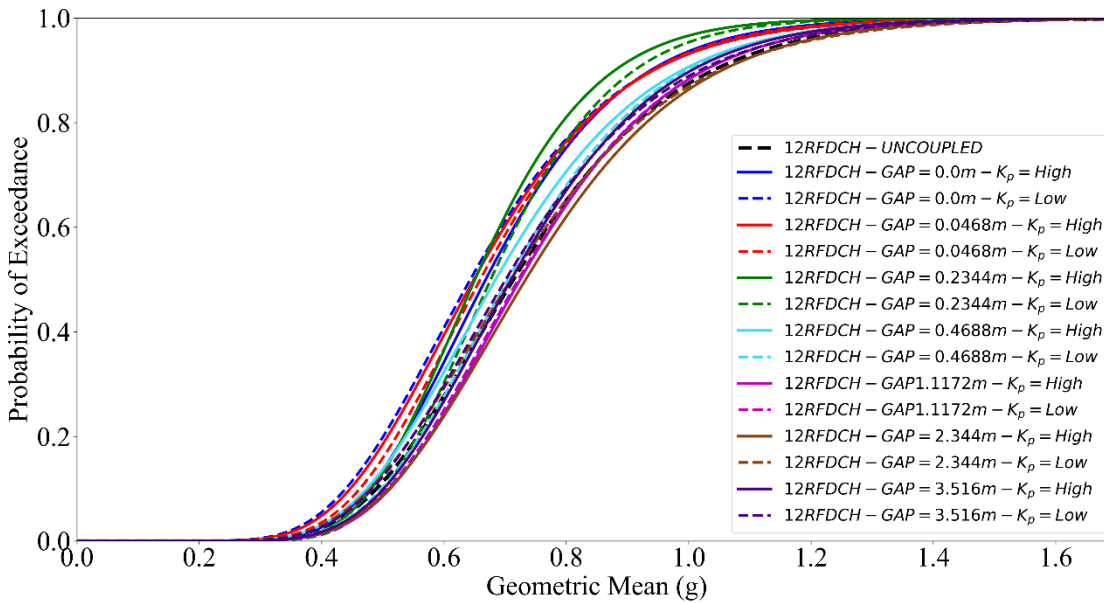


Figure D.14: Fragility curves for the 12RFDCH non-linear SDOF system. Pounding between 12RFDCH and 8SWDCH is modelled using the linear visco-elastic pounding model. Fragility curves are derived for all considered gap and  $K_p$  values for the severe damage limit state (1.441 m).

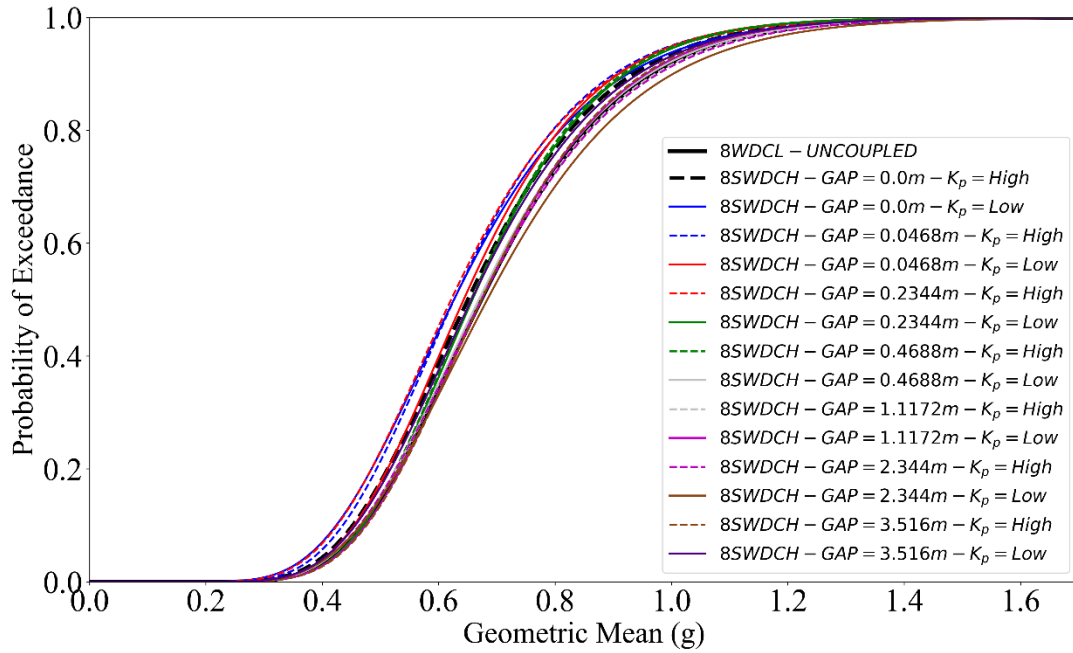


Figure D.15: Fragility curves for the 8SWDCH non-linear SDOF system. Pounding between 12RFDCH and 8SWDCH is modelled using the linear pounding model. Fragility curves are derived for all considered gap and  $K_p$  values for the severe damage limit state (0.962 m).

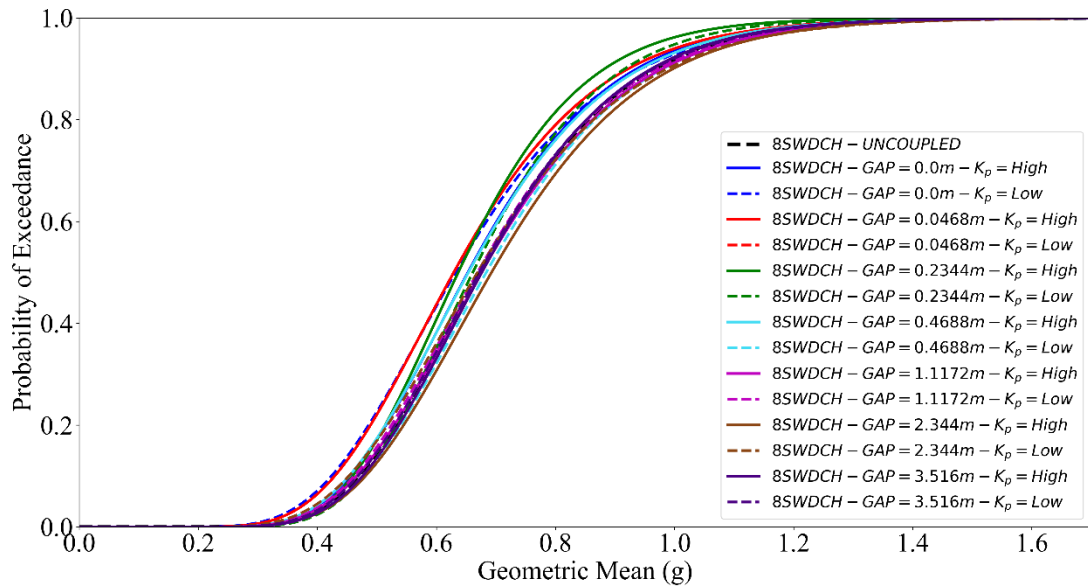


Figure D.16: Fragility curves for the 8SWDCH non-linear SDOF system. Pounding between 12RFDCH and 8SWDCH is modelled using the linear visco-elastic pounding model. Fragility curves are derived for all considered gap and  $K_p$  values for the severe damage limit state (0.962 m).

## Appendix D

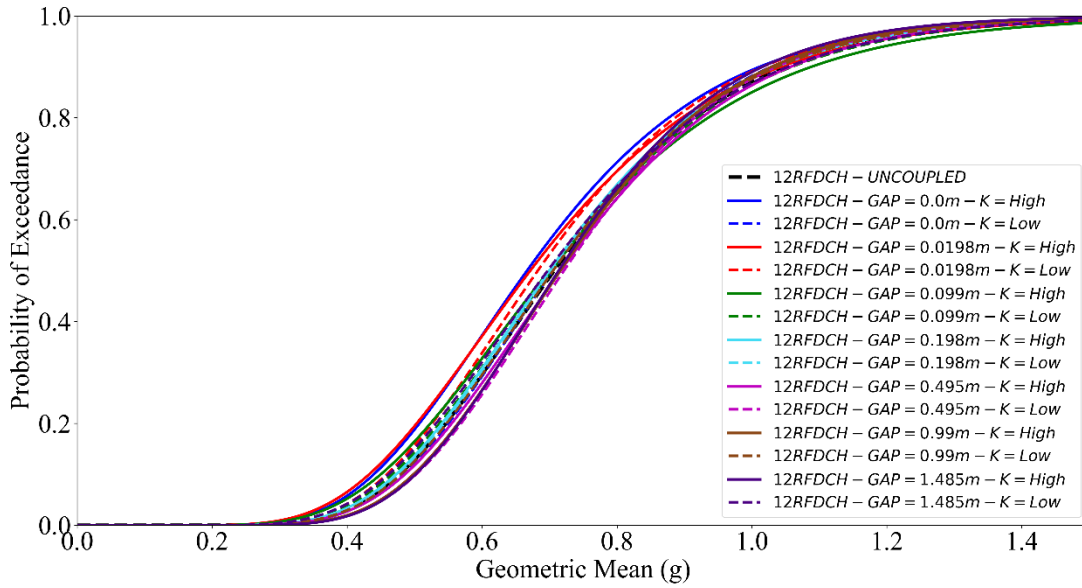


Figure D.17: Fragility curves for the 12RFDCH non-linear SDOF system. Pounding between 12RFDCH and 8WDCL is modelled using the linear pounding model. Fragility curves are derived for all considered gap and  $K_p$  values for the severe damage limit state (1.441 m).

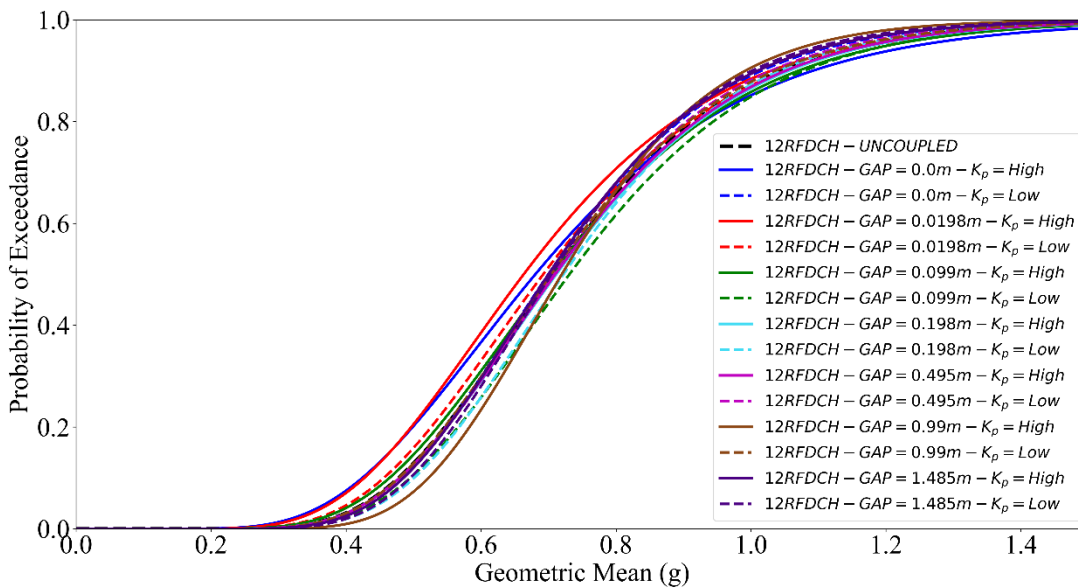


Figure D.18: Fragility curves for the 12RFDCH non-linear SDOF system. Pounding between 12RFDCH and 8WDCL is modelled using the linear visco-elastic pounding model. Fragility curves are derived for all considered gap and  $K_p$  values for the severe damage limit state (1.441 m).

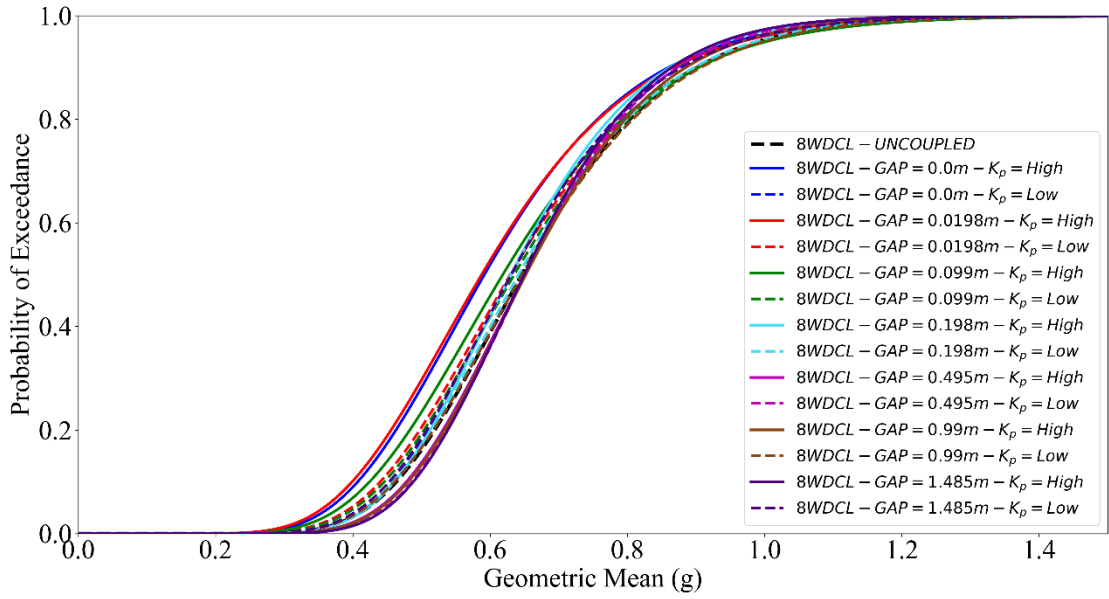


Figure D.19: Fragility curves for the 8WDCL non-linear SDOF system. Pounding between 12RFDCH and 8WDCL is modelled using the linear pounding model. Fragility curves are derived for all considered gap and  $K_p$  values for the severe damage limit state (0.658 m).

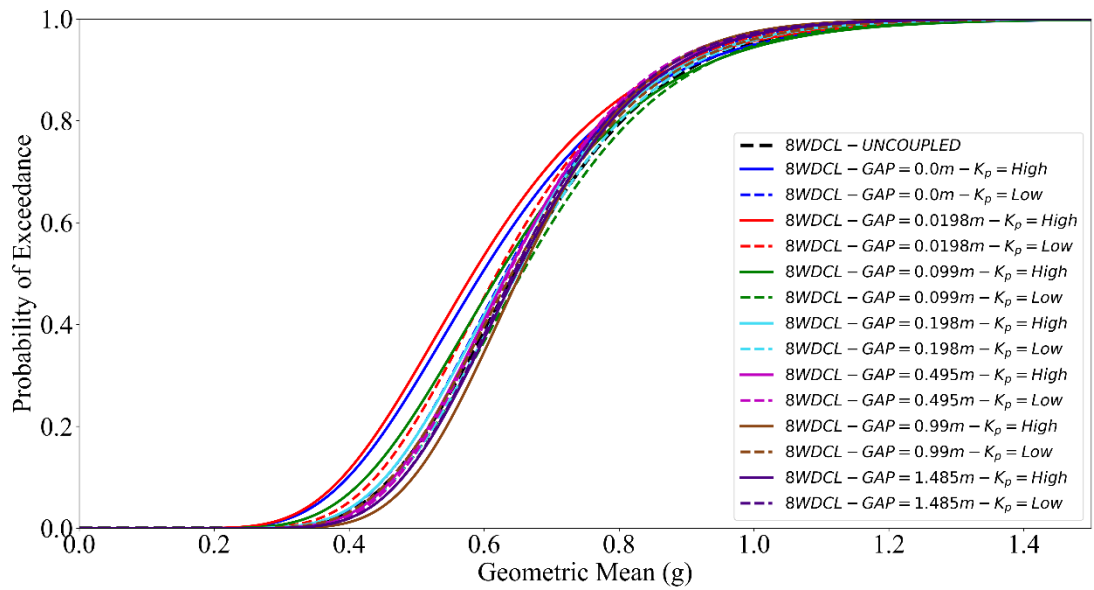


Figure D.20: Fragility curves for the 8WDCL non-linear SDOF system. Pounding between 12RFDCH and 8WDCL is modelled using the linear visco-elastic pounding model. Fragility curves are derived for all considered gap and  $K_p$  values for the severe damage limit state (0.658 m).

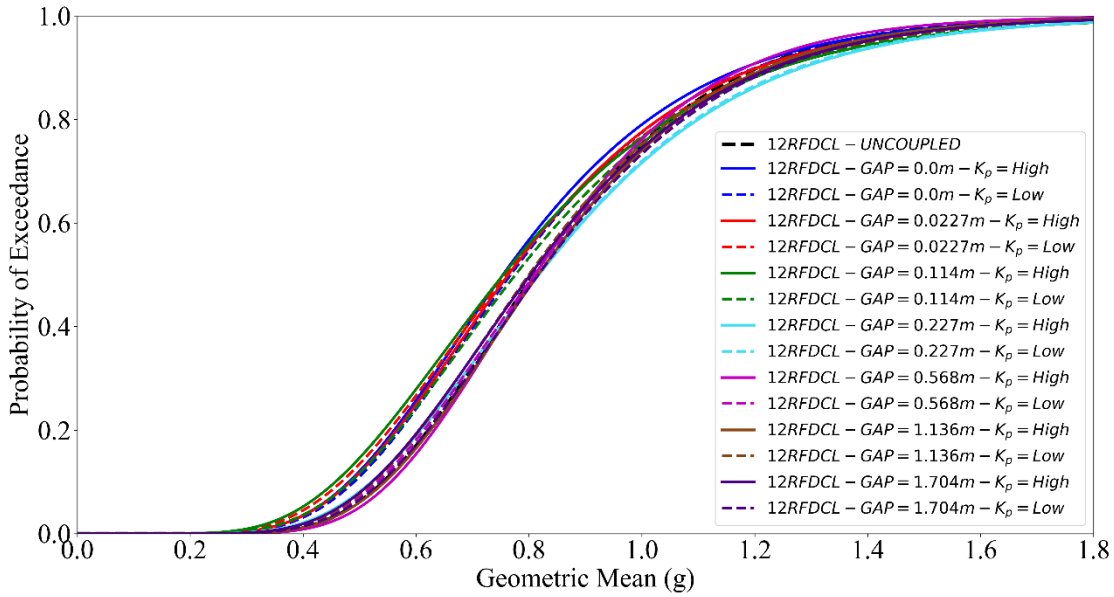


Figure D.21: Fragility curves for the 12RFDCL non-linear SDOF system. Pounding between 12RFDCL and 8IFDCH is modelled using the linear pounding model. Fragility curves are derived for all considered gap and  $K_p$  values for the severe damage limit state (1.505 m).

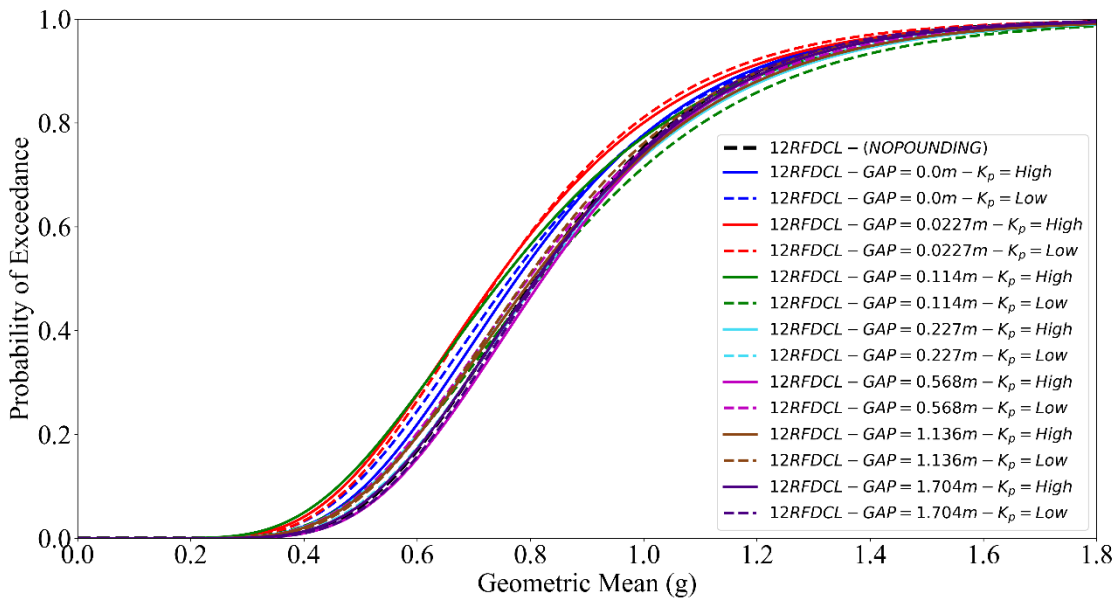


Figure D.22: Fragility curves for the 12RFDCL non-linear SDOF system. Pounding between 12RFDCL and 8IFDCH is modelled using the linear visco-elastic pounding model. Fragility curves are derived for all considered gap and  $K_p$  values for the severe damage limit state (1.505 m).

## Appendix D

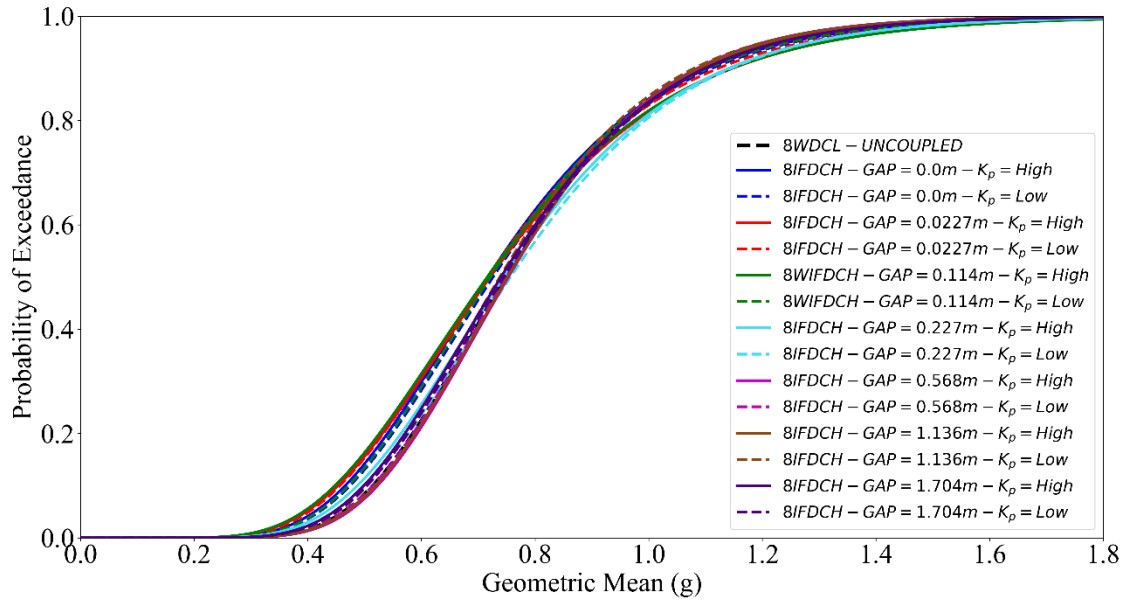


Figure D.23: Fragility curves for the 8IFDCH non-linear SDOF system. Pounding between 12RFDCL and 8IFDCH is modelled using the linear pounding model. Fragility curves are derived for all considered gap and  $K_p$  values for the severe damage limit state (1.021 m).

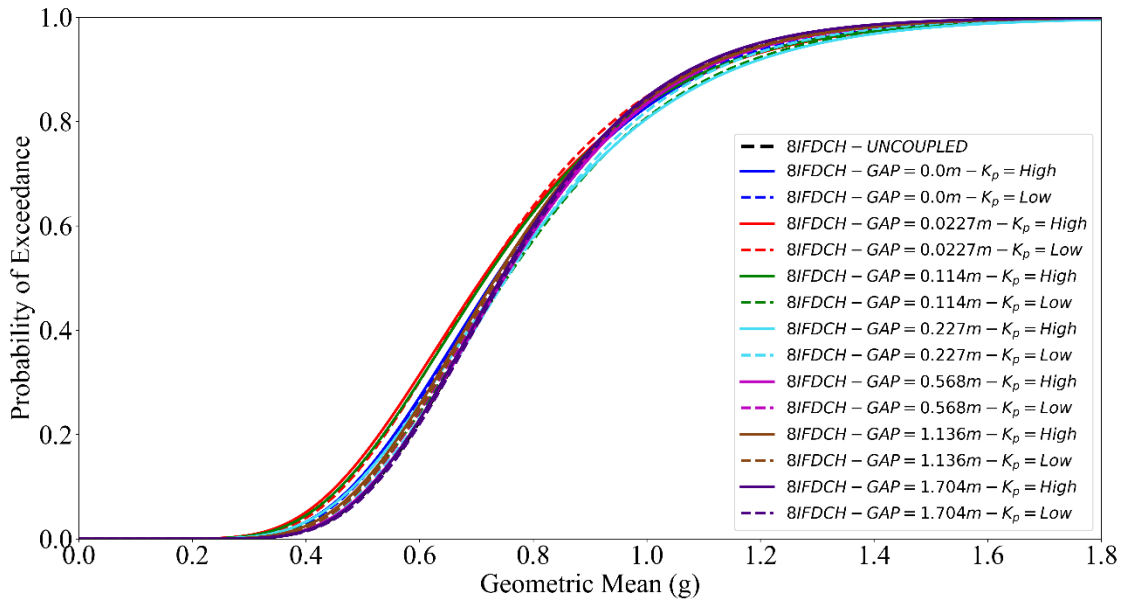


Figure D.24: Fragility curves for the 8IFDCH non-linear SDOF system. Pounding between 12RFDCL and 8IFDCH is modelled using the linear visco-elastic pounding model. Fragility curves are derived for all considered gap and  $K_p$  values for the severe damage limit state (1.021 m).

## Appendix E - Fragility Curves Statistics

Appendix E provides plots of statistical attributes used to compare all fragility curves produced (as a function of the separation distance) for the case where pounding forces were modelled by means of the linear elastic and linear viscoelastic contact models in Chapter 6.

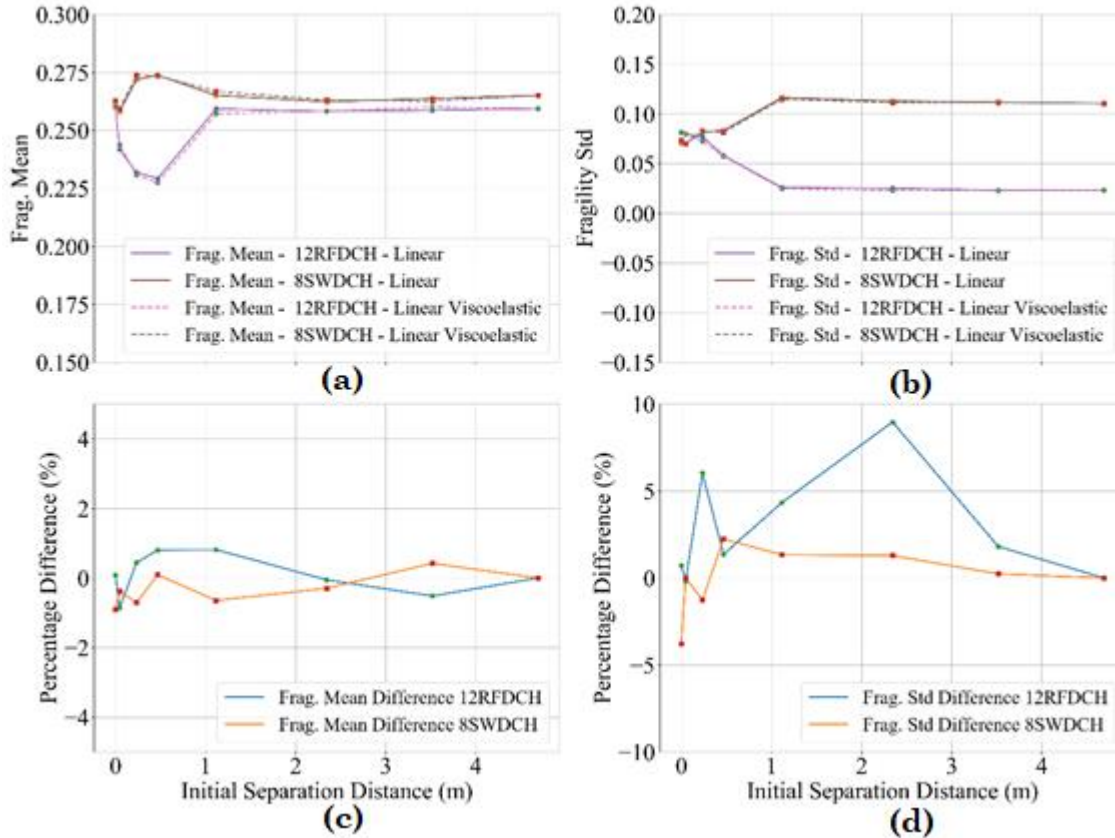


Figure E.1: Pounding between 12RFDCH and 8SWDCH SDOF systems - light damage limit state and  $K_p = High$  a) mean values of the fragility models of the two adopted contact models as a function of the initial separation distance b) standard deviation values of the fragility models for the two adopted contact models as a function of initial separation distance c) percentage difference between the mean values of the two adopted contact models as a function of the initial separation distance and b) percentage difference between the standard deviation values of the two adopted contact models as a function of the initial separation distance.

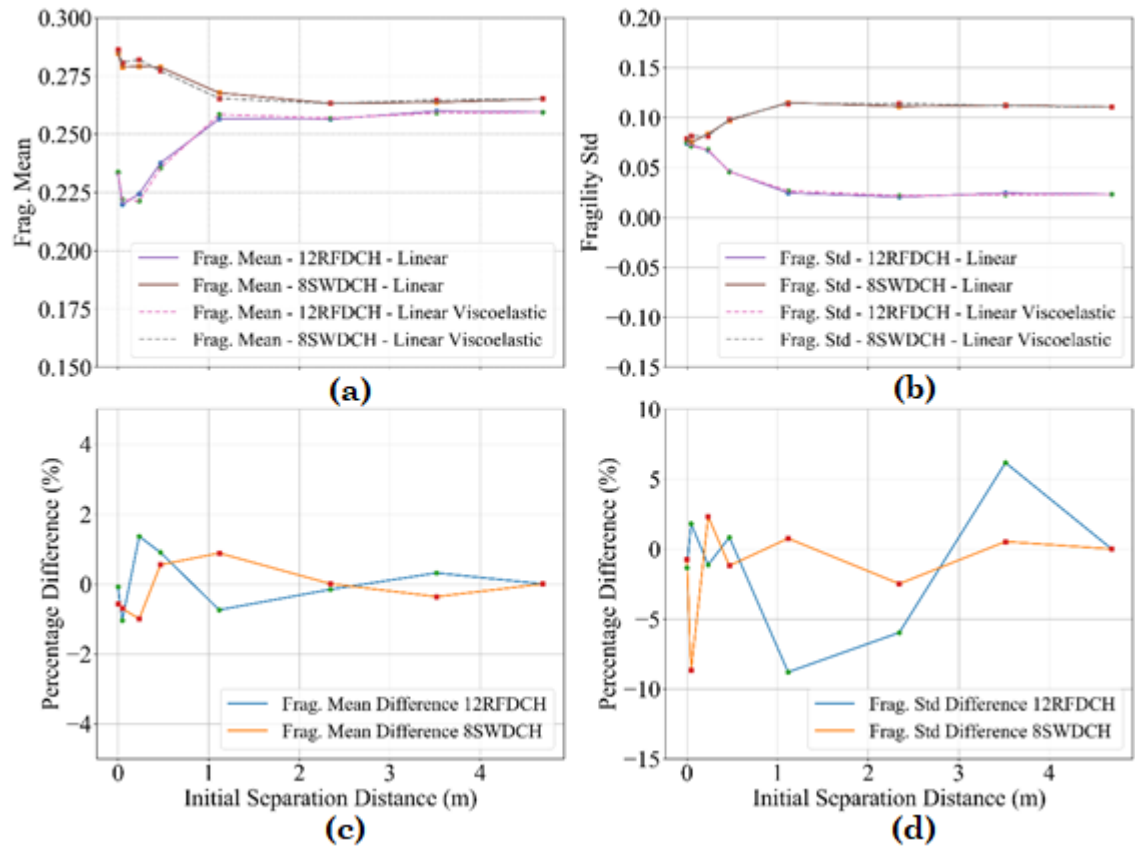


Figure E.2: Pounding between 12RFDCH and 8SWDCH SDOF systems - light damage limit state and  $K_p = Low$  a) mean values of the fragility models of the two adopted contact models as a function of the initial separation distance b) standard deviation values of the fragility models for the two adopted contact models as a function of initial separation distance c) percentage difference between the mean values of the two adopted contact models as a function of the initial separation distance and b) percentage difference between the standard deviation values of the two adopted contact models as a function of the initial separation distance.

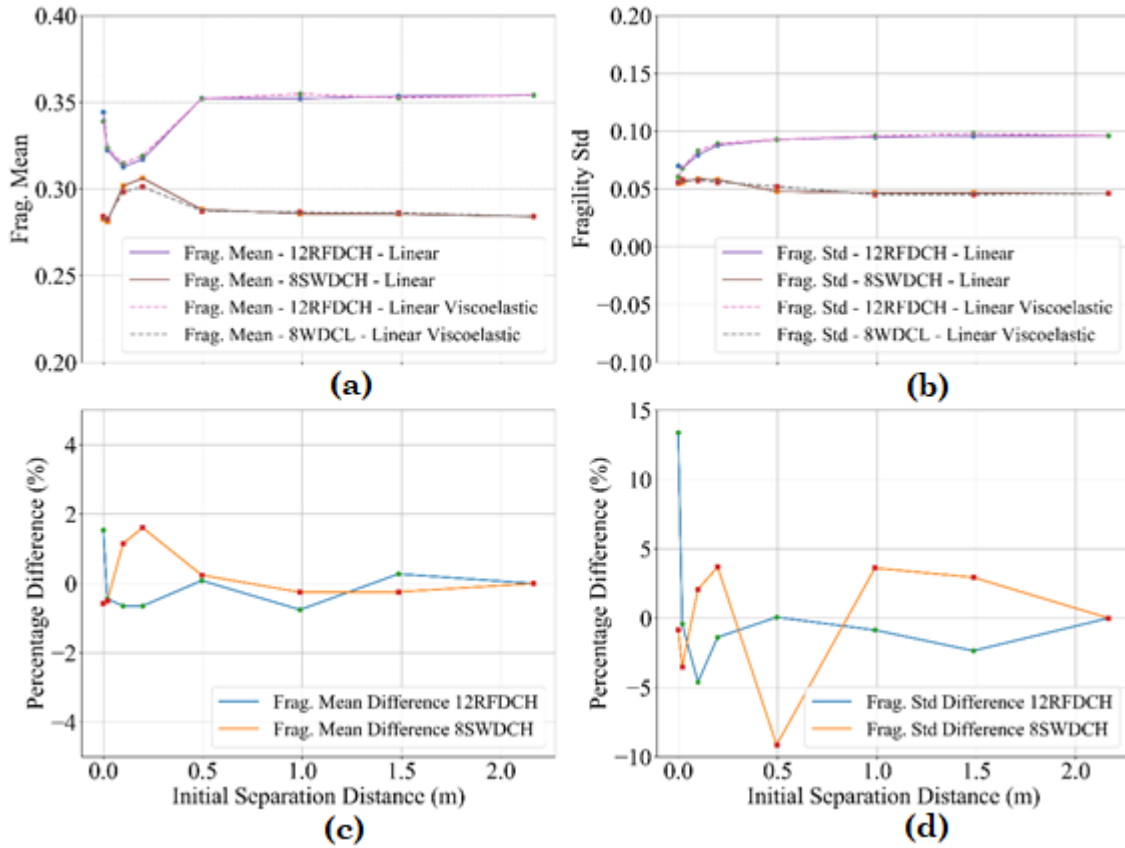


Figure E.3: Pounding between 12RFDCH and 8WDCL SDOF systems - light damage limit state and  $K_p = High$  a) mean values of the fragility models of the two adopted contact models as a function of the initial separation distance b) standard deviation values of the fragility models for the two adopted contact models as a function of initial separation distance c) percentage difference between the mean values of the two adopted contact models as a function of the initial separation distance and b) percentage difference between the standard deviation values of the two adopted contact models as a function of the initial separation distance.

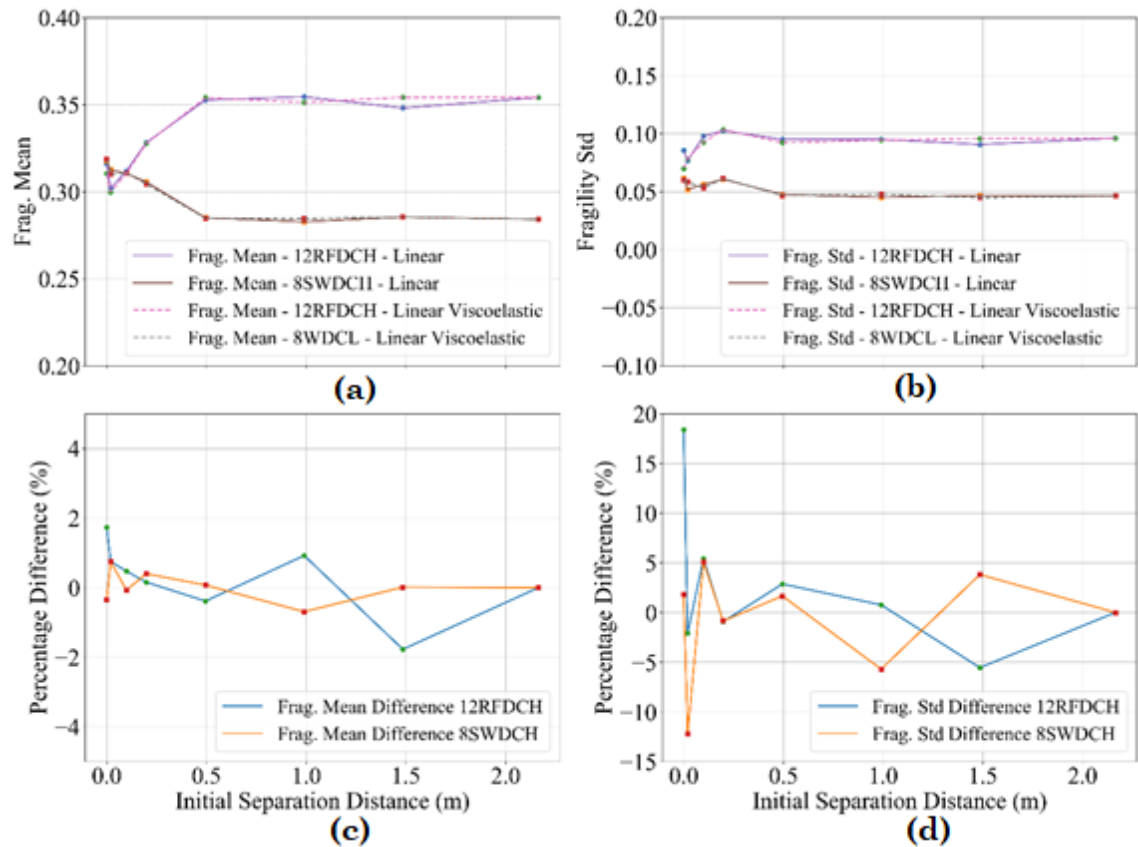


Figure E.4: Pounding between 12RFDCH and 8WDCL SDOF systems - light damage limit state and  $K_p = Low$  a) mean values of the fragility models of the two adopted contact models as a function of the initial separation distance b) standard deviation values of the fragility models for the two adopted contact models as a function of initial separation distance c) percentage difference between the mean values of the two adopted contact models as a function of the initial separation distance and b) percentage difference between the standard deviation values of the two adopted contact models as a function of the initial separation distance.

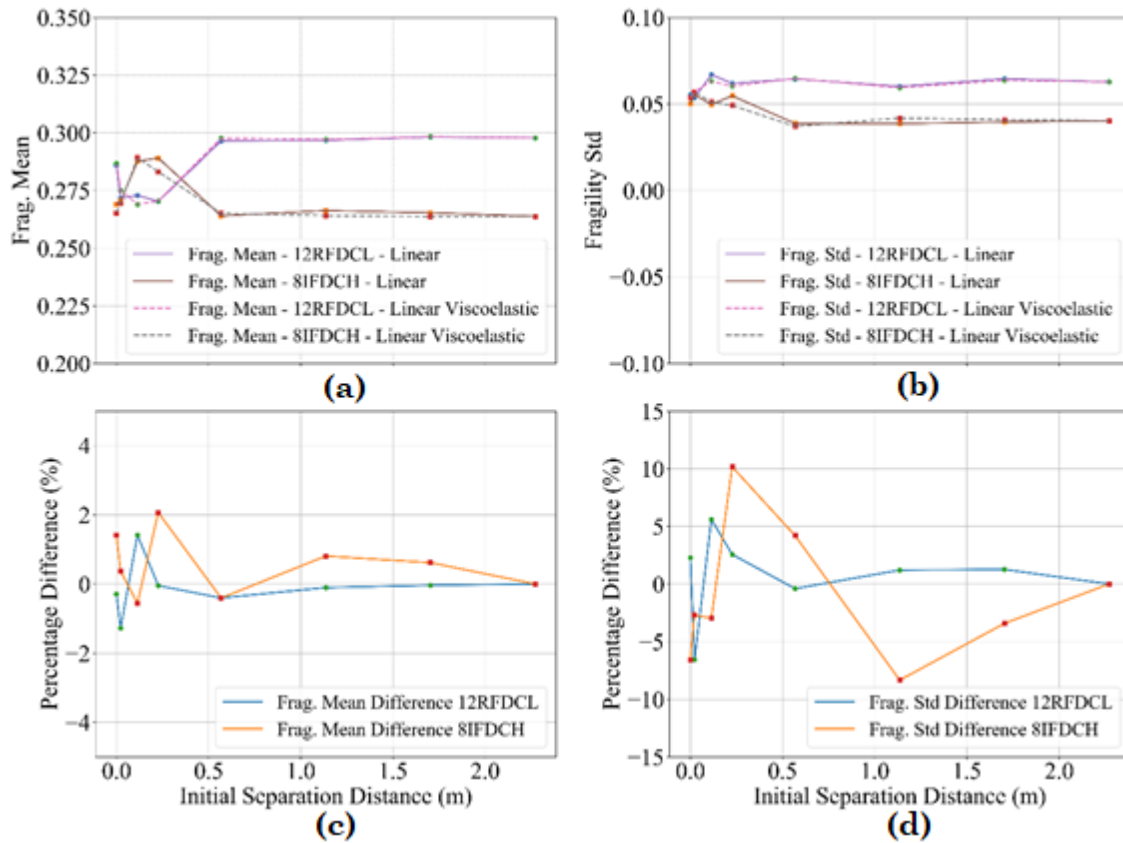


Figure E.5: Pounding between 12RFDCL and 8IFDCH SDOF systems - light damage limit state and  $K_p = High$  a) mean values of the fragility models of the two adopted contact models as a function of the initial separation distance b) standard deviation values of the fragility models for the two adopted contact models as a function of initial separation distance c) percentage difference between the mean values of the two adopted contact models as a function of the initial separation distance and b) percentage difference between the standard deviation values of the two adopted contact models as a function of the initial separation distance.

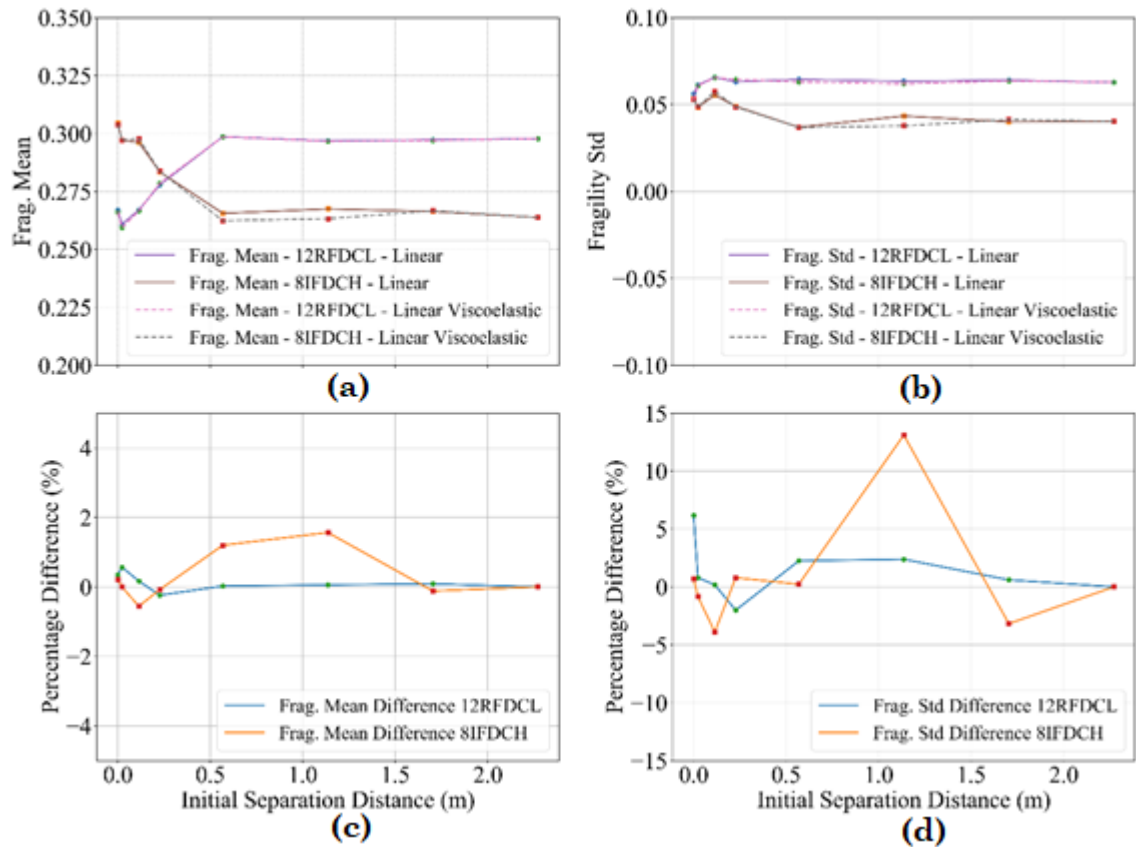


Figure E.6: Pounding between 12RFDCL and 8IFDCH SDOF systems - light damage limit state and  $K_p = Low$  a) mean values of the fragility models of the two adopted contact models as a function of the initial separation distance b) standard deviation values of the fragility models for the two adopted contact models as a function of initial separation distance c) percentage difference between the mean values of the two adopted contact models as a function of the initial separation distance and b) percentage difference between the standard deviation values of the two adopted contact models as a function of the initial separation distance.

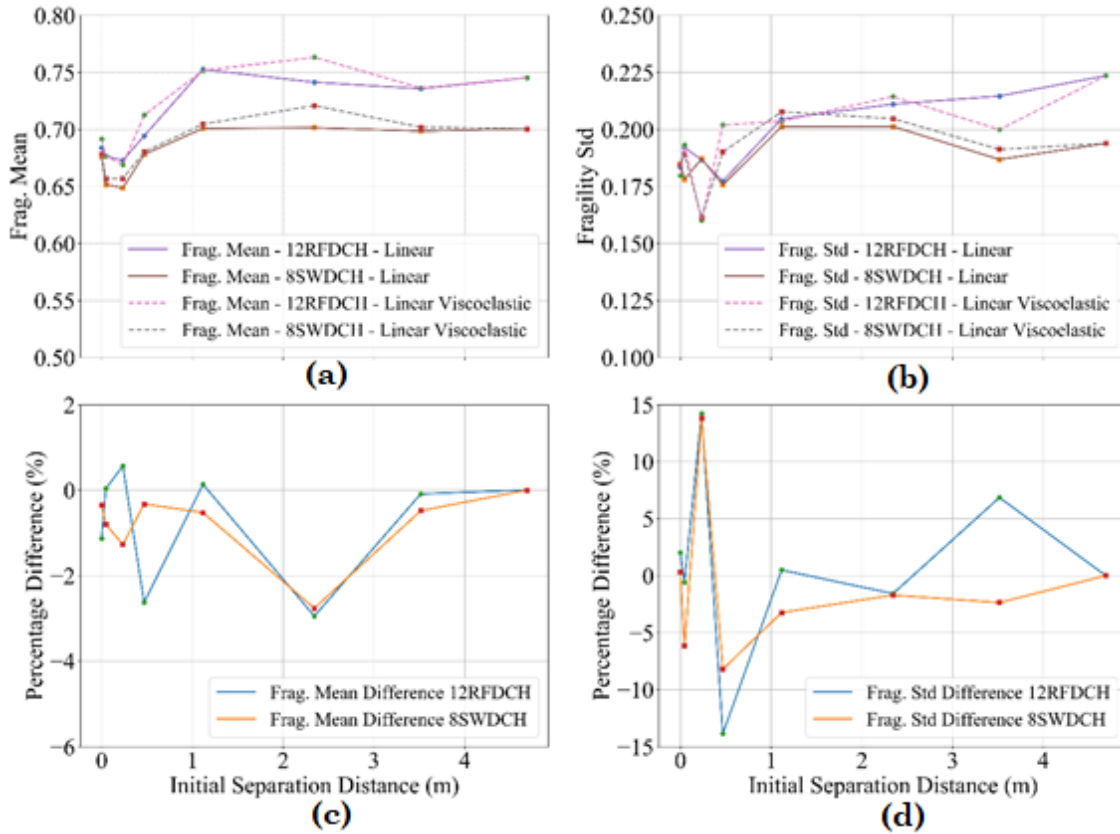


Figure E.7: Pounding between 12RFDCH and 8SWDCH SDOF systems - severe damage limit state and  $K_p = High$  a) mean values of the fragility models of the two adopted contact models as a function of the initial separation distance b) standard deviation values of the fragility models for the two adopted contact models as a function of initial separation distance c) percentage difference between the mean values of the two adopted contact models as a function of the initial separation distance and b) percentage difference between the standard deviation values of the two adopted contact models as a function of the initial separation distance.

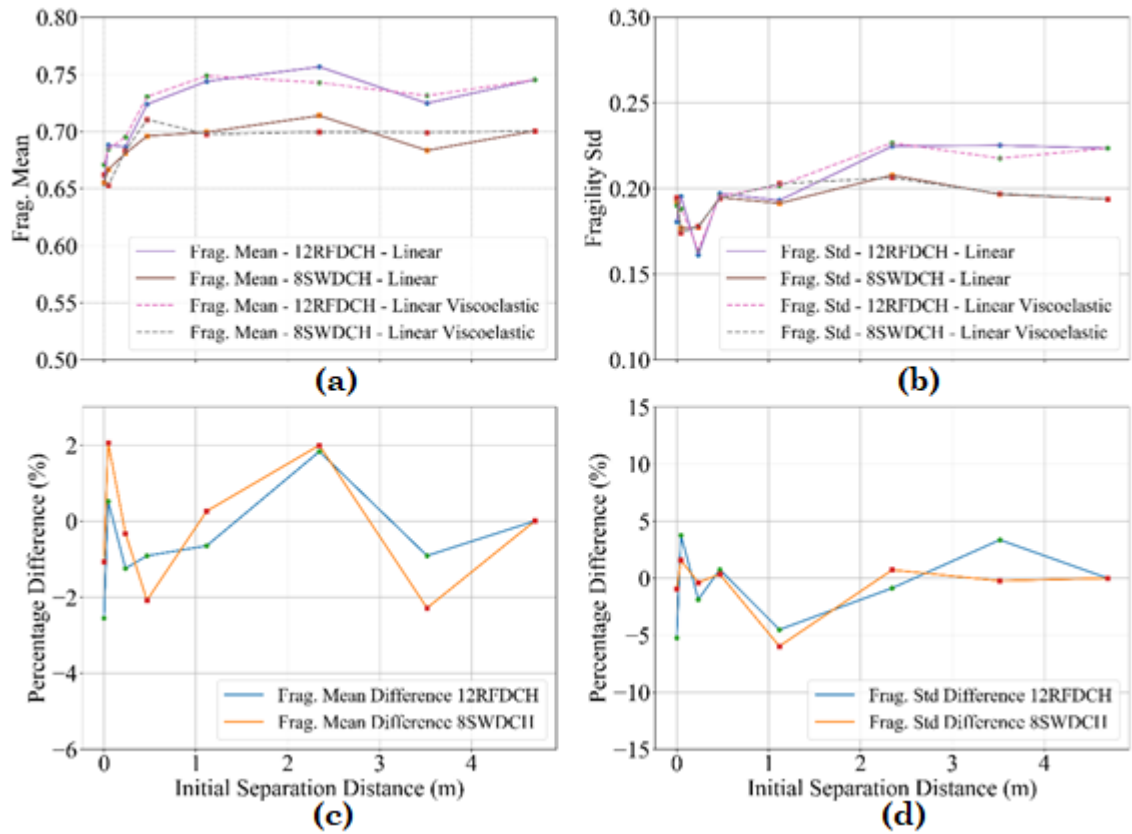


Figure E.8: Pounding between 12RFDCH and 8SWDCH SDOF systems - severe damage limit state and  $K_p = Low$  a) mean values of the fragility models of the two adopted contact models as a function of the initial separation distance b) standard deviation values of the fragility models for the two adopted contact models as a function of initial separation distance c) percentage difference between the mean values of the two adopted contact models as a function of the initial separation distance and b) percentage difference between the standard deviation values of the two adopted contact models as a function of the initial separation distance.

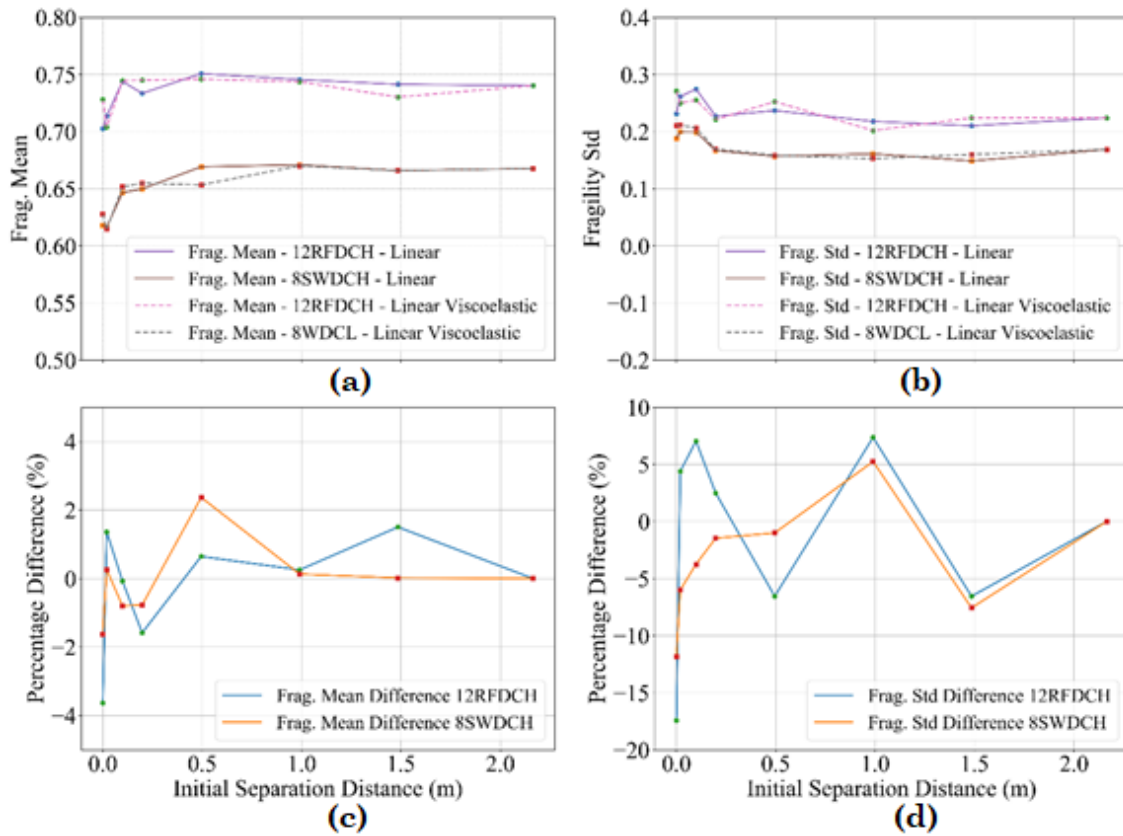


Figure E.9: Pounding between 12RFDCH and 8WDCL SDOF systems - severe damage limit state and  $K_p = high$  a) mean values of the fragility models of the two adopted contact models as a function of the initial separation distance b) standard deviation values of the fragility models for the two adopted contact models as a function of initial separation distance c) percentage difference between the mean values of the two adopted contact models as a function of the initial separation distance and b) percentage difference between the standard deviation values of the two adopted contact models as a function of the initial separation distance.

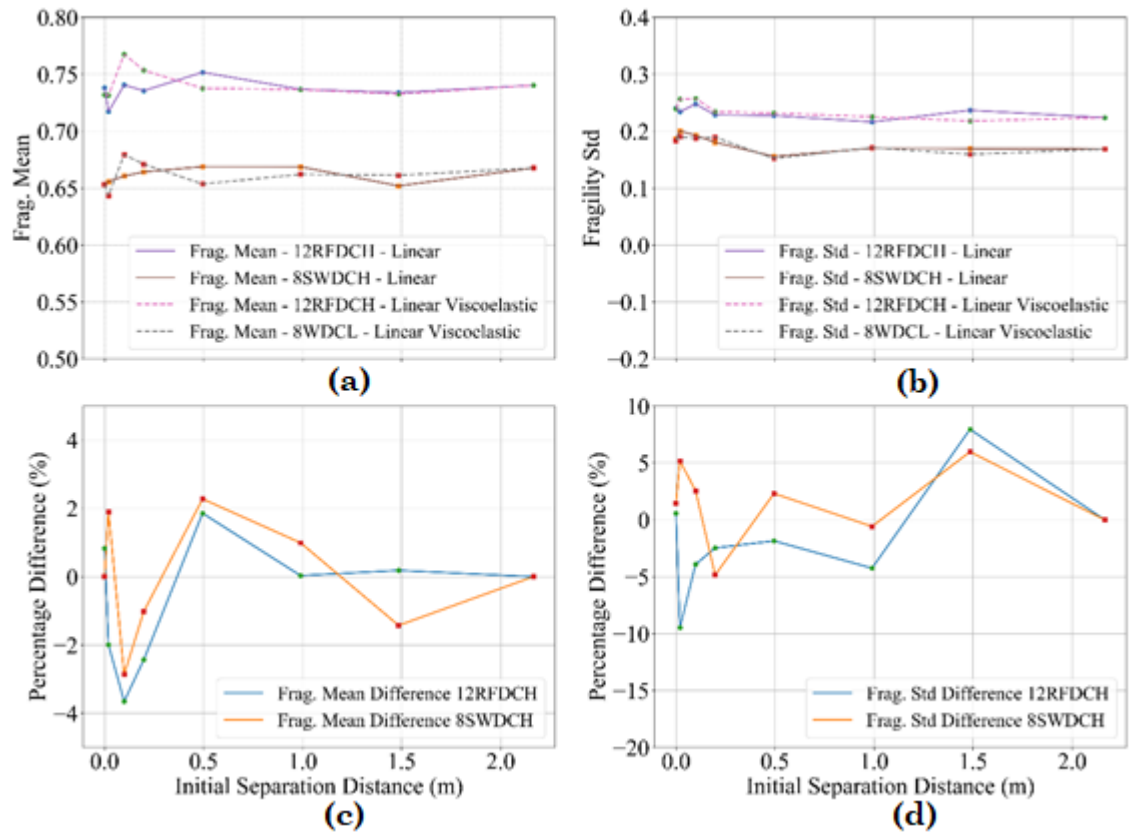


Figure E.10: Pounding between 12RFDCH and 8WDCL SDOF systems - severe damage limit state and  $K_p = Low$  a) mean values of the fragility models of the two adopted contact models as a function of the initial separation distance b) standard deviation values of the fragility models for the two adopted contact models as a function of initial separation distance c) percentage difference between the mean values of the two adopted contact models as a function of the initial separation distance and b) percentage difference between the standard deviation values of the two adopted contact models as a function of the initial separation distance.

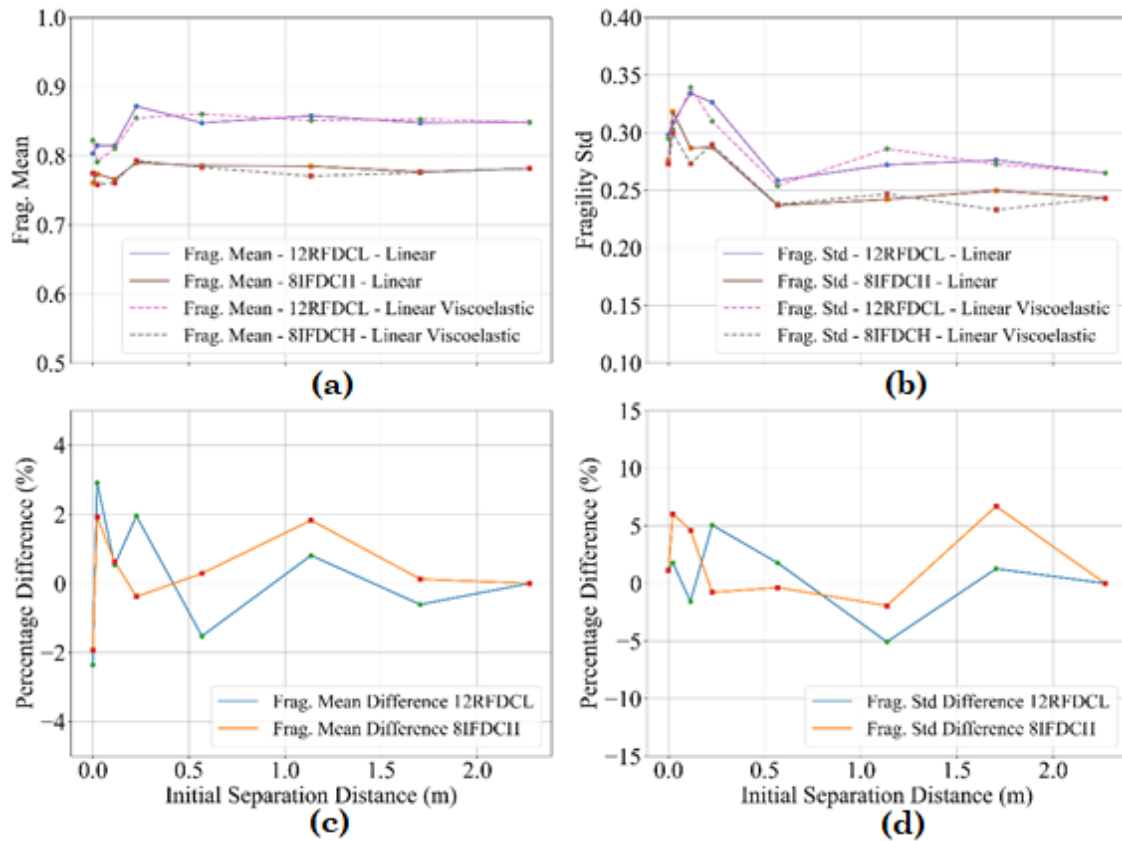


Figure E.11: Pounding between 12RFDCL and 8IFDCH SDOF systems - severe damage limit state and  $K_p = High$  a) mean values of the fragility models of the two adopted contact models as a function of the initial separation distance b) standard deviation values of the fragility models for the two adopted contact models as a function of initial separation distance c) percentage difference between the mean values of the two adopted contact models as a function of the initial separation distance and b) percentage difference between the standard deviation values of the two adopted contact models as a function of the initial separation distance.

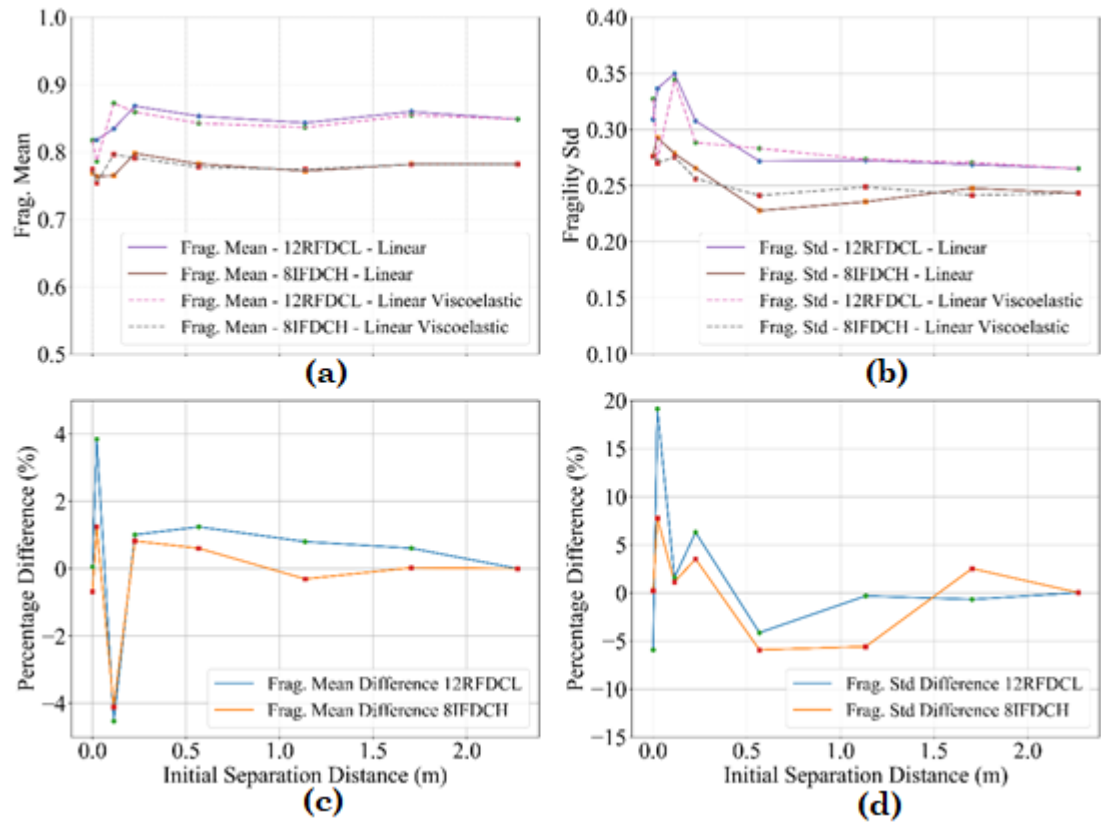


Figure E.12: Pounding between 12RFDCL and 8IFDCH SDOF systems - severe damage limit state and  $K_p = Low$  a) mean values of the fragility models of the two adopted contact models as a function of the initial separation distance b) standard deviation values of the fragility models for the two adopted contact models as a function of initial separation distance c) percentage difference between the mean values of the two adopted contact models as a function of the initial separation distance and b) percentage difference between the standard deviation values of the two adopted contact models as a function of the initial separation distance.

## Appendix F - Pounding Event Heat-maps

Plots of the number of pounding events (upper panel) and the pounding force magnitudes (lower panel) as a function of the seismic intensity.

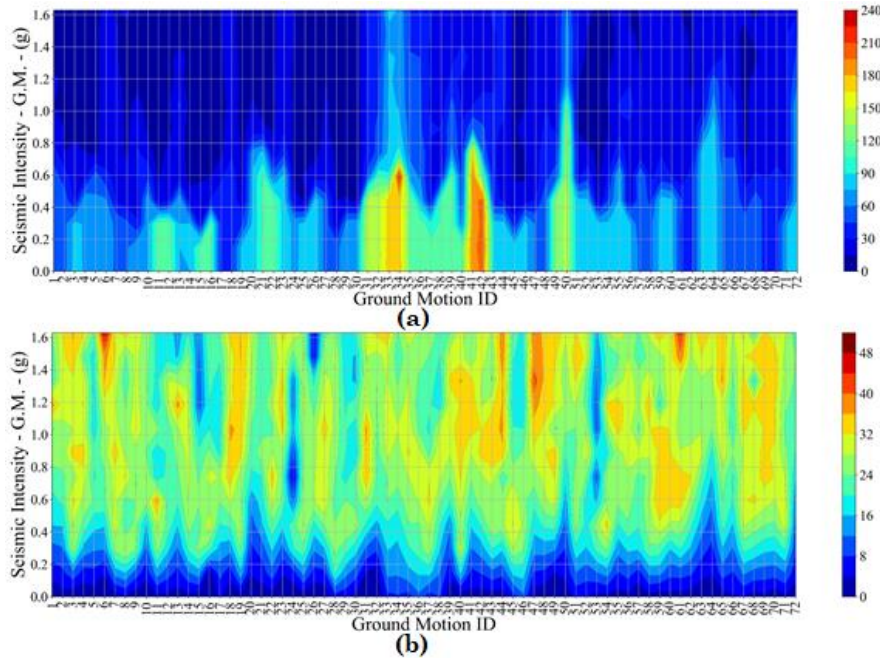


Figure F.1: Pounding between 12RFDCH and 8SWDCH - Linear pounding model - Gap = 0.00 (m) and  $K_p = \text{High}$  a) Number of pounding events per ground motion and intensity level b) Magnitudes of pounding forces per ground motion and intensity level.

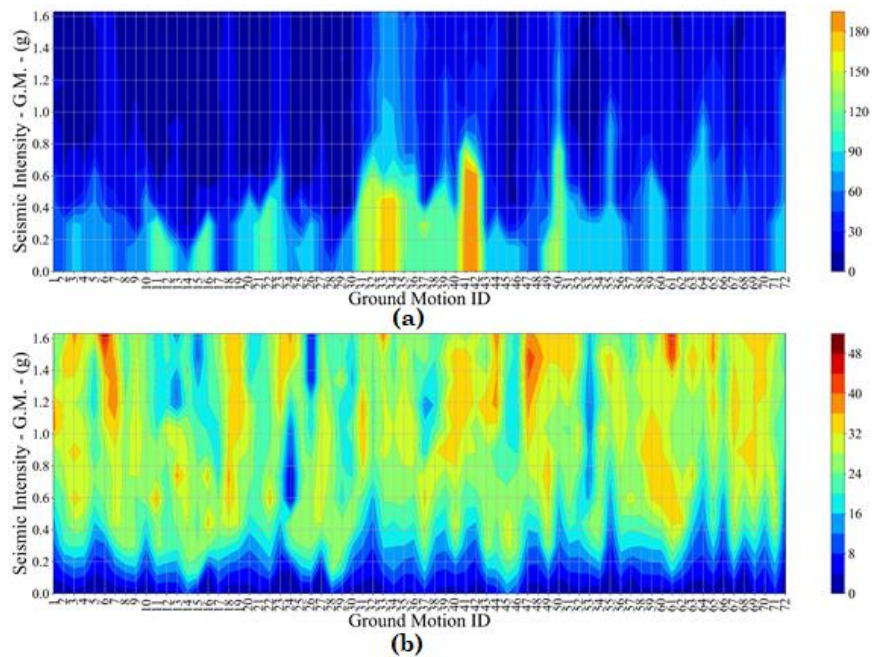


Figure F.2: Pounding between 12RFDCH and 8SWDCH - Linear viscoelastic pounding model - Gap = 0.00 (m) and  $K_p = \text{High}$  a) Number

of pounding events per ground motion and intensity level b) Magnitudes of pounding forces per ground motion and intensity level.

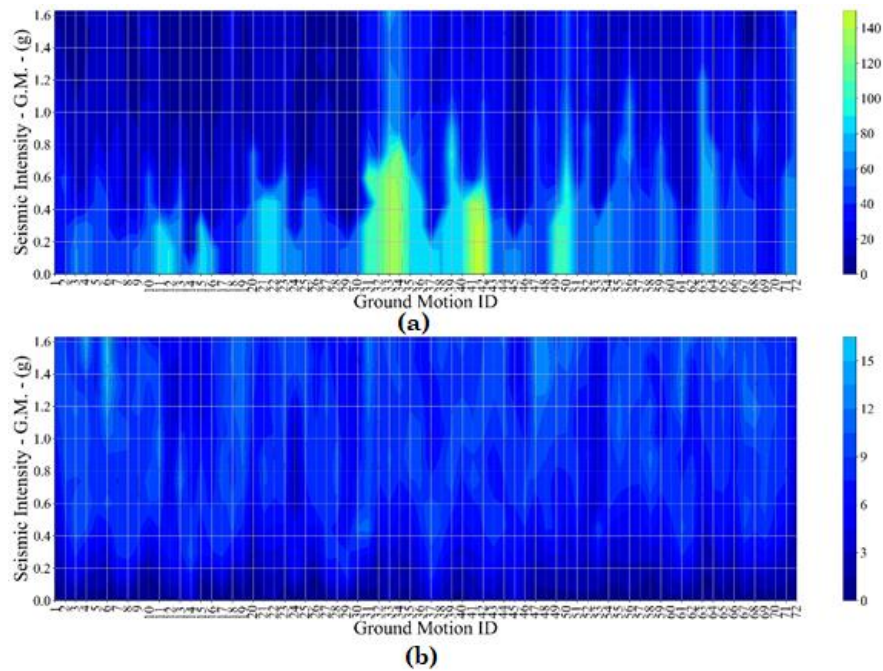


Figure F.3: Pounding between 12RFDCH and 8SWDCH - Linear pounding model - Gap = 0.00 (m) and  $K_p = \text{Low}$  a) Number of pounding events per ground motion and intensity level b) Magnitudes of pounding forces per ground motion and intensity level.

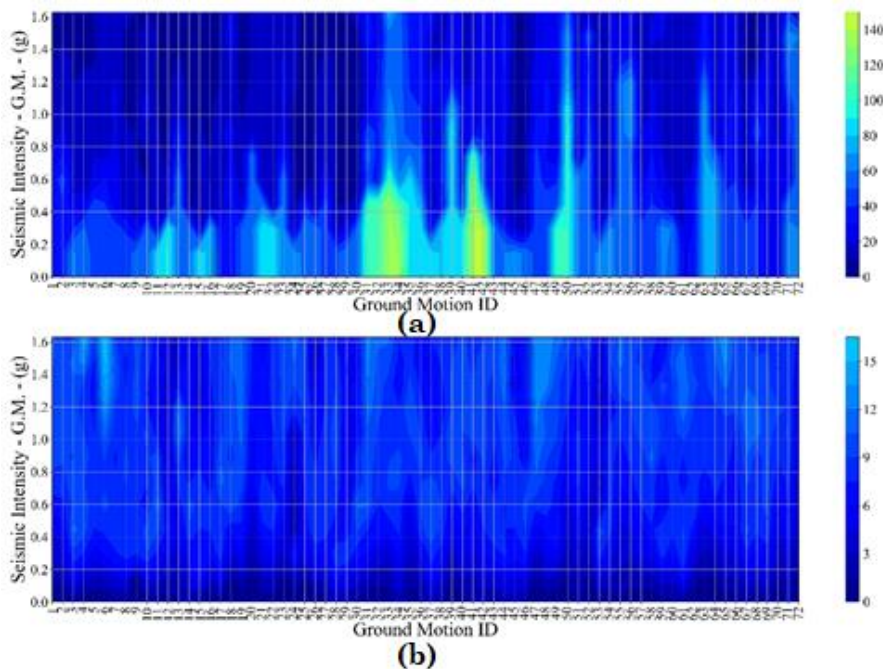


Figure F.4: Pounding between 12RFDCH and 8SWDCH - Linear viscoelastic pounding model - Gap = 0.00 (m) and  $K_p = \text{Low}$  a) Number of pounding events per ground motion and intensity level b) Magnitudes of pounding forces per ground motion and intensity level.

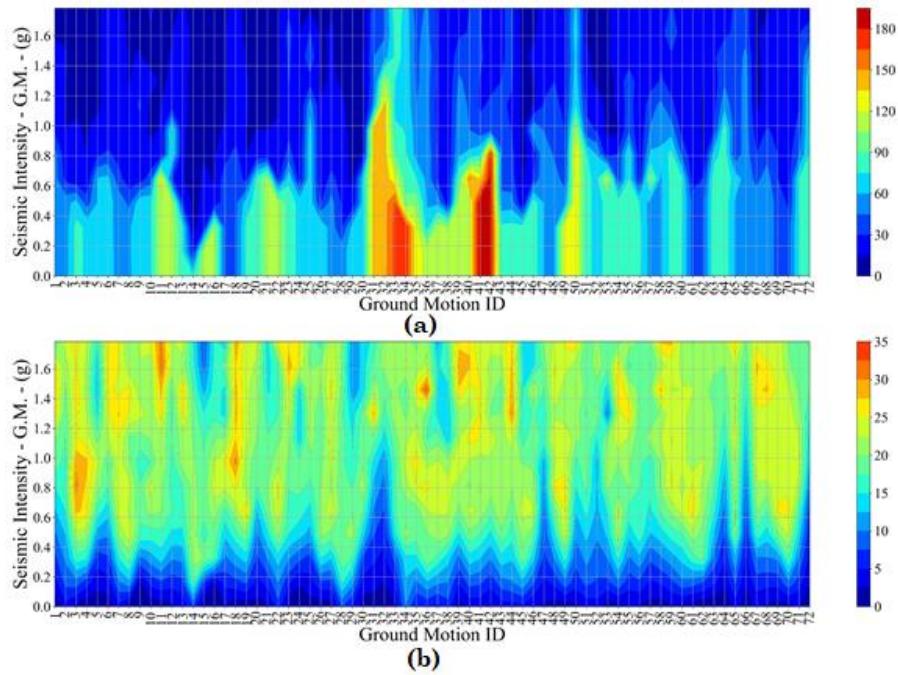


Figure F.5: Pounding between 12RFDCH and 8WDCL - Linear pounding model - Gap = 0.00 (m) and  $K_p = \text{High}$  a) Number of pounding events per ground motion and intensity level b) Magnitudes of pounding forces per ground motion and intensity level.

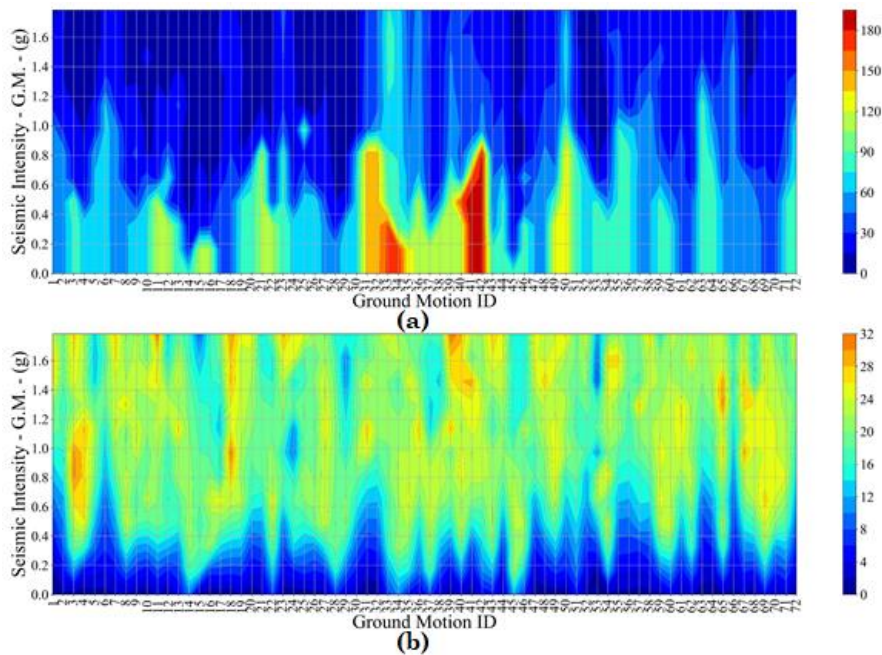


Figure F.6: Pounding between 12RFDCH and 8WDCL - Linear viscoelastic pounding model - Gap = 0.00 (m) and  $K_p = \text{High}$  a) Number of pounding events per ground motion and intensity level b) Magnitudes of pounding forces per ground motion and intensity level.

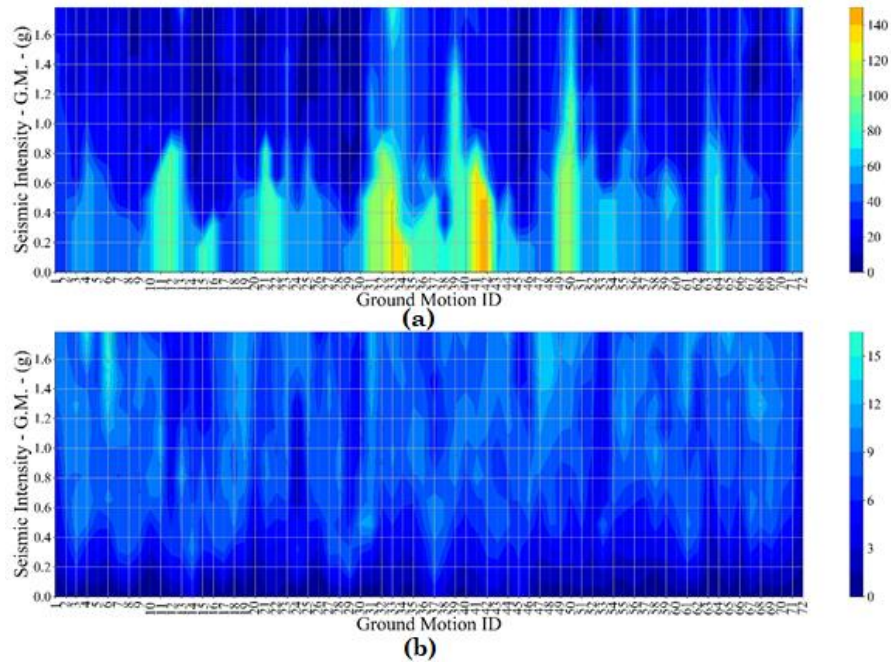


Figure F.7: Pounding between 12RFDCH and 8WDCL - Linear pounding model - Gap = 0.00 (m) and  $K_p = \text{Low}$  a) Number of pounding events per ground motion and intensity level b) Magnitudes of pounding forces per ground motion and intensity level.

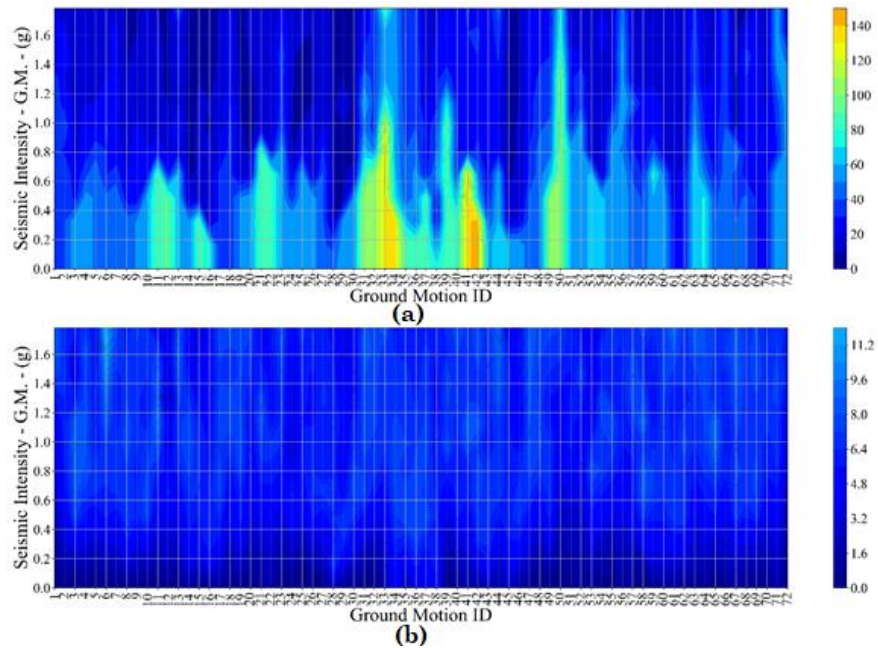


Figure F.8: Pounding between 12RFDCH and 8WDCL - Linear viscoelastic pounding model - Gap = 0.00 (m) and  $K_p = \text{Low}$  a) Number of pounding events per ground motion and intensity level b) Magnitudes of pounding forces per ground motion and intensity level.

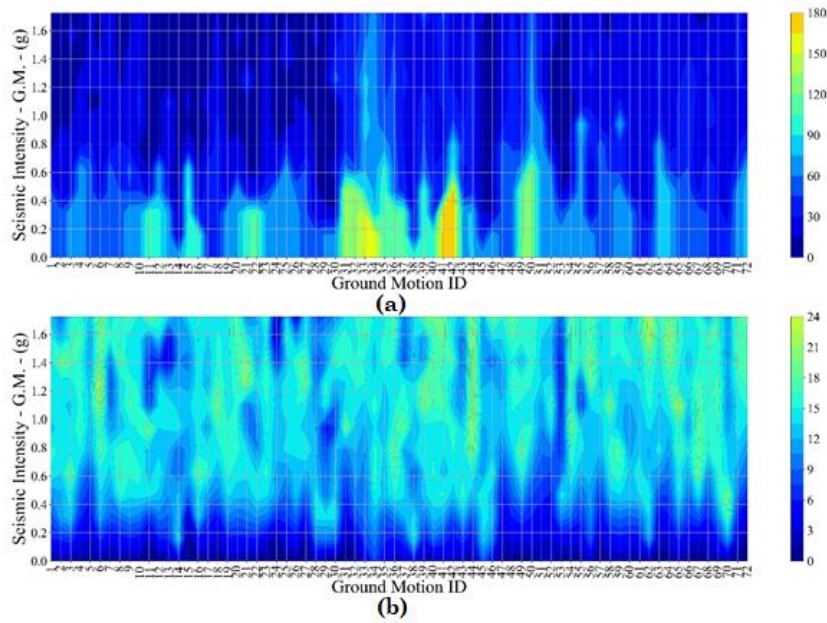


Figure F.9: Pounding between 12RFDCL and 8IFDCH - Pounding forces are modelled by means of the linear pounding model - Gap = 0.00 (m) and  $K_p = \text{High}$  a) Number of pounding events per ground motion and intensity level b) Magnitudes of pounding forces per ground motion and intensity level.

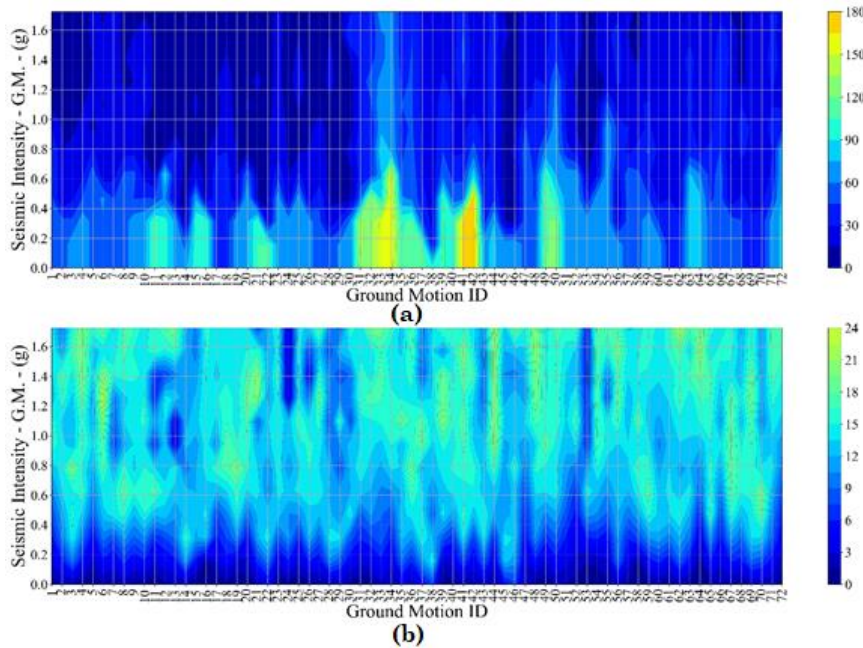


Figure F.10: Pounding between 12RFDCL and 8IFDCH - Linear viscoelastic pounding model - Gap = 0.00 (m) and  $K_p = \text{High}$  a) Number of pounding events per ground motion and intensity level b) Magnitudes of pounding forces per ground motion and intensity level.

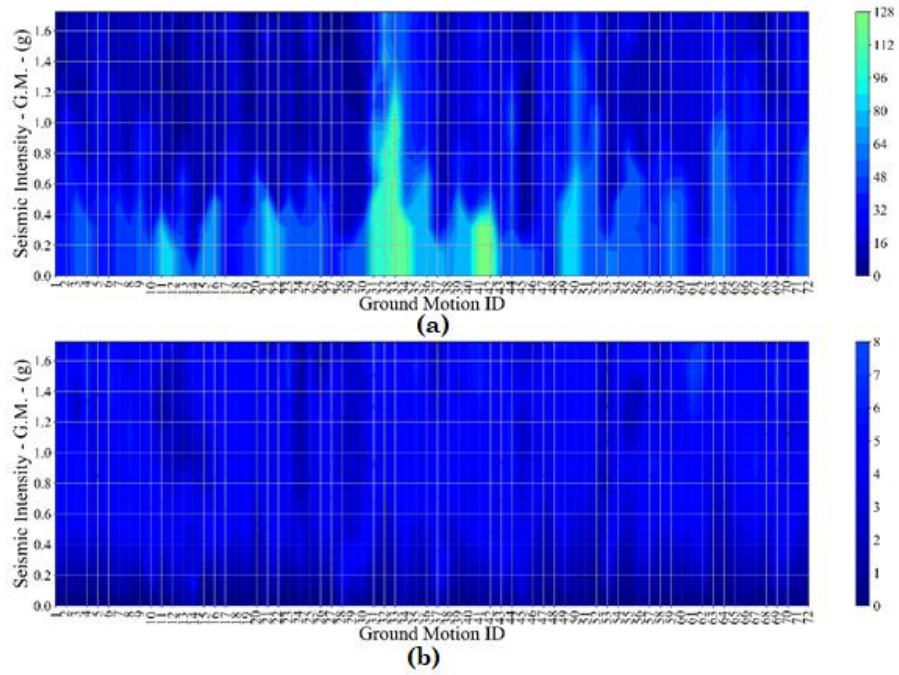


Figure F.11: Pounding between 12RFDCL and 8IFDCH - Linear pounding model - Gap = 0.00 (m) and  $K_p = \text{Low}$  a) Number of pounding events per ground motion and intensity level b) Magnitudes of pounding forces per ground motion and intensity level.

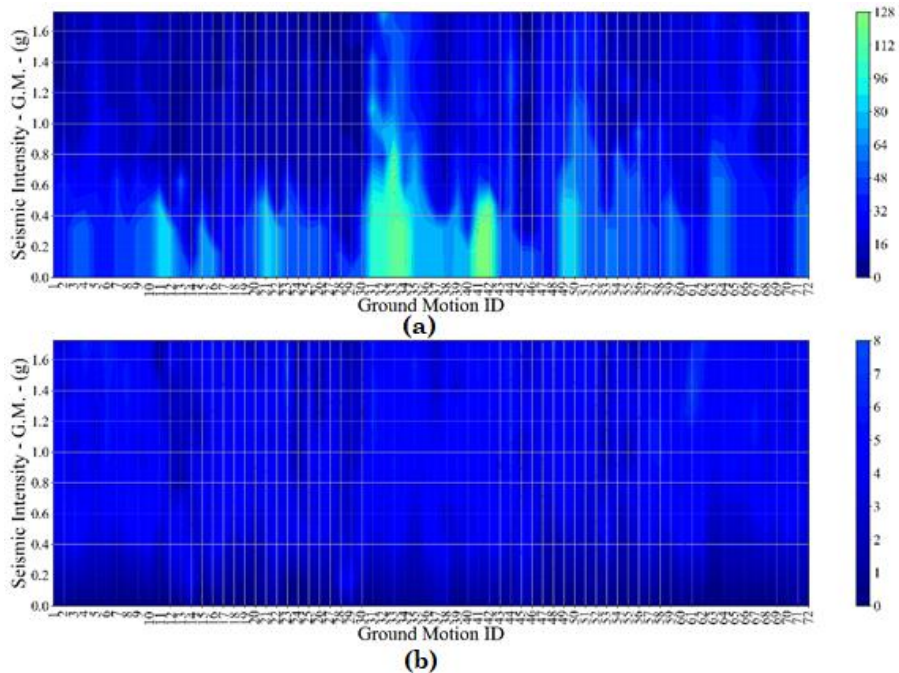


Figure F.12: Pounding between 12RFDCL and 8IFDCH - Linear viscoelastic pounding model - Gap = 0.00 (m) and  $K_p = \text{Low}$  a) Number of pounding events per ground motion and intensity level b) Magnitudes of pounding forces per ground motion and intensity level.

## Appendix G - Co-authored Publications

List of published journal and conference papers co-authored by the candidate.

### ***Journal Publications***

Skrekas, P., Sextos, A. and Giaralis, A. (2014). Influence of bi-directional seismic pounding on the inelastic demand distribution of three adjacent multi-storey R/C buildings. *Earthquakes and Structures*, 6(1), pp.71-87

### ***Conference Publications***

Skrekas, P., and Giaralis, A. (2013) , “Influence of near-fault effects and of incident angle of earthquake waves on the seismic inelastic demands of a typical Jack-Up platform.”, *The Jack-Up conference*, City University London.

Skrekas, P., Giaralis, A. (2012). On the use of incremental dynamic analysis for evaluating the seismic performance of off-shore jack-up platforms. In: *Proceedings of the 6th International ASRANet Conference for Integrating Structural Analysis Risk and Reliability*, London, paper #35.